The role of protein persulfidation in cellular stress response



Doctoral thesis

for

the award of the doctoral degree

of the Faculty of Mathematics and Natural Sciences

of the University of Cologne

submitted by

Dunja Petrovic

2024

The work presented in this dissertation has been performed between October 2018 and September 2024 under the supervision of Dr. Milos Filipovic at the Institute of Cellular Biochemistry and Genetics (Bordeaux, France) and at the Leibniz Institute for Analytical Sciences - ISAS – eV (Dortmund, Germany). This research was supported by the European Research Council (ERC) Consolidator Grant.





European Research Council

Established by the European Commission

Abstract

For centuries, hydrogen sulfide (H_2S) was considered as an important constituent and energy source in early life forms, while in higher organisms it was primarily viewed as a toxic molecule. However, the discovery of its endogenous production in various organisms, including humans, challenged this perspective, revealing that in low doses, H_2S is not only non-toxic but rather essential for proper function of different cell types, tissues, organs and the organism as a whole. Its reactivity, chemical instability and very low concentrations under physiological conditions largely influenced the notion of its minor contribution in more complex organisms.

H_2S is now recognized as an important redox signaling molecule involved in regulation of numerous physiological processes and protein persulfidation, an oxidative post-translational modification of cysteine residues, is postulated to be a main cellular mechanism through which H_2S acts. Persulfidation has been shown to protect proteins from excessive oxidation, regulate cellular stress response, promote survival and influence longevity. Notably, endogenous H_2S production and persulfidation levels diminish with age, leading to impaired cellular function and increased sensitivity to damage.

In this study, we employed model systems such as nematode *C. elegans* and mammalian cells lines to study the importance of H_2S and protein persulfidation in aging and cellular stress responses. We further explored the potential of sulfur-containing dietary compounds to serve as natural H_2S donors to compensate for age-related decline in both H_2S and persulfidation levels.

Using a chemoselective proteomic approach, we monitored persulfidation dynamics throughout the lifespan of *C. elegans*, revealing significant remodeling of the persulfidome at different life stages. The identified proteins were implicated in a wide range of cellular processes, highlighting the importance of persulfidation in this organism.

Additionally, we identified a novel mechanism of action of a known cytoprotective molecule ergothioneine (ET). Through behavioral, high-throughput proteomic and metabolomic as well as kinetic studies, we demonstrated that ET is a new substrate for cystathionine-γ-lyase (CSE), the primary enzyme responsible for endogenous H_2S production. Mostly known for its direct antioxidant properties, our discoveries largely broaden the aspects of ET action. We discovered that ET is metabolized in the cells of higher organisms and exerts life-extending and cytoprotective effects through CSE-mediated H_2S release.

Given the known role of CSE in integrated stress response (ISR), we further investigated the role of H_2S and persulfidation in stress responses related to mitochondria and the Golgi apparatus, organelles particularly vulnerable to oxidative stress. Our findings revealed substantial remodeling of both the proteome and persulfidome, identifying potential persulfidation targets involved in stress adaptation. Furthermore, the absence of CSE increased cellular sensitivity to mitochondrial stress, exacerbating mitochondrial damage and altering ISR dynamics.

Zusammenfassung

Seit Jahrhunderten wurde Schwefelwasserstoff (H_2S) als wichtiger Bestandteil und Energiequelle in frühen Lebensformen betrachtet, während er in höheren Organismen primär als toxisches Molekül angesehen wurde. Die Entdeckung seiner endogenen Produktion in verschiedenen Organismen, einschließlich des Menschen, stellte jedoch diese Sichtweise in Frage. Es zeigte sich, dass H_2S in niedrigen Dosen nicht nur ungiftig ist, sondern vielmehr essenziell für die ordnungsgemäße Funktion verschiedener Zelltypen, Gewebe, Organe und des Organismus als Ganzes. Seine Reaktivität, chemische Instabilität und die sehr niedrigen Konzentrationen unter physiologischen Bedingungen trugen erheblich zu der Annahme bei, dass H_2S nur eine geringe Rolle in komplexeren Organismen spielt.

Heute wird H_2S als ein wichtiges Redox-Signalmolekül anerkannt, das an der Regulierung zahlreicher physiologischer Prozesse beteiligt ist. Die Persulfidierung von Proteinen, eine oxidative posttranslationale Modifikation von Cysteinresten, gilt als der Hauptmechanismus, durch den H_2S auf zellulärer Ebene wirkt. Es wurde gezeigt, dass die Persulfidierung Proteine vor übermäßiger Oxidation schützt, die zelluläre Stressreaktion reguliert, das Überleben fördert und die Langlebigkeit beeinflusst. Bemerkenswerterweise nehmen die endogene H_2S-Produktion und die Persulfidierung im Alter ab, was zu einer Verschlechterung der Zellfunktionen und einer erhöhten Empfindlichkeit gegenüber Schäden führt.

In dieser Studie nutzten wir Modellsysteme wie den Fadenwurm *C. elegans* und Säugetierzelllinien, um die Bedeutung von H_2S und der Proteinpersulfidierung im Alterungsprozess und bei zellulären Stressreaktionen zu untersuchen. Wir untersuchten

außerdem das Potenzial schwefelhaltiger diätetischer Verbindungen, als natürliche H2S-Donoren zu dienen, um den altersbedingten Rückgang sowohl der H_2S- als auch der Persulfidierungsebenen auszugleichen.

Mithilfe eines chemoselektiven proteomischen Ansatzes überwachten wir die Dynamik der Persulfidierung während des Lebenszyklus von *C. elegans* und stellten eine signifikante Umgestaltung des Persulfidoms in verschiedenen Lebensphasen fest. Die identifizierten Proteine waren an einer Vielzahl von zellulären Prozessen beteiligt, was die Bedeutung der Persulfidierung in diesem Organismus unterstreicht.

Darüber hinaus identifizierten wir einen neuartigen Wirkmechanismus des bekannten zytoprotektiven Moleküls Ergothionein (ET). Durch Verhaltens-, proteomische High-throughput-Proteomik- und Metabolomikstudien sowie kinetische Analysen zeigten wir, dass ET ein neues Substrat für die Cystathionin-γ-Lyase (CSE) ist, das primäre Enzym, das für die endogene H_2S-Produktion verantwortlich ist. Unsere Entdeckungen erweitern die bisher bekannten antioxidativen Eigenschaften von ET erheblich. Wir fanden heraus, dass ET in den Zellen höherer Organismen metabolisiert wird und durch CSE-vermittelte H_2S-Freisetzung lebensverlängernde und zytoprotektive Effekte ausübt.

Angesichts der bekannten Rolle von CSE in der integrierten Stressantwort (ISR) untersuchten wir weiter die Rolle von H_2S und der Persulfidierung in Stressreaktionen, die mit Mitochondrien und dem Golgi-Apparat zusammenhängen – Organellen, die besonders anfällig für oxidativen Stress sind. Unsere Ergebnisse zeigten eine beträchtliche Umgestaltung sowohl des Proteoms als auch des Persulfidoms und identifizierten potenzielle Persulfidierungsziele, die an der Stressanpassung beteiligt sind. Zudem erhöhte das Fehlen von CSE die zelluläre Empfindlichkeit gegenüber mitochondrialem Stress, was mitochondriale Schäden verschlimmerte und die Dynamik.

Table of Contents

ABSTRACT ..... **I**

ZUSAMMENFASSUNG ..... **III**

TABLE OF CONTENTS ..... **V**

LIST OF ABBREVIATIONS ..... **VIII**

LIST OF MAIN FIGURES ..... **XIII**

LIST OF SUPPLEMENTARY TABLES ..... **XVI**

1. INTRODUCTION **1**

1.1. PHYSICAL AND CHEMICAL PROPERTIES OF H_2S 2

1.2. H_2S DONORS 3

1.2.1. Thiol-triggered H_2S donors *5*

1.2.2. Hydrolysis-triggered H_2S donors *5*

1.2.3. Other classes of H_2S donors *6*

1.3. MEASUREMENT OF H_2S 7

1.4. ENDOGENOUS H_2S PRODUCTION AND REMOVAL 8

1.4.1. Transsulfuration pathway as a source of H_2S *11*

1.4.2. CSE structure and regulation of its activity *16*

1.5. H_2S IN ACTION 19

1.5.1. H_2S interacts with metal centers *19*

1.5.2. H_2S interacts with RONS *21*

1.6. PROTEIN PERSULFIDATION 22

1.6.1. Chemical properties and reactivity of persulfides *23*

1.6.2. Methods for detecting persulfides *25*

1.6.3. Persulfide formation *30*

1.6.4. Persulfide removal in biological systems *36*

1.7. PHYSIOLOGICAL ROLES OF H_2S AND PROTEIN PERSULFIDATION 37

1.8. ERGOTHIONEINE, MORE THAN JUST AN ANTIOXIDANT? 41

1.8.1. Chemical properties of ergothioneine *42*

1.8.2. Ergothioneine synthesis ... *42*

1.8.3. Ergothioneine reactivity ... *45*

1.8.4. Ergothioneine catabolism ... *47*

1.8.5. Cellular uptake of ergothioneine ... *48*

1.8.6. Physiological roles of ergothioneine ... *50*

1.9. *C. ELEGANS*, TINY BUT POWERFUL MODEL SYSTEM ... 54

1.9.1. Endogenous production of H_2S in C. elegans ... *55*

1.9.2. Effects of exogenous H_2S on C. elegans ... *57*

1.10. INTERPLAY BETWEEN H_2S AND AGING PROCESS ... 61

1.10.1. H_2S as an anti-aging molecule ... *64*

1.10.2. H_2S effect on proteostasis in the context of aging ... *64*

1.11. ROLE OF H_2S IN CELLULAR STRESS RESPONSE ... 66

1.11.1. Integrated stress response ... *67*

1.11.2. ISR and mitochondria ... *70*

1.11.3. ISR activation in ER and Golgi ... *74*

1.11.4. Role of CSE in ISR ... *74*

2. PROJECT AIMS ... 78

3. ERGOTHIONEINE IMPROVES HEALTHSPAN OF AGED ANIMALS BY ENHANCING CGPDH ACTIVITY THROUGH CSE-DEPENDENT PERSULFIDATION. ... 79

3.1. ABSTRACT ... 82

3.2. INTRODUCTION ... 84

3.3. RESULTS ... 85

3.3.5. Ergothioneine improves healthspan and lifespan of C.elegans ... *85*

3.3.6. Ergothioneine is a substrate for CSE ... *95*

3.3.7. Ergothioneine's beneficial effects are CSE-dependent ... *103*

3.3.8. Ergothioneine-induced GDPH persulfidation improves muscle health ... *110*

3.4. DISCUSSION ... 119

3.5. LIMITATIONS OF THE STUDY ... 121

3.6. MATERIAL AND METHODS ... 122

3.6.1. Experimental models and subject details 126

3.6.2. Method details 128

3.6.3. Quantification and statistical analysis 159

3.7. REFERENCES 160

4. AGE-INDUCED PERSULFIDATION CHANGES IN *C. ELEGANS* 167

4.1. INTRODUCTION 168

4.2. RESULTS 169

4.3. DISCUSSION 181

4.4. EXPERIMENTAL METHODS 186

4.5. REFERENCES 192

5. ROLE OF H_2S AND PROTEIN PERSULFIDATION IN CELLULAR STRESS RESPONSE 195

5.1. INTRODUCTION 196

5.2. RESULTS 197

5.3. DISCUSSION 210

5.4. EXPERIMENTAL METHODS 214

5.5. REFERENCES 222

6. CONCLUSIONS AND FUTURE PERSPECTIVES 225

REFERENCES 229

List of abbreviations

$^{\bullet}NO$	Nitric oxide
$^{\bullet}NO_2$	Nitrogen dioxide
$^1O_2$	Singlet oxygen
3-MP	3-mercaptopyruvate
3-NP	3-nitropropionic acid
ABC	ATP-binding cassette
AdoMet	Adenosylmethionine
ALT	L-alanine transaminase
ATF4	Activating transcription factor 4
BTA	Biotin thiol assay
CA	carbonic anhydrase
CAT	Cysteine aminotransferase
CBS	Cystathionine β-synthase
CcO	Cytochrome c oxidase
CO	Carbon monoxide
CO_2	Carbon dioxide
$CO_3^{\bullet-}$	Carbonate radical
CoQ	Coenzyme Q
COS	carbonyl sulfide
CREB	cAMP responsive element binding protein 1
CSE, CTH	Cystathionine γ-lyase
CuAAC	Copper(I)-catalyzed azide-alkyne cycloaddition
CYS	Cysteine synthase
Cys-SSH	Cysteine persulfide
DADS	Diallyl disulfide
DAO	D-amino acid oxidase
DAS	Diallyl sulfide
DATS	Diallyl trisulfide
DCPBio1	3-(2,4-dioxocyclohexyl) propyl biotin

DELE1L	Long form of DELE1
DELE1S	Short form of DELE1
DMD	Duchenne muscular dystrophy
DTTs	1,2-Dithiole-3-thiones
EGF	Epidermal growth factor
EGFR	Epidermal growth factor receptor
eIF2	Eukaryotic translation initiation factor 2
eIF2α	Eukaryotic translation initiation factor 2, alpha subunit
ER	Endoplasmic reticulum
ESSE	ET disulfide
ET	Ergothioneine
ETC	Electron transport chain
ETDO	Thiol deoxygenase
ETSD	ET sulfinic acid desulfinase
$ETSO_2$	ET sulfinic acid
$ETSO_3$	ET sulfonic acid
FDA	The Food and Drug Administration
FTX1	Frataxin-1
GCN2	General control non-derepressible 2
GIT	Gastrointestinal tract
GR	Glutathione reductase
Grx	Glutaredoxin
GSH	Glutathione
GSSH	Glutathione persulfide
GTP	Guanosine 5’-triphosphate
GYY4137	morpholin-4-ium metoxyphenyl(morpholino) phosphino-dithioate
H_2O	Water
H_2O_2	Hydrogen peroxide
H_2S	Hydrogen sulfide
H_2SO_3	Sulfurous acid
HCN	Hydrogen cyanideo
Hcy-SSH	Homocysteine persulfide

HD	Huntington’s disease
HIF-1	Hypoxia-inducible factor
$HO^{\bullet}$	Hydroxyl radical
HOCl	Hypochlorite
HPLC	high-performance liquid chromatography
HRI	Heme-regulated eIF2a kinase
HS^{-}	Hydrosulfide anion
HSR	Heat shock response
$HSSnS^{-}$	Polysulfide
IL-6	Interleukin 6
IMM	Inner mitochondrial membrane
IMS	Intermembrane space
ISR	Integrated stress response
K^{+}	Potassium ion
K_{ATP}	ATP-dependent potassium channel
LMW	Low molecular weight
LPS	Lipopolysaccharide
Met-tRNAi	Methionyl-initiator tRNA
MFN1	Mitofusin 1
MFN2	Mitofusin 2
MGL	Methionine γ-lyase
MM	Mitochondrial matix
mRNA	Messenger RNA
MS	mass spectrometry
MSBT	methylsulfonyl benzothiazole
MSBT-A	(benzothiazole-2-sulfonyl)-acetic acid
MST, MPST	Mercaptopyruvate sulfurtransferase
Na_2S	Sodium sulfide
NaHS	Sodium hydrogen sulfide
NBD-Cl	4-chloro-7-nitrobenzofuran
NH_3	Ammonia
Nrf2	Nuclear factor erythroid 2-related factor 2

NSAID	Non-steroidal anti-inflammatory drug
O_2	Oxygen
$O_2^{\bullet-}$	Superoxide
OCTN1	Organic cation transporter N1
OMM	Outer mitochondrial membrane
$ONOO^-$	Peroxynitrite
PDO, ETHE1	Persulfide dioxygenase
PERK	PKR-like ER kinase
PKR	Double-stranded RNA-dependent protein kinase
PLP	Pyridoxal 5'-phosphate
PP1	Protein phosphatase 1
PP1c	Protein phosphatase 1, catalytic subunit
PPG	Propargylglycine
PTM	Post-translational modification
PTP1B	Protein tyrosine phosphatase 1B
QTRP	Quantitative thiol reactivity profiling
RNAi	RNA interference
RONS	Reactive oxygen and nitrogen species
ROS	Reactive oxygen species
RS^-	Thiolate
RSH	Thiols
RSO_2H	Sulfinic acid
RSO_3H	Sulfonic acid
RSOH	Sulfenic acids
RSS^-	Anionic form of persulfide
RSSH	Protein or LMW persulfide
$RSSO_2H$	Perthiosulfinic acid
$RSSO_3H$	Perthiosulfonic acid
RSSR	Protein or LMW disulfide
S/T	serine/threonine
$S^{\bullet-}$	Sulfanyl radical
S_2^-	Sulfide anion

SAM	S-adenosylmethionine
SCA3	Spinocerebellar ataxia 3
sGC	Soluble guanylate cyclase
SIR 2.1	Sirtuin 2.1
SIRT1	Sirtuin 1
SKN-1	Skinhead-1
SO_2	Sulfur dioxide
SP1	Specificity protein 1
SQR	Sulfide quinoneoxidoreductase
SRX	Sulfiredoxin
SUOX	Sulfite oxidase
TC	Ternary complex
TMA	Trimethylamine
TNFα	Tumor necrosis factor alpha
TPP	Triphenylphosphonium group
tRNA	Transfer RNA
Trx	Thioredoxin
TrxR	Thioredoxin reductase
TST	Rhodanese
UPR	Unfolded protein response
UPRmt	Mitochondrial unfolded protein response
UV	Ultraviolet light
WT	wild type
α-KB	α-ketobutyrate

List of main figures

Figure 1.1 Overview of different classes of H_2S donors. 4

Figure 1.2 H_2S metabolism within the cell. 10

Figure 1.3 Reactions catalyzed by cystathionine β-synthase (CBS). 12

Figure 1.4 Reactions catalyzed by cystathionine γ-lyase (CSE). 13

Figure 1.5 CSE and CBS-dependent generation of low molecular (LMW) persulfides. 15

Figure 1.6 Tetrameric structure of CSE and close look at its active site (PDB:2NMP). 17

Figure 1.7 Different mechanisms of H_2S action. 19

Figure 1.8 Concentration dependent stimulation or inhibition of cytochrome c oxidase (CcO) by H_2S. 20

Figure 1.9 Cysteine residues are prone to wide range of oxidative posttranslational modifications. 23

Figure 1.10 Methods for persulfide detection based on its nucleophilic properties. 29

Figure 1.11 Different mechanisms of persulfide formation. 30

Figure 1.12 Transpersulfidation as an integral part of iron-sulfur cluster and thionucleoside formation. 35

Figure 1.13 TRX-dependent depersulfidation. 37

Figure 1.14 Examples of biological processes regulated by H_2S and protein persulfidation. 40

Figure 1.15 Tautomeric forms of ergothioneine (ET). 42

Figure 1.16 Two distinct ET synthetic pathways. 44

Figure 1.17 Different metabolites derived from ET. 46

Figure 1.18 Different ET catabolic pathways 47

Figure 1.19 ET accumulation in different organs and within the cells. 49

Figure 1.20 Beneficial effects of ET. 53

Figure 1.21 *C. elegans* lifecycle 55

Figure 1.22 *C. elegans* senses H_2S. Survival and lifespan extending properties of exogenously administrated H_2S are dependent on SIRT2.1, HIF-1 and SKN-2 activity. 59

Figure 1.23 The hallmarks of aging. 63

Figure 1.24 Potential protective mechanism of protein persulfidation 65

Figure 1.25 Activation of integrated stress response (ISR). 69

Figure 1.26 Mitochondrial ISR. 73

Figure 1.27 Role of CSE in cellular stress response. 76

Figure 3.1. Ergothioneine (ET) improves lifespan and healthspan of *C. elegans*. . 89

Figure 3.2. Ergothioneine is a substrate for cystathionine gamma lyase (CSE) to produce H_2S. 99

Figure 3.3. Lifespan and healthspan benefits of ergothioneine treatment are CSE dependent. 107

Figure 3.4. Ergothioneine increases the NAD^+ levels and improves the muscle health by causing persulfidation of glycerol 3-phosphate dehydrogenase. 116

Figure 4.1 Expression profiles of genes encoding for putative H_2S producing enzymes in *C. elegans* genome. 171

Figure 4.2 Persulfidome remodeling in aging *C. elegans.* 173

Figure 4.3 Persulfidome remodeling in aging *C. elegans* and its correlation to the changes in total proteome. 175

Figure 4.4 Aging induces profound remodeling of *C. elegans* proteome. 178

Figure 4.5 Age-specific changes in *C. elegans* proteome. 180

Figure 5.1 Chemoproteomic analysis of protein persulfidation reveals substantial alternations in persulfidome upon monensin-induced Golgi stress. 199

Figure 5.2 Effects of persulfidome normalization to total protein levels. 203

Figure 5.3 Proteome remodeling in monensin-induced Golgi stress. 204

Figure 5.4 Mitochondrial stress increases persulfidation in CSE-dependent manner. 207

Figure 5.5. Treatment with rotenone significantly affects mitochondrial morphology. 209

List of supplementary tables

Chapter 3:

Supplementary Table S3.1. Lifespan quantification.

Supplementary Table S3.2. RNAseq analysis of ET treated D10 worms.

Supplementary Table S3.3. Full proteome analysis of ET treated D10 worms.

Supplementary Table S3.4. RNAseq analysis of ET treated D4 worms.

Supplementary Table S3.5. Full proteome analysis of ET treated D4 worms.

Supplementary Table S3.6. Persulfidome analysis of ET treated D10 worms.

Supplementary Table S3.7. Thermal proteome profilling.

Chapter 4:

Supplementary Table S4.1. Persulfidome analysis of aging worms.

Supplementary Table S4.2. Total proteome analysis of aging worms.

Chapter 5:

Supplementary Table S5.1. Persulfidome analysis of MEF cells treated with monensin.

Supplementary Table S5.2. Persulfidome normalized to total proteome of monensin treated MEF.

Supplementary Table S5.2. Total proteome of MEF cells treated with monensin.

1. Introduction

Hydrogen sulfide (H_2S) played a pivotal role in the development of life on Earth. Reducing power of this molecule along with hydrogen cyanide (HCN) and ultraviolet light (UV), was sufficient to synthetize precursors of biomolecules such as lipids, amino acids and ribonucleotides (1). Beyond its role in early synthetic processes, H_2S has long served as a vital source of metabolic energy in green and purple bacteria (2). Its significance in higher organisms was neglected for centuries as early research was primarily devoted to toxic properties of H_2S. The discovery of endogenous H_2S production and its high concentrations in organs such as brain, liver and kidney shed light on the potential physiological roles of this gas. A pioneering study at the end of 20^{th} century demonstrated that H_2S can modulate synaptic signaling in the brain and opened the door to ever growing field of H_2S research (3). Nowadays H_2S has been acknowledged as an endogenous signaling molecule that plays a fundamental role in regulation of numerous physiological processes including smooth muscle relaxation, protection against myocardial ischemic injury, inflammation regulation and induction of suspended-like animation state in mice, among the others (4–7).

Even with all the current knowledge in our hands, the mechanisms by which H_2S mediates its diverse physiological roles remains elusive. In addition to its direct actions, such as scavenging of reactive oxygen and nitrogen species (RONS) or interaction with metal centers, H_2S can also modulate cellular signaling and protein function through post-translational modification of cysteine residues, known as persulfidation (2).

1.1. Physical and chemical properties of H_2S

H_2S is a small covalent hydride, similar to water (H_2O), although with slightly smaller bond angles compared to H_2O (92° versus 104°) (8). Due to sulfur's lower electronegativity and greater polarizability compared to oxygen, H_2S exhibits weaker intermolecular interactions. Consequently, H_2S is a gas at room temperature and normal pressure, compared to liquid state of H_2O under the same conditions. H_2S is a water soluble, weak diprotic acid that exists in fast equilibrium with [H_2S], hydrosulfide anion [HS^-] and sulfide anion [S^{2-}]:

$$H_2S \rightleftharpoons HS^- + H^+ \quad (1)$$

$$HS^- \rightleftharpoons S^{2-} + H^+ \quad (2)$$

In aqueous solution, the pK_{a1} is within physiological range (6.76 at 37 °C) [Eq. (1)] while pK_{a2} value is significantly higher (17-19) [Eq. (2)], suggesting that in the cellular environment (pH of 7.4 and 37 °C), H_2S is predominately present in its deprotonated form HS^- (~80%) while the concentration of S^{2-} is negligible (2,9,10). Since both pK_a values vary with the temperature and salinity, failure to account for these parameters can dramatically affect the expected amount of dissolved H_2S (11).

Besides its solubility in water, H_2S is also highly soluble in various lipophilic solvents, allowing it to freely permeate biological membranes without the need for transporters. H_2S can be therefore easily taken up by the cells and could act both locally and remotely from the place of its generation (12,13).

H_2S is a highly toxic and flammable gas with standard dose-dependent toxicity curve. Exposure to 10 ppm can cause eye-soreness, 100 ppm H_2S leads to olfactory loss and concentrations exceeding 500 ppm are lethal (2).

1.2. H_2S donors

A deeper understanding of the physiological roles of H_2S was enabled through its exogenous delivery in different model systems. Administration of sulfide salts, sodium sulfide (Na_2S) and sodium hydrogen sulfide (NaHS) was important in uncovering the roles of H_2S as a signaling molecule, however several classes of donors have since been developed to overcome the limitations of these H_2S sources (14–16). Sodium salts are solid analogs of the gas, leading to immediate release of H_2S upon dissolution, without possibility to regulate the duration and concentration of released H_2S. Use of high doses reported in the literature leads therefore to instant boost to supraphysiological H_2S concentrations followed by its rapid drop, in contrast to tightly regulated low endogenous H_2S levels (2,17). A need for more controlled exogenous supplementation which is mirrored in defined dose, duration and location of released H_2S led to discovery and constant improvement of naturally and synthetically produced donors. Possibility to mimic physiological conditions of H_2S production and removal led to better understanding of possible roles of H_2S within a cell but also on the organismal level.

To date, numerous classes of donors with different mechanisms of H_2S release have been reported (Figure 1.1). The release can be triggered by reactions with nucleophiles such as thiols, by hydrolysis, through enzymatic activation or some other reactions (2,17). H_2S donors also have certain limitations, often related to the unclear chemistry of H_2S release, their stability or potential side reactions which can confound the observed outcomes. Consequently, continuous improvement of existing donors along with the development of new molecules and a more thorough characterization of their roles in different biological contexts is essential to advancing the future use of H_2S-based therapeutics. It is important to note that despite all efforts in H_2S donor development none

of the currently available compounds could fully mimic the spatio-temporal release and physiological effects akin to endogenously produced H_2S.

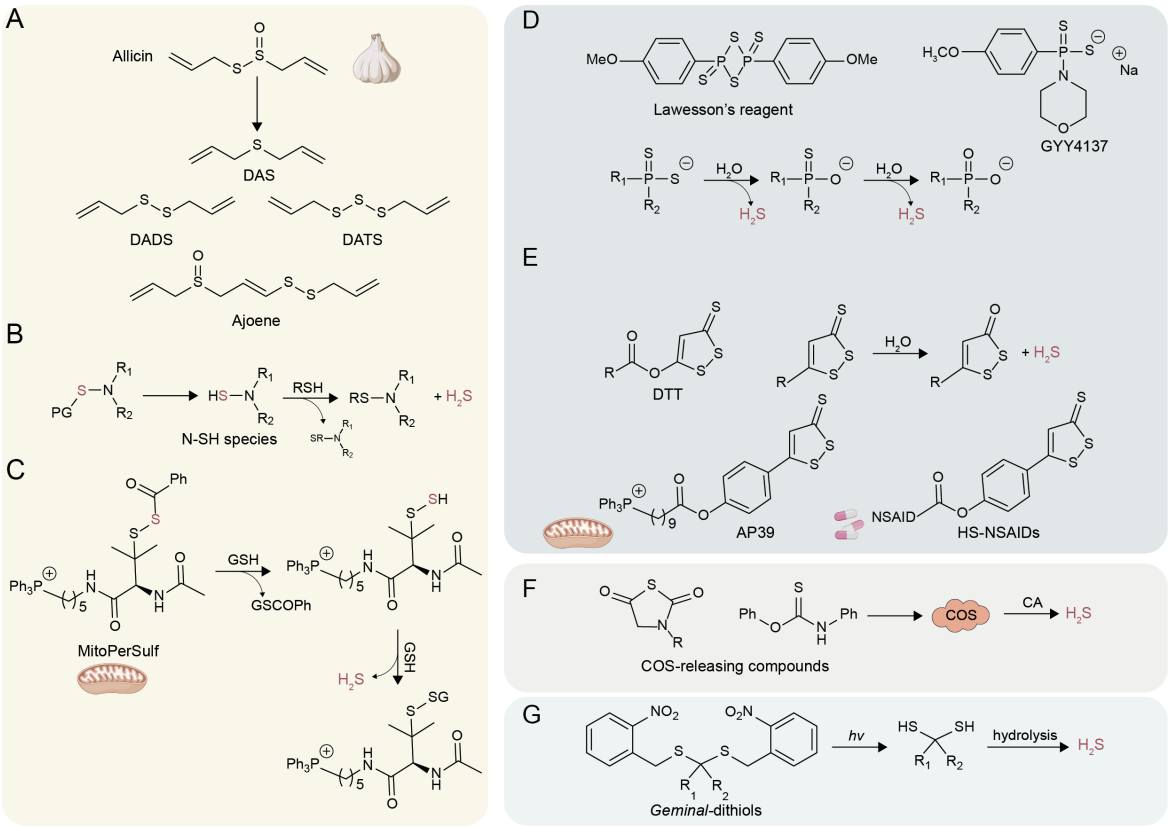


Figure 1.1 Overview of different classes of H_2S donors.

(**A**) DAS, DADS, DATS and ajoene are thiol-activated H_2S releasing compounds found in garlic. (**B**) An example of synthetic thiol-activated donor based on N-mercapto template (N-SH) species with the proposed mechanism of H_2S release. PG refers to a protective group added to enhance the stability of the molecule and protect mercapto group. (**C**) MitoPerSulf is a thiol-activated H_2S donor which accumulates in mitochondria due to the presence of triphenylphosphonium (TPP) group. (**D**) Chemical structures of Lawesson's reagent and its derivative GYY4137 as examples of hydrolysis triggered H_2S donors. Proposed mechanism of H_2S release from GYY4137, the most widely used donor. (**E**) Another group of hydrolysis-triggered donors are 1,2-dithiole-3-thiones (DTTs). They can be coupled to nonsteroid anti-inflammatory drugs (NSAID) or TPP moiety (AP39) which directs them to mitochondria. (**F**) COS-releasing compounds are indirect H_2S donors releasing COS which forms H_2S upon reaction with carbonic anhydrase (CA). (**G**) Geminal-dithiols as an example of light-triggered H_2S donors.

1.2.1. Thiol-triggered H_2S donors

Naturally occurring thiosulfinates present in garlic such as allicin can be precursors of H_2S-releasing compounds. Byproducts of allicin breakdown, diallyl disulfide (DADS), diallyl sulfide (DAS), diallyl trisulfide (DATS) and ajoene release H_2S in the presence of thiols (18) (Figure 1.1A). Although efficient, their poor solubility in water and lack of chemical flexibility led to synthesis of compounds with the same mode of action (17). Thiol-triggered H_2S donors were among the first synthetic donors to be developed. Manipulation of their chemical structures can finely tune H_2S-releasing properties in the presence of thiols (Figure 1.1B). High abundance of endogenously produced thiols such as glutathione (GSH) and cysteine make these compounds relevant chemical tools to study H_2S in biological systems. On the other hand, reaction with thiols can lead to formation of other reactive sulfur-containing byproducts which can also act as signaling molecules and therefore mask the real effects coming from H_2S. Recently, a new mitochondria-targeted donor MitoPerSulf has been developed. Presence of triphenylphosphonium group (TPP) enables its accumulation in mitochondria and formation of H_2S upon reaction with mitochondrial thiols (Figure 1.1C). MitoPerSulf administration and rapid generation of mitochondrial H_2S showed protective effects against cardiac ischemia reperfusion injury (19).

1.2.2. Hydrolysis-triggered H_2S donors

Lawesson’s reagent and its derivative morpholin-4-ium metoxyphenyl (morpholino) phosphino-dithioate (GYY4137) have phosphorodithioate core structure which releases H_2S through spontaneous hydrolysis in aqueous solution (Figure 1.1D). GYY4137, a

water-soluble form of Lawesson's reagent and a widely used cytoplasmic donor in biological studies, releases H_2S in a pH-dependent manner, with lower pH increasing the rate of release. Its protective effects have been described across different species and pathological conditions (20–23). GYY4137 served as a backbone for synthesis of other compounds which releases H_2S in a more controlled way (24,25). JK donors undergo intramolecular cyclization in slightly acidic conditions (pH ≤ 6) which promotes slow and more controllable H_2S production. Administration of this donor proved to have cytoprotective effects under oxidative stress as well as cardioprotective effects in ischemia-reperfusion injury characterized by reduced pH at the place of injury (24).

1,2-Dithiole-3-thiones (DTTs) present another class of hydrolysis-triggered H_2S donors (Figure 1.1E). Ease of synthesis and possibility to couple different moieties such as non-steroidal anti-inflammatory drugs (NSAIDs) or adenosine significantly expand their possible purposes (2). One example is AP39, a DTT derivative coupled with TPP group which enables its accumulation in mitochondria and localized H_2S release (26). Nanomolar and even picomolar AP39 concentrations proved to be sufficient to improve health span in *C. elegans*, preserve mitochondrial function, increase cellular persulfidation levels as well as resistance to oxidative stress (27–31).

1.2.3. Other classes of H_2S donors

H_2S can be also released from carbonyl sulfide (COS) through activity of ubiquitously present enzyme carbonic anhydrase (CA) (Figure 1.1F). Certain molecules can act as indirect H_2S donors by releasing COS. This release can occur through chemical reaction, or via recently developed mechanisms that require triggers such as RONS, light or presence of an enzyme (17). Recent discoveries showed that COS itself possesses

signaling properties, suggesting that potential beneficial effects could not be solely attributed to H_2S (32).

Light-triggered H_2S donors have also been described. Advantages of this class lay in the more specific and controlled spatial and temporal H_2S release (Figure 1.1G). On the other hand, limited penetration of UV and visible light limits the application of these donors in biological setting. Future development of near-infrared light-triggered donors could solve the abovementioned problem expanding its potential in vivo application (17).

Enzymatic release of sulfur containing compounds is another source of H_2S. Tissue and substrate specificity of endogenous enzymes target H_2S production to a tissue or organ of interest. Development of phenolic thioester substrates enable esterase-dependent release of H_2S. The speed and efficiency of H_2S production can be altered through modifications of the ester group as well as methyl groups in aromatic ring. Conjugation to NSAIDs can further expand potential application of these donors as therapeutic agents (17,33).

1.3. Measurement of H_2S

Due to the limited stability, fast oxidation and high reactivity of H_2S, one of the main challenges is the development of a rapid, yet selective and sensitive method for its measurement both in vitro and in vivo. In recent decades there has been a surge in H_2S detection techniques, but each comes with certain limitations. Real-time monitoring of H_2S dynamics under physiological conditions remains the golden standard for unraveling its role in living organisms. Most commonly used methods are methylene blue method

(2,10,34), led acetate (35,36), gas-chromatography (2), monobromobimane-based method (2,11,37) and fluorescence probe-based detection (2,38–40).

However, precise determination of endogenous H_2S concentrations remains a challenge. Values reported so far can differ in few orders of magnitude for the same biological entity, and the precision decreases with increasing complexity of a measured sample (11,41). Reasons are numerous: H_2S volatilization and fast oxidation, its release from bound states upon different chemical treatments, interference of similar sulfur-containing species such as thiols, persulfides and polysulfides. These artefacts can lead to overestimation of H_2S content. Combination of described methods still gave important insights in H_2S concentration in different cell types, tissues and organs. In most cases, endogenous concentrations are very low (picomolar or nanomolar ranges) and highly dependent on formation and decay rates of H_2S in a measured entity (2,42,43).

1.4. Endogenous H_2S production and removal

To be recognized as a gasotransmitter, H_2S had to meet the criterion of endogenous and enzymatically regulated synthesis and removal. In mammals, there are at least three known enzymes responsible for H_2S production (Figure 1.2). Cystationine β-synthase (CBS) and cystathionine γ-lyase (CTH/CSE) are pyridoxal-5'-phosphate (PLP)-dependent, dominantly cytosolic enzymes involved in transsulfuration pathway. Although these enzymes are significant sources of H_2S, its production does not rely on the canonical reactions catalyzed by CBS and CSE but rather their substrate and reaction promiscuities. The third enzyme, mercaptopyruvate sulfurtransferase (MST, MPST) uses 3-mercaptopyruvate (3-MP) as a sulfur donor for H_2S generation. 3-MP could be a product

of both L-cysteine (in further text only cysteine) and D-cysteine catabolism catalyzed by cysteine aminotransferase (CAT) and D-amino acid oxidase (DAO), respectively. While CAT-mediated 3-MP production occurs in the cytoplasm of most cell types, DAO-dependent 3-MP generation is restricted to the peroxisome and is solely found in the cerebellum and kidneys (44). MST is predominantly mitochondrial protein and the main source of H_2S in this organelle (2,45,46). H_2S-producing enzymes exhibit differential expression across various cell types and tissues. CSE is more broadly expressed compared to CBS which is predominantly detected in the brain (3,4). Within the brain, CBS is mainly expressed in glial cells while CSE is localized in the neurons (47–49). Additionally, CSE is highly expressed in the liver, kidney and cardiovascular system (50). MST also has a more ubiquitous expression, with higher activity in the heart, liver and kidney (2,45,46).

Intracellular H_2S concentration has to be maintained within narrow range in order to avoid its toxicity. Therefore, the process of H_2S formation has to be tightly regulated with its removal and transformation to chemically inactive forms. Since H_2S is a known inhibitor of mitochondrial respiration through inactivation of cytochrome c oxidase (CcO), the main enzymatic hub for its detoxification is localized within mitochondria (51,52). The eight-electron oxidation of H_2S to sulfate is catalyzed by enzymatic chain comprised of sulfide quinoneoxidoreductase (SQR), persulfide dioxygenase (PDO/ETHE1), rhodanese (TST) and sulfite oxidase (SUOX). H_2S oxidation pathway couples sulfide catabolism to oxidative phosphorylation through reduction of coenzyme Q (CoQ) by SQR. H_2S is therefore a first known inorganic substrate for human electron transfer chain (2,53,54) (Figure 1.2).

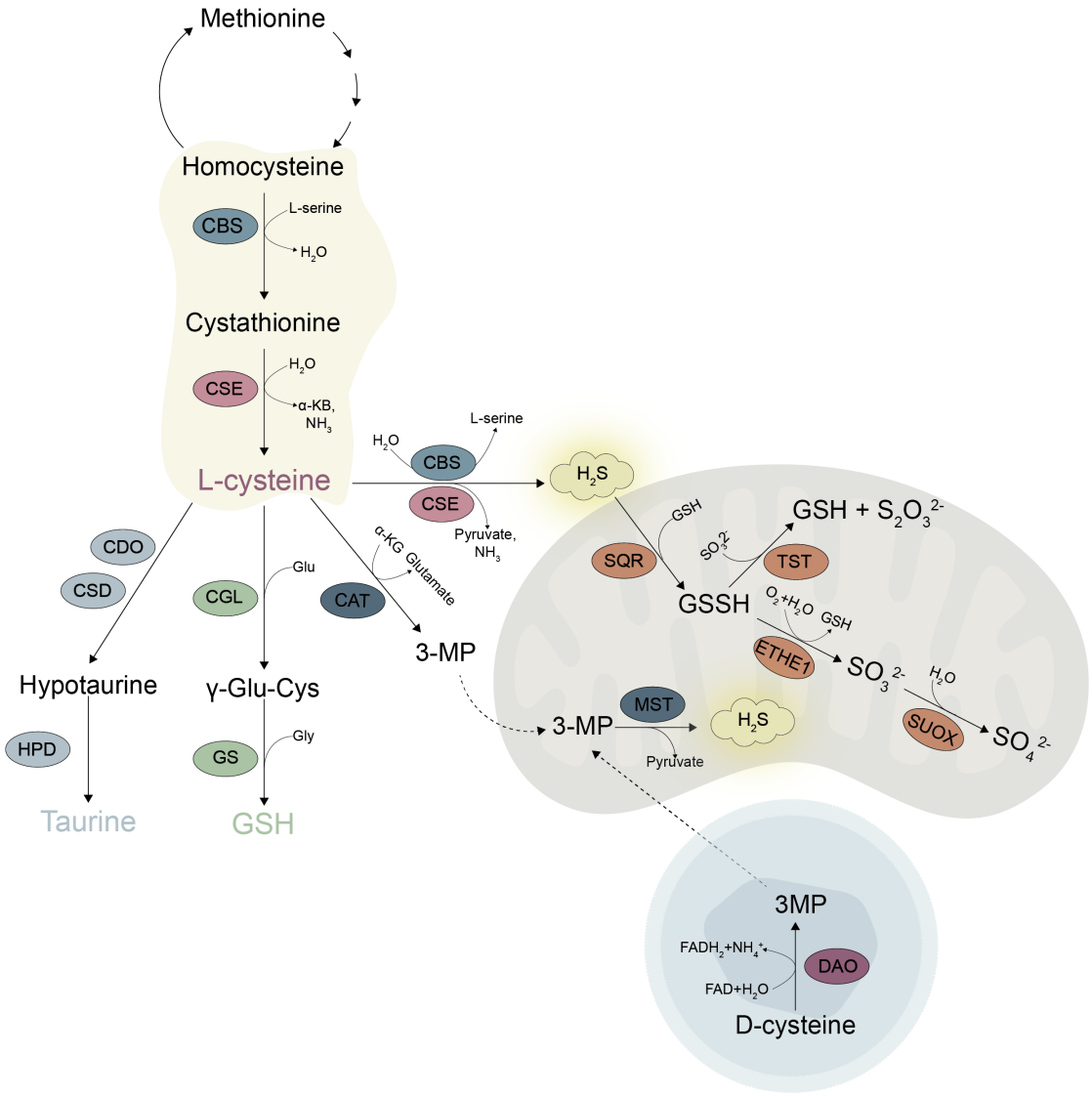


Figure 1.2 H_2S metabolism within the cell.

H_2S can be produced by two cytoplasmic enzymes, CBS and CSE and mainly mitochondrial MST. CBS and CSE are part of transsulfuration pathway which is also a source of cysteine, taurine and glutathione. The eight-electron oxidation of H_2S is located in mitochondria resulting in sulfate as a final product. α-KB, α-ketobutarate; α-KG, α-ketoglutarate; Glu, glutamate; Gly, glycine; 3-MP, 3-mercaptopyruvate; GSH, glutathione; CBS, cystathionine β-synthase; CSE, cystathionine γ-lyase; CGL; γ-Glu-Cys, γ-glutamylcysteine; γ-glutamylcysteine synthetase; GS, glutathione synthetase; MST, mercaptopyruvate sulfur transferase; SQR, sulfide:quinone oxidoreductase; SUOX, sulfite oxidase; TST, thiosulfate sulfur transferase; ETHE1, persulfide dioxygenase; CAT, cysteine aminotransferase; DAO, D-amino acid oxidase; CDO, cysteine dioxygenase; CSD, cysteinesulfinic acid decarboxylase; HPD, hypotaurine dehydrogenase. Modified from Vignane et al., 2023 (55).

1.4.1. Transsulfuration pathway as a source of H_2S

Transsulfuration pathway is a conserved pathway for cysteine synthesis from essential amino acid methionine. CBS catalyzes cystathionine synthesis from serine and homocysteine with release of water (Reaction 1, Figure 1.3). Cystathionine is further a substrate for CSE which through γ-elimination forms cysteine, α-ketobutyrate (α-KB) and ammonia (NH_3) (56) (Reaction 1, Figure 1.4). Cysteine serves as a sulfur pool for numerous cellular factors including GSH, taurine and H_2S. Tripeptide GSH acts as a cellular antioxidant while taurine is important metabolite involved in numerous processes such as neuromodulation, modulation of Ca^{2+} homeostasis and osmoregulation (2,57) (Figure 1.2).

Both CSE and CBS exhibit substrate ambiguity and reaction promiscuity which consequently leads to catalysis of plentiful reactions and formation of a wide spectra of sulfur-containing metabolites. Cysteine can serve as a substrate for both CBS and CSE to generate H_2S. To produce H_2S, CBS can catalyze β-replacement of cysteine by homocysteine (Reaction 2, Figure 1.3), another molecule of cysteine (Reaction 3, Figure 1.3) or by water (Reaction 4, Figure 1.3).

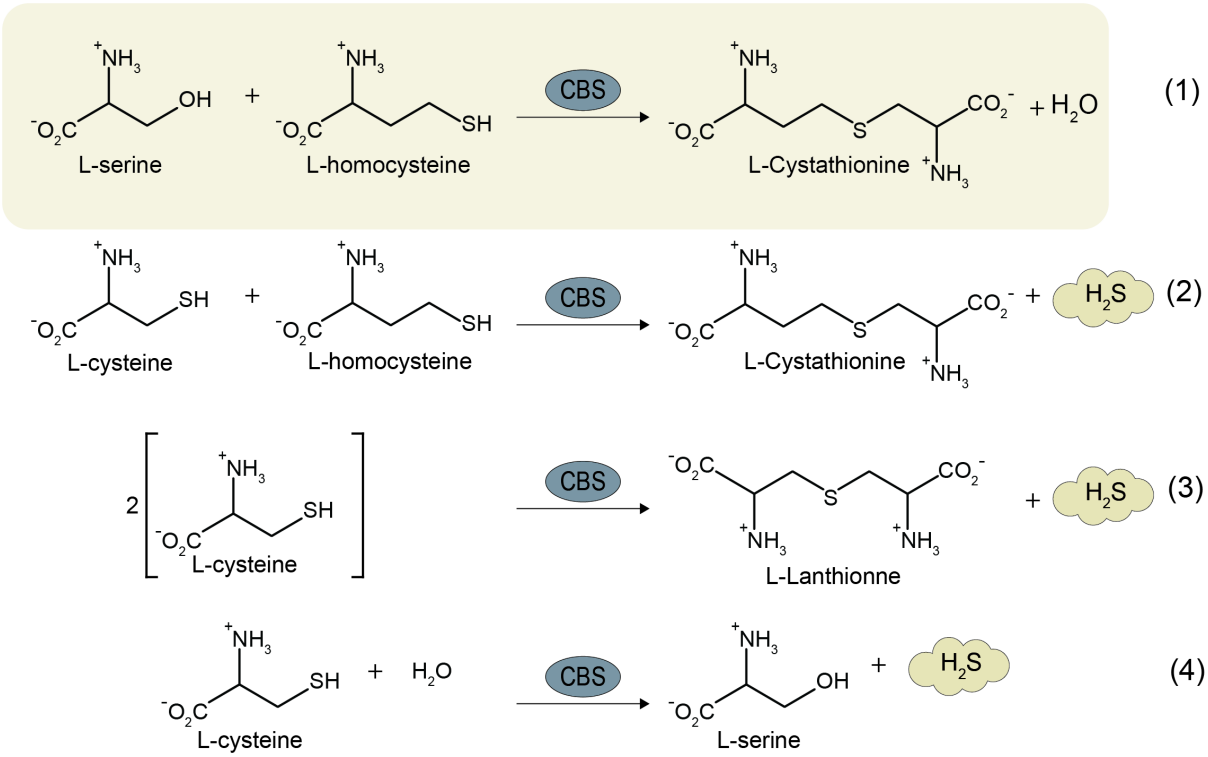


Figure 1.3 Reactions catalyzed by cystathionine β-synthase (CBS).

The canonical reaction of CBS is highlighted in yellow (1). Due to its substrate promiscuity, CBS can catalyze additional reactions resulting in H_2S production (2-4).

CSE, in contrast to CBS, can form a Schiff base with cysteine or homocysteine bound to PLP leading to chemical transformations at either β- or γ-carbon of the substrates. CSE can generate H_2S and α-ketobutyrate from homocysteine through an α,γ-elimination (Reaction 2, Figure 1.4), or H_2S and homolanthionine through a γ-replacement of homocysteine by a second molecule of homocysteine (Reaction 3, Figure 1.4). Furthermore, two molecules of cysteine can generate H_2S and L-lanthionine through a β-replacement reaction (Reaction 4, Figure 1.4), while α,β-elimination of cysteine leads to a release of H_2S and pyruvate (Reaction 5, Figure 1.4). CSE can also catalyze β-replacement of cysteine with homocysteine resulting in formation of cystathionine and H_2S (Reaction 6, Figure 1.4).

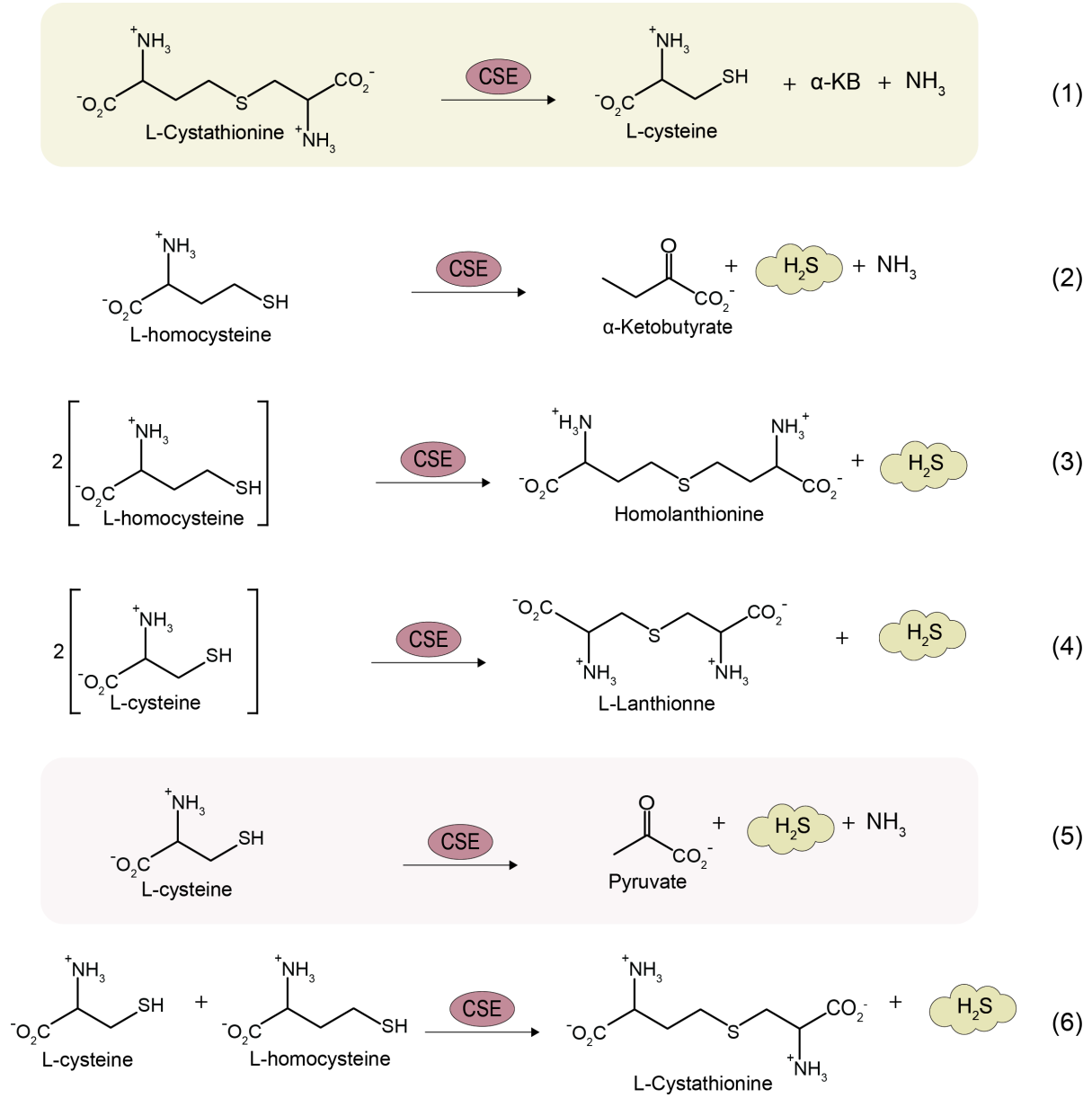


Figure 1.4 Reactions catalyzed by cystathionine γ-lyase (CSE).

The canonical reaction of CSE is highlighted in yellow (1). Due to its substrate promiscuity, CSE can catalyze several additional reactions resulting in H_2S production (2-6). Reaction 5 (highlighted in pink) is the major source of H_2S under physiological conditions.

Preference of human CSE for different substrates was extensively studied. Chiku et al. showed that under physiological concentrations of substrates (10 μM homocysteine, 100 μM cysteine and 5 μM cystathionine), cystathionine is a preferred substrate. On the

other hand, majority of H_2S (around 70%) produced under these conditions comes from α,β-elimination of cysteine rather than α,γ-elimination of homocysteine (around 30%) (Reactions 2,5 Figure 1.4). In hyperhomocysteinemic conditions where cysteine/homocysteine ratio is significantly decreased, condensation of 2 molecules of homocysteine will be the main source of H_2S production (Reaction 3, Figure 1.4). Presence of homolanthionine, more stable product of this reaction, was reported in urine of homocystinuric patients, confirming the relevance of this reaction, and potentially toxic effects of excessive H_2S production in these patients (36).

On the other hand, under saturating substrate conditions, homocysteine will be a major source of H_2S, while combination of both homocysteine and L-cysteine or L-cysteine alone will result in lower H_2S production over time. Measured specific activities under V_{max} conditions for homocysteine and cysteine are 6.6 ± 0.5 and 1.2 ± 0.3 units/mg, respectively. Therefore, both rate and amount of produced H_2S are dependent on substrate availability and combination (58).

It is also important to understand the contribution of CBS and CSE to total H_2S production by transsulfuration pathway. In vitro studies under equal amounts of both enzymes and at physiological substrate concentrations showed that CSE account for ~ 32% of produced H_2S while CBS contribution varies between 25 and 70% depending on the extents of its activation by allosteric modulator adenosylmethionine (AdoMet). This ratio significantly changes under hyperhomocysteinemic conditions where CSE-catalyzed γ-replacement of homocysteine becomes a dominant source of H_2S (58).

Both CSE and CBS can be involved in formation of cysteine persulfide (Cys-SSH) while CSE can also catalyze formation of homocysteine persulfide (Hcy-SSH) (Figure 1.5). Substrates for these reactions are cystine and homocystine, oxidized forms of

cysteine and homocysteine. In the reducing intracellular milieu, CSE catalyzed production of Cys-SSH and Hcy-SSH is negligible compared to production of H_2S. On contrary, increased intracellular levels of cystine under oxidizing conditions can favor production of Cys-SSH (59).

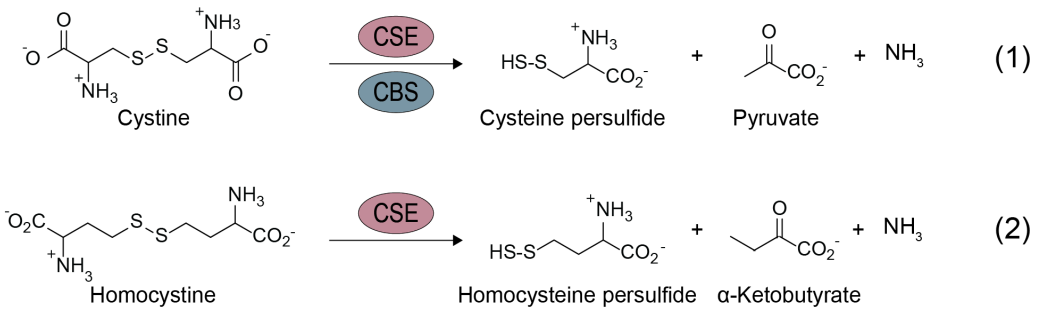


Figure 1.5 CSE and CBS-dependent generation of low molecular (LMW) persulfides.

(**1**) CSE and CBS can use cystine to produce cysteine persulfide while (**2**) CSE can also use homocystine to generate homocysteine persulfide. These reactions could be relevant under oxidizing conditions in the cell.

Having in mind the complexity of reactions catalyzed by those two enzymes, the main challenge is to understand how the cell can balance its needs for different substrates formed in transsulfuration pathway, presumably cysteine and H_2S. Differential expression of enzymes in different cell types, availability of the substrates and allosteric regulation in response to stimuli direct the favorable reaction. Under basal conditions (higher intracellular concentration of serine compared to cysteine) CBS dominantly catalyzes formation of cystathionine, and CSE downstream formation of cysteine. On contrary, upon inhibition of CBS and increased requirement for H_2S, CSE dominantly uses cysteine as a substrate for H_2S generation (2,60).

1.4.2. CSE structure and regulation of its activity

Human CSE is comprised of 4 identical monomers (45 kDa each) with 2 domains each: larger PLP-binding domain (residues 9-263) with the most of catalytically important residues and smaller C-terminal domain (residues 264-401) (Figure 1.6A) (61). Within each monomer, PLP is anchored through formation of a Schiff base between its carbonyl group and the amino group of Lys212 of the monomer. Several other residues are also involved in binding of PLP through hydrogen bonds with its nitrogen or phosphate groups or hydrophobic interactions (Figure 1.6B) (62). Close contact between monomers is maintained by hydrogen bonds and hydrophobic interactions while presence of PLP additionally stabilizes the tetrameric structure and is crucial in maintaining the conformation of enzyme's active site. Different residues determine reaction specificity catalyzed by CSE. Therefore, Tyr114 and Lys212 are crucial for reactions at substrate's γ-carbon while β-carbon reactions require only Lys212. Mutation of Tyr114 to phenylalanine will lead to enzymatic catalysis exclusively on β-carbon and enhanced H_2S production compared to wild-type CSE (62). CSE is completely inactivated by suicide inhibitor propargylglycine (PPG). The inhibition is achieved through covalent interaction of PPG and Tyr114, without PLP involvement in the reaction. Although very efficient, PPG lacks selectivity as it can also inhibit other PLP-dependent enzymes such as methionine γ-lyase (MGL) and L-alanine transaminase (ALT) (61,63). Development of CSE-specific inhibitors is crucial for better understanding of CSE's role in different cell types and organs. Recent study discovered a compound which seems to selectively inhibit CSE through formation of Schiff base with PLP in the active site of the enzyme. Unfortunately, its chemical structure has not been published, therefore rendering its use and validation by different groups (63).

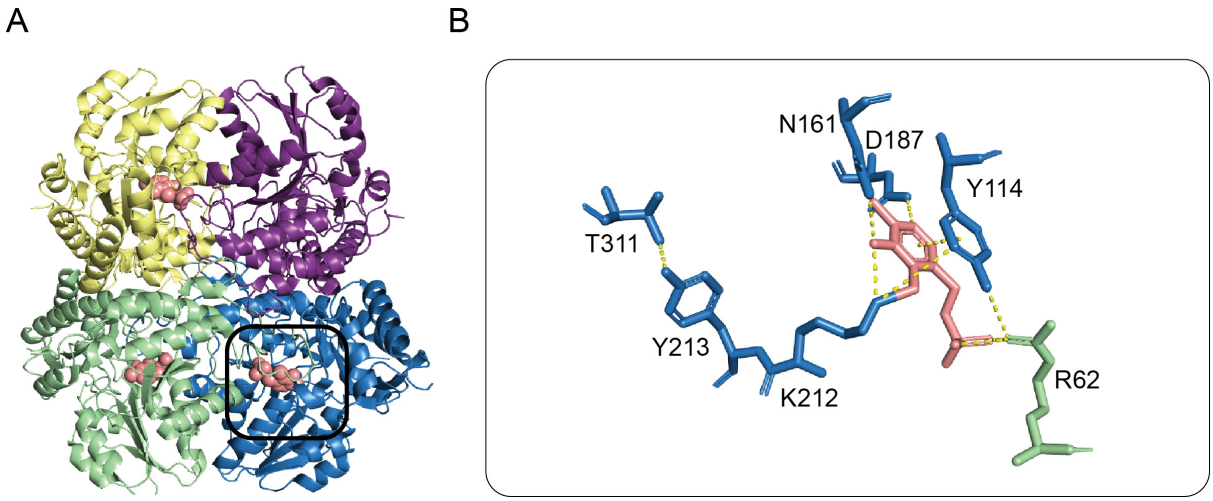


Figure 1.6 Tetrameric structure of CSE and close look at its active site (PDB:2NMP).

(**A**) Each of the four CSE monomers is shown in a different colour, while sphere representation of PLP molecule is shown in light orange. In this crystal structure there are three PLP molecules (**B**) Interaction between PLP (light orange) and residues belonging to two monomers (blue and green).

CSE abundance and activity can be regulated on both transcriptional and post-translational levels. Phosphorylation of Ser377 was shown to inhibit the enzymatic activity and H_2S production in carbon monoxide (CO) and protein kinase G-dependent way (64). Since this residue is burrowed deeply inside the enzyme, the main concern is how this reaction could happen due to steric limitations (2,64). On the other hand, Akt-dependent phosphorylation of the same residue was associated with increased catalytic activity of CSE (65). CSE was also shown to be prone to sumoylation of more than one lysine residue, although only in vitro. The potential effect on its activity and relevance of this mechanism within the cell has to be further characterized (66).

Specificity protein 1 (SP1) is the main transcriptional regulator of CSE under basal conditions, and its expression can be modulated upon different signals (67,68). Known inducers of inflammation such as bacterial lipopolysaccharide (LPS) as well as

proinflammatory cytokines tumor necrosis factor alpha (TNFα) and interleukin 6 (IL-6) stimulate CSE expression through activation of SP1, implying importance of produced H_2S in regulation of inflammation (67,69). Sulfur-containing CSE products have an important role in signaling and maintenance of cellular and protein homeostasis under diverse stress conditions, resulting in increased need for their synthesis. Therefore, CSE is a highly inducible enzyme whose expression can be regulated by known master regulators of transcription including nuclear factor erythroid 2-related factor 2 (Nrf2), activating transcription factor 4 (ATF4) and cAMP responsive element binding protein 1 (CREB) (70–72).

1.5. H_2S in action

There are 3 known mechanisms through which H_2S acts in biological systems: binding to metal centers, cross-talk with and scavenging of RONS and post-translational modification of cysteine residues known as persulfidation (Figure 1.7).

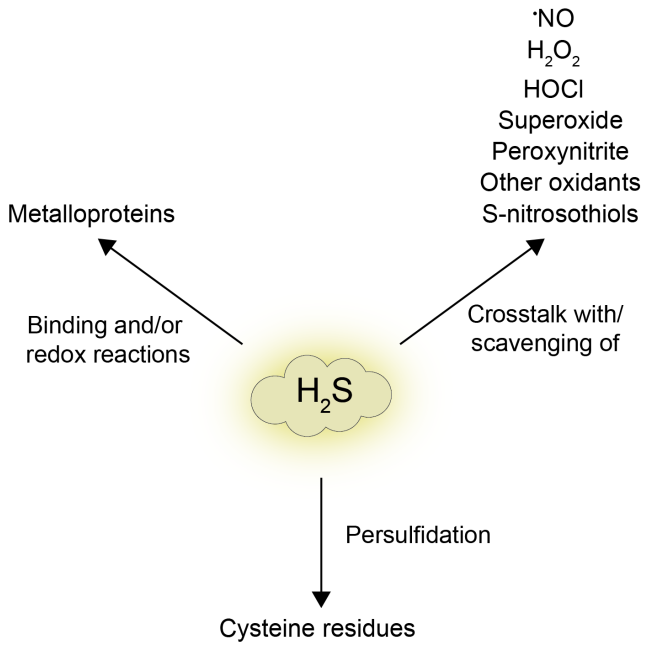


Figure 1.7 Different mechanisms of H_2S action.

1.5.1. H_2S interacts with metal centers

H_2S can coordinate metal ions, covalently modify heme porphyrins or reduce metal centers while forming $HS^{\bullet}$ radical and subsequent sulfur oxidation products. One of the examples is binding of H_2S to copper and heme iron centers of CcO. This interaction can both activate and inhibit the enzyme depending on the concentration of sulfide (51,73). CcO is a final component of electron transport chain which uses electrons delivered by cytochrome c to reduce oxygen (O_2) to H_2O. At lower concentrations, H_2S binds and

reduces ferric heme *a*$_3$ followed by formation of HS•. This interaction favors binding of oxygen and increases its consumption, therefore stimulating the respiration (73). On contrary, at moderate concentrations, H_2S first reduces Cu_B^{II} center to Cu_B^{I} which can further coordinate HS^- resulting in a formation of a complex which is difficult to oxidize. In the presence of high amounts of H_2S, Cu_B- HS^- complex induces conformational changes and further binding of H_2S to ferric heme center which results in its irreversible inhibition (Figure 1.8) (2).

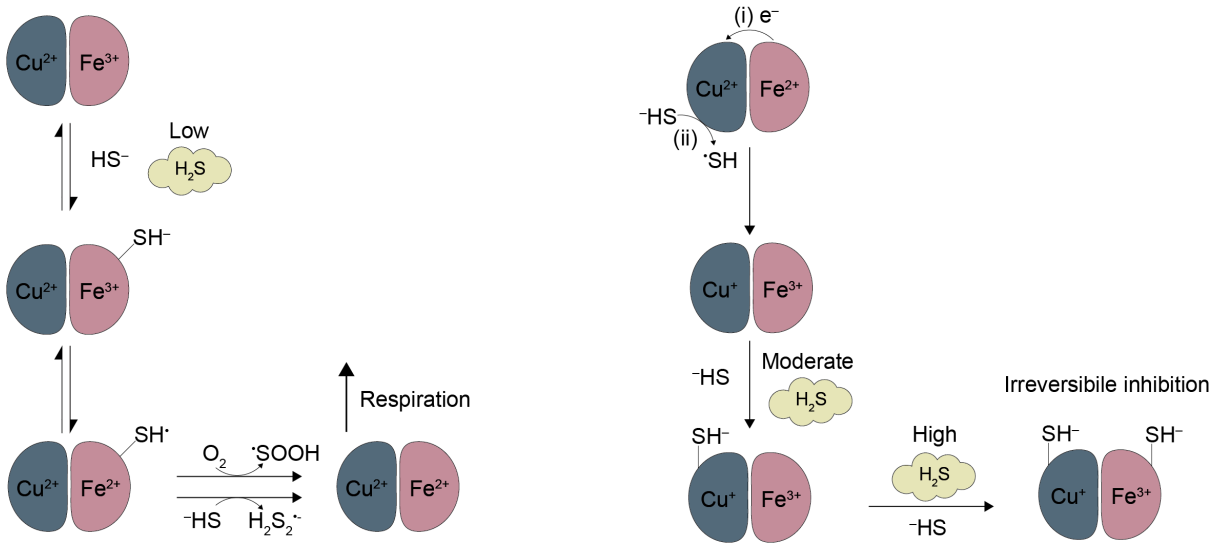


Figure 1.8 Concentration dependent stimulation or inhibition of cytochrome c oxidase (CcO) by H_2S.

At low concentrations, H_2S reduces ferric heme along with its oxidation to HS•. Heme iron reduction promotes binding of oxygen which results in increased respiration. HS• can react with HS^- forming $H_2S_2^{\bullet-}$ or it can react with oxygen to form HSOO•, therefore contributing to oxygen consumption. At moderate concentrations, H_2S first binds and reduces Cu^+ center forming a complex which is difficult to oxidize. At high concentrations, binding of H_2S induces conformational changes of Cu^+ center which results in H_2S binding to ferric hem and inhibition of respiration. Modified from Filipovic et al., 2017 (2).

H_2S can also covalently bind hemoglobin, myoglobin as well as Zn^{II}-containing proteins (2,74,75).

1.5.2. H_2S interacts with RONS

Sulfur in H_2S molecule has the lowest possible oxidation state of -2, and therefore, it can only form more oxidized products. H_2S can react with different oxidants through one-electron or two-electron oxidation.

Due to its high one-electron reduction potential, H_2S can be oxidized to sulfanyl radical ($S^{\bullet-}$) only by very strong oxidants such as hydroxyl radical ($HO^{\bullet}$), carbonate radical ($CO_3^{\bullet-}$) and nitrogen dioxide ($^{\bullet}NO_2$) with rate constants similar to cysteine and GSH oxidation (2,76,77). In the cell, $S^{\bullet-}$ can further react with electron donors such as another $S^{\bullet-}$ molecule, HS^-, O_2, ascorbate and GSH. Depending on the reaction conditions different sulfur reactive species can be formed in radical chain reactions which can be part of signal transduction but also potential source of oxidative damage in the cell (2,77). Reported rate constants for two-electron oxidation of H_2S in the presence of peroxynitrite ($ONOO^-$), hypochlorite (HOCl) and hydrogen peroxide (H_2O_2) are lower compared to the reactions with the most abundant cellular thiols. The reason may lay in the absence of an inductive group in HS^- and its weaker nucleophilicity compared to alkylated thiols (77).

Current knowledge leads to a conclusion that signaling and protective roles of H_2S can be hardly explained through its direct scavenging of RONS species in cellular milleu. Much lower endogenous H_2S concentrations coupled with its lower reaction rates compared to common cellular thiols limits the influence of H_2S in RONS regulation and

signaling in vivo. H_2S could become a favorable target in conditions which lead to local increase in its concentration.

Except scavenging properties, H_2S is also involved in signal transduction through crosstalk with another gasotransmitter nitric oxide ($^{\bullet}NO$). $^{\bullet}NO$ is a known activator of soluble guanylate cyclase (sGC)/cGMP cascade which is involved in neurotransmission, blood pressure regulation and immune defense. H_2S can modulate $^{\bullet}NO$ signaling through direct interaction with $^{\bullet}NO$, its downstream products or by modulating its production (2).

1.6. Protein Persulfidation

Post-translational covalent modifications of proteins (PTMs) present a rapid and site-specific way to convey chemical signal into biological response. Cysteine is a great candidate for this purpose due to the presence of a reactive thiol group prone to a wide spectrum of reversible and irreversible oxidative modifications (78) (Figure 1.9). Although in the eukaryotes more than 90% of the proteins have at least one cysteine, it is, overall, a rarely occurring amino acid in protein sequence. On the other hand, its content in proteins positively correlates with the complexity of the organism and they are often located at the positions which are evolutionary conserved among species (79). Cysteine's position together with its chemical versatility explain its involvement in processes such as catalysis, metal complexing and structure stabilization.

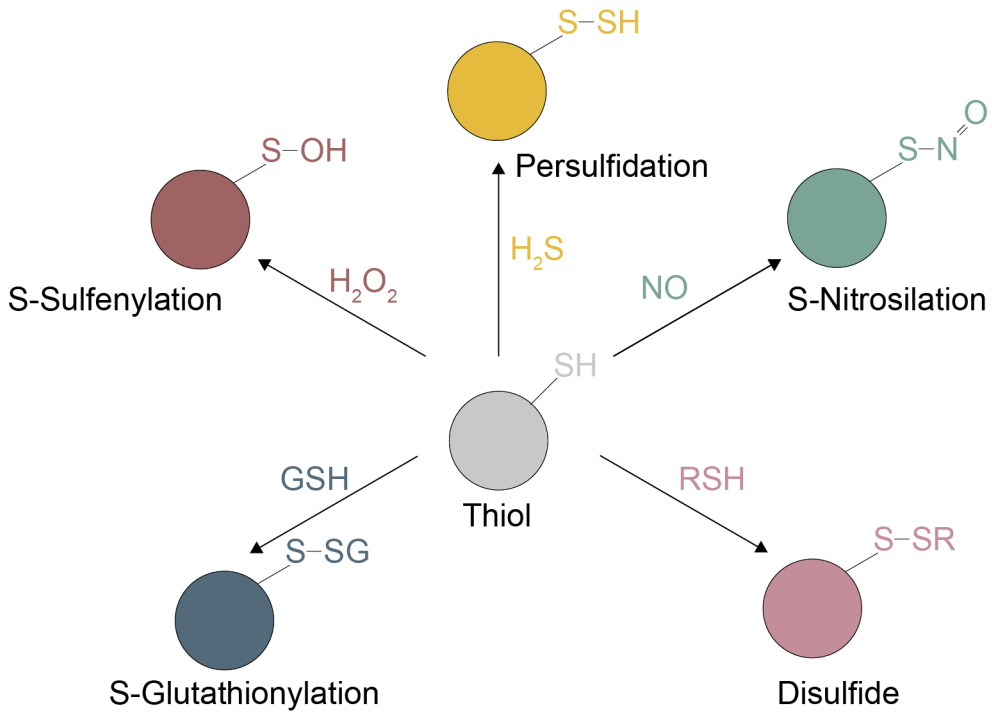


Figure 1.9 Cysteine residues are prone to wide range of oxidative posttranslational modifications.

Reaction of thiols with hydrogen peroxide (H_2O_2) results in formation of sulfenic acids (RSOH). H_2S effects are transmitted via protein persulfidation (RSSH). Thiols could also be modified by glutathione (GSH) and nitric oxide ($^{\bullet}NO$) resulting in glutathionylation and nitrosation, respectively. Reaction with another thiol result in formation of a disulfide. Modified from Filipovic, 2015 (80).

1.6.1. Chemical properties and reactivity of persulfides

H_2S can exhibit its biological function through oxidative post-translational modification of cysteine residues known as persulfidation. In the cell, persulfides exist as low molecular weight (LMW) persulfides such as Cys-SSH or glutathione persulfide (GSSH) or as protein persulfides where one or more cysteine residues within protein sequence is modified. Persulfides (RSSH) belong to a class of compounds named sulfanes referring to a presence of a sulfur atom covalently bound to two or more sulfur atoms or bound to a sulfur atom and ionizable hydrogen (2,81).

Persulfide acidity

RSSH ionizes in the solution to form the corresponding anionic, deprotonated form [Eq. (3)]:

$$RSSH \rightleftharpoons RSS^- + H^+ \quad (3)$$

Since the S-H bond is weaker than in thiols (RSH), persulfides ionize at a lower pH compared to thiols. At physiological pH (7.4), persulfides will be dominantly present in their ionized form compared to partial ionization of their corresponding thiols. Therefore, under the same conditions, persulfides will be more reactive compared to thiols (2,82). One of the beautiful examples is a recently published study showing that pK_a of GSSH (5.45) is 3.49 units below GSH (8.94). This means that at pH 7.4, 99% of GSSH will be in deprotonated form compared to 2.8% of GSH (83). The acidity of persulfidated residues within protein will be dependent on the chemical microenvironment and can be modulated by adjacent functional groups (2,82).

Persulfide nucleophilicity

Ionized persulfides (RSS^-) act as nucleophiles with the outer sulfur being a nucleophilic center [Eq. (4)]:

$$RSS^- + E^+ \rightarrow RSSE \quad (4)$$

Their stronger nucleophilicity compared to thiols is a consequence of alpha effect induced by lone electron pairs of the inner sulfur atom. Therefore, persulfides can readily react with two-electron oxidants forming different oxidation products dependent on the oxidant concentration. In the presence of excess oxidant, thiols are oxidized to sulfinic (RSO_2H) and sulfonic acids (RSO_3H) which are generally irreversible modifications (78,84). On contrary, oxidation products of persulfides, perthiosulfinic ($RSSO_2H$) and

perthiosulfonic acids ($RSSO_3H$) can be reduced back to thiol forms by common disulfide-bond reductants. Combined properties of higher reactivity towards oxidants and formation of reversible oxidation products imply that persulfidation can be an important protective mechanism against irreversible protein oxidation (2,49). Due to their prompt oxidation, persulfides are also better scavengers of radicals and one-electron oxidants compared to thiols and H_2S.

Persulfide electrophilicity

In contrast to thiols, protonated persulfides can also act as electrophiles with both sulfurs being targets for nucleophiles. When the nucleophile attack happens on the inner sulfur, H_2S is a leaving group [Eq. (5)], and an attack on outer sulfur leads to release of a thiol [Eq. (6)]. Choice of the nucleophilic site largely depends on the microenvironment of persulfide molecule and acidity of the leaving group. Although H_2S is a better leaving group, steric and inductive effects of adjacent groups can favor attack on the outer sulfur.

$$RSSH + Nu^- \rightarrow RSNu + HS^- \quad (5)$$

$$RSSH + Nu^- \rightarrow RSH + NuS^- \quad (6)$$

1.6.2. Methods for detecting persulfides

Due to their reactivity, persulfides are highly unstable in solution with both nucleophilic and electrophilic reactions being involved in their rapid decay. Furthermore, they share common features with other sulfur-containing molecules such as thiols, sulfenic acids, disulfides and polysulfides. All those properties pose a challenge for a specific, fast and reliable in vitro and in vivo persulfide detection.

Currently available methods can be grouped in two categories depending on the property of persulfide used for detection. First category is based on the nucleophilic property of outer sulfur, while the other is based on their electrophilic properties and sulfane sulfur detection.

Some of the commonly used methods based on persulfide nucleophilicity employ blocking of persulfides with common thiol blocking reagents resulting in the formation of products which can be discerned from corresponding thiol products. This approach can be used for MS detection since derivatization with alkylating agents stabilizes persulfides and improves their detection. Choice of the right blocking reagent is crucial since its specificity and rate of alkylation largely define the outcome.

Biotin thiol assay (BTA) and its variants ProPerDP and qPerS-SID use an alkylating agent bound to biotin to block RSH and RSSH generating thioeter and mixed disulfide, respectively. Upon streptavidin enrichment, selective release of persulfidated proteins or peptides is performed with reducing agents (Figure 1.10A) (85–87). The main limitation of this method lays in lack of selectivity, since sulfenic acids can be also alkylated in the first step, leading to a formation of a reducible adduct and false positive results (88).

Recently developed “direct” method named Low-pH quantitative thiol reactivity profiling (QTRP) follows the same principle with few modifications. Alkylating step is performed at pH (5.0) where RSSH are expected to be reactive compared to protonated RSH. Use of ultraviolet-cleavable probes and click chemistry enables enrichment of RSSH peptides without a reduction step resulting in higher specificity. Identification of modified cysteine residues is done by MS through direct detection of additional sulfur atom in persulfidated peptides (Figure 1.10B) (89).

Another category of methods for selective persulfide detection are tag-switch methods. These approaches are based on labelling of both thiols and persulfides with an aromatic blocking reagent. Upon blocking, persulfides are transformed to a mixed aromatic disulfide with enhanced electrophilicity of one of the sulfur atoms. The newly formed molecule is therefore a perfect target for a properly chosen nucleophile. On the other hand, thioether formed upon blocking of thiol is not expected to react with the nucleophile, enabling selective labelling of persulfides. Nucleophile used for the switch reaction can be bound to different reporter molecules which will enable selective enrichment and detection of persulfidated proteins (Figure 1.10C, D) (31,49,90,91).

Original version of the tag-switch method implied use of methylsulfonyl benzothiazole (MSBT) or its more water-soluble analog (benzothiazole-2-sulfonyl)-acetic acid (MSBT-A) as a thiol blocking reagent. Disulfide formed by RSSH blocking is a target for cyanoacetic acid-based nucleophiles (Figure 1.10C) (31,90,91). The main disadvantage of this method is very poor solubility of MSBT in aqueous solution and fast degradation of cyanoacetic acid-based compounds under MS conditions which complicates the analysis.

Recent improvement of this method involves use of 4-chloro-7-nitrobenzofuran (NBD-Cl) as a blocking agent in the first step and dimedone-based probes for the following switch step. NBD-Cl is a more soluble, fluorescent compound, which additionally blocks RSOH and amino groups. Blocking of RSOH in the first step is important since dimedone is a known compound for RSOH labeling. On the other hand, labeling of amino groups with NBD-Cl is an advantage, as corresponding green fluorescence can be used as a measure of total protein load. Besides its nucleophilic properties, dimedone probes are useful tools since they can be coupled with various reporter molecules substantially

increasing the versatility of the method. Use of biotinylated form of dimedone (DCPBio-1) could allow for Western blot detection or enrichment of persulfidated proteins for immunoprecipitation or proteomic analysis. Coupling of dimedone to a Cy5 fluorescent dye using Copper(I)-catalyzed azide-alkyne cycloaddition (CuAAC, click chemistry) enables RSSH detection in gel, by microscopy or using antibody microarray approach (Figure 1.10D). In this case, red fluorescence corresponds to persulfide levels while green fluorescence at 488 nm originates from amino groups labeled with NBD-Cl. The ratio of those two values can be used for the comparison of persulfidation between samples (49). Although dimedone-switch method can be used for proteomic analysis of persulfides, at the moment it is only developed for enrichment on protein level limiting the direct detection of modified cysteines.

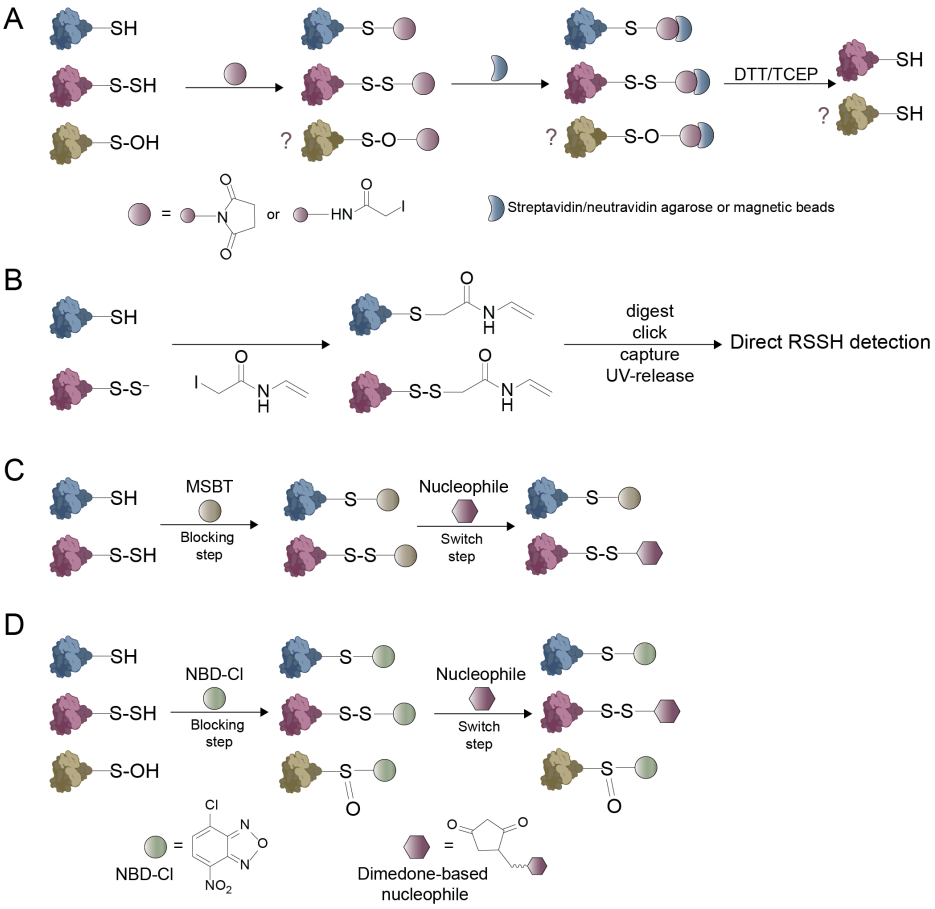


Figure 1.10 Methods for persulfide detection based on its nucleophilic properties.

(**A**) Principle of biotin thiol assay (BTA), and its variants. The main limitation of these methods is the non-selective blocking of sulfenic acids (RSOH) in the initial step, followed by reduction of the resulting product along with RSSH. (**B**) The low pH Quantitative Thiol Reactivity Profiling (QTRP) principle resides in higher reactivity of persulfides at low pH, allowing them to be preferentially blocked over more abundant thiols. This method enables direct detection of persulfidated cysteines via MS, due to the use of UV-cleavable probe, which enables selective enrichment of cysteine-containing peptides. (**C**) Chemical principle of the Tag-switch method. In the first step, various cysteine modifications are labelled with the blocking reagent MSBT which forms an aromatic disulfide upon reaction with persulfides. This molecule is an ideal target for nucleophilic attack, enabling the specific labelling of persulfides. (**D**) An improved version of the Tag-switch method, the dimedone-switch method, offers better solubility and stability of the reagents and broader application. The blocking step uses NBD-Cl, while dimedone-based probes are used for the nucleophilic attack. Dimedone can be linked to different moieties, making this method suitable for in-gel and MS detection, as well as microscopic analysis of persulfides. Modified from Vignane et al, 2023 (55).

1.6.3. Persulfide formation

In biological systems, persulfides can be formed through direct, non-enzymatic reactions of H_2S or sulfur-containing species with proteins or LMW molecules. Additionally, some enzymes generate persulfides as a part of their catalytic cycle or they may be a final product of an enzymatic reaction (80) (Figure 1.11). The contribution of each mechanism highly depends on the cellular redox state, subcellular location and presence of a stimuli.

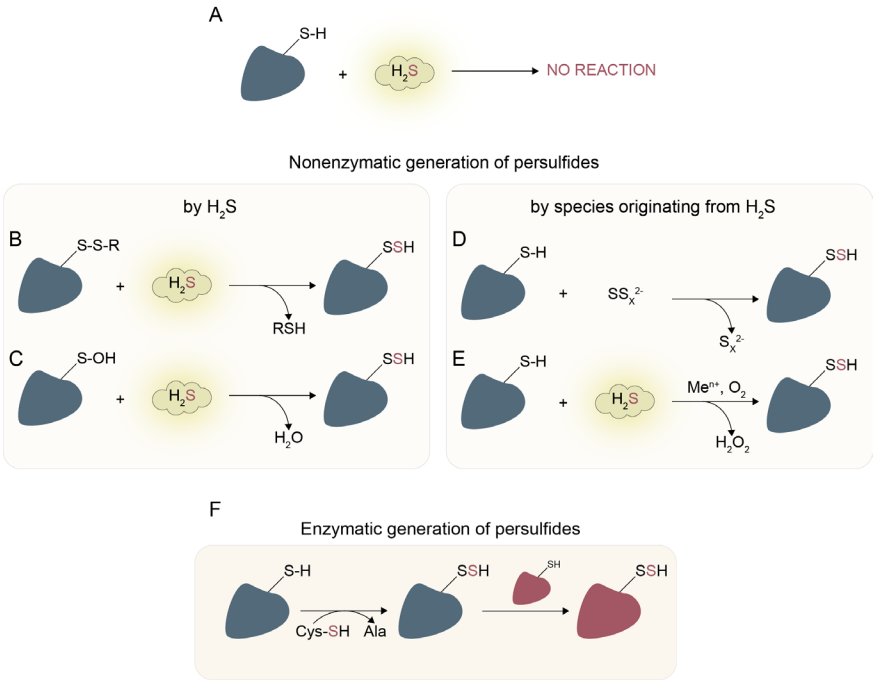


Figure 1.11 Different mechanisms of persulfide formation.

(**A**) H_2S cannot react directly with the thiol to form persulfide. Nonenzymatic formation of persulfides can be dependent on direct reaction of H_2S with disulfide (**B**) or sulfenic acid (**C**). Persulfides can be also formed in reaction with species originating from H_2S, such as polysulfides (**D**), or metal centers (**E**) could act as oxidants for the formation of persulfides from thiols and H_2S. (**F**) Some enzymes can form persulfudes in their active center, using cysteine as a sulfur donor. Sulfur can be further transferred to another molecule through mechanism known as transpersulfidation.

H_2S reacts with disulfides

H_2S cannot react directly with thiols to form persulfides (Figure 1.11A), but reaction with oxidized thiol derivates such as disulfides (RSSR) results in formation of persulfides (Figure 1.11B). A reaction with LMW or protein disulfides yields a persulfide and a corresponding thiol (2,93) [Eq. (7)]:

$$HS^- + RSSR \rightleftharpoons RSSH + RS^- \quad (7)$$

This mechanism is kinetically challenged under physiological conditions due to low intracellular concentrations of both disulfides and H_2S and very low rate constants. Importance of these reactions might increase in cellular compartments with oxidizing environment such as endoplasmic reticulum and extracellular space or in the presence of an oxidative signal (2,93,94).

H_2S reaction with sulfenic acids

Biologically more relevant mechanism of persulfide formation is the reaction between H_2S and sulfenic acids (Figure 1.11C; [Eq. (8)]):

$$HS^- + RSOH \rightleftharpoons RSSH + OH^- \quad (8)$$

RSOH is formed upon thiol oxidation by H_2O_2 (92,93). H_2O_2 is the most abundant two-electron oxidant in the cell with an important role as a second messenger. Under tightly regulated H_2O_2 concentrations, transient RSOH formation is usually associated with signal transduction, while aberrant H_2O_2 levels can lead to previously mentioned irreversible thiol overoxidation and loss of protein function (2,78). Exposure of cells to H_2O_2 leads to an increase in global persulfidation. This phenomenon is dependent on the activity of H_2S-producing enzymes since lack of CSE leads to massive decrease in RSSH and persistent increase in RSOH or even RSO_2H (49,92).

An example of interplay between RSOH and RSSH is redox regulation of epidermal growth factor (EGF) signaling. Binding of EGF to its receptor EGFR results in a boost of H_2O_2 generation, which consequently leads to a sulfenylation of EGFR and an increase of its kinase activity towards downstream proteins involved in signaling cascade (78). Increase in sulfenylation is followed by a wave of persulfidation in a phase-shifted manner. This phenomenon is dependent on endogenous H_2S production as its decreased levels lead to changes in the response. Furthermore, EGFR stimulation increases the expression of all 3 H_2S-producing enzymes. RSSH can therefore serve as a redox switch which regulates the length and amplitude of EGFR signaling and restores cysteine residues back to their thiol forms (49) .

Role of polysulfides in persulfide formation

Persulfides can also be products of reaction between thiols and oxidized sulfur derivates, polysulfides (HSS_nS^-, Figure 1.11D) (94). Polysulfides are stochastically formed upon oxidation of H_2S and some beneficial effects of H_2S have been assigned to them. Due to the presence of sulfane sulfur atoms, polysulfides are prone to nucleophilic attack by thiolates (RS^-) resulting in the formation of polythiolated cysteine with different number of sulfur atoms [Eq. (9)].

$$RS^- + SS_n^{2-} \rightleftharpoons RSS^- + S_n^{2-} \quad (9)$$

Contribution of endogenously formed polysulfides to cellular persulfide pool is questionable due to their inherent instability, as well as reducing cellular environment which does not favor their formation but promotes their reduction and degradation. Furthermore, there is no evidence of regulated or enzymatically catalyzed process of

polysulfide production in the cell, limiting their involvement as signaling molecules in cellular processes (2).

Persulfide formation via radical reactions

Radical chain reactions can also be source of persulfides under specific cellular conditions. Reaction of H_2S with oxidized metal center leads to a formation of $HS^{\bullet}$ which can further react with thiols, initially forming the radical anion $RSSH^{\bullet-}$. In the presence of oxygen, $RSSH^{\bullet-}$ will oxidize into RSSH with formation of $O_2^{\bullet-}$ (Figure 1.11E). Since some metaloproteins as CcO localize in mitochondria, this mechanism might be involved in controlling protein persulfidation in the areas of locally increased H_2S concentration (2,95).

Enzymatic formation of persulfides

Persulfide formation is not always dependent on H_2S, other molecules such as thiols or disulfides can also serve as sulfur donors. As previously mentioned, CBS and CSE can use cystine, while CSE can also use homocystine and cysteine-homocysteine disulfide to form corresponding LMW persulfides (Figure 1.5). However, contribution of this mechanism to total RSSH pool is minor under physiological conditions.

Flux of persulfides can be also regulated through enzymes which produce, transfer and/or react with persulfides (Figure 1.11F). During the reaction known as transpersulfidation, sulfane sulfur is transferred from one protein to another.

Catalytical cycles of MST and SQR enzymes involved in H_2S metabolism, are dependent on the formation of active site persulfide. MST uses 3-MP as a donor of a sulfur atom which will be further transferred to an acceptor such as LMW thiol or enzyme thioredoxin (Trx) and subsequently released as H_2S gas (96,97). SQR catalyzes two-

electron oxidation of H_2S through formation of an active site persulfide intermediate. The sulfane sulfur from persulfide can then be transferred to a GSH or to a sulfite, which serve as acceptor molecules, resulting in formation of GSSH and thiosulfate, respectively (54,98).

Sulfurtransferases are crucial enzymes for sulfur incorporation into essential cofactors such as iron-sulfur clusters and biotin or into tRNA thionucleosides involved in fine regulation of protein translation (Figure 1.12). In the first step, PLP-dependent cysteine desulfurases (IscS in prokaryotes or NFS1 in eukaryotes) convert cysteine to alanine while forming an intermediate persulfide on the cysteine residue in the enzyme's active site. Formed persulfide can be then transferred to cysteines of acceptor proteins through formation of a new persulfide in their active site. These reactions are particularly important for thionucleoside biosynthesis and iron sulfur cluster assembly (55,99,100) (Figure 1.12).

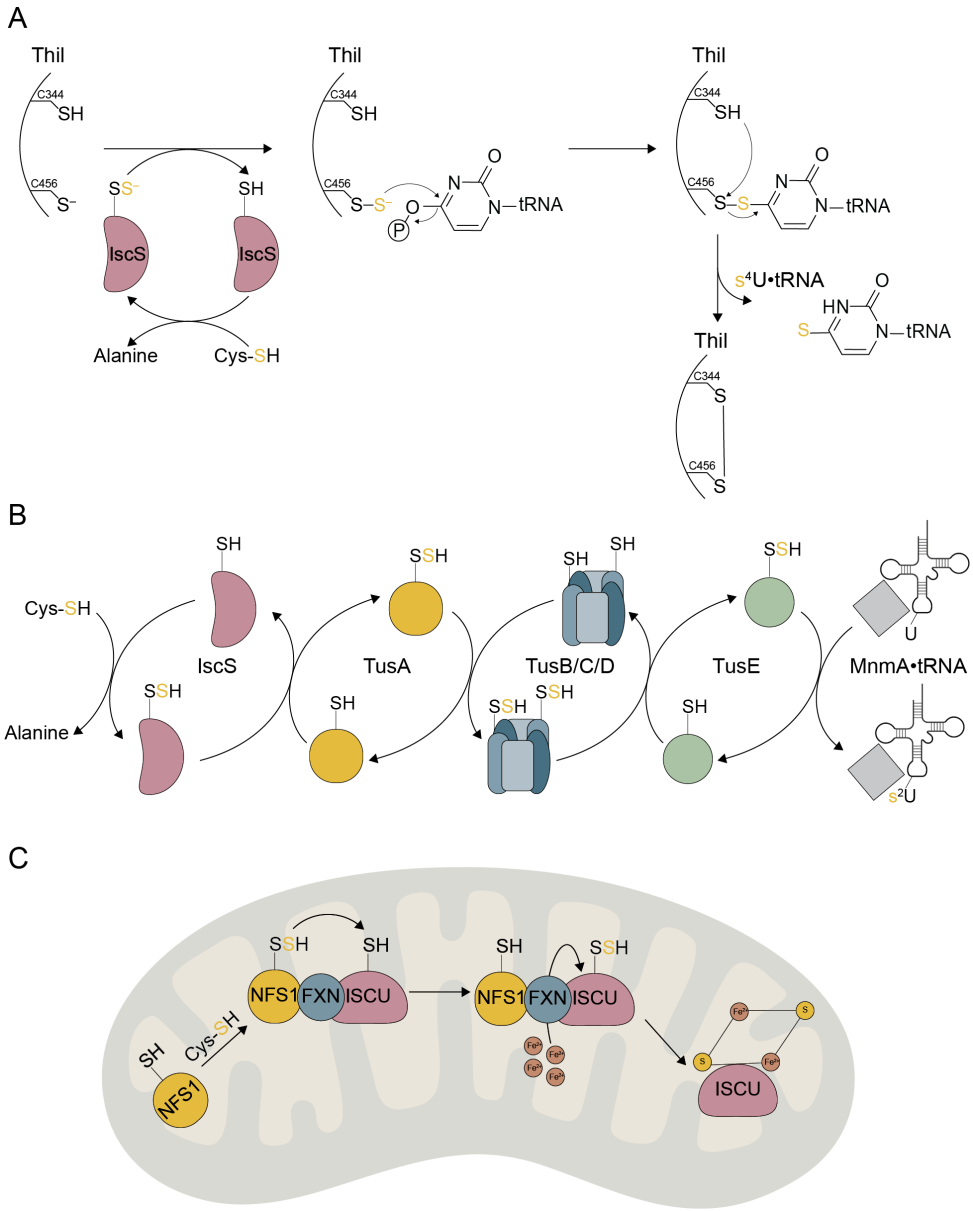


Figure 1.12 Transpersulfidation as an integral part of iron-sulfur cluster and thionucleoside formation.

Cysteine desulfurase (NFS1 in eukaryotes or IscS in prokaryotes) uses cysteine as a substrate to form an intermediate persulfide. (**A**) In bacteria, formation of s^4U-tRNA is dependent on IscS and ThiI protein which transfers sulfur to tRNA. Modified from Vignane et al., 2023 (55). (**B**) On the other hand, sulfane sulfur is transferred from IscS through a chain of Tus proteins (Tus A, Tus B/C/D, TusE) to a final acceptor MnmA which catalyzes sulfur incorporotation in tRNA resulting in formation of s^2U-tRNA. Modified from Mueller, 2006 (100). (**C**) Transfer of the sulfane sulfur from NFS-1 to ISCU is required for formation of iron-sulfur clusters in mitochondria. Frataxin-1 (FXN1) serves as a donor of ferrous ion.

1.6.4. Persulfide removal in biological systems

If persulfidation is to be involved in cell signaling and transient protection under oxidative stress, cells would need a mechanism to reduce cysteine residues back to thiols upon termination of stimuli or stress. Specific enzymatic systems involved in reduction of disulfide bonds have been proposed to play this role (31,101).

Thioredoxins, main disulfide reductases in the cells, coupled with thioredoxin reductases (TrxR) comprise a system involved in the regulation of endogenous persulfidation. Trx contains 2 cysteines in an active site CXXC motif labeled as catalytic and resolving cysteines based on their roles (102,103). There are two possible mechanisms through which Trx can reduce persulfidated client proteins (31) (Figure 1.13). First one involves the transfer of the outer sulfur atom from the persulfide to Trx catalytic cysteine with a transient formation of Trx-SSH which then reacts with the resolving cysteine, leading to a release of HS^- and formation of intramolecular disulfide bond in Trx. Another mechanism involves nucleophilic attack of Trx catalytic cysteine to the inner sulfur resulting in release of H_2S and a formation of the intermolecular mixed disulfide between Trx and the client protein. Resolving cysteine in Trx can attack the inner sulfur in disulfide bond leading to a release of a thiol and fully oxidized Trx. Trx can be restored by NADPH dependent enzyme TrxR (2,31,55,86).

Glutaredoxin system (GSH/glutathione reductase (GR)/glutaredoxin (Grx)) which is a regulator of GSH redox status could also catalyze depersulfidation in the cellular environment (86).

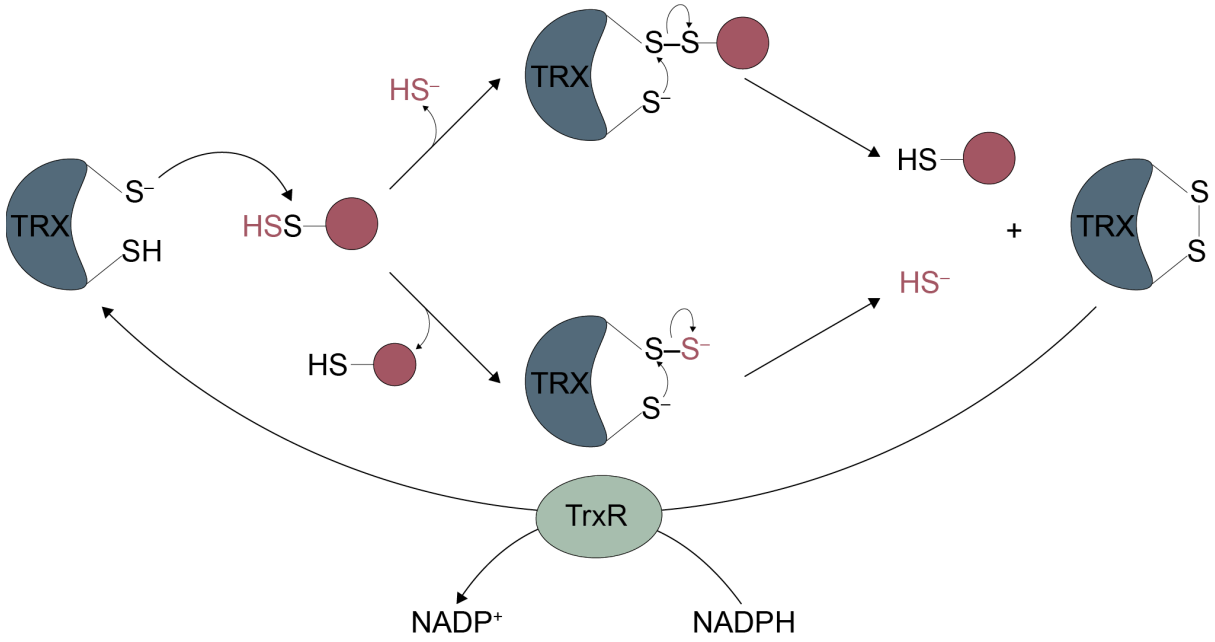


Figure 1.13 TRX-dependent depersulfidation.

Thioredoxin (TRX) can remove persulfides via two distinct mechanisms which result in a formation of oxidized TRX and a release of H_2S. Intramolecular disulfide bond can be reduced by Thioredoxin reductase (TrxR) at the expense of NADPH. Modified from Vignane et al., 2023 (55).

1.7. Physiological roles of H_2S and protein persulfidation

Once H_2S was recognized as an important modulator of physiological processes, numerous studies highlighted its role in various mammalian systems including nervous, cardiovascular, respiratory, digestive, renal and reproductive systems (3,104–107). The physiological role of H_2S was first described in the central nervous system where it has been linked to associative learning by enhancing NMDA receptor-mediated responses and hippocampal long-term potentiation (3,108). Additionally, H_2S modulates synaptic activity by regulating ion channels in both neurons and astrocytes and acts as a neuroprotectant (109–113). H_2S is an important mediator in cardiovascular system. Through cross-talk with $^{\bullet}NO$, H_2S regulates smooth muscle cells relaxation, controls blood

pressure and promotes angiogenesis (5,114–116). It also has cardioprotective roles in ischemia reperfusion injury (5). In the lungs, H_2S has been shown to attenuate pulmonary fibrosis and downregulates pro-fibrosis master regulator TGF-β1 (117,118). Furthermore, H_2S is a modulator of inflammation exhibiting both pro- and anti-inflammatory properties (119–121). At the cellular level, H_2S plays a cytoprotective role under wide range of cellular stress conditions. It promotes cell survival through activation of anti-apoptotic pathways and stimulates cell proliferation (120).

Recent advances in techniques for selective labeling of persulfides, along with growing interest in studying this modification, have significantly contributed to the understanding of mechanism underlaying some of the well-known beneficial effects of H_2S. The importance of persulfides has been demonstrated both through modulation of individual enzyme activity and the regulation of cellular signaling pathways.

The effects of persulfidation on protein function and activity vary depending on the position and number of modified cysteine residues. Persulfidation of C152 in the active site of GAPDH was reported to increase its activity nearly sevenfold, while persulfidation of C156 and C247 completely inhibits its enzymatic function (122,123). Persulfidated E3-ligase parkin has enhanced ubiquitination activity, exhibiting neuroprotective role in mice models of Parkinson's disease (124).

H_2S and persulfidation also play key roles in regulating antioxidant response through Nrf2-mediated pathway (Figure 1.14A). Under basal conditions, the transcription factor Nrf2 is bound to its negative regulator Keap1, which sequesters it in the cytoplasm, resulting in Nrf2 proteasomal degradation. Keap1 acts as a sensor of oxidative stress, as its cysteine residues can be modified by ROS and electrophiles. Persulfidation of these critical cysteines causes its dissociation from Nrf2, which then translocates to nucleus and

upregulates a battery of defense genes (125,126). Additionally, persulfidation has cytoprotective effects by inhibiting p66Shc protein and reducing mitochondrial ROS production (127). Increased activity of persulfidated MEK facilitate DNA damage repair through its downstream signaling, while the modulation of NF-kB pathway via persulfidation promotes the expression of anti-apoptotic genes and cell survival (120,128) (Figure 1.14B). Vasorelaxant effect of H_2S are also partially mediated by persulfidation of ATP-dependent potassium channels (K_{ATP}) in vascular smooth muscle cells (Figure 1.14C). Persulfidation causes K_{ATP} channel opening which leads to potassium ion (K^+) influx, cell hyperpolarization and consequent vasorelaxation. This mechanism is independent from the previously described H_2S-$^{\bullet}NO$-mediated vasorelaxation (129).

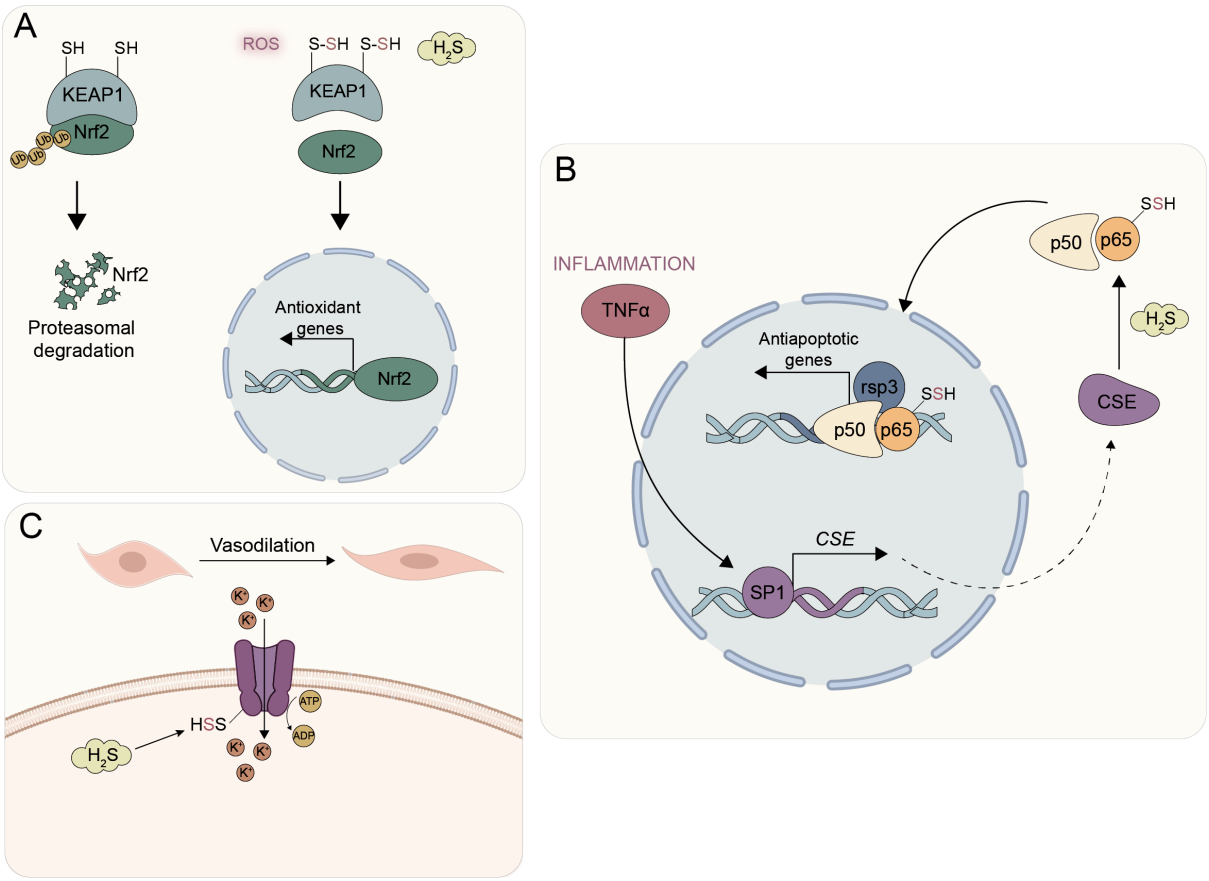


Figure 1.14 Examples of biological processes regulated by H_2S and protein persulfidation.

(**A**) H_2S can regulate cellular antioxidant defence through persulfidation of KEAP1. Under basal conditions, KEAP1 binds to Nrf-2 subjecting it to proteasomal degradation. Persulfidation of KEAP1 leads to its conformational change and release of Nrf2 which translocates to nucleus and upregulates expression of antioxidant genes. (**B**) H_2S can regulate inflammation and apoptosis. Proinflammatory cytokine TNFα stimulates CSE expression through activation of SP1 transcription factor. CSE-mediated H_2S production results in persulfidation of p65 subunit of NF-kB, increasing its binding to a coactivator RSP3. Activated complex regulates transcription of antiapoptotic genes and promotes cell survival. (**C**) Persulfidation of K_{ATP} channel in vascular smooth muscle cells enhances its activity resulting in K^+ influx and consequent vasodilatation.

1.8. Ergothioneine, more than just an antioxidant?

In recent years, more attention has been drawn towards health benefits of naturally produced sulfur-containing compounds. Active principles of garlic exhibit wide spectrum of protective effects including scavenging of reactive oxygene species (ROS), reduction in cholesterol and glucose levels along with hypotensive and cardioprotective effects (130). Furthermore, sulforaphane and erucin, isothiocyanates highly abundant in cruciferous vegetables, also exhibit benefits which are at least partially mediated through their H_2S releasing properties (131–133). Antioxidant and cytoprotective properties of another organosulfur compound, ergothioneine (ET), have led to its acceptance as an important food supplement, with a current vitamin-like status. Although its benefits have been described in different model systems and in pathological conditions affecting various tissues and organs, mechanisms of its action mostly stay elusive.

ET structure was initially described by Charles Tanret in early 20^{th} century as a new compound isolated from ergot fungi (134). ET is a sulfur-containing derivative of amino acid histidine which can be synthesized by mycobacteria, cyanobacteria, methylobacteria, and some non-yeast fungi (135). In microbial organisms, ET can be involved in cellular redox regulation together with main intracellular thiols such as GSH and mycothiol. Most gram-positive bacteria lack GSH, therefore ET together with other LMW thiols might be crucial in maintaining redox and metabolic homeostasis under oxidative stress and exposure to antibiotics (135,136). ET cannot be endogenously produced by plants and animals and its uptake in these organisms is largely dependent on the environment and diet.

1.8.1. Chemical properties of ergothioneine

ET is a 2-mercaptohistidine trimethylbetaine with a thiol group attached to the C_2-position of the imidazole ring (137). It is a colorless and odorless compound, highly soluble in aqueous solutions where it exists in tautomeric equilibrium between two forms (Figure 1.15). Thione form, with sulfur bound via double bond to the nitrogen ring is a dominant form at physiological pH, compared to more reactive thiol form. This property accompanied with its high redox potential, make ET less prone to autoxidation and more stable compared to other thiols (135). Due to its aromatic properties, ET absorbs in ultraviolet UV part of spectra with λ_{max} at 257 nm, therefore also serving as a UV filter in biological systems (138).

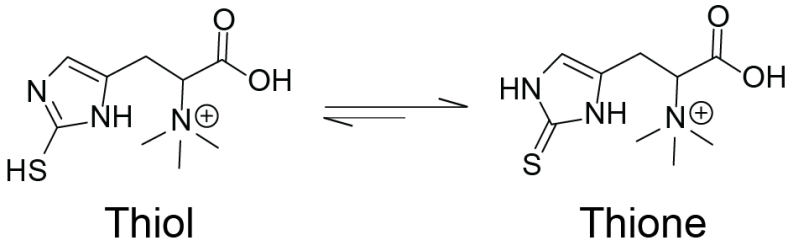


Figure 1.15 Tautomeric forms of ergothioneine (ET).

ET exists in tautomeric equilibrium between its thione and thiole form. ET thione is a stable, more dominant and less reactive form of ET.

1.8.2. Ergothioneine synthesis

In microorganisms, ET can be produced via two distinct oxygen-dependent biosynthetic pathways. Both involve its synthesis from L-histidine through formation of an intermediate molecule hercynine followed by incorporation of sulfur to form the final product (139). In Mycobacteria, this process is catalyzed by five enzymes EgtA-E which

are encoded by ET biosynthetic operon (Figure 1.16, Path A), while in *Neurospora crassa* this process is catalyzed only by two enzymes Egt-1 and Egt-2 (Figure 1.16, Path B) (135,140).

In the first step L-histidine is converted to L-hercynine by trimethylation of its free amino group. Transfer of methyl groups is catalyzed by S-adenosylmethionine (SAM)-dependent histidine methyltransferase EgtD in Mycobacteria or Egt-1 in *N. crassa* (140,141). The next step involves conjugation between sulfur donor and the imidazole ring of hercynine (142). The mycobacterial pathway involves EgtA-dependent synthesis of γ-glutamyl cysteine, as an alternative thiol source which is then used for oxidative formation of S-hercynyl-γ-glutamylcysteine sulfoxide by EgtB. In the next step, glutamine amidotransferase EgtC eliminates glutamate to generate hercynylcysteine sulfoxide (140,142). In *N. crassa* hercynylcysteine sulfoxide is directly formed from L-hercynine and L-cysteine through activity of Egt-1 (141,142). In the last step, ET is formed through C-S bond cleavage catalyzed by PLP-dependent lyase EgtE in Mycobacteria or Egt-2 in *N. crassa* (140,143).

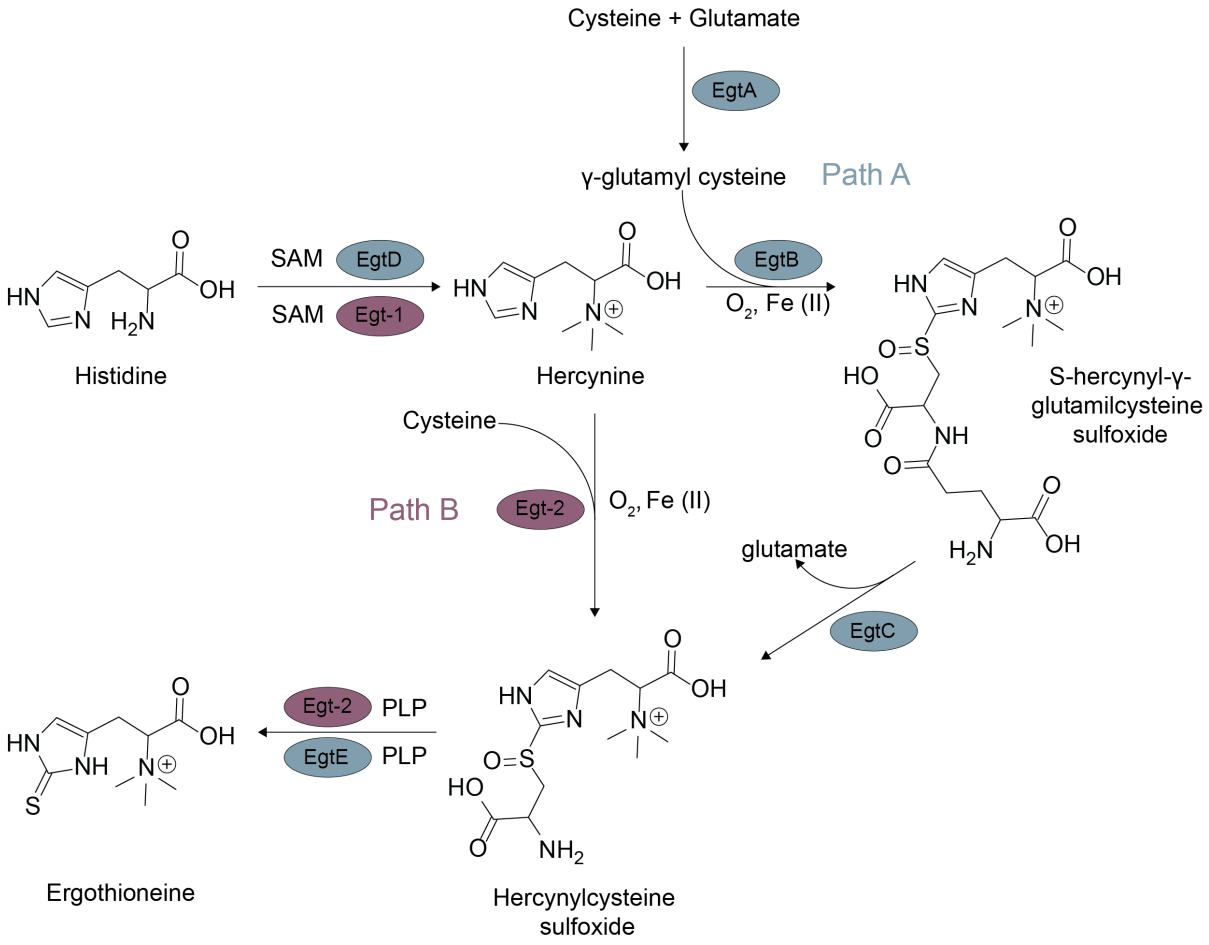


Figure 1.16 Two distinct ET synthetic pathways.

Both pathways require histidine as a starting molecule and oxygen-dependent formation of hercynylcysteine sulfoxide. Path A, characteristic for mycobacteria, is dependent on the presence of 5 enzymes (EgtA-EgtE) and the γ-glutamyl cysteine as a sulfur donor. Path B is characteristic for *Neurospora crassa* and it involves two enzymes Egt-1 and Egt-2 as well as cysteine as a source of sulfur.

Although initially believed that ET synthesis is restricted to aerobic organisms due to oxygen-dependent formation of sulfoxide intermediate, a recent study discovered a novel ET biosynthetic pathway in anoxic green-sulfur bacterium *C. limicola.* Conversion of hercynine to ET is dependent on a sulfur transferase EanB which is a unique example of rhodanese-like enzyme that transfers sulfur to a nonactivated carbon (144). ET

synthesis in anoxic conditions expands its possible roles mostly described in context of its antioxidant properties and direct scavenging of RONS.

1.8.3. Ergothioneine reactivity

ET's reduction potential (Em ~ -60 mV) is less reducing than many other antioxidants but is still effective radical scavenger of singlet oxygen ($^1O_2$), $HO^\bullet$, HOCl and $ONOO^-$ (145–148). However, its potential to quench the most abundant cellular ROS, H_2O_2 and superoxide ($O_2^{\bullet-}$) is much lower and might be irrelevant in the presence of other more abundant alkyl thiols with higher reaction rates toward these molecules. ET can form stable complexes with metal ions including Cu^{2+} and Fe^{2+} or have protective role against reactive species created upon reaction between hemoglobin or myoglobin with H_2O_2 (145,149).

Recent studies have identified multiple forms of ET, suggesting that it can be metabolized or chemically modified upon reaction with other molecules (Figure 1.17). These findings indicate that ET can undergo oxidation in the presence of different oxidating agents at the following rate HOCl > $ONOO^-$ > H_2O_2+myoglobin > H_2O_2. MS analysis revealed several ET oxidation products including hercynine, ET disulfide (ESSE) and ET sulfonic acid ($ETSO_3$). Among these, $ETSO_3$ was dominantly formed upon reaction with HOCl while its levels remained negligible in the presence of other oxidants. The study also proposed a mechanism through which ESSE spontaneously decomposes at physiological pH, contrary to the thiol disulfides. Specifically, two molecules of ESSE lead to formation of 3 mol of ET,1 mol of hercynine and 1 mol of sulfurous acid (H_2SO_3).

This observation suggests that ET can be spontaneously regenerated from its oxidized form without need for reducing agents (150).

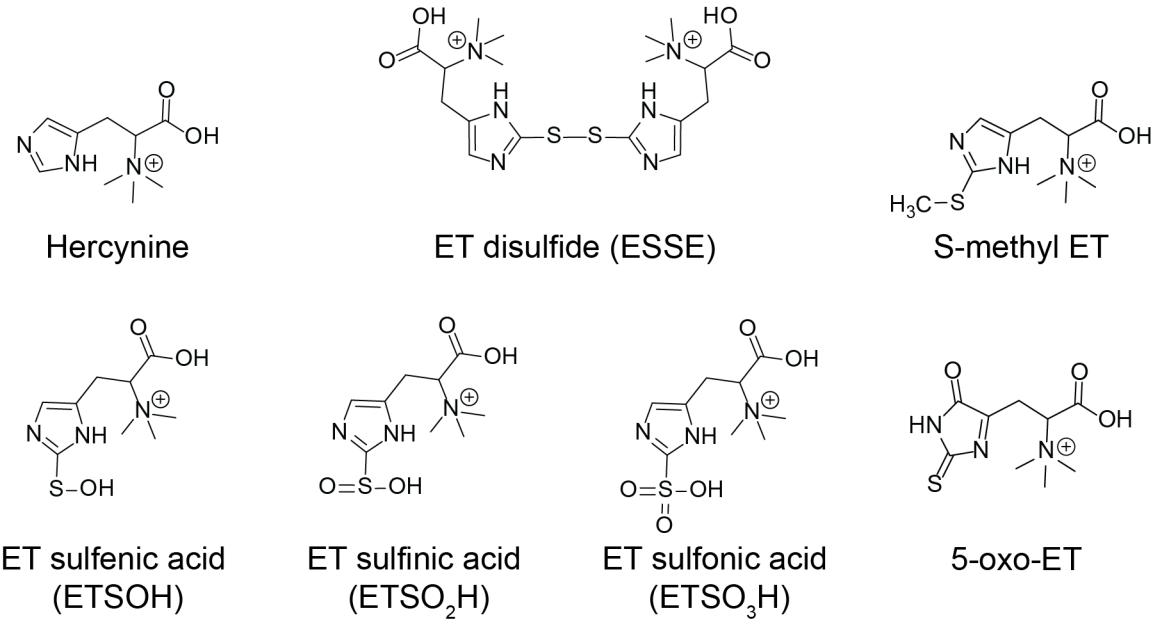


Figure 1.17 Different metabolites derived from ET.

Hercynine, S-methyl ET and $ETSO_3H$, were also detected in vivo, while other forms were mostly detected in vitro.

Further in vitro studies demonstrated that ESSE can be reduced back to 2 molecules of ET by the Trx/TrxR, as well as by the GR/GSH systems. Although latter mechanism seems to be more efficient, GR cannot reduce ESSE directly but only after formation of a mixed disulfide with GSH. In contrast, TrxR can directly use ESSE as a substrate. TrxR/Trx system can also reduce 5-oxo-ET which is formed upon reaction of ET and $^1O_2$ (151). While these findings provide important insights into ET metabolism, it remains unclear how relevant these reactions are in complex biological setting, such as within cells. Therefore, further research is needed to determine whether these in vitro mechanisms play a significant role in vivo.

1.8.4. Ergothioneine catabolism

Synthesis of ET has been studied in detail from the moment of its discovery, but there was not a known mechanism for its enzymatic degradation. Few different studies showed that both ET-producing and ET-nonproducing bacteria possess enzymatically catalyzed ET catabolic pathways (152–156). In vitro reconstitution of a five-step ET degradation pathway characteristic for the ET-nonproducing organisms identified L-glutamate, trimethylamine (TMA), H_2S, carbon dioxide (CO_2), and ammonia as final products (Figure 1.18, in purple) (155). In ET-producing actinobacteria, ET can be converted to sulfinic acid ($ETSO_2$) by thiol deoxygenase (ETDO), which is then a substrate for ET sulfinic acid desulfinase (ETSD) leading to formation of hercynine and sulfur dioxide (SO_2) (Figure 1.18, in blue) (156). Contrary to prokaryotes, in higher organisms ET-metabolizing enzymes have still not been discovered.

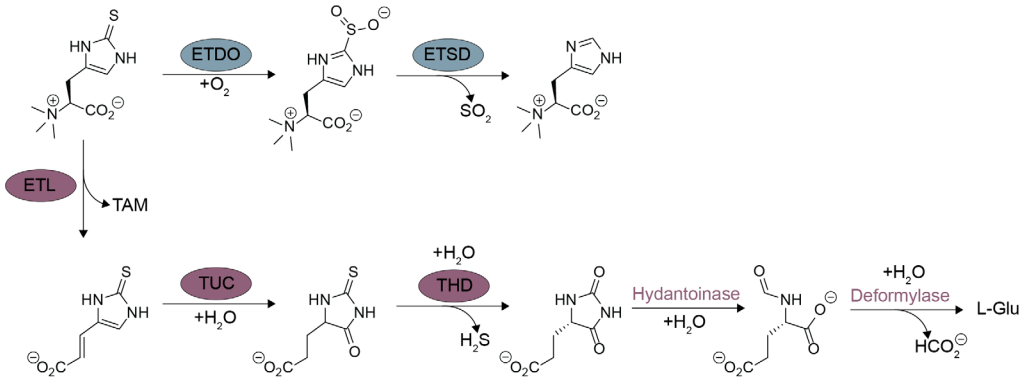


Figure 1.18 Different ET catabolic pathways.

ET-non producing bacteria (in purple) possess a five-step ET degradation pathway which results in formation of L-glutamate, trimethylamine (TMA), H_2S, carbon dioxide (CO_2), and ammonia as final products. On contrary in ET-producing bacteria (in blue) ET is converted to ET-sulfinic acid by thiol dioxygenase (ETDO) which is then converted to hercynine and sulfur dioxide (SO_2) by ET sulfinic acid desulfinase (ETSD). ETL, ergothionase; TUC, thiourocanate hydratase; THD, thiohydantoin desulfurase.

The current knowledge clearly shows that physiological role of ET cannot be simply described through its uncatalyzed and stochastic encounter with RONS. Possibility of different organisms to enzymatically catabolize ET sheds the light on much more regulated process involved in its flux in living organisms. So far, no such system has been detected in vertebrates posing the question how higher organisms regulate ET amounts and whether there are cell-type specific enzymatic machineries involved in this process.

1.8.5. Cellular uptake of ergothioneine

ET is a hydrophilic zwitterion compound which cannot freely pass through the cell membrane. Uptake of exogenous ET in higher organisms is consequently dependent on the presence of a specific transporter. SLC22A4 transporter, also known as organic cation transporter N1 (OCTN1), was initially related to carnitine and tetraethylammonium cation transport. Work by Gründemann et al. showed that SLC22A4 efficiently and specifically transports ET in a sodium-dependent manner. ET is taken up by SLC22A4 hundred folds faster than tetraethylammonium cation (157). Another transporter from the same family, SLC22A15 can also, although not exclusively and with lower efficiency, transport ET in a sodium-dependent manner. Both SLC22A4 and SLC22A15 are almost ubiquitously expressed, but SLC22A15 seems to be a dominant transporter in the brain (158). SLC22A4 is highly expressed on the apical membranes of enterocytes and proximal tubular cells in the kidney which reflects efficient ET uptake from the food and its recovery from the urine (Figure 1.19). High levels of SLC22A4 were also identified in blood cells, including erythrocytes, granulocytes, neutrophils and monocytes (159–161). Depletion of SLC22A4 transporter in different cellular or animal models affects cell proliferation and leads to an increased protein, lipid and DNA oxidative damage under stress (162–165).

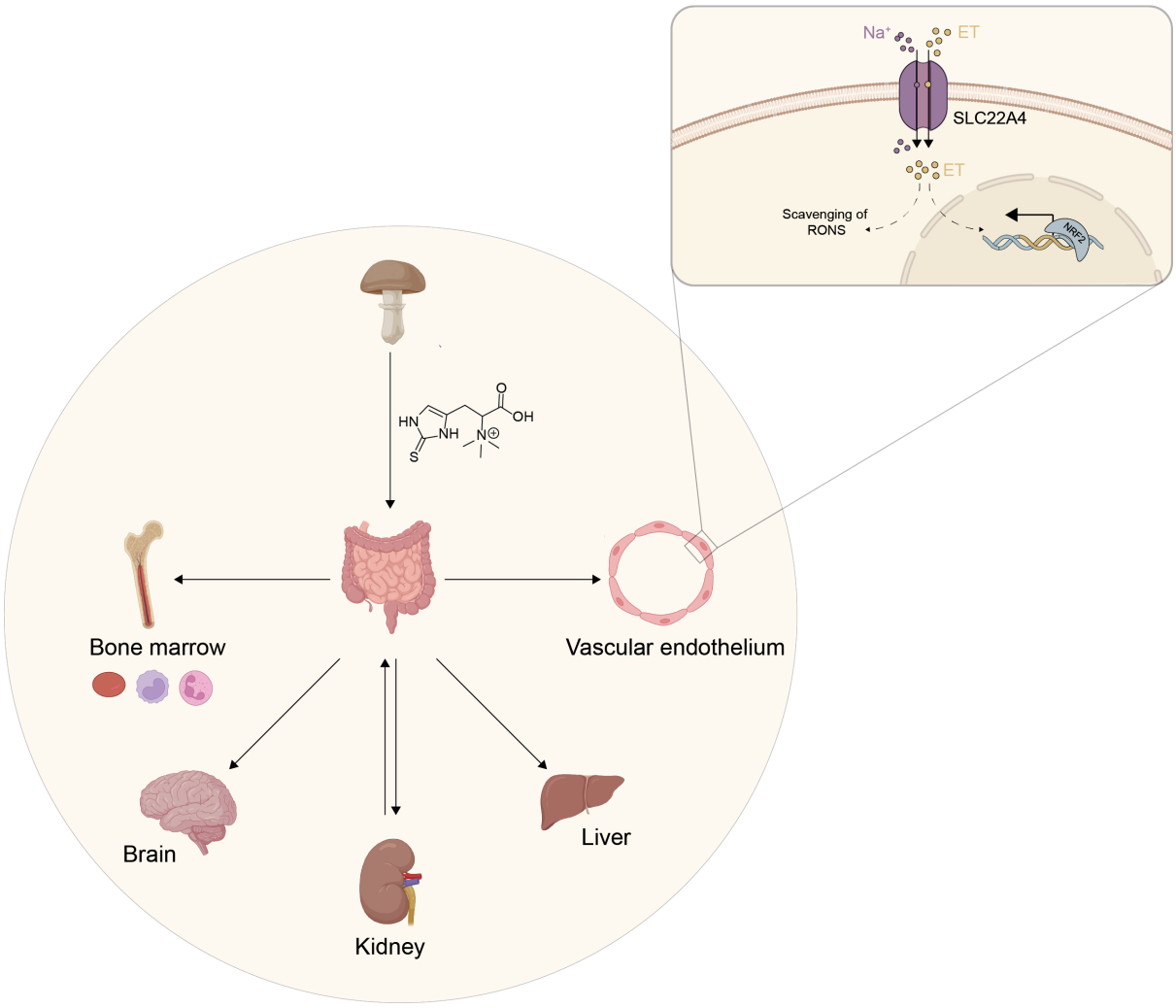


Figure 1.19 ET accumulation in different organs and within the cells.

Upon administration, ET is readily absorbed by enterocytes in the gut and it accumulates in high concentrations in the presented tissues/structures. Cells possess SLC22A4 transporter which enables fast uptake of ET together with natrium ions (Na^+). Within the cell ET is proposed to act as a RONS scavenger or it can activate antioxidant pathways. Modified from Tian et al., 2023 (166).

Abundance of the transporter correlates with ET accumulation in different organs in both mice and humans where it can reach millimolar concentrations (Figure 1.19) (167). The highest levels detected immediately after administration are in small intestine, liver and kidney, while after prolonged time ET levels also increased in other organs as spleen,

bone marrow, heart, eye and lungs (164,167,168). Substantial ET amount is detected in the blood while very low urine levels show its accumulation and retention within the body. ET metabolites including hercynine, ET-SO_3H as well as S-methyl ET were also detected but whether they are just products of ET metabolism or have specific roles still stays unclear (Figure 1.18) (167,168).

Different class of ET transporters, named EgtU/EgtUV, are broadly present and conserved in both commensal and pathogen microbial species colonizing vertebrate gastrointestinal tract (GIT). EgtU transporter belongs to the ATP-binding cassette (ABC) superfamily where substrate translocation through membrane is dependent on ATP hydrolysis. Current knowledge suggests that inter-kingdom competition for ET in GIT largely affects its distribution and absorption by the host. ET intake by pathogens does not only decreases ET's availability but can further improve the survival and colonization of GIT by pathogens (159,169).

1.8.6. Physiological roles of ergothioneine

Over more than a century of research, the multifaceted properties of ET have gradually been uncovered across different kingdoms, from bacteria to humans. While not vital for survival under healthy conditions, ET readily accumulates in the cells and fully manifests its potential in various pathological states. ET administration decreases cell senescence, ROS levels and oxidative damage of biomolecules while promoting cellular survival upon exposure to various stressors such as UV-irradiation, H_2O_2, pyrogallol, hyperglycemia and xanthine/xanthine oxidase (162,170–177). The wide range of observed benefits cannot be solely attributed to the direct antioxidant properties of ET, further complicating its role in the stress response. Independent studies across various

model systems have observed the activation of antioxidant and viability signaling pathways in the presence of ET. UV-induced damage in fibroblasts and keratinocytes is significantly ameliorated by ET-dependent activation and nuclear localization of Nrf2, leading to the upregulation of components in the cellular antioxidant defense system (172,173,175). ET's benefits are also at least partially mediated by Nrf2 in animal models, confirming the relevance of this mechanism in vivo (178–180). The activation of Nrf2 by ET remains a mystery, leaving potential explanations open to exploration. ET could directly interact and modify Nrf-2 or its inhibitor Keap1 or its potential enzymatic transformation could produce metabolites which would then indirectly convey the signal. ET also exhibits anti-inflammatory properties by inhibiting NF-κB signaling induced by oxidative stress and the pro-inflammatory cytokine TNFα (181). Additionally, the expression of *SLC22A4* gene is upregulated upon NF-κB pathway activation (182). This suggests a potential feedback mechanism where increased ET uptake could provide protection against chronic inflammation induced by excessive NF-κB activity. Exposure to ET restores sirtuin (SIRT6 and SIRT1) levels in aging mice and high-glucose-induced senescence in endothelial cells (171,177). Sirtuin 1 (SIRT1) and Sirtuin 6 (SIRT6) are highly expressed in the vasculature with pivotal roles in preserving integrity of endothelial cells and vascular system in oxidative stress and aging (171).

This small but powerful molecule is often addressed as "longevity vitamin" with a potential to promote healthy aging. Treating mice for one week with ET improves the endurance and running distance while not affecting post-exercise inflammatory response and metabolic stress compared to control animals (180). *C. elegans*, *D. melanogaster* and mice exposure to ET increased life span and health span in a dose dependent manner (177,183). Studies in humans revealed that plasma ET levels were significantly lower in

dementia and Parkinson's disease patients compared to the age-matched healthy individuals (184,185). Furthermore, decreased ET in plasma and blood has been associated with frailty in the elderly population, while its presence positively correlates with decreased risk of cardiovascular diseases and mortality (186–188). ET can pass blood-brain barrier and accumulate in the brain, possibly playing an important role in its functioning. ET protects against neuronal injury induced by cisplatin and β-amyloid as well as learning and memory deficits induced by D-galactose (189–191). Its importance in β-amyloid protection has also been showed in cellular models, neurororetina of a mouse model of Alzheimer's disease as well as in *C. elegans* expressing human β-amyloid peptide (192–194). Both health span and life span of transgenic β-amyloid worm models were improved in presence of ET (193). ET is a pleiotropic cytoprotectant with therapeutic potential to promote healthy aging and exert anti-inflammatory effects. However, the complexity of its mechanisms of action requires further investigation to fully understand its role across various biological systems, organs and tissues (Figure 1.20).

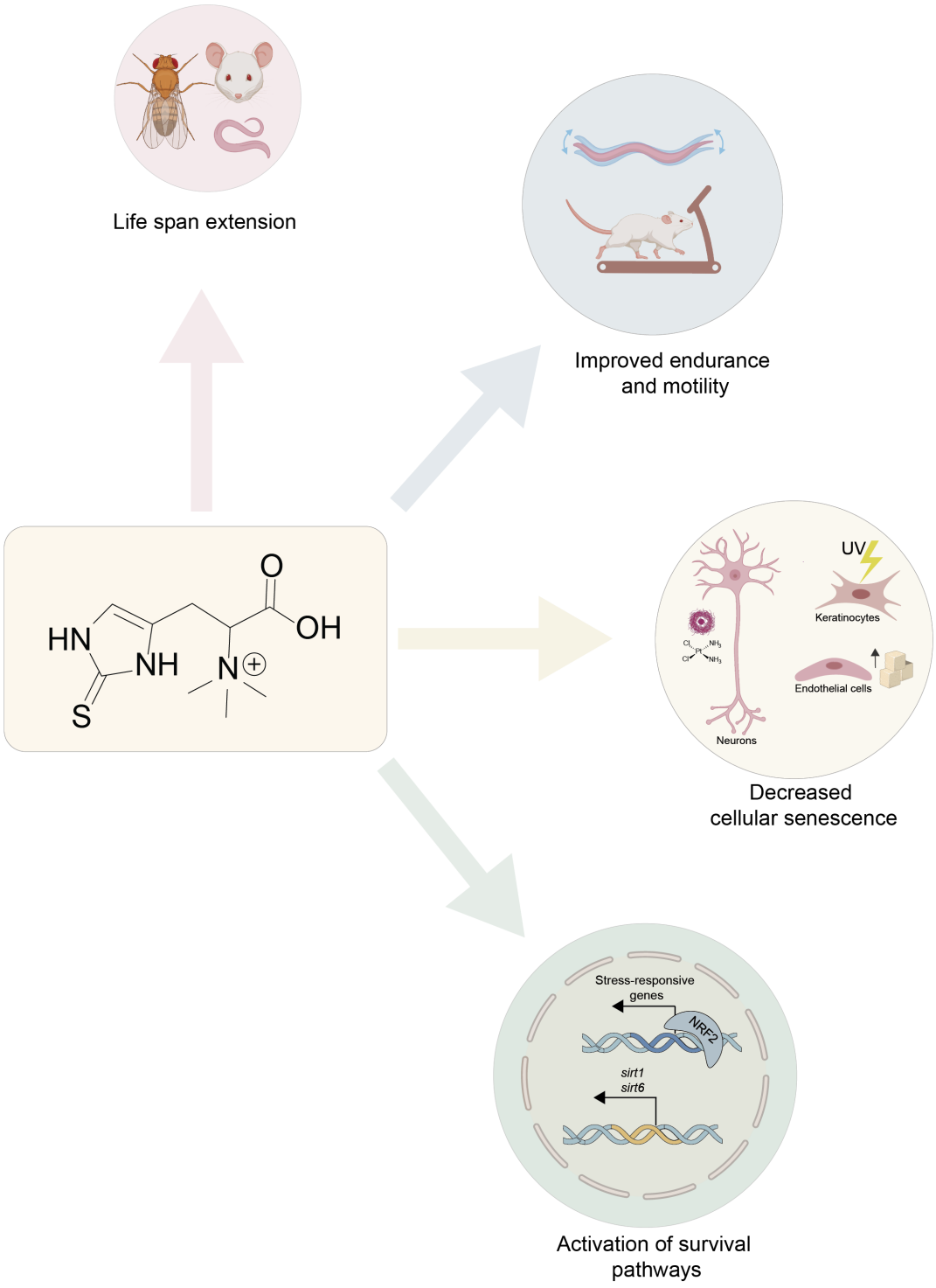


Figure 1.20 Beneficial effects of ET.

ET extends both lifespan and healtshan across different species. It has cytoprotective effects, preventing cellular senescence caused by UV irradiation in keratinocytes and fibroblasts, high glucose in endothelial cells or cisplatin and β-amyloid in neurons. ET also activates antioxidant and longevity promoting pathways.

1.9. *C. elegans*, tiny but powerful model system

The 20th century witnessed some of the greatest discoveries in molecular biology, yet Sydney Brenner felt that it was necessary to shift focus towards new, more complex and exciting biological problems such as development and the nervous system. While *C. elegans* was already an established model system, Brenner gradually brought this tiny nematode into the spotlight due to its numerous advantages as a multicellular organism compared to the previously studied bacteria and viruses. Once introduced, *C. elegans* became one of the most extensively studied organisms in the field of development, genetics, neurobiology and aging. This ~1-mm-long worm was the first organism to have its genome completely sequenced in 1998. Additionally, scientific world owns 3 Nobel prizes to this simple nematode for the elucidation of genetic regulation of organ development and programmed cell death, discovery of RNA interference as well as for the development of the green fluorescent protein (195–199).

C. elegans is a simple, transparent multicellular organism with a fixed number of cells organized into distinct functional entities, making it a powerful model system for studying cell differentiation and fate. Its short life cycle and lifespan of approximately three weeks further allow real-time investigation of both development and aging. *C. elegans* development is an approximately 3-day-long process comprised of 4 larval stages (L1-L4) which results in a reproductively mature adult (Figure 1.21). Each larval stage as well as the aging process of *C. elegans* are characterized by significant remodeling at the level of transcriptome, proteome and cell signaling (200,201). Although very distant at the first sight, worms and humans share similarities at many levels, including the high percentage of homologue genes as well as conserved molecular mechanisms involved in stress response and survival (202,203).

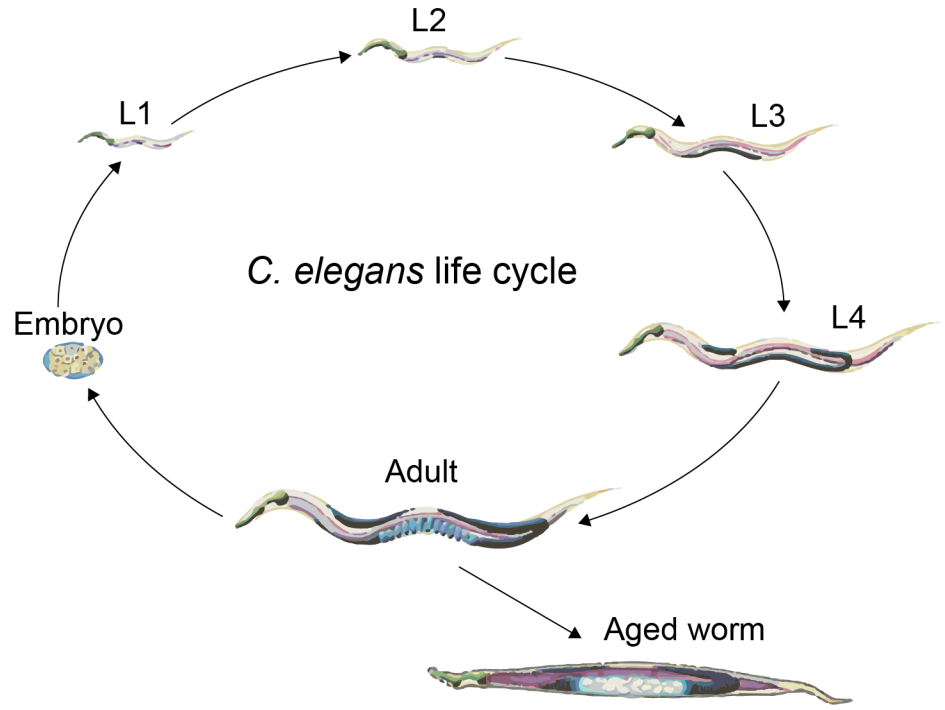


Figure 1.21 *C. elegans* lifecycle.

A three-day-long lifecycle is comprised of 4 larval stages (L1-L4) which result in a formation of a gravid adult. With time C. elegans exhibits all usual features characteristic for aging process.

1.9.1. Endogenous production of H_2S in *C. elegans*

H_2S production in *C. elegans* depends on orthologues of three H_2S-producing enzymes found in mammals. The *C. elegans* genome contains two genes coding for CSE (*cth-1* and *cth-2*), two genes for CBS (*cbs-1* and *cbs-2*) and 7 genes coding for orthologues of MST (*mpst1-7*). Several studies have shown that knocking down or deleting some of these genes impact both health span and life span. While the absence of *cth-1 and cth-2* genes does not affect the survival or phenotype of unstressed worms, *cth-1* mutants are more sensitive to oxidative stress compared to wild type (WT) animals (49). On the other hand, deletion of *mpst-1* or *mpst-3* genes reduces the lifespan and negatively impacts healthspan and stress resistance. *mpst-1* mutants exhibit dramatically

impaired healthspan, reduced fertility, and higher levels of mitochondrial DNA damage, while *mpst-3* knockouts live shorter and die faster than WT when exposed to paraquat (23,49,204). The presence of several *mpst* genes in *C. elegans* genome complicates the interpretation of the observed phenotypes, as deletion of one gene leads to compensatory overexpression of the others (23). Silencing *cbs-1* gene via RNA interference (RNAi) significantly delays *C. elegans* development and causes abnormalities in the gut and pharynx, alongside elevated cellular levels of homocysteine. While *cbs-1* appears to perform a similar role to human CBS in the transsulfuration pathway, the function of *cbs-2* remains elusive. Current literature suggests that *cbs-2* is not involved in H_2S metabolism but instead plays a role in DNA damage-induced apoptosis during meiosis (205).

Although the expression patterns and some functions of abovementioned gene products have been clarified, it is still not clear whether different homologues have overlapping functions distinguished only by their spatial and temporal expression, or if they serve entirely distinct roles within the cell. Therefore, further biochemical and functional analysis focused on single protein targets will be crucial for the understanding of H_2S metabolism in worms.

Since natural habitat of this free-living nematode is rich in H_2S, *C. elegans* evolved detoxification systems for its oxidation to non-toxic sulfates. Worms possess orthologues of human mitochondrial enzymes SQRD (SQRD-1) and ETHE (ETHE-1), as well as four genes (*cysl1-4*) encoding proteins closer to plant and bacterial cysteine synthases (CYS) (206). Animal homologues of CYS proteins seem to be present only in some nematodes and herbivorous arthropods (207). Although the functions of all four CYS-like proteins are not yet fully characterized, current evidence suggests that CYSL-1 is involved in the response to elevated H_2S and hydrogen cyanide levels and CYSL-2 produces H_2S via

HCN assimilation (207). Additionally, CYSL-1 and CYSL-2 play crucial roles in *C. elegans* adaptation to various pathogens (206,208).

1.9.2. Effects of exogenous H_2S on *C. elegans*

The pioneer experiment showing the effect of exogenous H_2S on *C. elegans* was performed by exposing worms to atmosphere containing the gas. Worms grown under 50 ppm H_2S are healthy, have significantly extended mean and maximum lifespan and increased thermotolerance compared to worms exposed to room air. On contrary, exposure to higher doses is toxic and worms die within a short period of time. Interestingly, the beneficial effect is only achieved when worms are exposed to H_2S from early larval stages and continuous exposure is required for lifespan extension (209). H_2S-dependent increase of the lifespan and thermotolerance in *C. elegans* is dependent on the presence of sirtuin 2.1 (SIR-2.1) and modulation of its activity (Figure 1.22) (209).

Following studies on *C. elegans*, using the same source and concentration of H_2S, showed that the coordinated transcriptional response of both hypoxia-inducible factor (HIF-1) and skinhead-1 (SKN-1) transcriptional factors is necessary for survival and growth in H_2S (Figure 1.22) (206,210). Animals lacking one of those two proteins die when exposed to low H_2S concentrations which are sublethal for WT animals. While HIF-1 is a transcriptional factor activated in a response to low oxygen concentrations, SKN-1 is an orthologue of mammalian Nrf2 involved in the regulation of stress response (211,212). Activation of HIF-1 in the presence of H_2S is differently regulated compared to its canonical activation in hypoxia. Proposed mechanism is dependent on CYSL-1 which serves as an H_2S sensor required for HIF-1 activation.

SKN-1 is a known master regulator of phase II response to oxidative stress and toxins (212). However, there is a small overlap of canonically induced genes under oxidative stress and those changing upon H_2S exposure (210). Activation of SKN-1 results in distinctive transcriptional pattern which comprise of noticeable upregulation of *cysl-2* and *rhy-1* genes. RHY-1 is a transmembrane protein localized in the ER with two different roles in mitigating H_2S toxicity. Both roles are dependent on its interaction with CYSL-1 which can result in the negative regulation of HIF-1 activity but also promote survival upon exposure to H_2S in HIF-1-independent manner (213). Inhibition of HIF-1 activity might be important for limiting the intensity and duration of the activated response. Furthermore, increased levels of RHY-1 are sufficient to rescue lethality of *hif-1* mutants when exposed to H_2S (214). Exposure to H_2S atmosphere before and during the hypoxic conditions can also reverse hypoxia-induced disruption of proteostasis, although through mechanisms different than the ones employed for lifespan extension (215).

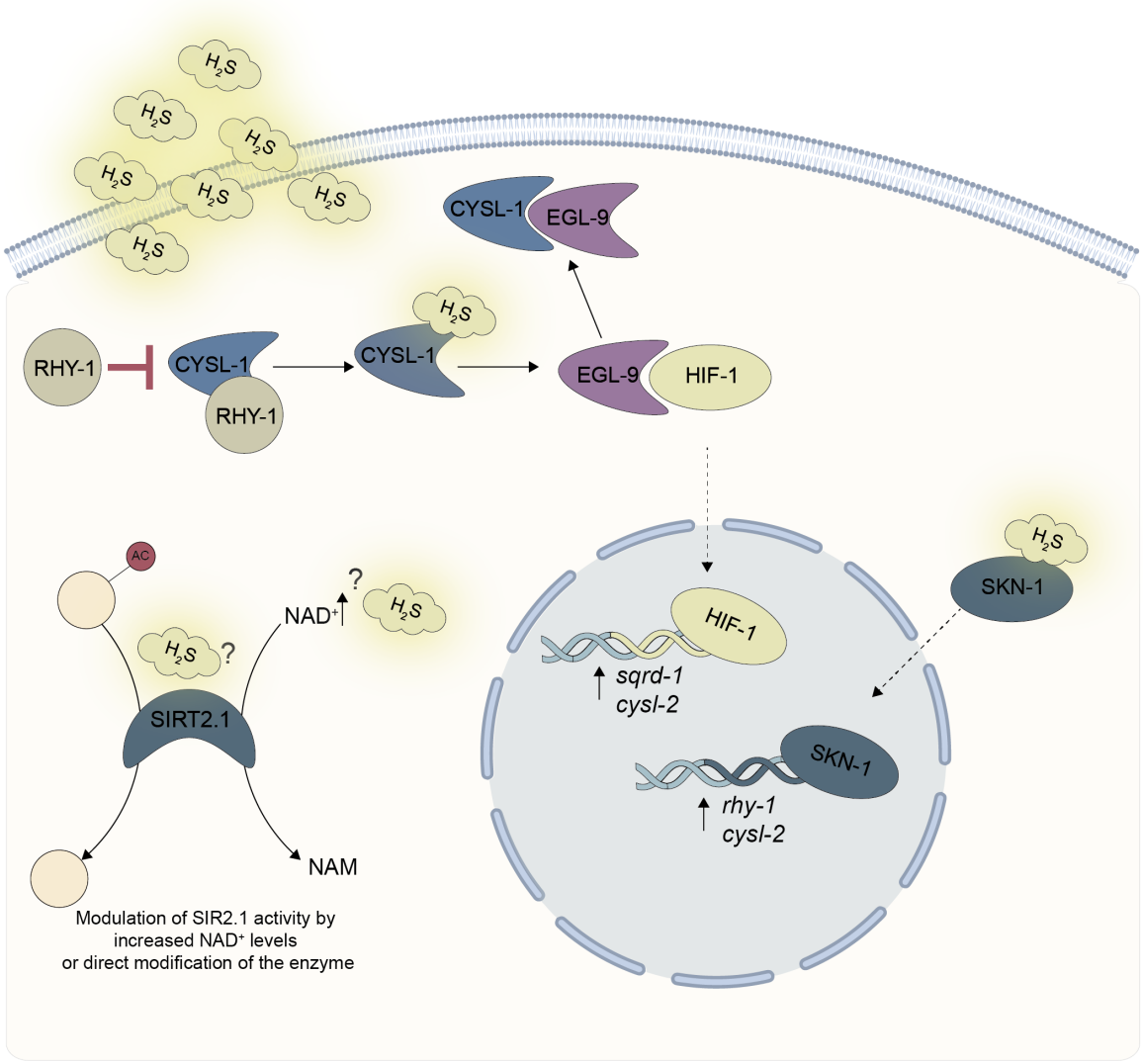


Figure 1.22 *C. elegans* senses H_2S. Survival and lifespan extending properties of exogenously administrated H_2S are dependent on SIRT2.1, HIF-1 and SKN-2 activity.

H_2S-dependent increase in SIRT2.1 activity is required for lifespan extension through an unknown mechanism. Upon exposure to H_2S, CYSL-1 binds to EGL-1, a known inhibitor of HIF-1. Released HIF-1 translocates to nucleus where it regulates transcription of genes involved in H_2S metabolism. SKN-1 is also required for survival upon exposure to H_2S and it regulates transcription of distinct set of genes. One of its targets, RHY-1 is essential for survival in H_2S and it also acts as a negative regulator of HIF-1.

Although growth in 50 ppm H_2S gave an important insight into response of *C. elegans* to H_2S, administrated concentration was much higher than the concentration worms encounter in their natural habitat or endogenously produce. Therefore, use of slow-releasing donors proved to be a better solution to mimic concentrations of physiologically produced H_2S. Both healthspan and lifespan were improved in WT and *mpst-1* mutant when worms were treated with GYY4137 from L1 larval stage (23,216). Recently developed slow-releasing H_2S donor FW1256 also showed beneficial effects but only under continuous exposure from early life stages (217). GYY4137 and AP39 both has protective effects in *C. elegans* Duchenne muscular dystrophy (DMD) models (28). DMD worms displayed profound loss of skeletal muscle mass, impaired movement and mitochondrial structure, a phenotype characteristic for aged animals (218). Treatment with both H_2S donors improves numerous aspects of worm physiology such as strength, movement and mitochondrial structure, although without affecting the lifespan (28). Exposure to thiosulfate, a mimetic of H_2S releasing compounds and FDA approved therapeutic, also promotes longevity together with persulfidation increase in WT animals (49).

Furthermore, a removal of germline prolongs life in worms, a phenomenon dependent on H_2S and moderate ROS production (219). CBS-1-dependent increase in H_2S production promotes longevity through activation of SKN-1 signaling pathway (219). Interestingly, increased levels of both CBS-1 and H_2S are inherent part of lifespan extension at low temperatures which is completely dependent on the presence of germ cells and their robust proliferation (220). It becomes obvious that the worm physiology and signaling are drastically affected by the temperature and other environmental conditions.

Longevity benefits of dietary restriction in *C. elegans* are also mediated by H_2S. Genetic model of dietary restriction, *eat-2* mutant, lives longer and has higher global persulfidation compared to WT. The observed effects are completely abolished upon silencing of H_2S producing enzymes, with both lifespan and persulfidation levels reduced back to control levels in *cth-1* or *mpst-3* mutant background. Furthermore, treatment with 2-deoxy glucose, a chemical mimetic of dietary restriction, also extends lifespan in WT animals but not in *cth-1* mutants (49). On the other hand, genetically manipulated overexpression of CBS-1 mimics beneficial effects of dietary restriction without any intervention (221). Although a common mediator of longevity promoting interventions, H_2S most probably employs different mechanisms (217).

1.10. Interplay between H_2S and aging process

Aging is a complex phenomenon characterized by progressive, time-dependent deterioration on molecular, cellular and ultimately systemic level. Functional decline affects nearly all living organisms, from simple unicellular forms to more complex multicellular organisms such as mammals. The urge to better understand the underlying causes of this multifaceted process has led to the characterization of initially nine and currently twelve hallmarks of aging which follow a certain level of hierarchy (Figure 1.23). The primary hallmarks involve progressive accumulation of damage at the levels of genome, epigenome, proteome and cellular organelles. The antagonistic hallmarks reflect the processes and pathways that are beneficial for organismal survival and response to stress, however, when these pathways are excessively or chronically activated, they become harmful and contribute to cellular damage later in life. The third category, defined

as the integrative hallmarks, arises when homeostatic mechanisms fail to mitigate the damage induced by the primary and antagonistic hallmarks. This group involves chronic inflammation, alternation of intercellular communication, stem cell exhaustion and dysbiosis (Figure 1.23). Although the hallmarks may appear distinct at the first sight, they are functionally and spatially interconnected and interdependent. For example, genomic instability impacts not only the genome and epigenome but also disrupts proteostasis through transcription and translation of aberrant proteins, induces cellular senescence, triggers mitochondrial dysfunction through mitochondrial DNA damage, and can also promote dysbiosis. This intricate interplay among various aspects of aging is further reflected in anti-aging therapies which often target multiple hallmarks simultaneously (222,223).

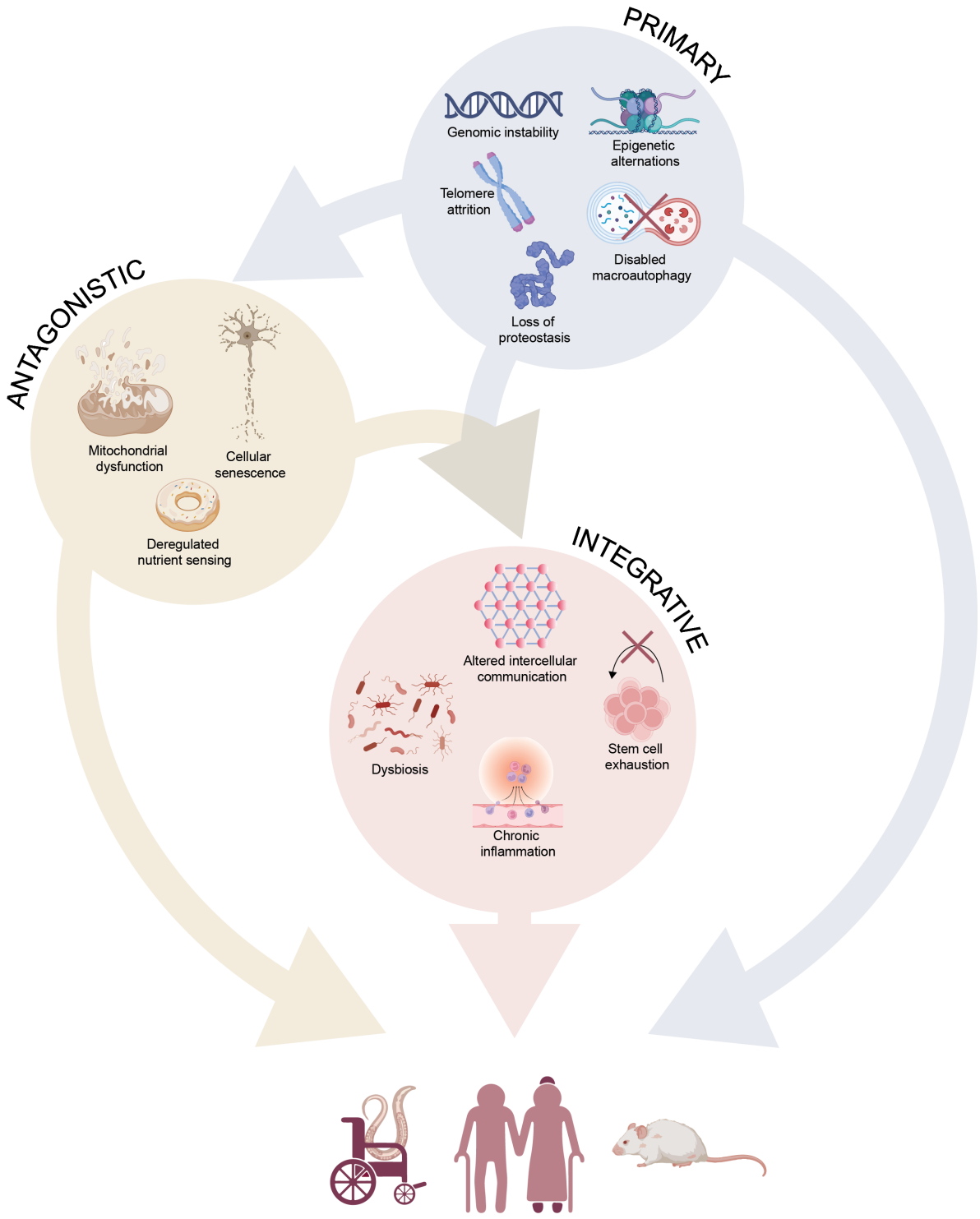


Figure 1.23 The hallmarks of aging.

The scheme represents 12 hallmarks of aging grouped into three categories: primary, antagonistic and integrative. All three categories are interconnected and interdependent and they all contribute to the aging process.

1.10.1. H_2S as an anti-aging molecule

After its acceptance as a physiological modulator, H_2S slowly started being regarded as a potential longevity molecule due to its effects on certain age-related pathologies. Although produced in very low concentrations, endogenous H_2S is pivotal for proper cell function. Several studies have shown that levels of H_2S producing enzymes decrease with aging in different model systems such as *C. elegans*, rodents and aging cardiomyocytes (49,201,224,225). Furthermore, deletions of their respective genes also affects both lifespan and healthspan across different species. H_2S has been linked to amelioration of all aging hallmarks except telomere attrition since it has not been studied in H_2S context so far (226). H_2S can promote DNA repair and genome integrity through modulation of MEK/ERK pathway and activation of Poly(ADP-ribose) polymerase 1 (128). Furthermore, H_2S has been shown to upregulate histone deacetylase SIRT1 (226–228).

1.10.2. H_2S effect on proteostasis in the context of aging

Impaired proteostasis caused by the failure of the systems for protein synthesis, folding, maintenance and removal is one of the primary hallmarks of aging. An additional level of proteostasis disruption involves the dysregulation of PTMs, dynamic and reversible modifications critical for proper protein function. One of the reasons is the increased RONS production which induces irreversible oxidative PTMs and loss of protein function and structure with age. The decline of ubiquitin-proteasomal and autophagy-lysosomal degradation pathways further contributes to the accumulation and aggregation of aberrant proteins, resulting in proteotoxicity and cell damage (229–231). The aging signature associated with protein aggregation is well conserved among different species

and displays a strong tissue-specific pattern (231). *C. elegans* proteome is also largely affected by protein aggregation with several hundred proteins becoming more insoluble with age (201,230). This process impacts the lifespan and promotes further aggregation of known disease-inducing proteins. Interestingly, highly insoluble proteins detected in aged worms are also found in aggregates associated with neurodegeneration in humans such as Alzheimer's disease (230).

Small size, high production flux and diffusibility of H_2S contribute to its potential role in maintenance of proteostasis through persulfidation-dependent protection of cysteine residues (Figure 1.24).

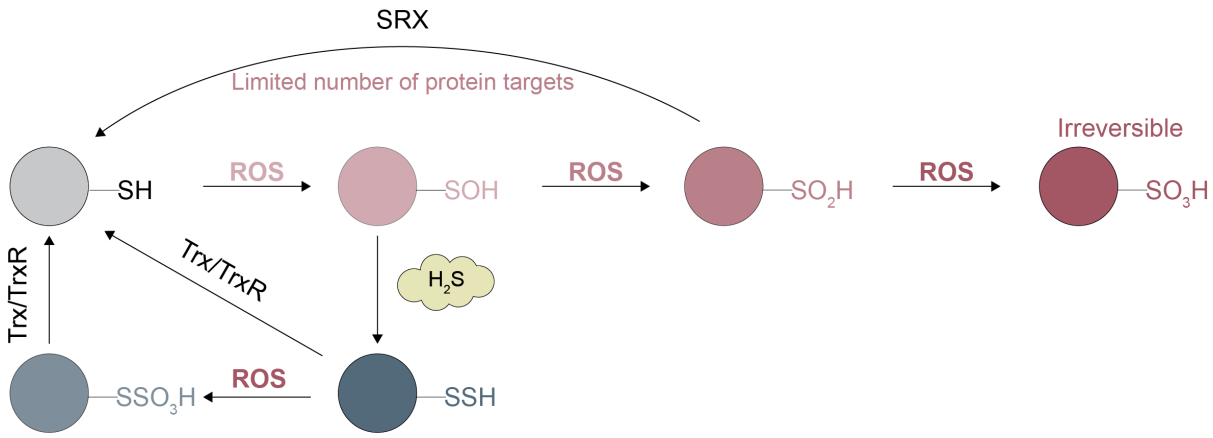


Figure 1.24 Potential protective mechanism of protein persulfidation.

Increased protein persulfidation can serve as a mechanism to prevent protein overoxidation and loss of function which contributes to overall disruption of proteostasis in aging. While sulfinic acids (RSO_2H) of certain protein can be reduced by sulfiredoxin (SRX) (232), RSO_2H and RSO_3H are mostly irreversible modifications. Modified from Zivanovic et al., 2019 (49).

Decrease of H_2S production with age is followed by a drop in RSSH levels and by an increase in RSO_2H in worms, rats and aged human fibroblasts (49). Perturbation in H_2S production and metabolism have been associated with human neurodegenerative

and age-related diseases. Both cellular and animal models of Huntington's disease (HD) have profoundly reduced CSE levels accompanied with diminished H_2S and cysteine formation, lower persulfidation levels and reduced survival upon cysteine deprivation (48,49,233). Furthermore, mice lacking CSE exhibit hypertension and motoric abnormalities characteristic for HD mice models (48,234). In the brains of HD patients, CSE levels are significantly depleted in striatum, a structure mostly affected by the disease (48). Diminished CSE and persulfidation levels are also detected in *D. melanogaster* model and humans with spinocerebellar ataxia 3 (SCA3), another example of neurodegenerative disease (49,235). Important role of H_2S and persulfidation has also been associated with Parkinson's and Alzheimer's disease where decreased persulfidaton of specific protein targets drives the pathology (124,236). Therefore, genetic or pharmacological interventions to boost H_2S and persulfidation levels could be beneficial to fight certain aspects of aging process on both cellular and systemic level.

1.11. Role of H_2S in cellular stress response

Cells are highly dynamic systems that continuously sense and respond to the changing environmental conditions. Their function relies on the proper synthesis, folding, localization and degradation of proteins. Perturbation of protein homeostasis (proteostasis) can be triggered by various stress conditions. Cells evolved signaling mechanisms to respond and adapt to a wide range of intrinsic and extrinsic stimuli which alter their function. Accumulation of misfolded proteins in endoplasmic reticulum (ER) activates phylogenetically conserved pathways named unfolded protein response (UPR) while accumulation of aberrantly folded proteins in the cytoplasm activates heat shock

response (HSR) (237,238). On the other hand, the term integrated stress response (ISR) refers to the cellular response to the pathological changes in both cellular organelles and cytoplasm (239).

1.11.1. Integrated stress response

ISR is a central, evolutionarily conserved signaling network in eukaryotic cells which nucleates diverse stress stimuli such as nutrient deprivation, hypoxia, viral infection and accumulation of unfolded proteins into a common output which is global remodeling of protein synthesis. The converging point for different stress inputs is phosphorylation of the alpha subunit of eukaryotic translation initiation factor 2 (eIF2α) by four “stress sensing” kinases. EIF2α phosphorylation (eIF2α-P) leads to a global suppression of protein translation while stimulating translation of specific messenger RNAs (mRNAs) (**Figure 1.25**) (240).

Heterotrimeric translation initiation factor eIF2 (consisting of α, β and γ subunit), guanosine 5’-triphosphate (GTP) and methionyl-initiator tRNA (Met-tRNA$_i$) are involved in formation of the ternary complex (TC) required for initiation of canonical translation of AUG-containing mRNAs. Under stress conditions, phosphorylation of eIF2α subunit at Ser51 results in inhibition of TC formation and reduction in translation initiation rates (239). In metazoan four serine/threonine (S/T) kinases are responsible for initiation of ISR and eIF2α phosphorylation: PKR-like ER kinase (PERK), double-stranded RNA-dependent protein kinase (PKR), heme-regulated eIF2a kinase (HRI), and general control non-derepressible 2 (GCN2) (241–247). Although they have homologue catalytic domains, each of them has unique regulatory domain which defines its sensitivity toward a specific stress type. They can also have overlapping functions important for fine modulation of

cellular response and lack of one kinase can be compensated by the upregulation of another one (240).

ISR activation enables TC-independent translation of a subset of mRNAs encoding for effector proteins involved in further mediation of the stress response. In metazoan, transcriptional factor ATF4 is the best characterized effector of the ISR and the master regulator of stress-responsive gene expression (239,240). Besides ATF4, other important mediators whose levels are increased through TC-independent translation are CHOP, ATF5 and GADD34 (248–250). Through interaction with various partner proteins, ATF4 selectively regulate expression of gene subsets, tailoring the cellular response towards different stresses (240).

ISR duration and intensity need to be finely tuned to avoid unwanted cell damage. Consequently, ATF4 expression is tightly regulated on transcriptional, translational and post-translational levels (251–254).

Attenuation of ISR is crucial for cell survival and restoration of protein synthesis and basal cell functioning. This process is dependent on the dephosphorylation of EIF2α-P by protein phosphatase 1 (PP1) complex containing a unique catalytic subunit (PP1c) but different regulatory subunits, CReP or GADD34. While CReP is constitutively expressed and involved in a slow and basal EIF2α-P dephosphorylation in unstressed cells, GADD34 expression is, as above mentioned, induced by ISR and acts as a negative feedback loop to halt ISR overactivation (251,252).

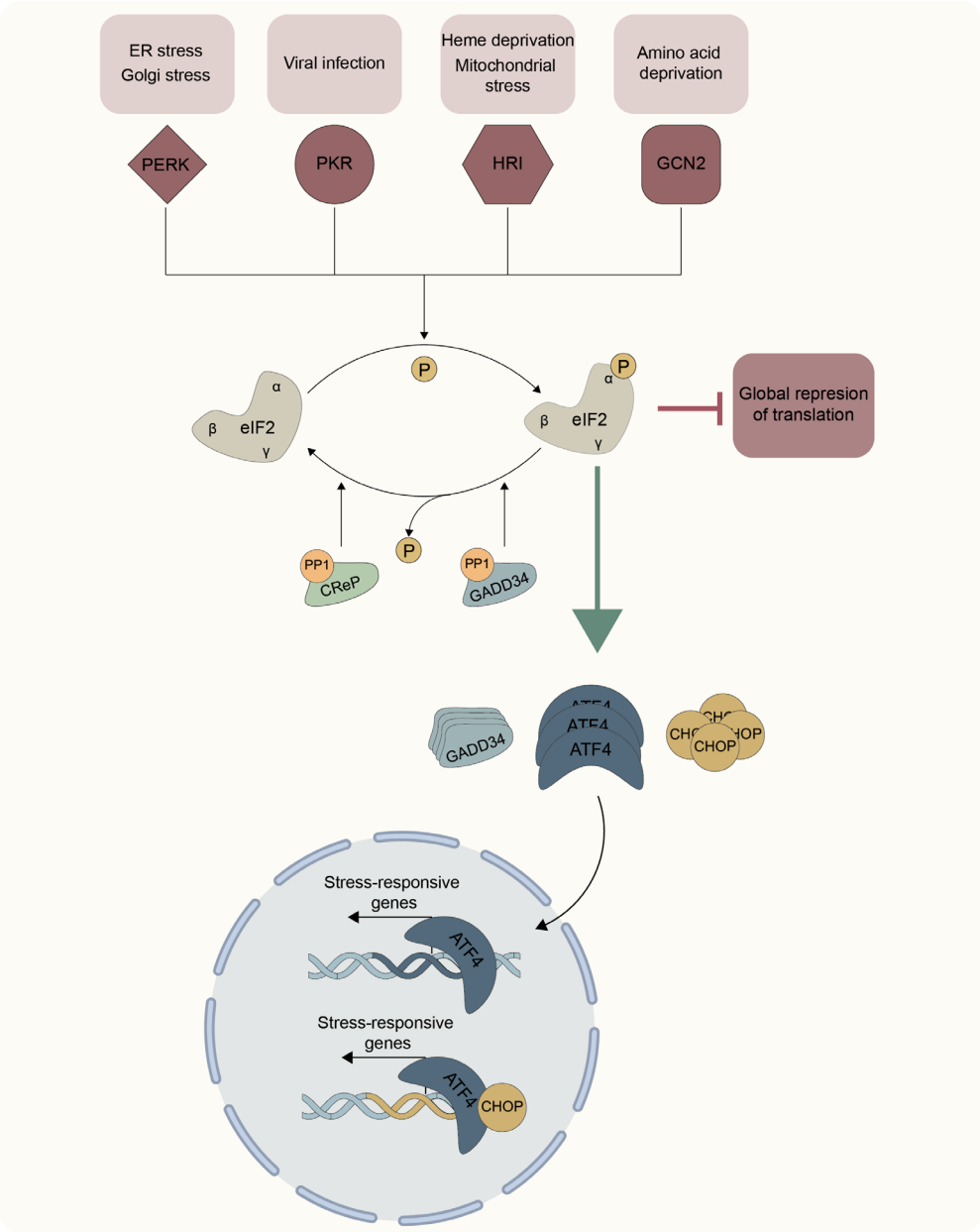


Figure 1.25 Activation of integrated stress response (ISR).

Different stress stimuli activate one of the four stress sensing kinases: PERK, PKR, HRI and GCN2. Downstream phosphorylation of α subunit of eIF2 results in global attenuation of canonical translation along with the enhanced translation of specific ISR effector proteins: ATF4, GADD34, CHOP. ATF4 is a master regulator of stress-responsive gene expression required for the cellular survival. Its interaction with other transcription factors such as CHOP direct transcription of specific gene subsets. To avoid excessive ISR activation, phosphatases PP1-GADD34 and PP1-CreP decrease the levels of phosphorylated eIF2, therefore promoting the termination of ISR.

Dysfunction of different cell organelles induces organelle-specific stress responses with distinct effector proteins and outcomes, which are usually accompanied by additional activation of ISR as a more global cellular protective mechanism.

1.11.2. ISR and mitochondria

Cellular homeostasis is highly dependent on the proper function of cellular organelles. Mitochondria have essential role in bioenergetics, metabolism and signaling (255,256). They are source of ATP and cofactors such as iron-sulfur clusters, biotin and hem. Mitochondria are also hubs for synthesis of lipids and amino acids, citric acid and urea cycles and fatty acid degradation (257). They do not only exist as isolated organelles but interconnected networks in continuous fusion and fission processes. The dynamics and balance of those two processes are pivotal for inheritance of mitochondria, trafficking, mitochondrial quality control, communication with other organelles and stress response (258).

Mitochondrial dynamics is highly regulated process. Fusion involves joining of two adjacent mitochondria through interaction of proteins on both outer mitochondrial membrane (OMM) and inner mitochondrial membrane (IMM). In mammals, this process is regulated by GTPases mitofusin 1 (MFN1) and mitofusin 2 (MFN2) on OMM and OPA1 on IMM (259,260). *C. elegans* has only one orthologue of MFNs named FZO-1 while EAT-3 is orthologue of OPA-1 (261–263). Fission process in mammalian cells requires interaction with ER and OMM-bound proteins FIS1, MFF, MiD49 and MiD51 which recruit DRP1, main factor involved in ER-mediated constriction of mitochondria (264). *C. elegans* orthologs of DRP1 and FIS1 proteins are DRP-1 and FIS-1 and FIS-2, respectively (265).

Deterioration of both mitochondrial function and dynamics is one of the main hallmarks of aging and age-related diseases.

Better understanding of mitochondrial role in the stress and aging can be studied through directed perturbation of mitochondrial homeostasis using toxins targeting components of electron transport chain (ETC), mitochondrial translation, protein import, mitochondrial membrane potential or mitochondrial DNA (243,258,266–268). Specific inhibitors for different ETC components enable understanding of the contribution of each complex to cellular function and different pathological conditions. Commonly used inhibitors of ETC are rotenone, paraquat and metformin for Complex I, 3-nitropropionic acid (3-NP) and malonate for complex II, antimycin A as an inhibitor of complex III, cyanide for complex IV and oligomycin for ATP synthase.

The rescue signaling pathways vary among different groups of organisms. Invertebrates such as *C. elegans* and *D. melanogaster* activate mitochondrial unfolded protein response (UPR^{mt}) which induces transcription of genes coding for chaperones, metabolomic enzymes and proteases (269–272). However, canonical UPR^{mt} is not a main defense mechanism in mammals, but it falls under much more complex ISR (243,267).

Various mitochondrial toxins converge into eIF2α-dependent translational attenuation and ATF4 upregulation, with HRI being a main kinase mediating ISR activation upon mitochondrial stress (243,267). HRI activation is dependent on its physical interaction with DELE1 protein in the cytoplasm. Under basal conditions, long form of DELE1 ($DELE1_L$) localizes dominantly in the mitochondrial inner membrane. Upon stress stimuli, OMA1, a known stress-sensing protease, cleaves $DELE1_L$ to produce its short form ($DELE_S$) which is transported from the mitochondria and accumulates in the cytoplasm where it activates HRI (Figure 1.26) (243). OMA1 is also responsible for OPA-

1 proteolytic cleavage, another marker of mitochondrial stress, which promotes fission and removal of damaged mitochondria (258). While some stressors simultaneously activate both pathways, DELE1$_S$ accumulation in the cytoplasm is independent of OPA-1 cleavage (243). Although initiated in mitochondria, the response is conveyed to cytoplasm, nucleus and other organelles, therefore affecting the overall cellular metabolism. ATF4-dependent remodeling of metabolic processes includes upregulation of serine, phospholipid and lipid synthesis, cholesterol and prostaglandin, as well as components of GSH synthetic pathway (266,267). Remodeling of cytosolic translation is coupled with ATF4-independent mitochondrial response, which attenuates mitochondrial translation through reduced expression of mitochondrial ribosomal proteins and therefore also locally preserves mitochondrial proteostasis and function (267).

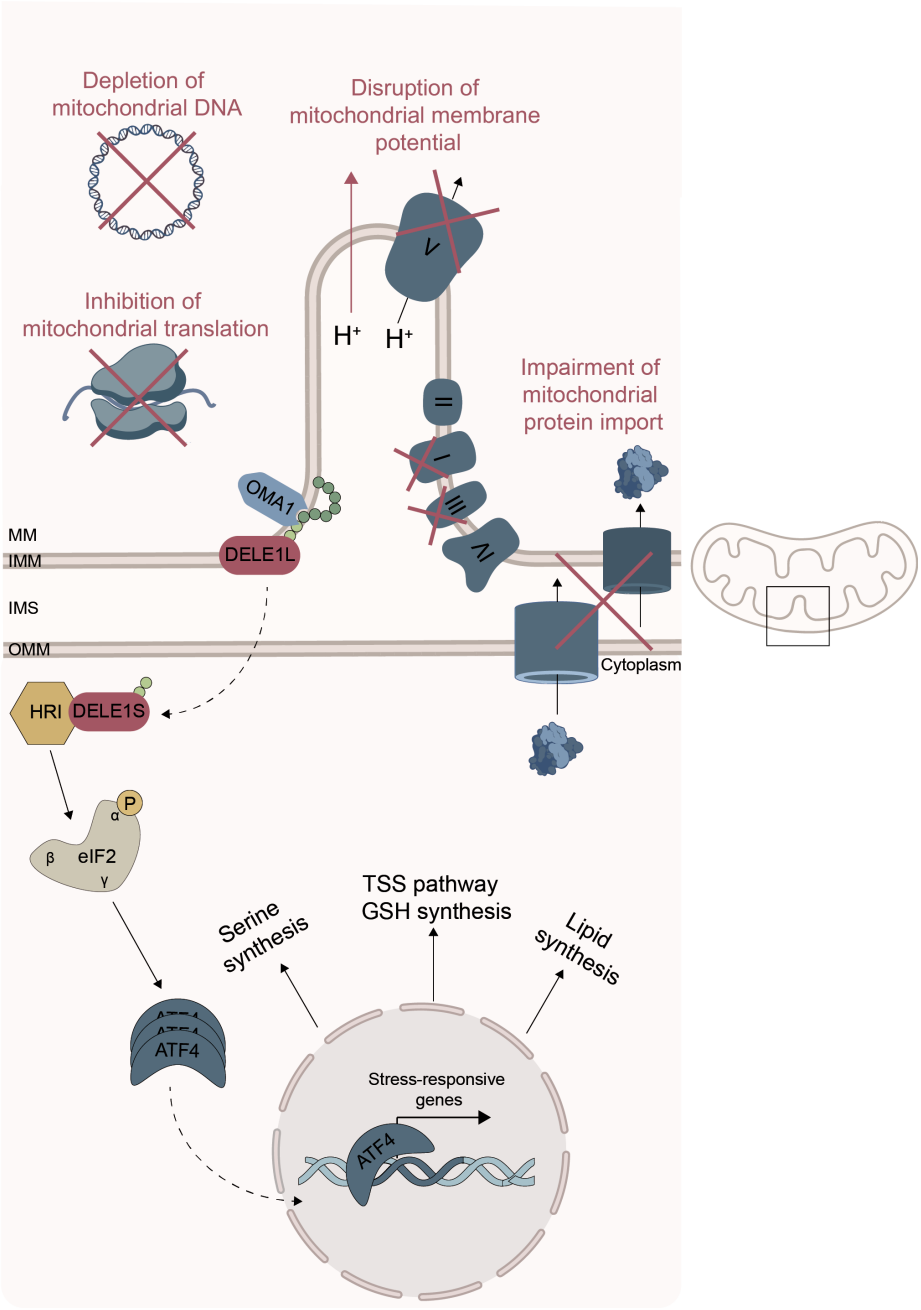


Figure 1.26 Mitochondrial ISR.

Damage of mitochondrial structure and function induces ISR which is sensed by inner-membrane protease OMA-1. OMA-1 cleaves long form of DELE1 protein (DELE1L) to form a short form (DELE1s) which accumulates in the cytoplasm and interacts with kinase HRI. Activated HRI phosphorylates eIF2α and activates ISR. ATF-4 upregulates genes whose protein products are involved in amino acid and lipid metabolism. ISR can be induced by perturbating different aspects of mitochondrial morphology and function. MM, mitochondrial matrix; IMM, inner mitochondrial membrane; IMS, intermembrane space; OMM, outer mitochondrial membrane.

1.11.3. ISR activation in ER and Golgi

ER and Golgi together with lysosomes are distinct compartments of highly dynamic endomembrane system crucial for intracellular and extracellular transport of molecules. ER and Golgi are organelles pivotal for protein folding and maturation, processing, transport and secretion out of the cell (273,274). Although not in physical contact, their function is fully dependent on the vesicular transport of molecules between them. Given their central role in protein metabolism, ER and Golgi are important cellular sensors of stress stimuli affecting proteostasis (273,275). ER stress has been extensively studied and well characterized in different model system, and it is tightly connected with unfolded protein response (275,276). UPR is mediated through distinct protein effectors including ATF6 and IRE1 involved in increased synthesis of chaperones and ER-associated degradation components (277). Both ER and Golgi induced ISR are mediated through PERK activation and ATF4-dependent translational control. Communication between those two organelles is also crucial for complete response under stress. ATF4 regulates expression and transport of ATF6 from the ER to the Golgi where the protein is activated (247).

1.11.4. Role of CSE in ISR

Given its central role in the production of metabolites involved in regulation of cellular redox status, CSE is a highly inducible enzyme in response to stress conditions. Activation of ISR upon amino acid starvation, ER and Golgi stress, as well as mitochondrial stress, leads to the ATF4-dependent upregulation of *CSE* gene which results in increased CSE protein levels and consequent increase of GSH and H_2S cellular

pools (Figure 1.27) (101,233,278,279). Levels of cystine/glutamate transporter Slc7a11 are also enhanced in certain cell types and stress conditions (85). Increased uptake of cystine and its reduction to cysteine within the cell present an additional source of CSE's substrate. Since production of cysteine and H_2S by CSE are competitive reactions, the main question is which reaction is favored in different phases of the response. Induction of ER stress by thapsigargin leads to production of both GSH and H_2S but with different time scales (60). Initial boost of GSH is followed by the switch from the canonical reaction in transsulfuration pathway towards H_2S producing reaction from cysteine (60). This change could be at least partially explained through the inhibition of CBS by CO produced under ER stress. The resulting lower cystathionine levels favor H_2S production by CSE (60).

Increased H_2S production in ER stress was shown to modulate persulfidation levels of protein targets involved in energy metabolism resulting in decreased oxidative phosphorylation and stimulation of glycolysis as a main energy source in β pancreatic cells (85). Another target whose persulfidation levels are changing in ER stress is protein tyrosine phosphatase 1B (PTP1B). Persulfidation of Cys215 residue leads to its inhibition, and subsequent increase in phosphorylation and activation of its downstream target PERK (101). Later studies demonstrated that exogenous supplementation of H_2S could modulate eIF2α-P levels through persulfidation and consequent inhibition of PP1c (280). Although the relevance of this mechanism in the regulation of ISR is still unknown, it postulates an additional route through which H_2S and persulfidation can affect cellular survival and response to different stimuli (280).

Exposure of cells to monensin, a known inducer of Golgi stress, boosts CSE expression and intracellular H_2S and persulfidation levels (49,233,281,282). Monensin is

an ionophore that binds and transports sodium ions and protons across membranes, resulting in protein leakage from acidic cellular organelles (283). Exposure of HD cellular model to non-toxic doses of monensin restores CSE levels and promotes survival upon cysteine deprivation. HD cells have disrupted transsulfuration pathway and negligible CSE levels which can be enhanced by induction of ISR (233).

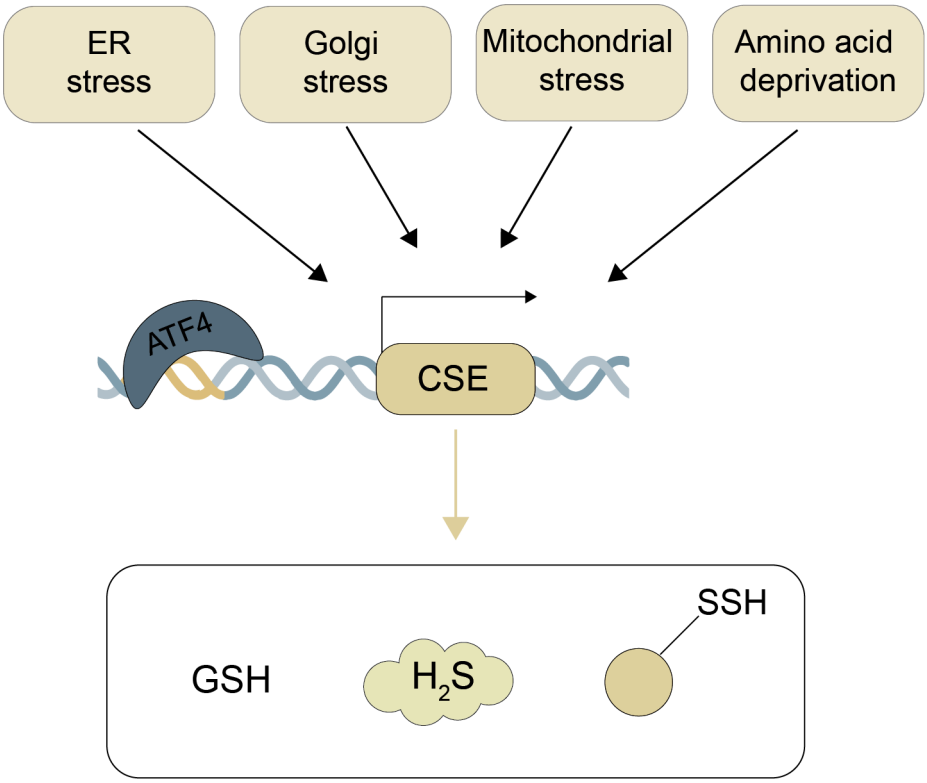


Figure 1.27 Role of CSE in cellular stress response.

CSE is a highly inducible enzyme whose expression is upregulated upon exposure to different stress types and in ATF4 dependent way. Increased CSE levels result in boost of GSH and H_2S production followed by an increase in cellular persulfidation.

Therefore, CSE and its catalytic products could play an important role in the regulation of cellular stress response, converging the signals from different inputs. The current literature is predominantly focused on the importance of GSH and its antioxidant

activity as the final outcome of that CSE-controlled effect. However, contribution of H_2S-controlled persulfidation could be even more essential for understanding whether and how different organelles employ distinct strategies to cope with the stress.

2. Project aims

The relevance of H_2S and protein persulfidation in regulating key biological processes across species requires a deeper understanding of the underlying mechanisms. It is evident that endogenous production of H_2S and consequent persulfidation of proteins are highly regulated processes, which play critical roles in signaling, cellular stress response, longevity and aging. As the complexity of organisms used in research increases, deciphering their contribution to various cellular and organismal functions becomes more challenging. Therefore, a simple yet highly relevant model organisms such as *C. elegans* offer a valuable starting point for such studies.

Moreover, the observed decline in the expression of H_2S-producing enzymes along with associated decrease in H_2S and PSSH levels suggests that manipulating these factors could promote healthier aging. In recent years, more attention has been drawn towards naturally occurring compounds as alternatives to synthetic therapeutics. Sulfur-containing compounds derived from natural dietary sources could therefore present a cost-efficient and potentially healthier therapeutic strategy.

The different goals of this thesis were:

1. Uncovering the potential H_2S releasing properties and mechanism of action of the sulfur-containing compound ergothioneine, which is found in natural dietary sources.
2. Mapping *C. elegans* persulfidome and investigating its role and dynamics in the aging process.
3. Studying the role of H_2S and protein persulfidation in cellular stress response.

3. Ergothioneine improves healthspan of aged animals by enhancing cGPDH activity through CSE-dependent persulfidation.

Dunja Petrovic,[1] Luke Slade,[1] Yiorgos Paikopoulos,[1] Davide D'Andrea,[1] Nevena Savic,[2] Ana Stancic,[2] Jan Lj Miljkovic,[3] Thibaut Vignane,[1] Maria Kyriaki Drekolia,[4] Dusan Mladenovic,[5] Nikola Sutulovic,[6] Alice Refeyton,[7] Milica Kolakovic,[8] Vladimir M. Jovanovic,[9] Jasmina Zivanovic,[2] Marko Miler,[2] Valentina Vellecco,[10] Vincenzo Brancaleone,[11] Mariarosaria Bucci,[10] Alva M. Casey,[3] ChakShun Yu,[3] Siva Swapna Kasarla,[1] Karl William Smith,[1] Ayten Kalfe,[1] Martin Stenzel,[1] Antonio Miranda-Vizuete,[12] Roland Hergenröder,[1] Prasad Phapale,[1] Olivera Stanojlovic,[6] Ivana Ivanovic-Burmazovic,[8] Marija Vlaski-Lafarge,[7] Sofia-Iris Bibli,[4] Michael P. Murphy,[3,13] Vesna Otasevic,[2] Milos R. Filipovic1*

[1]Leibniz Institute for Analytical Sciences, ISAS e.V., Dortmund, Germany

[2]Institute for Biological Research "Sinisa Stankovic" – National Institute of the Republic of Serbia, University of Belgrade, Belgrade Serbia

[3]MRC Mitochondrial Biology Unit, University of Cambridge, Keith Peters Building, CB2 0XY, UK

[4]Department of Vascular Dysfunction, European Center for Angioscience, Medical Faculty Mannheim, Heidelberg University, Mannheim, Germany

[5]Institute for Pathophysiology "Ljubodrag Buba Mihailovic", Faculty of Medicine, University of Belgrade, Belgrade Serbia

[6]Laboratory for Neurophysiology, Institute for Medical Physiology "Richard Burian", Faculty of Medicine, University of Belgrade, Belgrade, Serbia

[7]Inserm U1211 Maladies Rares : Génétique et Métabolisme, Université de Bordeaux, Bordeaux, France

[8]Department of Chemistry, Ludwig-Maximilians-University of Munich, Munich, Germany

[9]Bioinformatics Solution Center, Institute for Informatics, Freie Universität Berlin, Berlin, Germany

[10]Department of Pharmacy, School of Medicine and Surgery, University of Naples Federico II, Naples, Italy

[11]Department of Science, University of Basilicata, Potenza, Italy

[12]Redox Homeostasis Group, Instituto de Biomedicina de Sevilla (IBIS), Hospital Universitario Virgen del Rocío/CSIC/Universidad de Sevilla, Seville, Spain

[13]Department of Medicine, University of Cambridge, Cambridge, CB2 0QQ, United Kingdom

*milos.filipovic@isas.de

under review in Cell metabolism

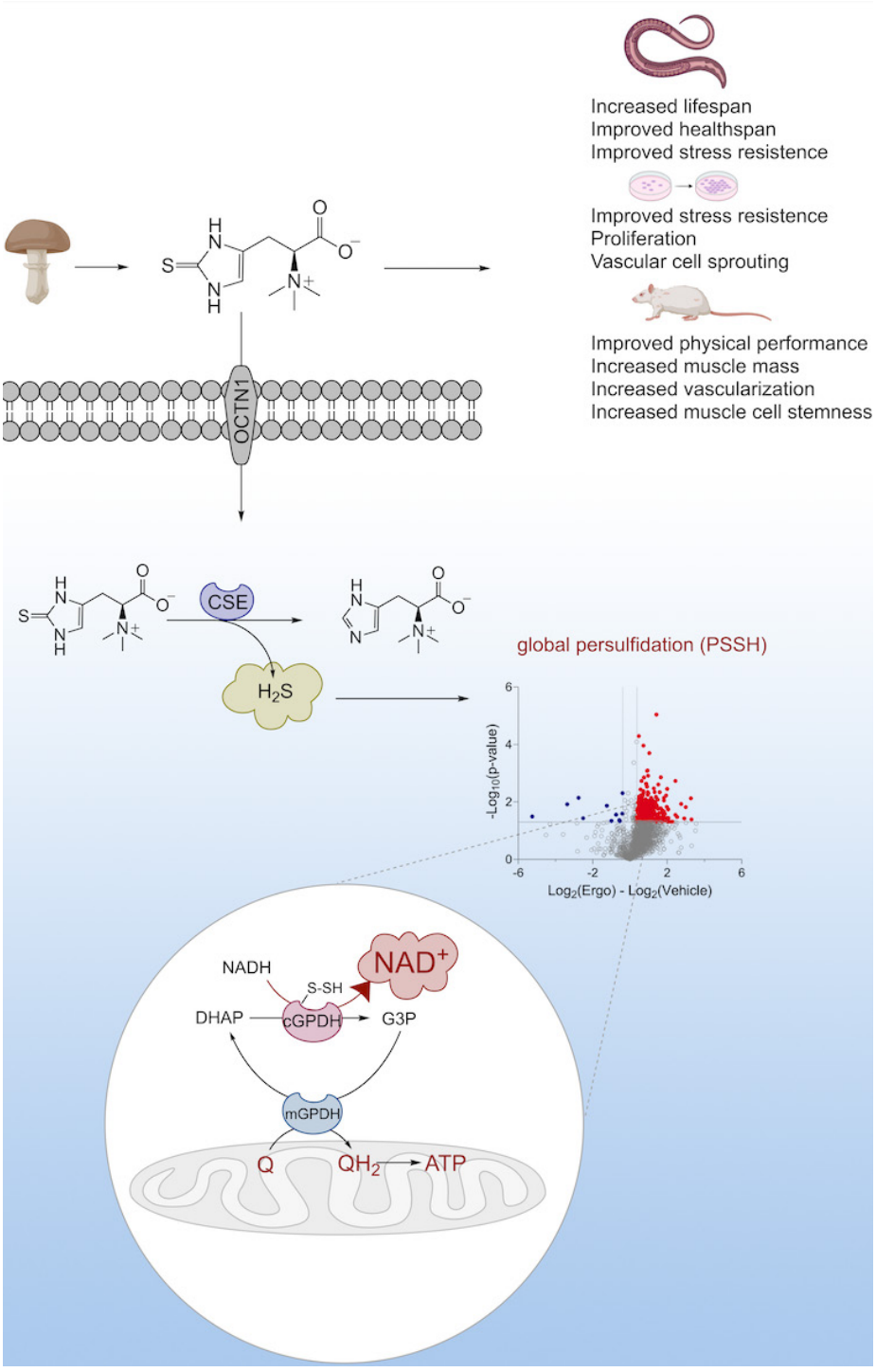
Author contributions:

Milos R Filipovic conceived the study. **DP**, LS, YP **performed all *C. elegans* experiment**. **DP** and DD **performed all MEF cell experiments**. **DP performed all proteomics, purified protein and enzymology experiments.** TV performed thermal proteome profiling, JLjM, AMC and CSY performed the analysis of intracellular H_2S production, CoQ levels, and LC-MS detection of hercynine. VMJ performed bioinformatic analysis of RNA-Seq data and MKD HUVEC experiments. NS, AS, DM, NS and VO performed experiments on rats. Seahorse analysis of mitochondrial function was performed by AR and MVL, MALDI imaging and amino acid quantification by LC_MS was done by KWS and PP, while ET detection by NMR was performed by AK and RH. MK did NMR detection of the PLP reaction. JZ and MM performed TEM. MS, AMV, OS, IIB, MVL, SIB, MPM and VO also provided tools and intellectual input, and helped with data analysis. **DP analysed the data and prepared the figures**. **MRF and DP wrote the manuscript with the help from all co-authors.**

3.1. Abstract

Ergothioneine (ET), a dietary thione/thiol, has been receiving growing attention for its possible benefits in healthy aging and metabolic resilience. Our study investigates ET's effects on healthspan in aged animals, revealing extension of lifespan and enhanced mobility in Caenorhabditis elegans, accompanied by improved stress resistance and reduced age-associated biomarkers. In aged rats, ET administration enhances exercise endurance, muscle mass, and vascularization, concomitant with increased NAD+ levels in muscle tissue. Mechanistically, ET acts as an alternative substrate for cystathionine gamma lyase (CSE), stimulating H2S production which increases protein persulfidation of more than 300 protein targets. Among these, protein persulfidation-driven activation of cytosolic glycerol-3-phosphate dehydrogenase (cGPDH) primarily contributes to ET-induced NAD+ increase. ET’s effects are abolished in cells and animals lacking CSE or cGPDH, highlighting essential role of H2S signaling and protein persulfidation. These findings elucidate ET's multifaceted actions and provide insights into its therapeutic potential for combating age-related muscle decline and metabolic perturbations.

Keywords: ergothioneine, hydrogen sulfide, healthspan, persulfidation, NAD



Highlights:

- Ergothioneine enhances lifespan and healthspan in aged *C. elegans* and rats
- These effects are dependent on CSE-catalyzed H_2S production and persulfidation
- Ergothioneine boosts NAD^+ levels
- Ergothioneine-induced persulfidation of cGPDH enhances its NAD^+ formation

3.2. Introduction

The aging process is inevitably accompanied by a decline in healthspan and physiological function, posing considerable challenges to healthcare systems worldwide. Seeking solutions to mitigate age-related deterioration and enhance overall well-being has become a pressing endeavour in recent years. One intriguing avenue of exploration involves the investigation of natural compounds with potential therapeutic properties (1–4). Among these, ergothioneine (ET) (Figure 3.1A), a naturally occurring thiol compound found in dietary sources such as fungi and Actinomycetes (5), has emerged as a promising candidate for promoting healthy aging and improving metabolic resilience (6–9).

ET accumulates in cells in high amounts via the OCTN1 (Slc22a4) transporter (10), which is present not only in mammals but also in *C. elegans* (analogue of the gene is *oct-1*) (11). Although it was initially suggested that ET exerts beneficial effects through antioxidant action (6,12), its reduction potential (Em ~ -60 mV) is less reducing than many other antioxidants, and therefore ET is unreactive towards most oxidants produced in cells, such as hydrogen peroxide (6,13). Recent studies suggested that administration of ET promotes longevity and healthy aging in male mice (14). Blood ET levels inversely correlate with aging and several aging-related diseases, such as Parkinson's and Alzheimer's diseases, irrespective of dietary source (9,15). Furthermore, administration of ET has shown protective effects against β-amyloid-induced neuronal injury and cytotoxicity, and demonstrates improvements in ischemia-reperfusion injury (8).

In this study, our objective was to explore the potential impact of ET supplementation on the healthspan of aged animals and to elucidate the underlying mechanisms driving such effects. Our findings reveal that ET serves as an alternative

substrate for cystathionine gamma lyase (CSE), a pro-longevity gene (16), leading to enhanced H_2S production and subsequent protein persulfidation. ET treatment resulted in increased mitochondrial respiration, ATP production, and cell growth, accompanied by elevated NAD^+ levels, both in vitro and in vivo. These changes occurred through persulfidation and activation of cytosolic glycerol 3-phosphate dehydrogenase (cGPDH), which increased NAD^+ levels to improve muscle mass, vascularization, muscle cell stemness, and treadmill endurance in aged rats. By unravelling the molecular intricacies of ET's actions, our research provides a foundation for further investigation into its clinical applications and therapeutic implications.

3.3. Results

3.3.5. Ergothioneine improves healthspan and lifespan of *C.elegans*

We started with testing the effect of ET on lifespan of *C. elegans*. Treatment with 5 mM ET from day 1 adulthood (D1) resulted in significant median lifespan extension (20 ± 2 %, Supplementary Figure S3.1A). Even when reducing the concentration to 450 μM we could still observe small but significant extensions in both median and maximal lifespans (Figure 3.1B, Supplementary Table S3.1). More importantly, we noticed that mobility (thus, healthspan) of ET-treated worms was markedly improved. *C. elegans* display age-related decline in thrashing performance (17) and 450 μM ET maintained those rates quite high even in day-10 adults (D10) (Figure 3.1C). We, therefore, focused on ET's effects on healthspan parameters during aging.

ET treatment increased resistance of D10 adults to H_2O_2, paraquat, arsenite and heat stress (Figure 3.1D, Supplementary Figure S3.1 B-D), suggesting global healthspan

benefits even in old animals. Age-related increase in intestinal autofluorescence (sometimes referred to as lipofuscin or “age pigment”) measured via blue, green and red-wavelength autofluorescence (18) was significantly lower in ET-treated animals (Figure 3.1E). Lipid accumulation, assessed by both Oil Red and Nile Red fluorescence was also significantly lower in ET-treated D10 adults (Supplementary Figure S3.1E-F). Interestingly ET-treatment did not affect the levels of 4-hydroxynonenal-modified proteins (Supplementary Figure S3.1G) suggesting that ET has no effect on age-related lipid peroxidation.

It is important to note that the observed effects are not caused by OP50 bacteria used to feed *C. elegans*. Namely, ET effects on median and maximal lifespan (Supplementary Figure S3.1H, Supplementary Table S3.1) and on healthspan (Supplementary Figure S3.1I,J) were still retained when animals were grown on UV-killed bacteria.

Structural deterioration of mitochondria represents a key aging hallmark in *C. elegans* (19). We compared the mitochondrial network in SJ4103 [Pmyo-3::mitoGFP] animals expressing GFP in body wall mitochondria to observe that ET treatment results in fewer fragments and more elongated mitochondria when compared to untreated aged animals (Figure 3.1F), which would explain the strong effect that ET has on motility.

To understand lifespan/healthspan-preserving mechanisms of ET, we performed global proteome and transcriptome analyses of D4 and D10 adult worms. Aging is known to induce strong proteome and transcriptome remodelling in *C. elegans* (20,21), so it came as a surprise that very small number of targets was found to be significantly changing (± 1.5-fold change for proteomics and ± 2-fold change for transcriptomic analysis) in response to ET treatment, with no overlap between transcriptomic-proteomic datasets

(Figure 3.1G,H, Supplementary Figure S3.2A-C, Supplementary Tables S3.2-3.5). Although no particular GO term pathway enrichment could be observed, transcriptionally upregulated genes encompassed a family of proteins containing ALS2cr12 signatures (*pals-1*, *pals-3*, *pals-16,* etc) known to be affected in *daf-16* mutants, as well as by the treatments of different organosulfuric compounds. Therefore, we tested the possibility that *daf-16* might be responsible for the beneficial effects of ET. The *daf-16* mutants exhibited the same lifespan extension observed in N2 animals (Supplementary Figure S3.2D, Supplementary Table S3.1), suggesting that *daf-16* expression is dispensable for ET's beneficial effects. Together, these data strongly suggest that the ET's effects are not caused by the transcriptional and translational regulation but most probably by the posttranslational modifications of the proteins.

ET is an organosulfur compound, a derivative of thiourea (Figure 3.1A), and thiourea derivates are known to decompose to hydrogen sulfide (H_2S) or elemental sulfur (22,23). As H_2S is an emerging regulator of cellular function that acts through a posttranslational modification of proteins called protein persulfidation (PSSH) (24,25), we tested the hypothesis that the beneficial effects of ET might come from changes in PSSH. PSSH levels are reported to decrease in aging animals and their restoration via sulfide donors improves the resistance of the animals to oxidative stress (26). We applied the dimedone-switch method for persulfidomic analysis and compared PSSH levels in untreated and ET-treated D10 worms. Unlike in the case of global proteome and transcriptome, we found that PSSH levels of > 300 out of 2737 endogenously persulfidated proteins significantly increased in ET-treated worms (Figure 3.1I, Supplementary Table S3.6). The one-sided volcano plot indicates a strong unidirectional effect towards the increase in protein persulfidation. Normalization to the protein

expression levels found in total proteome did not have major effects on the observed changes (Supplementary Figure S3.2E). Identified protein targets are particularly enriched within cytoplasmic vesicle lumen and mitochondrial ATP-synthase complex and have antioxidant activity, copper, NAD and FAD binding activity, among others (Supplementary Figure S3.2G,H). These proteins play a role in mitochondrial electron transport process, cellular redox homeostasis and embryogenesis but also in translation and metabolic processes such as fatty acid and glycerol-3-phosphate metabolism (Figure 3.1J).

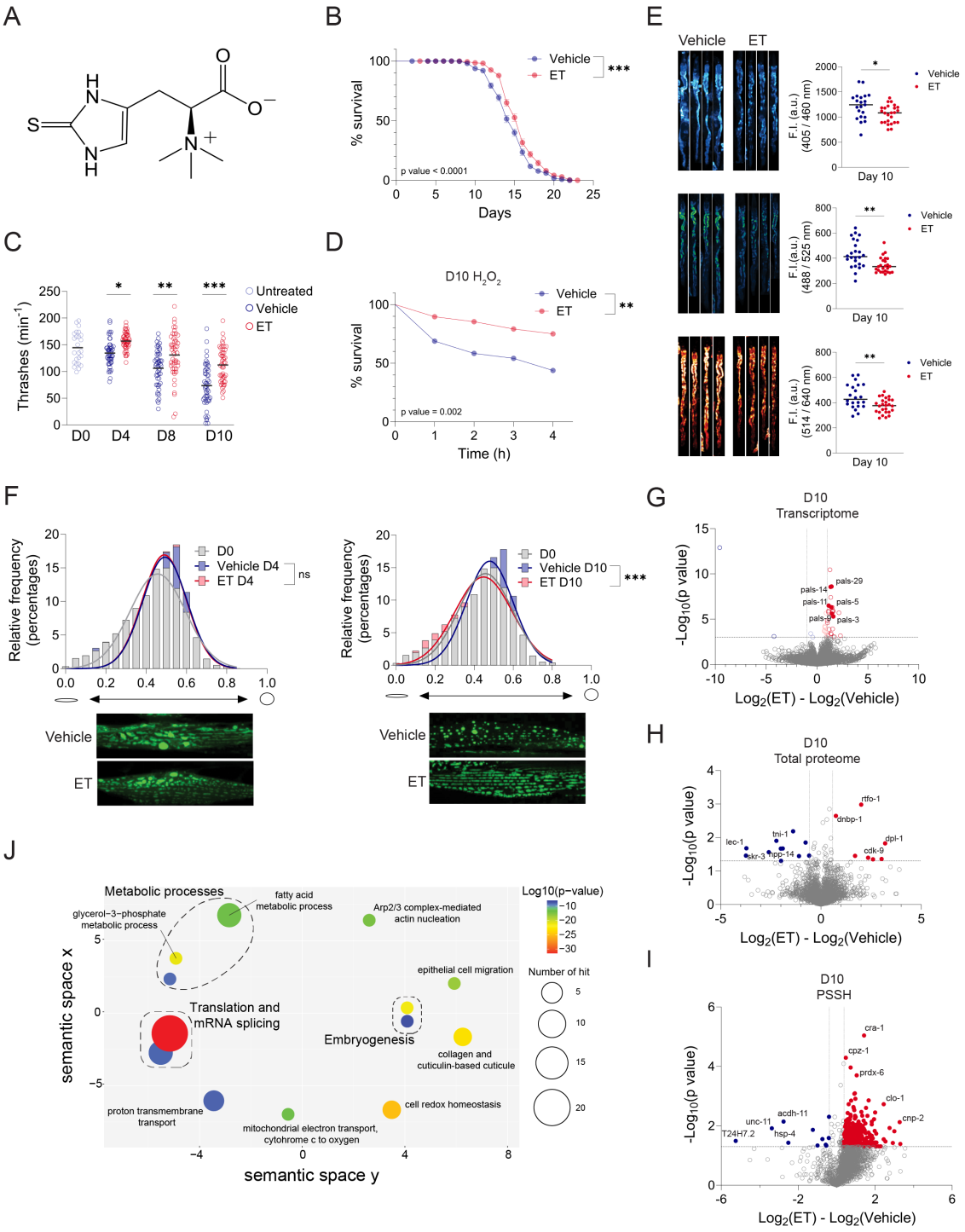
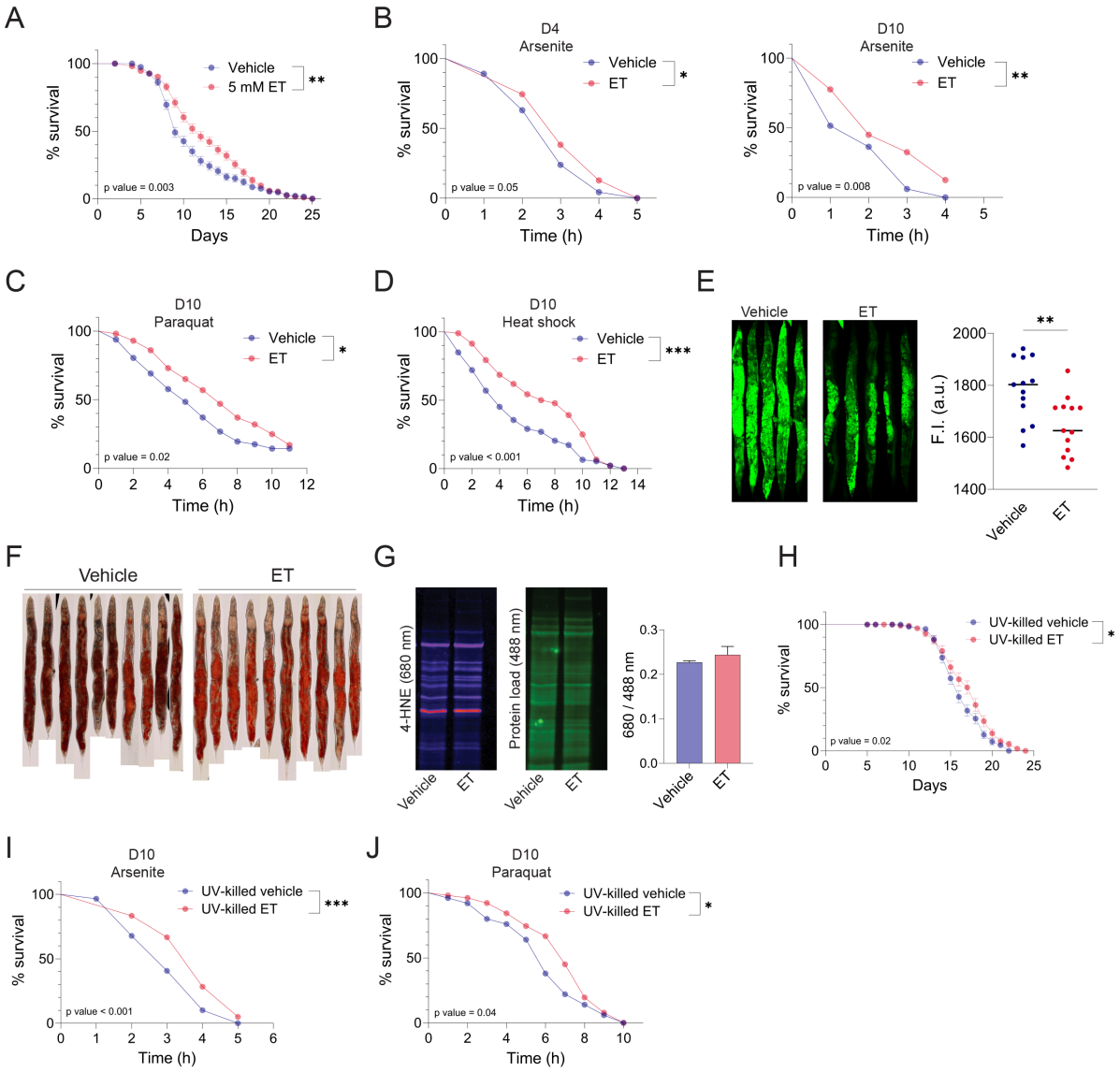


Figure 3.1. Ergothioneine (ET) improves lifespan and healthspan of *C. elegans*.

(**A**) Chemical structure of ET. (**B**) Lifespan of ET (450 μM)-treated wild type (N2) worms (6.8 ± 0.3 % for median and 22 vs 23 days for the maximal lifespan; n ≥ 460 animals per group, Kaplan-Meier survival analysis, Mantel-Cox long rank test). (**C**) Movement capacity (the number of thrashing movements made by each worm in 60 s) of aged worms treated with 450 μM ET (n = 50

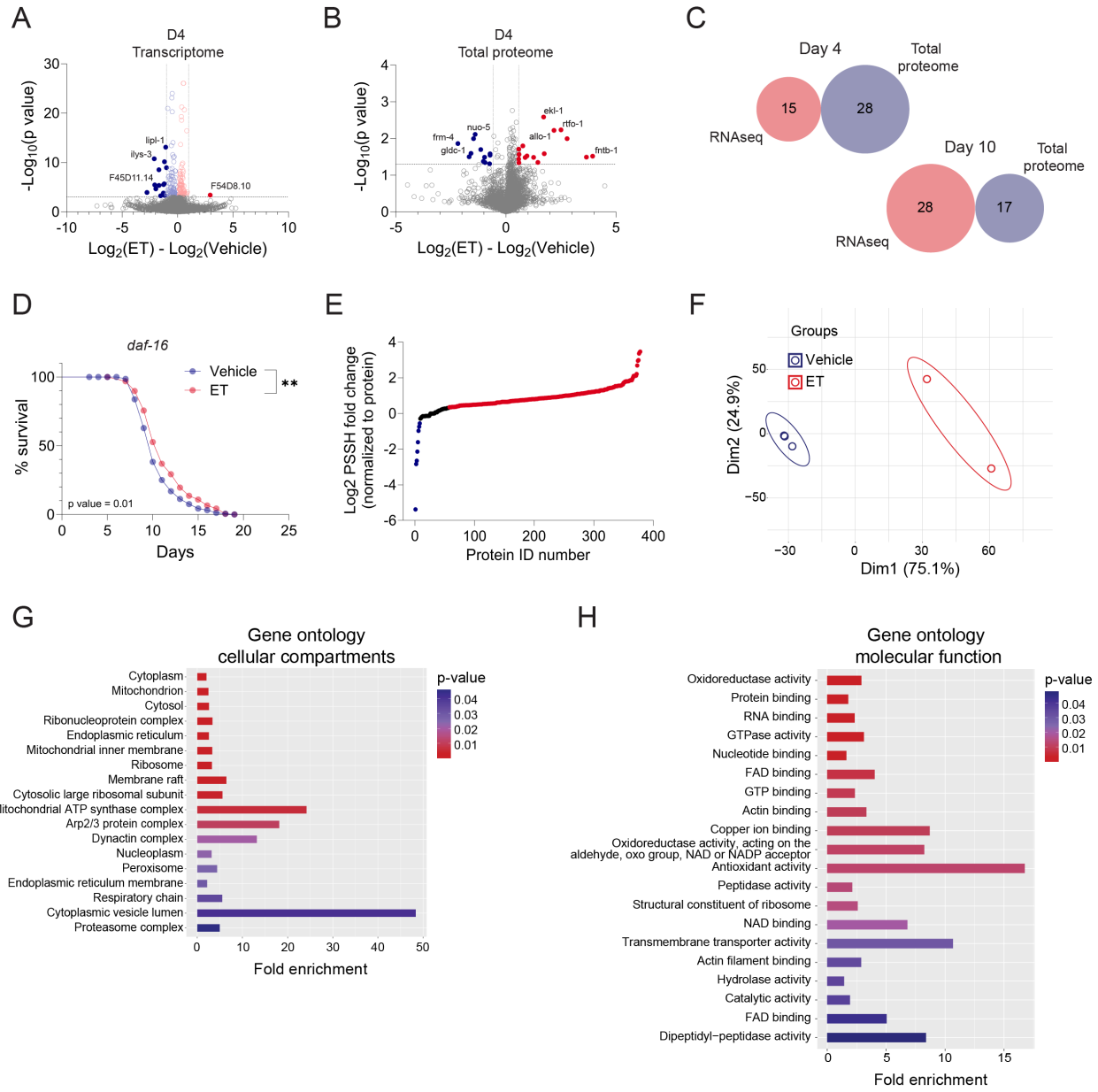
per experimental group, two-way ANOVA, * $p < 0.05$, ** $p < 0.01$, *** $p < 0.001$).(**D**) Survival curves of ET (450 μM)-treated D10 worms exposed to 100 μM H_2O_2 (n = 48 per experimental group; Mantel-Cox long rank test, **$p < 0.01$).(**E**) Blue, green and red autofluorescence of D10 worms treated with 450 μM ET (n > 20, unpaired Student's t-test, * $p < 0.05$, ** $p < 0.01$).(**F**) Mitochondrial morphology of worms treated with 450 μM ET. Confocal images and quantification of mitochondrial roundness in green fluorescent protein (GFP)-labelled mitochondria in young adults (D0) and aged (D4 and D10) Pmyo-3::mitoGFP worms (n > 20 worms, one or more muscle cells per worm, one-way ANOVA, *** $p < 0.001$).(**G**) Volcano plot of RNA-seq data showing differentially regulated genes (upregulated genes in red, down-regulated genes in blue) in D10 animals treated with 450 μM ET. (**H**) Volcano plot analysis of total proteome changes (upregulated proteins in red, down-regulated proteins in blue) in D10 animals treated with 450 μM ET. (**I**) Volcano plot analysis of persulfidome changes in D10 animals treated with 450 μM ET. (**J**) GO term enrichment (biological process) of the 368 proteins exhibiting significantly higher persulfidation levels in ET treatment. Enrichment was performed using DAVID and the results visualized through REVIGO (p-value $\leq$ 0.01).



Supplementary Figure S3.1 (related to Figure 3.1). Ergothioneine (ET) improves the healthspan of *C. elegans*.

(**A**) Lifespan of ET (5 mM)-treated wild type (N2) worms (20 ± 2 % increase of median lifespan; n ≥ 194 animals per group; Kaplan-Meier survival analysis; Mantel-Cox long rank test). (**B**) Survival curves of ET (450 μM)-treated D4 and D10 worms exposed to 5 mM and 2 mM sodium arsenite, respectively (n = 46 per experimental group for D4 and 33-40 for D10; Mantel-Cox long rank test, *p < 0.05, **p < 0.01). (**C-D**) Survival curves of ET (450 μM)-treated D10 worms exposed to (B) 62.5 mM paraquat or (C) heat shock (35 °C) (n > 92 per experimental group for heat shock and > 97 for paraquat; Mantel-Cox long rank test, *p < 0.05, ***p < 0.001). (**E**) Nile Red staining of lipid accumulation in D10 worms treated with ET (450 μM) and quantification of fluorescence intensity. n = 13 animals per group, unpaired Student's t-test, **p < 0.01. (**F**) Oil raid staining of lipid

accumulation of D10 treated with ET (450 μM). Ten representative animals per group are shown. (**G**) Detection of 4-hydroxynonenal-modified proteins in lysates of D10 worms treated with 450 μM ET. Anti-HNE-antibody was used to visualize the modification. Proteins were labelled with NBF-Cl for total load. Experiments were performed in duplicates. (**H**) Lifespan of ET (450 μM)-treated wild type (N2) worms on UV-light killed OP50 bacteria (9 ± 4 % increase of median lifespan; 2 days increase in maximal lifespan, $n \geq 130$ animals per group, Kaplan-Meier survival analysis, Mantel-Cox long rank test). (**I**) Survival curves of ET (450 μM)-treated D10 worms fed with UV-light killed OP50 bacteria and exposed to 2 mM sodium arsenite. (n = 59 per experimental group, Mantel-Cox long rank test, ***$p < 0.001$). (**J**) Survival curves of ET (450 μM)-treated D10 worms fed with UV-light killed OP50 bacteria and exposed to 62.5 mM paraquat (n = 50 per experimental group; Mantel-Cox long rank test, *$p < 0.05$).



Supplementary Figure S3.2 (related to Figure 3.1). ET improves the healthspan of *C. elegans* by increasing protein persulfidation.

(**A**) Volcano plot of RNA-seq data showing differentially regulated genes (upregulated genes in red, down-regulated genes in blue) in D4 animals treated with 450 μM ET. (**B**) Volcano plot analysis of total proteome changes (upregulated proteins in red, down-regulated proteins in blue) in D4 animals treated with 450 μM ET. (**C**) Venn-diagram of targets found to be significantly changing their RNA or protein levels in D4 or D10 ET-treated worms. (**D**) Lifespan of ET (450 μM)-treated *daf-16* mutant strain (10 % increase of median lifespan, n = 227 animals per group, Kaplan-Meier survival analysis, Mantel-Cox long rank test). (**E**) Changes in protein persulfidation in D10

ET (450 μM)-treated worms, normalized to the protein expression levels. (**F**) Principal Component Analysis showing a notable differentiation in the persulfidome in D10 ET (450 μM)-treated worms. (**G-H**) GO Term enrichment analysis of 368 proteins exhibiting significantly higher persulfidation levels in ET treatment for (G) cellular compartmentalization and (H) molecular function.

3.3.6. Ergothioneine is a substrate for CSE

How does ET affect the protein persulfidation? Although thiourea derivatives do decompose to produce H_2S (22), this effect has not been observed in ET, which is quite stable under a physiological range of pHs and temperatures (6,13). Using lysates of mouse embryonic fibroblasts (MEF) treated with ET in the presence or absence of SDS (2%) we could observe that ET-induced increase of PSSH is catalyzed by an enzyme (Supplementary Figure S3.3A).

We used thermal proteome profiling (27,28) to identify potential binding targets for ET in MEFs (Figure 3.2A). A small number of proteins responded to ET treatment with significant thermal shift (Supplementary Table S3.7). Among them cystathionine gamma-lyase (CSE) was the only target that could potentially explain the PSSH effects (Figure 3.2A).

CSE is one of the three main H_2S producing enzymes (24). Treatment of MEFs with ET resulted in an increase of intracellular H_2S levels (Figure 3.2B). As expected, CSE knockout cells showed significantly impaired H_2S production, and the addition of ET did not change H_2S levels (Figure 3.2B), confirming that ET-induced H_2S production is controlled by CSE. To understand where in CSE structure ET could bind, we performed *in silico* prediction of CSE - ET interaction using SeamDock (29). We found that ET binds in the enzyme's active site pocket with binding affinity similar to that for its most preferred substrate, cystathionine (5.8 kcal/mol for ET vs 5.5 kcal/mol for cystathionine; Figure 3.2C). Two ligands showed strong overlay (Supplementary Figure S3.3B-C), which suggested that ET could serve as an alternative substrate for the CSE.

We assessed the ability of human recombinant CSE to consume ET and generate H_2S by incubating CSE with ET alone, or in conjunction with cysteine (Figure 3.2D). H_2S

production was faster and greater when ET was present, and ET alone produced H_2S confirming that (i) ET is an alternative substrate for CSE and (ii) it does not inhibit H_2S production from cysteine. Using a competitive two-substrate equation to estimate the kinetic parameters for CSE-catalyzed H_2S formation from ET we could estimate V_{max} and K_m for the reaction (Figure 3.2E). While V_{max} did not differ between ET and cysteine, the K_m was significantly lower than what has been observed for cysteine. It is worth noting that the observed K_m for cysteine probably represents the mix of two K_m: one for the reaction in which H_2S and pyruvate are produced and the other one resulting in formation of H_2S and lanthionine (30).

Although ET does not readily react with electrophilic thiol-blocking reagents (31), we found that it can react with 4-chloro-7-nitrobenzofurazan, to give an adduct with absorption maximum at ~400 nm. We used this feature to design an assay that allowed us to monitor the fate of ET's thione/thiol group in reaction with CSE. Indeed, we observed that CSE catalyzes "desulfuration" of ET to give hercynine (Supplementary Figure S3.3D), which was also confirmed by MS (Supplementary Figure S3.3E,F).

Mechanistically this reaction has to be catalyzed by pyridoxal phosphate (PLP) (Figure 3.2F) which is a main cofactor in CSE-catalyzed reactions (24). Incubation of PLP with ET resulted in UV-Vis spectral shift from ~390 to ~330 nm (Supplementary Figure S3.33G), characteristic for a Schiff base formation observed in other PLP reactions (32). MS analysis of reaction mixture suggest that reaction proceeds via initial formation of carbinolamine adduct (m/z 477.1244; Supplementary Figure S3.33H), which forms a Schiff base through a loss of water (Figure 3.2F). When assessed by ^{1}H NMR the reaction mixture clearly showed formation of a species with $\delta \approx 8$ ppm (32) that corresponds to the aldiminic proton of a Schiff base (Supplementary Figure S3.3I-J). MS analysis of reaction

mixture after one hour indicated formation of hercynine, as a product of this reaction (Supplementary Figure S3.3K).

Formation of hercynine from the Shiff base intermediate is difficult to envision without nucleophilic attack of another thiol (either another molecule of ET or cysteine) (Figure 3.2F). In that reaction, persulfide would be formed as an intermediate species that will give rise to H_2S (24). Indeed, ET persulfide could be observed in MS spectrum of the PLP/ET reaction mixture after 1 h of incubation (Supplementary Figure S3.3L). Furthermore, formation of cysteine persulfide could also be observed when cysteine, ET and PLP were incubated, as confirmed by characteristic CysS-S-NBF adduct (26) that underwent either reduction with beta-mercaptoethanol or switching with dimedone (26) (Supplementary Figure S3.3M). Finally, addition of DTT or TCEP as a reducing agent into the reaction mixture of CSE and ET alone, increased the rate of H_2S formation (Figure 3.2D, Supplementary Figure S3.3N). The importance of CSE in metabolizing ET was also obvious in absence of protein persulfidation changes observed in ET-treated $CSE^{-/-}$ cells (Supplementary Figure S3.3O) in contrast to wild type cells (Supplementary Figure S3.3A).

We next monitored how this reaction affects levels of ET in cells, by ^1H NMR in WT and $CSE^{-/-}$ MEF cells treated with 200 μM ET. We observed that less ET could be found in WT cells, in accordance with our hypothesis that CSE plays a central role in its metabolism/consumption (Figure 3.2G). Furthermore, ET treatment did not affect the levels of homocysteine and cystathionine, but significantly higher intracellular levels of cysteine could be observed, in accordance with lower K_m for ET (Figure 3.2H).

To confirm that ET desulfuration occurs in CSE-dependent manner in *C. elegans* as well, we adapted matrix-assisted laser desorption/ionization-imaging mass

spectrometry (33). We could clearly see that product formation is a feature observed in N2 worms and not in *cth-1* mutants (Figure 3.2I, Supplementary Figure S3.3P). Taken together these data strongly suggested that beneficial effects of ET are dependent on its consumption by CSE and production of H_2S.

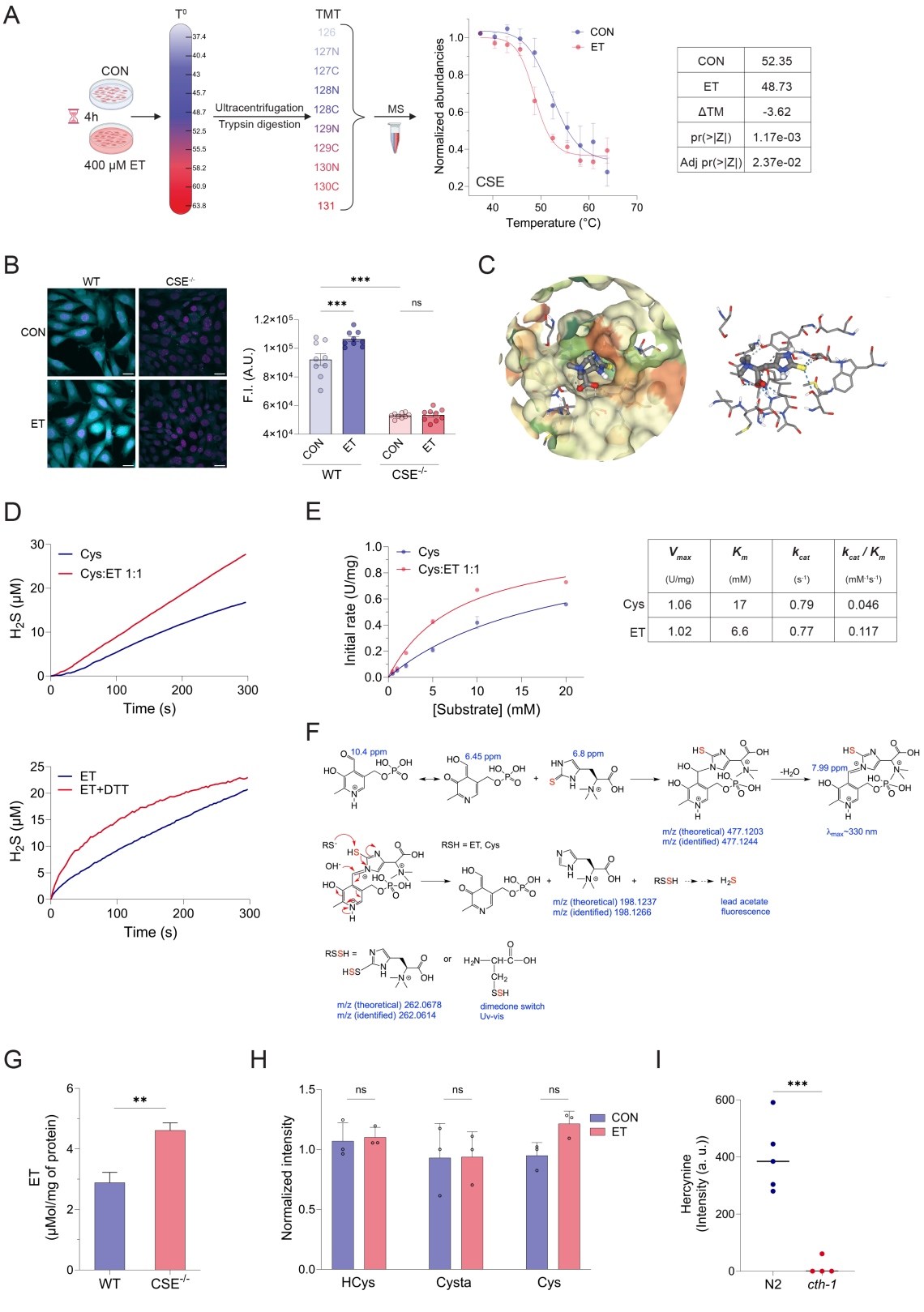
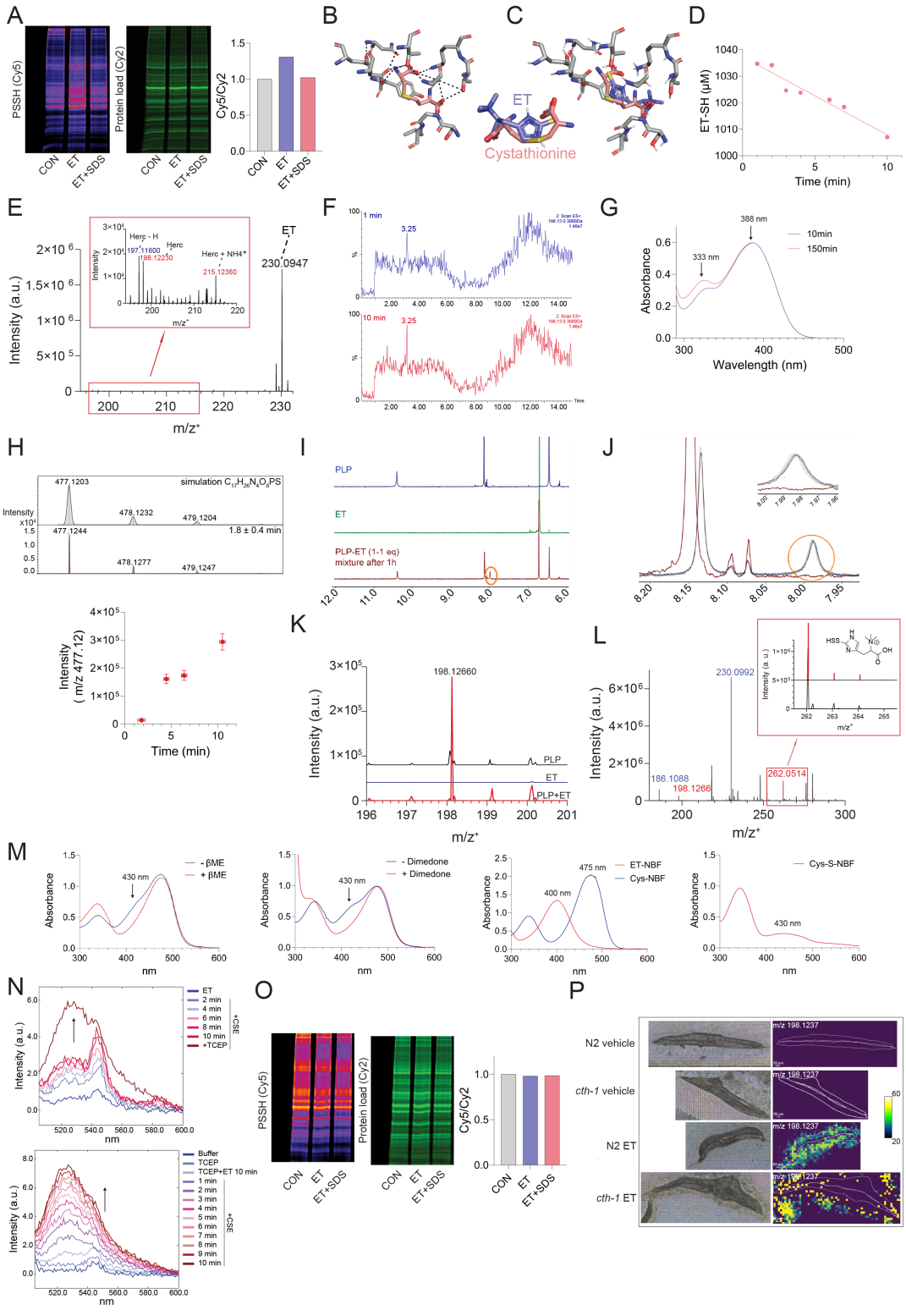


Figure 3.2. Ergothioneine is a substrate for cystathionine gamma lyase (CSE) to produce H_2S.

(**A**) Schematic representation of thermal proteome profiling of live, ET-treated MEFs (left) and observed melting curves for CSE (right). MEF cells were treated with 400 μM ET for 4 h. n = 3. (**B**) SF7-AM fluorescence probe-based detection of H_2S production in wild type (WT) and $CSE^{-/-}$ MEF cells treated with 200 μM ET for 4 h. 3-5 images were analysed per biological replicate (n = 3). Two-way ANOVA, ***p < 0.001. (**C**) Docking results from SeamDock are shown for ET and human CSE (PDB: 2NMP). Left: the zoom at the protein active site with the ball-and-stick model of ET (carbon atoms are colored gray, nitrogen atoms blue, oxygen atoms red and sulfur atoms yellow) fitting in it. Protein surface is colored based on hydrophobicity with the most hydrophilic being brown-red and the most hydrophobic green. Right: Interaction of ET with amino acid residues of the CSE active site. The hydrogen bonds are shown in dotted lines. (**D**) H_2S generation from the 10 mM cysteine or the mixture of 10 mM cysteine and 10 mM ET (upper figure) catalyzed by the human recombinant CSE (9 μg). H_2S generation from the reaction mixture containing CSE (9 μg) and 10 mM ET (with or without addition of 1 mM DTT) is shown in the lower figure. The reaction of H_2S with lead acetate to form lead sulfide was monitored by the increase in absorbance at 390 nm in 50 mM HEPES buffer pH 7.4 and at 37 °C. (**E**) Kinetic analysis of the reaction of cysteine (blue line) or cysteine:ET equimolar mixture (red line) with human recombinant CSE (9 μg). A competitive two-substrate equation was used to estimate the kinetic parameters for CSE-catalyzed H_2S formation from ET. (**F**) Proposed reaction mechanism for the pyridoxal phosphate (PLP)-catalyzed H_2S release from ET based on NMR, ESI-MS and UV-Vis measurements shown in Supporting Figure S3 ^1H NMR chemical shifts for the key protons identified are marked in red, m/z of identified products and the absorbance maximum of Shiff-base are marked in blue. (**G**) ^1H NMR detection of ET isolated from WT and $CSE^{-/-}$ MEF cells incubated with 200 μM ET for 18 h. Experiments were performed in biological triplicates and normalized to the protein content of each sample. Unpaired Student's t-test, **p < 0.01. (**H**) Intracellular levels of homocysteine (HCys), cystathionine (Cysta) and cysteine (Cys) in MEFs treated or not with ET (400 μM) for 2 h. (**I**) Quantification of hercynine formation in N2 and *cth-1 C. elegans* using MALDI imaging mass spectrometry. Related to the Supporting Figure S2L. Unpaired Student's t-test, ***p < 0.001.



Supplementary Figure S3.3 (related to Figure 3.2). H_2S release from ET is catalyzed by CSE.

(**A**) Persulfidation levels of MEF cell lysate treated with 400 μM ET in the presence or absence of 2% SDS as a denaturing agent. NBF-labelled amino groups were used as a total load and PSSH

levels expressed as a ratio of Cy5/Cy2 signal. (**B**) Interaction of cystathionine with amino acid residues of the CSE active site obtained by docking modelling in SeamDoc. The hydrogen bonds are shown in dotted lines. (**C**) Overlay of cystathionine and ET with the active site amino acids of CSE. (**D**) CSE (10 μg/ml)-catalyzed desulfuration of (1 mM) ET, monitored by the reaction with NBF-Cl. (**E**) ESI-TOF MS detection of hercynine as a product of the reaction of ET with CSE. 100 μM ET was incubated with 0.1 μM CSE in 25 mM ammonium bicarbonate buffer pH 7.4, for 30 min at room temperature. (**F**) LC-MS detection of hercynine formation. Hercynine peak (m/z 198.13) elutes at 3.25 min and its time-dependent increase could be observed only when 1.5 μg CSE was added to 100 μM ET in 50 mM phosphate buffer pH 7.4. (**G**) UV–Vis spectrum of the chemical interaction between PLP (150 μM) and ET (1.5 mM) in 50 mM HEPES buffer pH 7.4. (**H**) ESI-TOF MS time-resolved formation of the initial adduct formed by the addition of amine from the imidazole ring of ET (100 μM) to the aldehyde group of the PLP (100 μM) in 25 mM ammonium bicarobonate buffer pH 7.4. Simulated isotopic pattern is shown in black. (**I-J**) ^{1}H NMR spectra of PLP, ET, and the equimolar mixture after 1 h. (J) Zoom in to the 7.9-8.2 chemical shift range highlighting the appearance of a new peak at ~7.99 corresponding to the aldiminic proton of a Schiff base (reaction scheme in Fig. 2F). (**K**) ESI-TOF-MS detection of hercynine formation in the reaction of ET and PLP in 25 mM ammonium bicarobonate buffer pH 7.4. (**L**) ESI-TOF-MS spectrum of the reaction mixture as in K) showing broader range of m/z. Besides the main peaks of unreacted ergothioneine (blue), peaks of hercynine (m/z 198.1266) and ET persulfide (m/z 262.0514) shown in red, could also be observed. Inset: observed and simulated isotopic pattern distribution of ET persulfide. (**M**) Detection of persulfide formation in a PLP/ET/cysteine (10 μM/50 μM/50 μM) reaction mixture was achieved by trapping with NBF-Cl (100 μM). A characteristic absorbance maximum for persulfide at 430 nm was observed. The addition of 1 mM β-mercaptoethanol (left) or 0.5 mM dimedone (left center) reduced the persulfide, as indicated by the loss of absorbance at 430 nm. For comparison, spectra of the NBF-Cl adducts of cysteine and ET are shown in the right-center graph. The spectrum of the cysteine persulfide, formed by incubating CSE with cystine, and its NBF-Cl adduct is shown in the right graph. (**N**) Detection of H_2S release from 10 mM ET catalyzed by 9 μg of CSE in 50 mM phosphate buffer pH 7.4 and measured by fluorescent H_2S sensor SF7 in the absence (upper spectra) and presence of 100 μM TCEP (lower spectra). (**O**) Persulfidation levels of cell lysate from CSE$^{-/-}$ MEFs treated with 400 μM ET in the presence or absence of 2% SDS as a denaturing agent. NBF-labelled amino groups were used as a total load and PSSH levels expressed as a ratio of Cy5/Cy2 signal. (**P**) Representative images of *C. elegans* used for the MALDI imaging mass spectrometric detection of hercyinine in D4 wild type (N2) and *cth-1* mutant worms treated with 450 μM ET.

3.3.7. Ergothioneine's beneficial effects are CSE-dependent

In the light of these observations, we re-assessed the ET effects in *C. elegans*. Considering that hercynine is also transported into cells via the same transporter (albeit with lower efficiency),(34) we tested the effect of hercynine. We could observe no significant improvements of *C. elegans* lifespan or healthspan (Figure 3.3A-C). This strengthened the claims of ET being responsible for the benefits observed in Figure 3.1B-F, Supplementary Figure S3.1A-F.

Next, we analyzed the effect of ET on cystathionine gamma-lyase (*cth-1*) mutants. It became immediately apparent that neither lifespan nor motility of worms were affected by ET treatment (Figure 3.3D,E), in contrast to the wild type N2 strain (Figure 3.1B-C). Furthermore, the protective effects of ET observed in stress assays performed on wild type worms were completely abolished in *cth-1* mutant (Figure 3.3F,G). This is in accordance with our previous observations that the higher the PSSH levels the better the resistance to stressors (24). The *cth-1* mutants could not be rescued by the presence of ET alone, as beneficial effects of ET require CSE to produce H_2S and cause protein persulfidation. Although we did not identify mercaptopyruvate sulfur transferase (MPST) as a target for ET in our thermal proteome profiling of live MEF cells treated with ET (Supplementary Figure S3.4A), we did check the effect of ET on healthspan parameters of *mpst-3 C. elegans.* Like in the wild type animals, ET treatment improved stress resistance and movement in *mpst-3* mutants (Supplementary Figure S3.4B-C), akin to other H_2S donors (26), suggesting that MPST expression is dispensable for ET's beneficial effects.

Next, we tested the role of CSE on beneficial effects that ET exhibits in cells. ET's antioxidant activity is often claimed to be the main mechanisms behind its beneficial

effects in different studied models (6,12,35). While ET does prevent H_2O_2-induced cell death (Supplementary Figure S3.4D), we find that this effect is CSE dependent (Supplementary Figure S3.4E,F), and not caused by hercynine alone (Supplementary Figure S3.4G,H). This data further confirmed that beneficial effects of ET are not due to its antioxidant activity.

We also assessed the possibility that protective effects might come from the alleged antiferroptotic properties of reactive sulfur species (36,37). We found no evidence that polysulfide levels change in ET treated cells, nor that ET treatment could prevent erastin and RSL3-induced ferroptotic cell death (Supplementary Figure S3.4I,J) and lipid peroxidation (Supplementary Figure S3.4K).

Depending on the dose, H_2S could act either as a donor of electrons for electron transport chain (ETC) or as a powerful inhibitor of complex IV (38). Therefore, we assessed the mitochondrial respiration in WT and $CSE^{-/-}$ MEFs treated with ET (Figure 3.3H). ET treatment caused an increase in maximum respiration (Figure 3.3I), mitochondrial respiration (basal cellular respiration minus non-mitochondrial respiration, (Figure 3.3J) and ATP production of WT cells (Figure 3.3K). Basal respiration and nonmitochondrial respiration were also increased (Supplementary Figure S3.4L,M), as was the reserve respiratory capacity (RRC; maximal respiration minus basal respiration), which tripled (Figure 3.3L). All these effects were abolished in $CSE^{-/-}$ cells where ET either had no effect or even reduced the quantified parameters (Figure 3.3H-L, Supplementary Figure S3.4L,M). Interestingly, extracellular acidification rate (ECAR) remained unchanged with ET treatment (Figure 3.3M, Supplementary Figure S3.4N). While our data suggest that $CSE^{-/-}$ cell are highly glycolytic (implying an endogenous role of H_2S), we could observe no further change in glycolytic activity in either WT or $CSE^{-/-}$ cells treated

with ET (Supplementary Figure S3.4O). This suggests that the ET effects do not come from modulation of glycolytic flux but predominantly from mitochondrial ETC. Furthermore, no change in reduced CoQ levels in cells treated with ET suggests that there is no inhibition of the ETC (Supplementary Figure S3.4P).

When energy demand surpasses normal levels, the reserve respiratory capacity can step in to boost supply, preventing an 'ATP crisis'. Higher reserve respiratory capacity levels are linked to improved cell survival, whereas lower RRC levels have been linked to cell death and diseases (39). We next monitored the effect of ET treatment on cell growth. Regardless of the cystine levels in the medium, to provide the substrate for the CSE, ET increased the cell growth in a concentration-dependent manner, and this effect was completely abolished in $CSE^{-/-}$ MEFs (Figure 3.3N). Similar effects could be also observed in human umbilical vein endothelial cells (HUVEC), where silencing of CSE abolished the beneficial effects of ET on cell growth (Figure 3.3O). It is worth mentioning that these effects are not due to the activation of mTOR signalling pathway (Supplementary Figure S3.4Q). The ET treated cells replicate faster due to the activation of cell cycle, as observed by monitoring the % of cells in G2/M phase (Supplementary Figure S3.4R). This ability of ET to stimulate cell growth of HUVECs (Figure 3.3O) was also confirmed by their greater sprouting potential (Figure 3.3P). This is in accordance with recent studies, which also suggested that H_2S somehow stimulates NAD^+ levels in endothelial cells, akin to NAD precursor NMN, to prevent vascular aging (40). In fact, most of the observed beneficial effect of ET: improvement of lifespan and healthspan, mitochondrial morphology and function and cell proliferation could be potentially explained by an increase in NAD^+ levels (19,41–43).

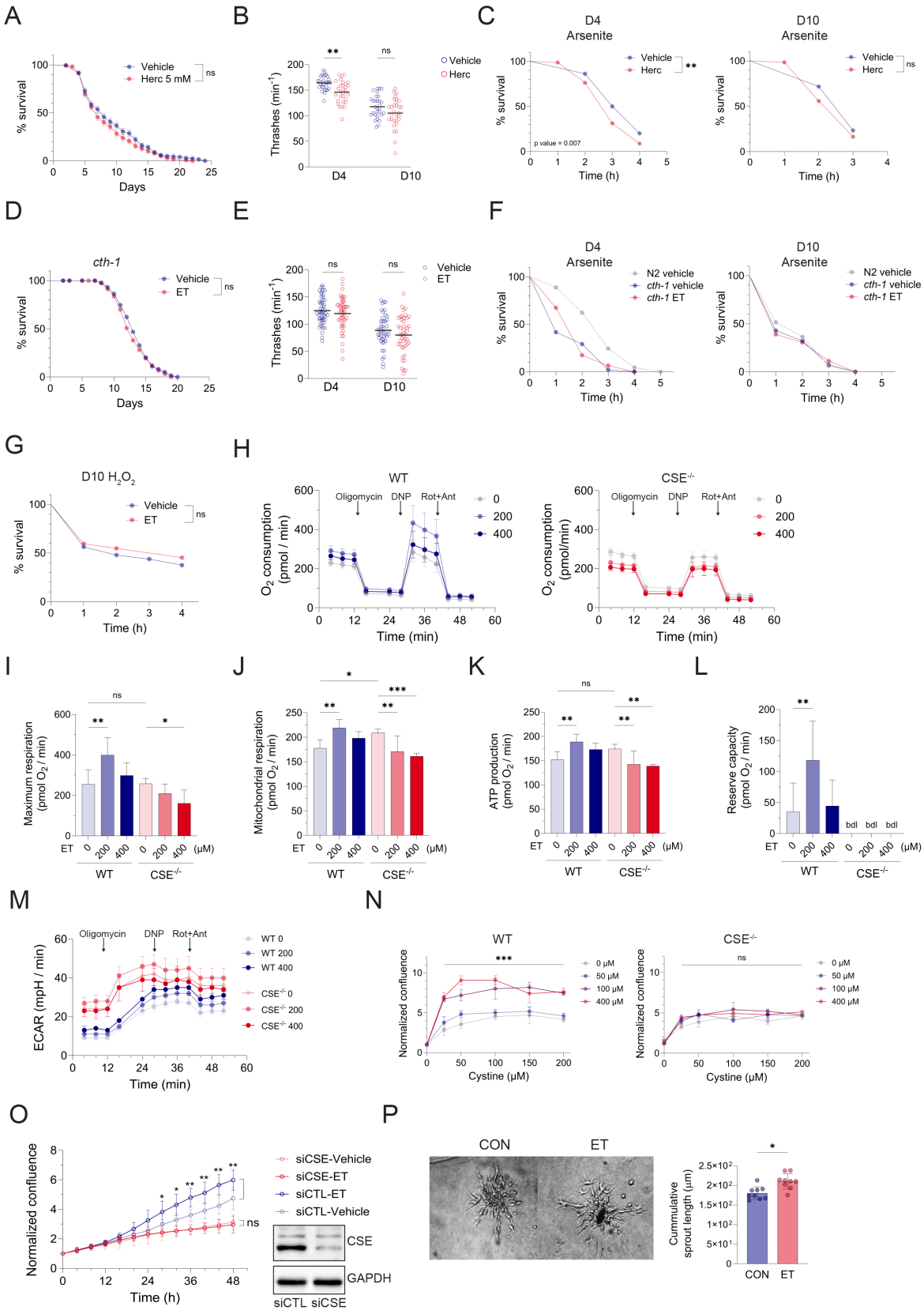
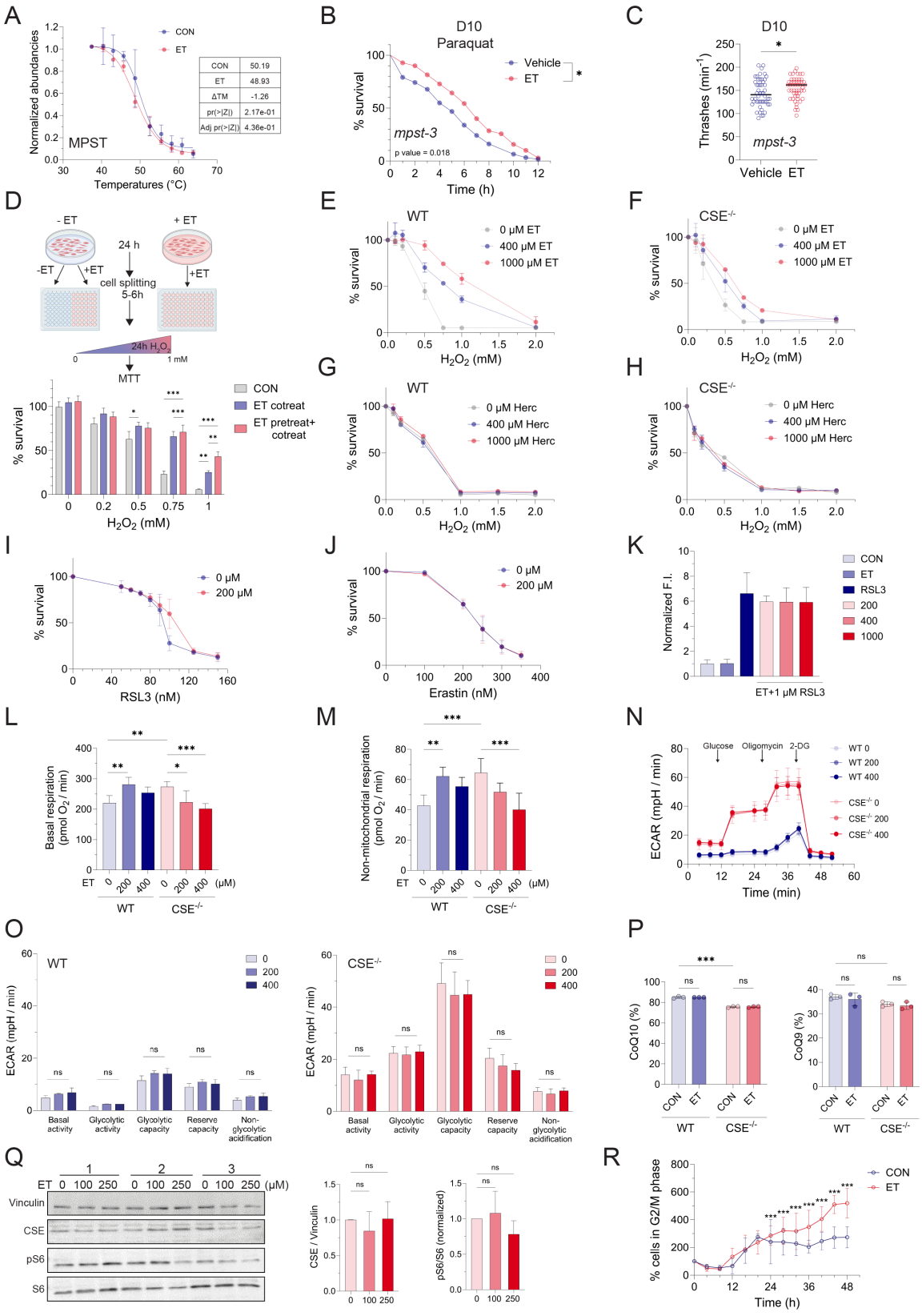

A
% survival
Vehicle
Herc 5 mM
ns
Days
B
Thrashes (min-1)
**
ns
Vehicle
Herc
D4
D10
C
D4 Arsenite
D10 Arsenite
Vehicle
Herc
**
ns
p value = 0.007
% survival
Time (h)
D
cth-1
Vehicle
ET
ns
% survival
Days
E
Thrashes (min-1)
ns
ns
Vehicle
ET
D4
D10
F
D4 Arsenite
D10 Arsenite
N2 vehicle
cth-1 vehicle
cth-1 ET
% survival
Time (h)
G
D10 H2O2
Vehicle
ET
ns
% survival
Time (h)
H
WT
CSE-/-
Oligomycin
DNP
Rot+Ant
0
200
400
O2 consumption (pmol / min)
O2 consumption (pmol/min)
Time (min)
I
Maximum respiration (pmol O2 / min)
ns
**
*
ET
0
200
400
(μM)
WT
CSE-/-
J
Mitochondrial respiration (pmol O2 / min)
*
***
**
**
K
ATP production (pmol O2 / min)
ns
**
**
**
L
Reserve capacity (pmol O2 / min)
**
bdl
M
ECAR (mpH / min)
Oligomycin
DNP
Rot+Ant
WT 0
WT 200
WT 400
CSE-/- 0
CSE-/- 200
CSE-/- 400
Time (min)
N
WT
CSE-/-
***
ns
Normalized confluence
0 μM
50 μM
100 μM
400 μM
Cystine (μM)
O
Normalized confluence
Time (h)
ns
siCSE-Vehicle
siCSE-ET
siCTL-ET
siCTL-Vehicle
CSE
GAPDH
siCTL siCSE
P
CON
ET
Cummulative sprout length (μm)
*
CON
ET

Figure 3.3. Lifespan and healthspan benefits of ergothioneine treatment are CSE dependent.

(**A**) Lifespan of hercyinine (5 mM)-treated wild type (N2) worms (-13 ± 20 % for median lifespan, n ≥ 180 animals per group, Kaplan-Meier survival analysis, Mantel-Cox long rank test, n.s. non-significant). (**B**) Movement capacity (the number of thrashing movements made by each worm in 60 s) of aged worms treated with 450 μM hercynine (n = 30 per experimental group, two-way Anova, **p < 0.01). (**C**) Survival curves of hercyinine (450 μM)-treated D4 and D10 N2 worms exposed to 5 and 2 mM sodium arsenite, respectively (n = 80 for D4 and n = 60 for D10; Mantel-Cox long rank test, n.s. non-significant). (**D**) Lifespan of ET (450 μM)-treated *cth-1* mutants (-7.4 ± 0.4 % for median lifespan, n = 260 animals per group, Kaplan-Meier survival analysis, Mantel-Cox long rank test, n.s. non-significant). (**E**) Movement capacity of D10 *cth-1* worms treated with 450 μM ET (n = 50 per experimental group, two-way ANOVA, n.s. non-significant). (**F**) Survival curves of ET (450 μM)-treated D4 and D10 *cth-1* mutants exposed to 5 and 2 mM sodium arsenite, respectively (n > 45 for D4 and n > 28 for D10; Mantel-Cox long rank test, n.s. non-significant). (**G**) Survival curves of ET (450 μM)-treated D10 *cth-1* mutants exposed to 100 μM H_2O_2 (n > 42 per experimental group; Mantel-Cox long rank test, n.s. non-significant). (**H**) Real-time mitochondrial respiration, depicted as oxygen consumption rate (OCR), in wild-type and $CSE^{-/-}$ MEFs treated with 200 and 400 μM ET. (**I-L**) Calculated values for respiratory parameters: (I) maximal respiration, (J) mitochondrial respiration, (K) ATP production and (L) reserve capacity. n= 6, two-way ANOVA, *p < 0.05, **p < 0.01, ***p < 0.001, bdl (below detection limit). (**M**) Extracellular acidification rate (ECAR) in WT and $CSE^{-/-}$ MEFs treated with 200 and 400 μM ET. (**N**) Cell proliferation in wild type (WT, left) and $CSE^{-/-}$ MEFs (right) with the varying concentrations of ET (0 - 400 μM) and cystine in the medium (0 – 200 μM). n = 3, Two-way ANOVA, ***p < 0.001, n.s. non-significant. (**O**) Human umbilical vein endothelial (HUVE) cells were exposed for 48 h in control siRNA (siCTL) or an siRNA directed against CSE (siCSE) and subsequently treated with 100 μM ET. Confluence over time and respective immunoblots for CSE and GAPDH. n=6 biological replicates in technical triplicates. Two-way ANOVA, *p < 0.05, **p < 0.01, n.s. non-significant. (**P**) Representative images and cumulative sprout length of HUVE cells treated with 100 μM ET. n=3 biological replicates in technical triplicates. Scale bar = 100 μm. *p<0.05. Paired Student‘s t-test.


A
Normalized abundances
CON
ET
MPST
Temperatures (°C)
CON 50.19
ET 48.93
ΔTM -1.26
pr(>|Z|) 2.17e-01
Adj pr(>|Z|) 4.36e-01
B
D10
Paraquat
Vehicle
ET
% survival
mpst-3
p value = 0.018
Time (h)
C
D10
Thrashes (min-1)
mpst-3
Vehicle ET
D
- ET
+ ET
24 h
-ET
+ET
+ET
cell splitting
5-6h
24h H2O2
0
1 mM
MTT
% survival
CON
ET cotreat
ET pretreat+ cotreat
H2O2 (mM)
E
WT
0 µM ET
400 µM ET
1000 µM ET
% survival
H2O2 (mM)
F
CSE-/-
0 µM ET
400 µM ET
1000 µM ET
% survival
H2O2 (mM)
G
WT
0 µM Herc
400 µM Herc
1000 µM Herc
% survival
H2O2 (mM)
H
CSE-/-
0 µM Herc
400 µM Herc
1000 µM Herc
% survival
H2O2 (mM)
I
0 µM
200 µM
% survival
RSL3 (nM)
J
0 µM
200 µM
% survival
Erastin (nM)
K
Normalized F.I.
CON
ET
RSL3
200
400
1000
ET+1 µM RSL3
L
Basal respiration (pmol O2 / min)
ET
(µM)
WT
CSE-/-
M
Non-mitochondrial respiration (pmol O2 / min)
ET
(µM)
WT
CSE-/-
N
Glucose
Oligomycin
2-DG
ECAR (mpH / min)
WT 0
WT 200
WT 400
CSE-/- 0
CSE-/- 200
CSE-/- 400
Time (min)
O
WT
CSE-/-
ECAR (mpH / min)
0
200
400
Basal activity
Glycolytic activity
Glycolytic capacity
Reserve capacity
Non-glycolytic acidification
P
CoQ10 (%)
CoQ9 (%)
CON
ET
WT
CSE-/-
Q
1
2
3
ET 0 100 250 0 100 250 0 100 250 (µM)
Vinculin
CSE
pS6
S6
CSE / Vinculin
pS6/S6 (normalized)
R
% cells in G2/M phase
CON
ET
Time (h)

Supplementary Figure S3.4 (related to Figure 3.3). ET improves mitochondrial respiration and cell survival in a CSE-dependent manner.

(**A**) Melting curves for MPST obtained by thermal proteome profiling experiment. MEF cells were treated with 400 μM ET for 4 h. n = 3. (**B**) Survival curves of ET (450 μM)-treated D10 *mpst-3* worms exposed to 62.5 mM paraquat. (n > 60 per experimental group; Mantel-Cox long rank test, *p < 0.05). (**C**) Movement capacity of D10 *mpst-3* worms treated with 450 μM ET (n = 50 per experimental group, unpaired Student's t-test, *p < 0.05). (**D**) Experimental design and subsequent analysis of cell survival of MEF cells treated with varying concentrations of H_2O_2 following the pretreatment with 400 μM ET. (**E-F**) Dose-dependent toxicity of H_2O_2 in (E) wild type and (F) $CSE^{-/-}$ MEF cells treated with either 400 μM or 1 mM ET. n=3. (**G-H**) Dose-dependent toxicity of H_2O_2 in (E) wild type and (F) $CSE^{-/-}$ MEF cells treated with either 400 μM or 1 mM hercynine. n=3. (**I-J**) The effect of ET treatment (200 μM) on dose-dependent induction of ferroptotic cell death by (I) RSL3 and (J) erastin. n=3. (**K**) Oxidation of BODIPY 581/591 c11 in MEF cells treated with varying concentrations of ET (200-1000 μM) and then exposed to RSL3 (1 μM) to induce ferroptosis. One-way ANOVA, n.s. non-significant. (**L-M**) Calculated values for respiratory parameters obtained from the experiment shown in Fig. 3H: (L) basal respiration and (M) non-mitochondrial respiration. n = 6, two-way ANOVA, *p < 0.05, **p < 0.01, ***p < 0.001. (**N-O**) Extracellular acidification rate (N) in WT and $CSE^{-/-}$ MEFs (treated with 200 and 400 μM ET) after sequential additions of 10 mM glucose, 2 μg/mL oligomycin, and 100 mM 2-deoxyglucose (2-DG) (left) and (O) metabolic parameters calculated from it n = 6, one-way ANOVA, n.s. non-significant. (**P**) Intracellular levels of oxidized coenzyme Q9 and Q10 in WT and $CSE^{-/-}$ MEFs treated with 400 μM ET for 4 h. n=3, two-way ANOVA, n.s. non-significant. (**Q**) Expression levels of CSE, ribosomal S6 kinase and phospho-S6 kinase in HUVE cells treated with 100 or 250 μM ET. One-way ANOVA, n.s. non-significant. (**R**) HUVE cells infected with FUCCI probes at passage 1. Percentage of cells in G2/M phase for up to 48 hours. Cells treated as in Fig. 3P. n=3 biological replicates in technical triplicates. ***p<0.001. Two-way Anova, Šídák's multiple comparisons test.

3.3.8. Ergothioneine-induced GDPH persulfidation improves muscle health

To understand if ET treatment affects NAD^+ levels, we first looked at aging *C. elegans*. While aging caused a decline in NAD^+, as previously reported (19), ET treatment significantly increased those levels (Figure 3.4A). Similarly, the treatment of MEF cells with ET resulted in concentration-dependent increase of NAD^+/NADH levels (Figure 3.4B).

Over the course of aging, NAD^+ levels decrease in various tissues, including skeletal muscle, where clinical evidence underscores age-related NAD^+ deficiency (19,40,42,44,45). The treatment with the above-mentioned precursors and supplements improves the age-related sarcopenia and muscle performance (42,46,47). Therefore, we designed the experiment where 9-month-old male rats (*Rattus norvegicus*) were treated with 20 mg/kg ET in the drinking water for 3 weeks (Figure 3.4C) and then subjected to exercise endurance test. ET-treated animals showed no difference in food and water consumption (Supplementary Figure S3.5A,B). Both time and distance run to exhaustion were approximately two times higher in ET treated rats (Figure 3.4C). 3-week treatment with ET also resulted in significant increase in muscle mass (m. gastrocnemius) (Figure 3.4D) and decrease of post-exercise serum and muscle lactate levels (Figure 3.4E). On the other hand, pyruvate and oxaloacetate levels were unaffected (Supplementary Figure S3.5C,D). Most importantly, the treatment resulted in significant increase of NAD^+/NADH levels in muscle tissue (Figure 3.4F). While this is consistent with the effects of ET increasing NAD^+ levels in cells and *C. elegans*, it is worth mentioning that neither of the NAD^+ precursors managed to significantly boost NAD^+ levels in muscle, even after much longer supplementation (3,44,46). Interestingly, the ET treatment also affected the $NADP^+$/NADPH levels shifting the equilibrium towards the more reduced form

(Supplementary Figure S3.5E) and providing the reducing equivalents for the antioxidant defence systems.

NAD^+ has been shown to improve muscular aging by stimulating angiogenesis of blood vessels (40). As we observed that ET stimulated HUVEC growth and sprouting (Figure 3.4O,P), we compared the vascularization of muscle tissue sections. An obvious increase in total number of blood vessels per muscle fiber was observed (Figure 3.4G). This was additionally confirmed by detecting higher protein levels of VEGF receptor in muscles of animals treated with ET (Supplementary Figure S3.5F). It is worth mentioning that unlike ET, NMN supplementation had no effect on the capillary density of sedentary young to middle-aged mice. Only when coupled with exercise training or after ischemia did NMN improve these parameters (40).

The maintenance and repair of skeletal muscle rely on dormant muscle stem cells (MuSCs), which become active following muscle injury to proliferate and generate specialized muscle cells, facilitating the regeneration of damaged muscle fibers (42). With aging the number and proliferative potential of those MuSCs decreases but it can be restored by NAD^+ precursors such as NR (42), which affects the mitochondrial biogenesis. To monitor the effect of ET treatment on MuSC numbers, we stained muscle tissue sections with paired box protein Pax-7 (PAX-7) antibody, a known MuSC marker. Our data show an increase of MuSC number upon ET treatment (Figure 3.4H) and they also show higher expression levels of mitochondrial import protein Tom 20 (Figure 3.4I). However, this effect does not appear to be controlled by the changed in SIRT1 or PGC1alpha protein levels (Supplementary Figure S3.5G), or by the change of total protein acetylation (Supplementary Figure S3.5H). High-electron density mitochondria were observed in

muscle tissue of ET-treated rats (Figure 3.4J), characteristic for highly active mitochondria (48,49).

Taken together, these data support the conclusion that ET treatment boosts the NAD^+ levels in treated cells, worms or rats, which in turns acts as “rejuvenating” agent via mechanisms reported previously (19,40,42,44,45). The ability of H_2S to increase the NAD^+/NADH ratio and stimulate the subsequent effects akin to NAD^+ precursors have been shown to have beneficial effects on vascular rejuvenation via unidentified mechanism (40).

Interestingly, 5-day treatment of both male and female 8-week-old rats with 20 mg/kg ET in the drinking water (Supplementary Figure S3.5I-K) also showed significant increase in time and distance run to exhaustion (Supplementary Figure S3.5L,M). Plasma levels of NAD+ in male but not female rats were also significantly higher (Supplementary Figure S3.5N) suggesting that metabolic remodelling caused by ET is enough to boost performance of those animals akin to performance enhancing drugs.

Next, we aimed to understand how ET controls NAD+/NADH ratio. One of the main regulators of NAD^+ regeneration in cells is glycerol-3-phosphate (G3P) dehydrogenase (GPDH) pathway (50,51). Because mitochondrial inner membrane is impermeable to NADH, cells use the G3P shuttle to directly transfer electrons from cytosolic NADH to ETC. Two enzymes, cytosolic (cGPDH) and mitochondrial (mGPDH) maintain this shuttle with the reaction of cGPDH being the one that generates NAD^+ (Figure 3.4K). Persulfidome analysis of ET treated *C. elegans* did find that this pathway is significantly enriched (Figure 3.1J) and that PSSH levels of cytosolic glycerol-3-phosphate dehydrogenase isoform (*gpdh-2*) are significantly higher without alterations in the protein expression levels (Supplementary Figure S3.5O). To test the hypothesis that cGPDH is a

regulator of ET's healthspan benefits in *C. elegans*, we treated D4 and D10 *gpdh-1* and *gpdh-2* mutants (those two genes are orthologs of mammalian cGPDH) with ET. ET failed to elicit any improvement on motility (Supplementary Figure S3.5P), suggesting that ET-induced protein persulfidation of this enzyme might be the key reason for the observed boosting of NAD+ levels.

Using dimedone switch method for persulfide labelling we also observed that ET treatment induced a significant increase in the persulfidation of GPDH in rat muscle (Figure 3.4L). This was further followed by an increase in G3P levels, which suggested that PSSH of GPDH might be increasing the enzyme's activity (Figure 3.4M). To address that we used purified cGPDH and treated it with sodium disulfide (Na2S2). Mammalian cGPDH contains 11 cysteines (Supplementary Figure S3.5Q). Therefore, we incubated cGPDH with varying concentrations of Na2S2 and measured the enzyme activity (conversion of NADH to NAD+ upon addition of dihydroxyacetone phosphate as a substrate). We observed that the disulfide to protein ratios up to 1:1 resulted in significant increase of enzyme activity (k_{obs} = 1.8 x 10^{-3} s^{-1} for untreated *vs* 3.6 x 10^{-3} s^{-1} for persulfidated), while higher ratios (expected to modify more than one cysteine) did not significantly affect the activity (Figure 3.4N). In order to identify which cysteine is undergoing persulfidation we subjected the samples to LC/MS/MS. Our data show that cysteine 243 is the main target for protein persulfidation (Figure 3.4O). Analysing the crystal structure of human GPD it becomes apparent that C243, located at the beginning of a beta strand, is surface exposed (Figure 3.4P) and therefore easily available for the reaction. Although significantly far away from the active site K204 (Figure 3.4P), mutational studies of distant regions have been shown to change the conformation of catalytic loop 292-297 leading to the increase of GPD activity (52). Indeed, when we

assessed the activity of cGPDH in the lysates of muscle tissue from untreated and ET-treated rats (experiments require a full inhibition of mitochondrial respiration to prevent the contribution of mGPDH part of the shuttle),(53) we could detect ~2-fold increase in enzyme activity (Figure 3.4Q-R).

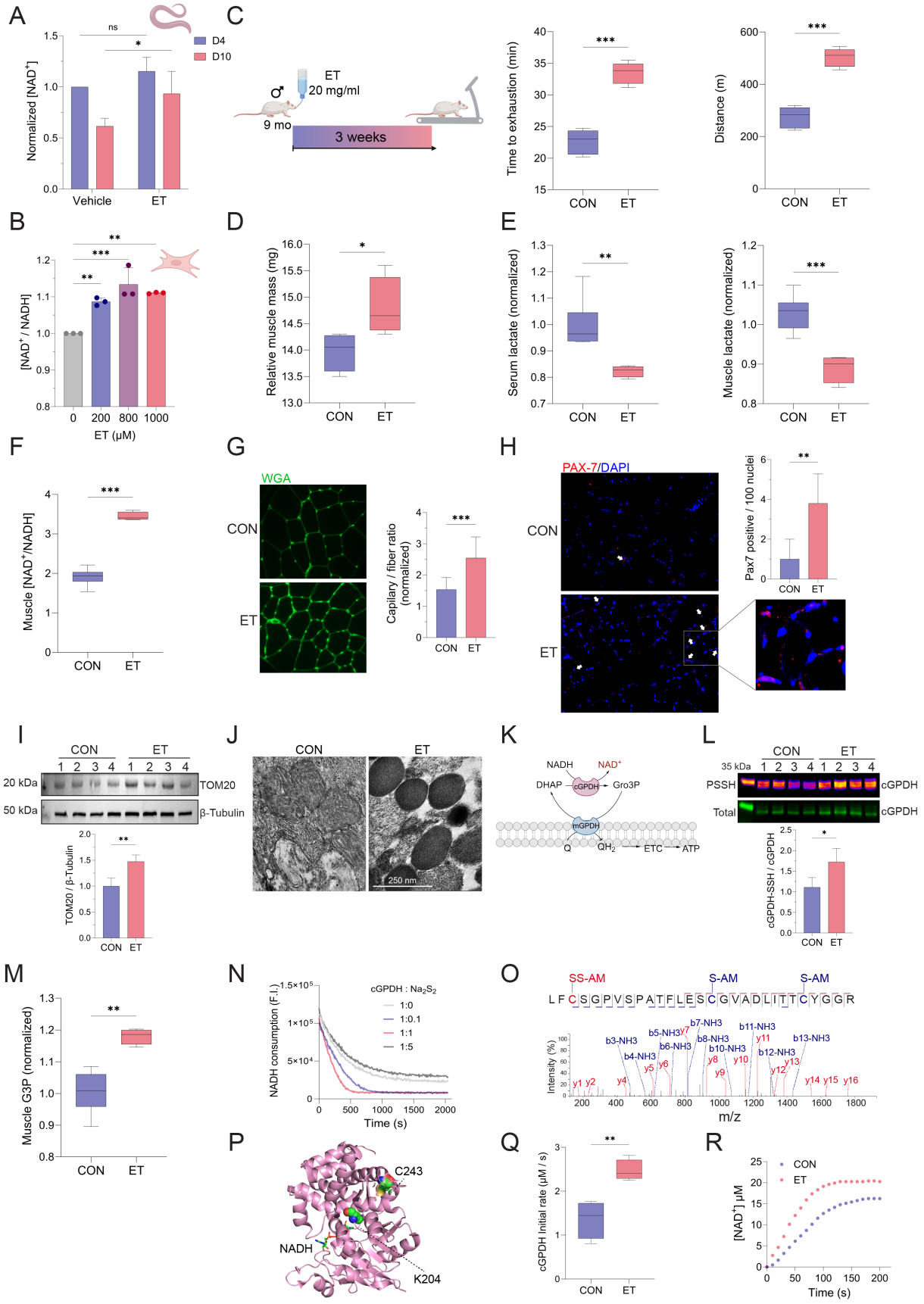
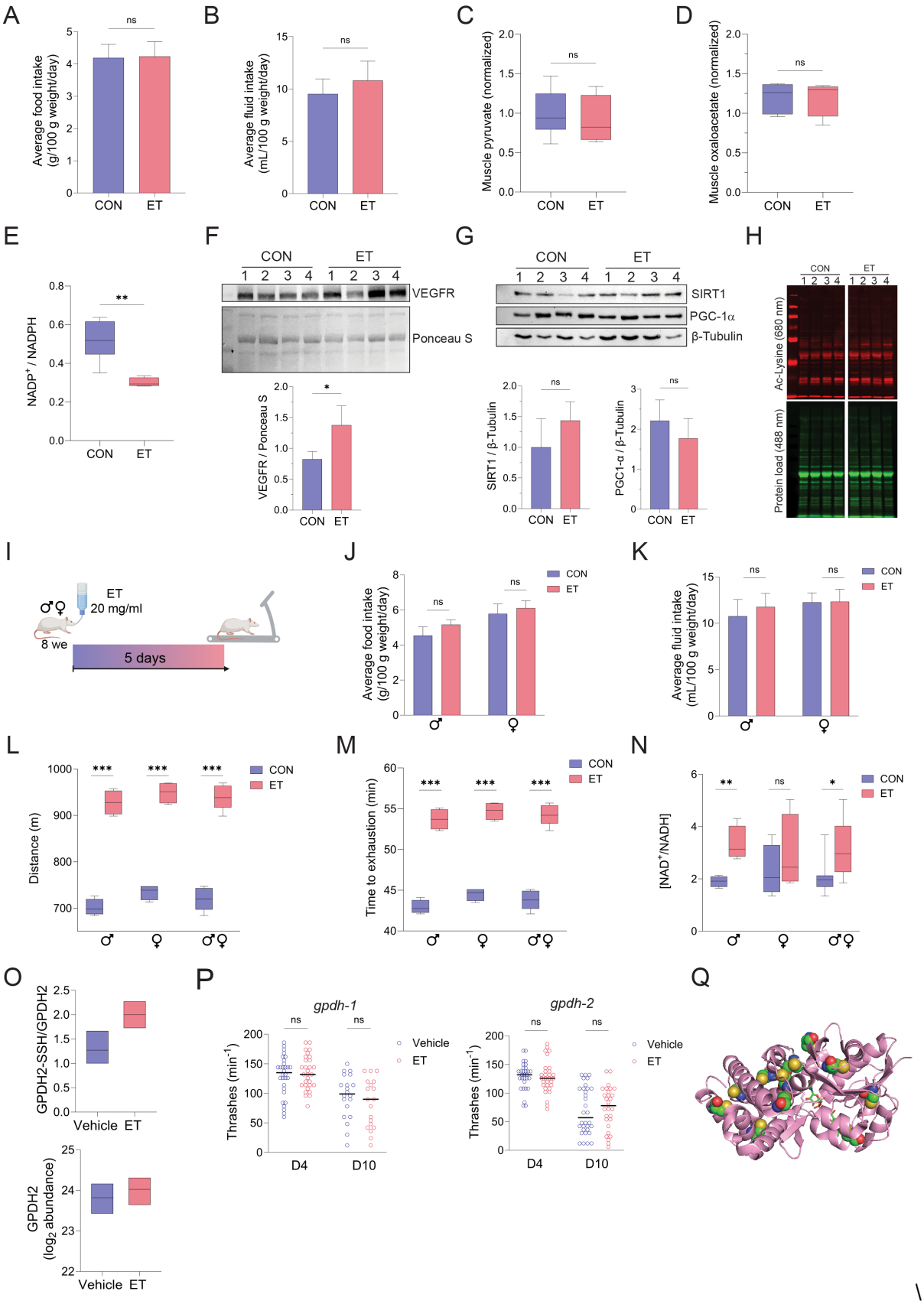

A
Normalized [NAD+]
D4
D10
Vehicle
ET
B
[NAD+ / NADH]
ET (μM)
C
ET
20 mg/ml
9 mo
3 weeks
Time to exhaustion (min)
Distance (m)
CON
D
Relative muscle mass (mg)
E
Serum lactate (normalized)
Muscle lactate (normalized)
F
Muscle [NAD+/NADH]
G
WGA
Capilary / fiber ratio (normalized)
H
PAX-7/DAPI
Pax7 positive / 100 nuclei
I
20 kDa
TOM20
50 kDa
β-Tubulin
TOM20 / β-Tubulin
J
250 nm
K
NADH
NAD+
DHAP
cGPDH
Gro3P
mGPDH
Q
QH2
ETC
ATP
L
35 kDa
PSSH
Total
cGPDH-SSH / cGPDH
M
Muscle G3P (normalized)
N
NADH consumption (F.I.)
cGPDH : Na2S2
1:0
1:0.1
1:1
1:5
Time (s)
O
SS-AM
S-AM
LFCSGPVSPATFLESCGVADLITTCYGGR
Intensity (%)
m/z
P
C243
NADH
K204
Q
cGPDH Initial rate (μM / s)
R
[NAD+] μM
Time (s)

Figure 3.4. Ergothioneine increases the NAD^+ levels and improves the muscle health by causing persulfidation of glycerol 3-phosphate dehydrogenase.

(**A**) NAD^+ levels in *C. elegans* treated with ET (450 μM) until D4 or D10 of adulthood. Two-way ANOVA, n = 3, *p < 0.05, n.s. non-significant. (**B**) NAD^+/NADH ratios in MEF cells treated with varying concentrations of ET. One-way ANOVA, n = 3, *p < 0.05, **p < 0.01, ***p < 0.001. (**C**) 9-month-old male rats were treated with 20 mg/kg ET through drinking water for 3 weeks and subjected to low-intensity test (left). Duration and distance run by rats until exhaustion (right). N = 6 per group. Unpaired Student's t-test, ***p < 0.001. (**D**) Muscle (m. gastrocnemius) mass of rats treated with 20 mg/kg ET through drinking water for 3 weeks. Unpaired Student's t-test, *p < 0.05. (**E**) Serum (left) and muscle tissue (right) lactate levels. Unpaired Student's t-test, **p < 0.01, ***p < 0.001. (**F**) NAD^+/NADH levels in rat muscle tissue. Unpaired Student's t-test, ***p < 0.001.
G) Wheat Germ Agglutinin (WGA) staining (left) and quantification of blood vessels (right) in muscle tissue sections. 2-3 images per animal were analysed. N = 4. Unpaired Student's t-test, ***p < 0.001. (**H**) Representative images of PAX7 (red) immunostained and DAPI (blue) stained muscle tissue sections. Arrows point to PAX7-positive stem cells. Quantification of PAX7-positive stem cells per 100 nuclei is presented. 2-3 images per animal were analysed. N = 4. Unpaired Student's t-test, **p < 0.01. (**I**) Expression levels of mitochondrial TOM20 protein in muscle tissue. N = 4. Unpaired Student's t-test, **p < 0.01. (**J**) Representative transmission electron micrographs of ultrathin sections of rat gastrocnemius. Left: Control, Right: ET-treated. Magnification 15,000x, scale bar 250 nm. n = 4. (**K**) Schematic presentation of glycerol-3-phosphate (G3P) shuttle for cytoplasmic NAD^+ generation. cGPDH; cytosolic G3P dehydrogenase; mGPDH: mitochondrial G3P dehydrogenase, ETC: electron transport chain. (**L**) Persulfidation levels of cytosolic GPDH in rat muscle tissue. N = 4. Unpaired Student's t-test, *p < 0.05. (**M**) G3P levels in rat muscle tissue. Unpaired Student's t-test, **p < 0.01. (**N**) cGPDH activity of purified enzyme (13.3 nM) pretreated with sodium disulfide (in ratios indicated in the figure) to induce protein persulfidation. (**O**) Annotated QExactiveHCD MS/MS spectrum displaying the persulfidated C243 residue in cGPDH. (**P**) Ribbon structure of human cGPDH (PDB:1wpq) highlighting the catalytic K204 and C243 as spheres. Solvent excluded surface of C243 is also shown. Wire-model of NADH is also shown. (**Q-R**) cGPDH activity (Q: Initial reaction rate, R: representative activity recordings) in muscle tissue lysates originating from control or ET-treated rats. UV-Vis recording of NADH oxidation was carried out in the presence of 0.2 mM NADH, 0.4 mM dihydroxyacetone phosphate, 7 μM FCCP, 4 μM rotenone.


A
Average food intake (g/100 g weight/day)
ns
CON
ET
B
Average fluid intake (mL/100 g weight/day)
ns
CON
ET
C
Muscle pyruvate (normalized)
ns
CON
ET
D
Muscle oxaloacetate (normalized)
ns
CON
ET
E
NADP+ / NADPH
**
CON
ET
F
CON
ET
1 2 3 4 1 2 3 4
VEGFR
Ponceau S
VEGFR / Ponceau S
*
CON
ET
G
CON
ET
1 2 3 4 1 2 3 4
SIRT1
PGC-1α
β-Tubulin
SIRT1 / β-Tubulin
ns
PGC1-α / β-Tubulin
ns
CON
ET
H
CON
ET
1 2 3 4 1 2 3 4
Ac-Lysine (680 nm)
Protein load (488 nm)
I
ET
20 mg/ml
8 we
5 days
J
Average food intake (g/100 g weight/day)
ns
CON
ET
♂
♀
K
Average fluid intake (mL/100 g weight/day)
ns
CON
ET
♂
♀
L
Distance (m)
***
CON
ET
♂
♀
♂♀
M
Time to exhaustion (min)
***
CON
ET
♂
♀
♂♀
N
[NAD+/NADH]
**
ns
*
CON
ET
♂
♀
♂♀
O
GPDH2-SSH/GPDH2
Vehicle
ET
GPDH2 (log2 abundance)
Vehicle
ET
P
gpdh-1
Thrashes (min-1)
ns
Vehicle
ET
D4
D10
gpdh-2
Thrashes (min-1)
ns
Vehicle
ET
D4
D10
Q

Supplementary Figure S3.5 (related to Figure 3.4). ET effects are cGPDH-dependent.

(**A-B**) Average food (A) and fluid (B) intake during 3 weeks of treatment. (**C**)Pyruvate levels in rat muscle tissue. (**D**) Oxaloacetate levels in rat muscle tissue. (**E**) $NADP^+$/NADPH levels in rat muscle tissue of 9-month-old animals treated with ET. Derived from the experiment depicted in Fig. 4C. For **A-E:** n = 4-6, Unpaired Student's t-test. **p< 0.01, n.s. non-significant. (**F-G**) Expression levels of (F) vascular endothelial growth-factor receptor (VEGFR) and (G) SIRT1 and PGC1α in rat muscle tissue of 9-month-old animals treated with ET. Unpaired Student's t-test. n.s. non-significant. (**H**) Lysine acetylation levels in rat muscle tissue of 9-month-old animals treated with ET. Fluorescence of NBF-labelled proteins was used as a measure of total load. (**I**) 8-week-old male and female rats were treated with 20 mg/kg ET through drinking water for 5 days and subjected to low-intensity running test. (**J-K**) Average food (J) and fluid (K) intake of both male and female rats during 5 days of treatment. (**L**) Distance run by rats until exhaustion. N = 4 per group. Unpaired Student's t-test, ***p < 0.001. (**M**) Time rats spent running until exhaustion. N = 4 per group. Unpaired Student's t-test, ***p < 0.001. (**N**) NAD^+/NADH levels in rat plasma. Unpaired Student's t-test, *p < 0.05, **p < 0.01. (**O**) Persulfidation and expression levels of GPDH2 protein in *C.elegans* treated with 450 μM ET until D10 of adulthood. (**P**) Movement capacity of *gpdh-1* and *gpdh-2* D4 and D10 worms treated with 450 μM ET (n = 30 per experimental group, unpaired Student's t-test, n.s. non-significant). (**Q**) Ribbon structure of human cGPDH (PDB:1wpq) highlighting all 11 cysteine residues.

3.4. Discussion

Through a series of experiments utilizing *C. elegans*, mammalian cell lines, and animal models, we have elucidated the molecular pathways underlying ET's beneficial effects, with implications for translational research and therapeutic development. Our findings highlight the pivotal role of CSE in mediating the beneficial effects of ET. The absence of CSE abolishes ET's protective effects, emphasizing the essential role of H_2S signaling in ET-induced metabolic resilience. This aligns with recent studies emphasizing CSE as one of the few pro-longevity genes universally upregulated in various lifespan extension interventions (16,54).

Given that ET accumulates in high concentrations due to the presence of the organic cation membrane transporter OCTN-1 (34), the low mM K_m for ET that we observed suggests that it could serve as a preferred substrate over cysteine, resulting in increased H_2S production. H_2S has been shown to stimulate respiration and cell proliferation (55,56) and it also extends lifespan and improves healthspan of *C. elegans* (57–59), effects similar to those we observed for ET. These benefits are not only due to modulation of respiration but also involve the widespread increase of protein persulfidation, which is an evolutionarily conserved modification that rescues cysteines from hyperoxidation (26,60). Indeed, ET increases protein persulfidation, maintaining high levels even at D10 *C. elegans*. These findings align with recent observations that increased persulfidation correlates with enhanced resistance to stress (26). While we cannot rule out that ET acts as a direct scavenger or reactive oxygen species, our results suggest that its direct antioxidant action is not a primary mechanism for its beneficial effects, as previously proposed (61).

Beyond global protection, protein persulfidation also serves as a regulatory posttranslational modification (25). One of the key targets of CSE-catalyzed, ET-induced persulfidation is cGPDH. cGPDH emerges as a key regulator of NAD^+/NADH homeostasis, potentially ameliorating mitochondrial disease (50,51). Its posttranslational modification, such as phosphorylation, has been reported in the skeletal muscle of hibernating ground squirrels (62). Our findings in cells, *C. elegans* and aging rats suggest that persulfidation of cGPDH enhances its activity, leading to an increase of NAD^+ levels. Notably, ET fails to elicit healtspan benefits in *C. elegans* lacking cGPDH.

NAD^+ is a crucial coenzyme vital for cellular and organismal metabolism, stemming from precursors within the vitamin B_3 family (41). Mammals possess the capability to generate NAD^+ from various dietary sources, such as nicotinamide riboside (NR), nicotinamide mononucleotide (NMN) and trigonelline (41,43,63). Supplementation with these compounds improves the age-related sarcopenia and muscle performance (42,46,47). Our data suggest that the effects of ET on aged *C. elegans* and aged rats are comparable to, if not more efficient than, those of NAD^+ precursors (NR, NMN, and trigonelline). This is consistent with observations in mice (14,64). Interestingly, H_2S has been shown to boost NAD^+, thereby improving muscle aging by stimulating angiogenesis (40). The CSE-H_2S-cGPDH-SSH-NAD^+ pathway we describe for ET could therefore account for the full range of beneficial effects observed in rats, including increased vascularization, muscle mass and stem cell number, improved mitochondrial morphology and better physical endurance. While some of those effects (such as improvement of mitochondrial morphology and both *C. elegans* and rats, as well as muscle stem cells count) suggest a rejuvenating action of ET, the performance-improving effects observed

with short-term ET exposure (5 days) imply that metabolic remodeling induced by this pathway could also be exploited for performance ehancement.

In conclusion, by unravelling the molecular intricacies of ET's actions, our research lays the groundwork for further exploration of its clinical applications and therapeutic implications. Future studies may explore the therapeutic potential of ET in mitigating age-related conditions and metabolic disorders, with a focus on translational approaches aimed at harnessing its rejuvenating properties for human health. Finally, recently reported edible mycelium bioengineered to boost both nutritional value and ET levels (65), holds promise as a potential future source to augment daily ET intake.

3.5. Limitations of the study

While holding great promise for healthspan improvements in humans, it is worth stating that ET beneficial effects might be reduced at much older ages, due to reported age-induced decline in CSE expression (26). Combination of ET with the activators of CSE expression might be a therapeutic venue to overcome those issues. Furthermore, several mutations that lead to partial or full inactivation of CSE have been described in humans (66), so ET supplementation can fail to elicit the beneficial effects in those individuals. Finally, being readily accumulated in the cells, the amount of consumed ET and the expression levels of CSE will define if the toxic threshold of H_2S production is achieved.

3.6. Material and methods

Key resources table

REAGENT or RESOURCE	SOURCE	IDENTIFIER
Antibodies		
anti-4-HNE, rabbit polyclonal	Invitrogen	Cat# BS-6313R
anti-SIRT1, rabbit polyclonal	Proteintech	Cat# 13161-1-AP
anti-TOM20, rabbit polyclonal	Proteintech	Cat# 11802-1-AP
anti-GPD1, rabbit polyclonal	Proteintech	Cat# 13451-1-AP
anti-PGC1 alpha, rabbit polyclonal	Novus Biologicals	Cat# NBP1-04676
anti-VEGFR2, mouse monoclonal	Santa Cruz Biotechnology	Cat# sc-6251
anti-GAPDH, mouse monoclonal	Santa Cruz Biotechnology	Cat# sc-47724
anti-PAX-7, mouse monoclonal	Santa Cruz Biotechnology	Cat# sc-81648
WGA-AF488	Invitrogen	Cat# W11261
Anti-Ac-Lysine, mouse monoclonal	Santa Cruz Biotechnology	Cat# sc-32268
anti- β-tubulin	Sigma Aldrich	Cat# TO198
anti-CSE	Proteintech	Cat# 12217-1-AP
anti-Vinculin	Invitrogen	Cat# MA5-11690
anti-S6	Cell Signaling Technology	Cat# 2217
anti-pS6	Cell Signaling Technology	Cat# 2211
anti-mouse-AF488, goat polyclonal	Abcam	Cat# ab150113
anti-mouse-AF680, goat polyclonal	Abcam	Cat# ab175775
anti-rabbit-AF680, donkey polyclonal	Abcam	Cat# ab175772
anti-rabbit-CY5, goat polyclonal	Invitrogen	Cat# A10523
anti-rabbit-HRP	Abcam	Cat# ab205718
anti-mouse-HRP	Cell Signaling Technology	Cat# 7076S
Bacterial and virus strains		
OP50-1	Caenorhabditis Genetics Center	N/A
Chemicals, peptides, and recombinant proteins		
Chelex-100	Sigma Aldrich	Cat# C7901
HEPES	VWR	Cat# 441485H
1M HEPES solution	Sigma Aldrich	Cat# H0887
EDTA	Sigma Aldrich	Cat# E5134
Neocuproine	Sigma Aldrich	Cat# N1501
IGEPAL	Thermofisher	Cat# J61055
SDS	Carl-Roth	Cat# 2326.2
TRIS	Carl-Roth	Cat# 5429.3
Sodium deoxycholate	Sigma Aldrich	Cat# D6750
Glycine	Carl-Roth	Cat# 3187.5
Ponceau S	Sigma Aldrich	Cat# P3504
Tween	Sigma Aldrich	Cat# P9416

Triton X-100	Sigma Aldrich	Cat# T8787
Protease inhibitor cocktail	Sigma Aldrich	Cat# P8340
4-Chloro-7-nitrobenzofurazan (NBF-Cl)	Sigma Aldrich	Cat# 163260
1,4-dithiothreitol (DTT)	ThermoFisher	Cat# R0861
Iodoacetamide	Sigma-Aldrich	Cat# I1149
Ammonium bicarbonate	Sigma Aldrich	Cat# 09830
Calcium chloride	Euromedex	Cat# T885-A
Guanidine hydrochloride	Sigma Aldrich	Cat# G3272
Triethylammonium bicarbonate buffer	Sigma Aldrich	Cat# 18597
Hydroxylamine solution	Sigma Aldrich	Cat# 467804
Trypsin	Promega	Cat# V5117
TMT10plex	Thermo Scientific	Cat# 90110
DCP-Bio1	Merck	Cat# NS1226
Copper (II)-TBTA complex	Lumiprobe	Cat# 21050
L-ascorbic acid	Sigma-Aldrich	Cat# A92902
Formic acid Suprapur	Supelco	Cat# 111670
TCEP	Sigma-Aldrich	Cat# 646547
AQC	Synchem	Cat# s041
AccQ-Tag Ultra Borate Buffer	Waters	Cat# 186009283
Cyanine5 alkyne	Lumirpobe	Cat# A30B0
Laemmli (4X) buffer	BioRad	Cat# 1610747
β-mercaptoethanol	Sigma Aldrich	Cat# M3148
Western Blotting Luminol Reagent	Santa Cruz Biotechnology	Cat# sc-2048
Ponceau S	Sigma Aldrich	Cat# P3504
Hydrogen Peroxide Solution	Sigma Aldrich	Cat# 216763
Erastin	Sigma Aldrich	Cat# E7781
1S,3R-RSL 3	Sigma Aldrich	Cat# SML2234
Thiazolyl Blue Tetrazolium Bromide	Sigma Aldrich	Cat# M5655
Methyl viologen dichloride hydrate	Sigma Aldrich	Cat# 856177
Sodium (meta)arsenite	Santa Cruz Biotechnology	Cat# sc-250986
Nile Red	Sigma Aldrich	Cat# 72485
Oil Red O	Sigma Aldrich	Cat# O0625
Bovine Serum Albumin	Sigma Aldrich	Cat# A7906
L-(+)-Ergothioneine	Thermo Scientific	Cat# J67861.03
L-Hercynine	Sigma Aldrich	Cat# SMB00978
DMEM	Gibco	Cat# 21969-035
DMEM, high glucose, no glutamine, no methionine, no cystine	Gibco	Cat# 21969-035
DMEM/F-12	Gibco	Cat# 21041025
DMEM, no phenol-red	Gibco	Cat# 31053028
Endothelial Cell Growth Medium 2 (ECGM2)	PromoCell	Cat# C-22011
Fetal bovine serum	Pan Biotech	Cat# P30-3031
L-glutamine	Pan Biotech	Cat# P64-80100
Penicillin-streptomycin	Pan Biotech	Cat# P66-07100
Polybrene	Santa Cruz Biotechnology	Cat# 28728-55-4
Lipofectamine™ RNAiMAX	Invitrogen	Cat# 13778075
DPBS	Sigma Aldrich	Cat# D8537
Hoechst 33342	Sigma Aldrich	Cat# B2261

L-Cystine	Sigma Aldrich	Cat# 30200
Pierce™ High Capacity NeutrAvidin™ Agarose beads	Thermofisher	Cat# 20357
Pierce™ NeutrAvidin™ Agarose beads	Thermofisher	Cat# 29200
DTAB	Thermo Scientific	Cat# A10761.09
Sodium disulfide	Dojindo Molecular Technologies	Cat# SB-02
Dihydroxyacetone phosphate hemimagnesium salt hydrate	Sigma Aldrich	Cat# 51269
β-Nicotinamide adenine dinucleotide, reduced disodium salt hydrate	Sigma Aldrich	Cat# N8129
Bio-Spin® P-6 Gel Columns	Bio-Rad	Cat# 7326227
Lead(II) acetate trihydrate	Thermo Scientific Acros	Cat# 423841000
Pyridoxal 5'-phosphate hydrate	Thermo Scientific	Cat# A12323
Granulated agar	BD Difco	Cat# BD 214530
Bacto™ Peptone	Gibco	Cat# 211677
LB Broth (Lennox)	Carl Roth	Cat# X964.1
NaCl	Carl-Roth	Cat# HN00.2
Potassium dihydrogen phosphate	Carl-Roth	Cat# P018.2
Di-sodium hydrogen phosphate dihydrate	Carl-Roth	Cat# 4984.1
Potassium phosphate dibasic	Euromedex	Cat# PB0447-B
Agarose D5	Euromedex	Cat# D5-C
Ethanol	Fisher BioReagents	Cat# BP2818500
TRIzol™ Reagent	Invitrogen	Cat# 15596026
Phenol:chloroform:isoamyl alcohol mix (25:24:1)	Sigma Aldrich	Cat# 77617
DMSO	Carl-Roth	Cat# 4720.3
Methanol, Optima™ LC/MS Grade	Fisher Scientific	Cat# A456-212
Trichloromethane/Chloroform	Carl-Roth	Cat# 7331.1
Acetone ROTIPURAN® ≥99.8%	Carl-Roth	Cat# 9372.2
Acetonitrile	Biosolve	Cat# 00012041001BS
Acetic acid	ThermoFisher	Cat# A/0406/PB15
Isopropanol	Fisher Chemicals	P/7507/17
Ammonia solution 28-30%	Sigma Aldrich	Cat# 5.33003
NaOH	Carl-Roth	Cat# 1CCX.2
Hydrochloric acid 1N	Carl-Roth	Cat# K025.1
Trifluoroacetic acid	Biosolve	Cat# 00202341A8BS
Glycerol-3-phosphate dehydrogenase (GDH)	Roche	Cat# 10127752001
Human recombinant CSE	From Prof. Bibli	Hu et al, 2023
BODIPY™ 581/591 C11	Invitrogen	Cat# D3861
Critical commercial assays		
DC protein assay	Biorad	Cat# 5000112
NAD/NADH-Glo™	Promega	Cat# G9081
NADP/NADPH-Glo™	Promega	Cat# G9071
PureLink™ RNA Mini Kit	Invitrogen	Cat# 12183018A
Glycerol-3-Phosphate Assay Kit	Sigma Aldrich	Cat# MAK207
L-Lactate Assay Kit	Sigma Aldrich	Cat# MAK443
Oxaloacetate Assay Kit	Sigma Aldrich	Cat# MAK070
Pyruvate Assay Kit	Sigma Aldrich	Cat# MAK071

Pierce™ High pH Reversed-Phase Peptide Fractionation Kit	Thermo Scientific	Cat# 84868
Deposited data		
Total proteome, persulfidome Thermal proteome profiling data	PRIDE repository	PXD051587 PXD051609
RNA Seq data		
Experimental models: Cell lines		
Mouse: MEF WT (Male)	From Prof. Snyder's lab (Johns Hopkins University School of Medicine)	(67)
Mouse: MEF CSE$^{-/-}$ (Male)	From Prof. Snyder's lab (Johns Hopkins University School of Medicine)	(67)
Human: HUVEC		
Human: HEK293T		
Experimental models: Organisms/strains		
C. elegans Wild-Type Bristol N2	Caenorhabditis Genetic Center	
C. elegans: strain MRF03 (*cth-1(ok3319)V)*	Caenorhabditis Genetic Center	strain VC2569
C. elegans: strain MRF09 *mpst-3(tm4387)V*	MITANI Lab, National Bio-Resource Project of the MEXT, Japan	strain FX04387
C. elegans: strain *CF1038 (daf-16 (mu86)I)*	Caenorhabditis Genetic Center	
C. elegans: strain *SJ4103 (zcIs14 [Pmyo-3::mitoGFP])*	From A.M. Vizuete (The Institute of Biomedicine of Seville)	
C. elegans: strain RB1373 *(F47G4.3(ok1558) I)*	Caenorhabditis Genetic Center	
C. elegans: strain RB1482 *(K11H3.1(ok1733) III)*	Caenorhabditis Genetic Center	
Male Wistar Rat	Institute for Biological Research "Sinisa Stankovic", Belgrade, Serbia	
Oligonucleotides		
siRNA directed against human CSE	Eurogentec	custom synthesis
Recombinant DNA		
psPAX2	Didier Trono Lab	Addgene Plasimd #12260
pMD2.G	Didier Trono Lab	Addgene Plasimd #12259
Cdt-mKO		Riken, Japan
Geminin-GFP		Riken, Japan
Software and algorithms		
R Environment	The R Project for Statistical Computing	https://www.r-project.org/

R studio	RStudio, Inc	https://www.rstudio.com/
PEAKS ONLINE	Bioinformatics Solutions Inc.	http://www.bioinfor.com/
ImageJ	Schneider et al.	https://imagej.nih.gov/ij/download.html
Fiji	Schindelin et al.	https://imagej.net/software/fiji/
BioVenn	Hulsen et al.	https://www.biovenn.nl/
GraphPad Prism 10.2.0	GraphPad Software	https://www.graphpad.com
FragPipe	Kong et al.	https://fragpipe.nesvilab.org/
DAVID Bioinformatics Database v6.8	Huang et al.	https://david.ncifcrf.gov/
EigenMS R script	Karpievitch et al.	https://rdrr.io/bioc/ProteoMM/src/R/EigenMS.R
Origin, Version 2022	OriginLab Corporation, Northampton, MA, USA	
ChemDraw 20.0.0.38	PerkinElmer Informatics, Inc	
Adobe Illustrator 28.4.1	Adobe	https://www.adobe.com/products/illustrator.html
BioRender		https://www.biorender.com/
Oasis	Yang et al.	https://sbi.postech.ac.kr/oasis/
CellProfiler	Stirling et al.	
SeamDock	Murail et al.	https://bioserv.rpbs.univ-paris-diderot.fr/services/SeamDock/

3.6.1. Experimental models and subject details

C. elegans

The following strains were used in this study: wild-type (N2), *cth-1(ok3319)V, daf-16 (mu86)I, mpst-3(tm4387)V, zcIs14[Pmyo-3::mitoGFP], F47G4.3(ok1558) I, K11H3.1(ok1733) III.* Worms were grown at 20 ºC on standard nematode growth medium (NGM) seeded with E. coli OP50-1 grown for 16 hours (37 ºC with shaking at 180 RPM)

as a food source. Worm maintenance was performed following standard techniques (68). 5-Fluoro-2′-deoxyuridine (FuDR) was not used in this study.

Cell lines

WT and $CSE^{-/-}$ Mouse Embryonic Fibroblasts (MEF) were grown in DMEM (4.5 g/L glucose) supplemented with 2 mM L-glutamine, 1% penicillin-streptomycin and 10% fetal bovine serum at 37°C and 5% CO_2. Human umbilical vein endothelial cells (HUVEC) were isolated and cultured as described (69) and cells up to passage 3 were used for the experiments. The use of human material in this study conforms to the principles outlined in the Declaration of Helsinki and the isolation of endothelial cells was approved in written form by the ethics committee. HEK293T cells were cultured in DMEM/F-12 supplemented with 10% fetal bovine serum, 100 U/mL penicillin-streptomycin and 0.01 mol/L HEPES.

Wistar Rats

Nine-month-old male and eight-week-old male and female Wistar rats were housed in the animal facility of the Institute for Biological Research “Sinisa Stankovic”, National Institute of the Republic of Serbia under the standard dark–light cycle (12 h light–12 h dark) and received commercial food and fresh water ad libitum. All experimental procedures were approved by the Ethics Committee of the Institute for Biological Research “Sinisa Stankovic” (App. No. 2-12/12 and No. 000169446 2024 14841 002 001 000 001) according to Directive 2010/63/EU. The animals were divided into two groups: control and ET-treated (20 mg/kg ET in drinking water for either 5 days or 3 weeks).

3.6.2. Method details

Origin of all chemicals are detailed in STAR METHODS. Buffers were prepared with Nanopure water and treated with Chelex-100 resins to remove traces of metal ions. All other experimental details are included either in the manuscript text, STAR METHODS or in the text that follows.

C. elegans experiments

C. elegans lifespan experiments

For lifespan experiments, worms were synchronized by picking several adults onto NGM plates and allowing them to lay eggs for 3h. Synchronized young adults (D0) were transferred to 35-mm plates containing a final concentration of 0.45 mM ET or vehicle plates containing the same volume of water. Treatment was added on top of the seeded plates, left to dry for a few hours and used on the same day. *For the experiments on dead bacteria, seeded plates were exposed to UV light for 10 min followed by the addition of the treatment. The efficacy of the killing protocol was checked by inoculating bacteria from UV-irradiated plates onto a fresh LB plate and incubating for 24 h at 37 ºC. Lack of bacterial colonies indicated efficient killing. Worms were grown on live bacteria until D0 and then transferred to treated plates with dead bacteria.* Each plate contained ~ 25 animals which were transferred every second day by picking and scored every day. Worms which crawled off the plate, contained bagged worms or vulva protrusion were censored. Death was scored as a failure to move in response to gentle prodding of animals with a platinum wire. Each lifespan experiment was repeated at least twice in a blinded manner.

For the automated lifespan experiments using Nemalife lifespan machine, worms were grown on regular NGM plates without treatment until D0. Young adults were washed with M9 and approximately 70 animals were loaded per microfluidic chip using syringe and blunt-end needle. Every day the chips were washed for 90 s with liquid NGM to remove progeny followed by 90 s recording of animals' survival and movement. Worms were then fed with 20 mg/mL OP50 in light NGM supplemented with the treatment or vehicle solution. Briefly, 30 µL of ET or Herc stock solutions in H_2O were mixed with 970 µL of concentrated OP50 to reach final concentrations of 5 mM treatment and 0.01% DMSO. Chips were stored in the incubator at 20 ºC. Survival counts were determined using the Nemalife analysis suite (Nemalife Inc., TX) as described previously. Briefly, 90-second recorded videos were segmented into three still-image frames (30s, 60s, 90s), with a bounding box automated around each animal. Animals were deemed alive if more than half their body length had displaced outside of the bounding box between two still-image intervals (i.e., > half body length displacement in the 90s vs 60s frame). Animals unable to move from the encompassing box across all three frames were deemed dead. All videos were manually corrected for any falsely implemented annotations made by the analysis software.

C. elegans thrashing rates

On the day of analysis, individual animals were picked into 10 µL of M9 buffer (3 g KH_2PO_4, 7.5 g Na_2HPO_4, 5 g NaCl, 1 mL 1 M $MgSO_4$, per L) on Superforst microscope slides (to avoid cuticle adhesion to slides) and were allowed to adapt to liquid environments for approximately 10 s. Thrashing rates were then counted for 20 s, with each full bend of the head and tail to one side marked as a count. Overall rates are displayed as thrashing counts per minute based on 20 s count.

C. elegans stress-assays

Worms were grown on treatment or vehicle plates from D0 of adulthood until the desired age for stress-assay tests. For paraquat stress assays, 1 mL of 250 mM paraquat solution in H_2O was added on top of seeded plates containing 3 mL of NGM (final concentration 62.5 mM) and were allowed to dry at room temperature (RT) for 4 hours. Worms were subsequently transferred to vehicle / paraquat plates, with survival monitored every hour until >80% of the population had died. For heat shock exposure, worms were transferred to fresh plates and incubated at 35 ^oC. Survival was scored every hour. For arsenite and H_2O_2 stress-assays, animals were picked into individual wells of a 96-well plate in 50 µL of M9 buffer. Freshly prepared stocks of sodium (meta) arsenite and H_2O_2 were dissolved in M9 buffer and prepared such that 50 µL of the solution was added to each well to a final volume of 100 µL at the indicated toxicant concentration (H_2O_2: 100 µM, arsenite: 5 mM at D4 and 2 mM at D10). Animals were assessed as being dead or alive by the presence or absence of a movement response to gentle tapping of the plates every hour.

C. elegance autofluorescence measurement

For live imaging, worms were picked by hand and placed in a drop of M9 buffer on a 2 % agarose pad. Imaging was performed using a Leica SP8 LIGHTNING Confocal Microscope and HC PL FLUOTAR 10X/0.30 air objective. The following excitation/emission settings were used: blue (405/460±25 nm), green (488/525±25nm), red (514/640±30 nm), in accordance with previous work (18). Acquired Z-stack images were load into ImageJ and compiled together with the Sum slices function. These images were then loaded into the Worm-align Bioformat in Fiji (70) to straighten all animals and perform fluorometric intensity analysis of the three respective autofluorescence

wavelengths. Brightness and contrast parameters were kept the same for all images within each fluorescent wavelength assessed. Worm-align was used to curate masks of each individual animal, and these metadata were uploaded into CellProfiler for quantification of fluorescence intensity of whole animals.

C. elegans mitochondrial imaging

SJ4103 animals were grown on vehicle or ET plates until D10. Worms were then picked by hand in a drop of M9 without any anaesthetic compounds (given their potent mitochondria-inhibiting properties) and carefully immobilized via cover slips. Recording was performed with an HC PL IRAPO 40 x/1.10 water objective and excitation/emission settings 488/520 ± 20 nm were used. Images of body-wall muscle cells were taken from both head and tail regions of each animal, avoiding vulval midbodies that exhibit frequent egg-laying induced tissue disruption. For morphological quantification, images were analyzed in Fiji using the Mosaic Suite SQUASSH (segmentation and quantification of subcellular shapes; *http://mosaic.mpi-cbg.de/*) as previously described (71). Image segmentation, to optimise computational annotations of mitochondrial networks and remove background interference, was performed in line with others (71): a background removal window size of 15 pixels, regularization of 0.07 and a minimum GFP fluorescence-intensity of 0.2. The SQUASSH plugin was then used to calculate individual mitochondrial size and perimeter, allowing the two-dimensional calculation of mitochondrial circularity: [circularity = $(4 \times \pi) \times (\text{Area}/\text{Perimeter}^2)$], fitting objects to a perfect circle and measuring its deviation from this where 1 = a perfect circle and 0 = a straight line. Data were then analyzed and presented as Gaussian distribution plots of mitochondrial circularity scores, using bins of 0.05 µm.

C. elegans Nile Red staining

D10 adults were collected and washed three times with PBST (PBS + 0.01% Tween). Worms were then fixed in 40% isopropanol for 3 min at RT while gently mixing. Traces of fixation solution were removed by two PBST washes and animals were immediately incubated in Nile Red staining solution following the protocol (72). Briefly, working solutions were prepared by adding 6 µl of Nile Red stock solution (0.05% in acetone) in 1 mL of 40% isopropanol. After 2 h of staining at RT in the dark, the solution was removed and worms were washed in PBST and mounted on glass slides. Images were recorded on a Leica SP8 LIGHTNING Confocal Microscope using an HC PL FLUOTAR 10X/0.30 air objective and excitation/emission wavelengths 488/588±27 nm.

C. elegans Oil Red staining

D10 adults were collected, washed two times with M9 and fixed in MRWB solution for 1 h at RT with occasional mixing. Worms were shortly centrifuged, supernatant was removed and pellet was washed 2 times with PBS + 0.1 % Triton X-100. Dehydration was performed by incubating worms in 60% isopropanol for 15 min. Worms were collected, supernatant removed and 600 µl of Oil Red working solution was added and incubated at 37 ^{o}C to stain the lipids. After 4 h, the dye was removed, and its excess was washed out 2 times for 30 min with PBS + 0.1 % Triton X-100. Worms were mounted on glass slides and recorded on a Leica DM6 B light microscope using HC PL FLUOTAR 10x/0.32 dry objective. Oil Red stock solution was prepared by dissolving 0.5 g of Oil Red O in 100 ml of isopropanol, while working solution was prepared by dilution of the stock solution with H_2O to reach 60% isopropanol. The working solution was then left to mix overnight at RT and it was filtered before the use.

C. elegans RNA sequencing

For RNA extraction, worms were synchronized by bleaching, and maintained as previously described with few modifications. Worms were transferred every day using M9 buffer. Animals were collected from plates and washed at least three times with M9 using gravity to remove bacteria and progeny. After the last wash, worms were spread over the treatment or vehicle plates. On the day of collection, 80 animals were transferred into a 1.5 ml tube, washed three times with M9 and excess buffer was removed. 500 µL of Trizol reagent was immediately added to the worm pellet and samples were flash frozen in liquid nitrogen. Samples were subjected to three freeze-thaw cycles (fast thawing in the water bath followed by 30 s vortexing and direct freezing in liquid nitrogen). After the third cycle, 200 µL of phenol/chloroform/ isoamyl alcohol mix (25/24/1, v/v/v) was added, samples were vigorously shaken by hand for 15 s, incubated for 2 min at RT and centrifuged at 12,000 x g for 15 min. The upper aqueous phase was carefully transferred to a new tube and mixed with an equal volume of 70% ethanol in RNAse free water. RNA purification was further performed using PureLink ® RNA Mini Kit following manufacturer's protocol. RNA quality and yield were checked using a NanoDrop spectrophotometer and immediately frozen at -80 ^{o}C. Sequencing was performed by the Beijing Genomic Institute (BGI, Hong Kong) using *DNBSEQ™ sequencing technology*. *High-quality adapter-free reads were directly mapped to the C. elegans reference genome (WBCel235) using HISAT2 v. 2.1.0* (73)*. Following duplicate removal, gene-level read assignments were performed with featureCounts v. 1.6.4* (74)*. Differential gene expression analysis was conducted using DESeq2 v. 1.42.1*(75)*.*

C. elegans persulfidome

For persulfidome analysis, worms were synchronized by bleaching. Isolated eggs were placed in M9 buffer and incubated for 14 h at 20 ºC with gentle shaking (130 rpm) to hatch. In order to have enough starting material and avoid starvation, worms were grown on 100-mm NGM plates (~ 1000 worms/plate) and transferred every day using M9 buffer. Plates were prepared by adding 1 mL of treatment or vehicle stock solution (10 mM aqueous ET solution) on top of the seeded plates (20 mL of NGM and 1 mL of *E. coli* OP50-1). The plates were left to dry overnight under the hood and used the day after. On the day of collection worms were collected into 15-mL falcons and washed at least three times to remove bacteria and progeny. After the last wash, M9 was removed and pellet corresponding to 150 µL was flash frozen in liquid N_2 and used for downstream analysis. Worm pellets were kept on ice and quickly defrosted by addition of 1 mL HEN lysis buffer (50 mM HEPES, 1 mM EDTA, 0.1 mM Neocuproine, 1% IGEPAL, 2% SDS, pH 7.4) supplemented with 10 mM NBF-Cl and 1% protease inhibitor prior to use. Suspension was mixed well and transferred to 15 mL Bioruptor® Pico Tubes (Diagenode, C30010017) containing 200 µL of glass beads. Samples were lysed by sonication in Biorputor Pico at +4 ºC. Lysates were incubated for 2 h at 37 ºC followed by centrifugation at 18,000 x *g* for 15 min at 4 ºC to remove debris. Proteins were precipitated twice by methanol/chloroform precipitation (water/methanol/chloroform, 4:4:1, v/v/v) and washed twice with ice-cold methanol. Pellets were dissolved in PBS supplemented with 0.2% SDS and equal amounts of protein were incubated with Pierce™ NeutrAvidin™ Agarose beads to remove endogenously biotinylated proteins. After 2 h of mixing at room temperature, supernatant was removed and precipitated once. Proteins were suspended in PBS supplemented with 2 % SDS and incubated for 1.5 h at 37 °C with 250 µM DCP-Bio1 to specifically label

persulfides. Excess probe was removed by precipitation and obtained pellets were dissolved in PBS supplemented with 0.1% SDS and adjusted to equal protein amount. Samples were then incubated for 4 h at RT with Pierce™ High-Capacity Streptavidin Agarose to enrich persulfidated proteins. Unbound proteins and detergent were removed by washing the beads with 28 mL of PBS and 8 mL of H_2O on Pierce™ disposable columns. Enriched proteins were eluted by incubating the beads with 2.25 M ammonium hydroxide solution for 16 h at RT. Eluates were then collected from the columns, lyophilized and subsequently dissolved in digestion buffer (50 mM ammonium bicarbonate (ABC), 1 mM $CaCl_2$). Trypsin was added at enzyme/protein ratio 1/20 and digestion was performed at 37 ^oC for 16 h. Samples were desalted using Oasis HLB cartridges (Waters, WAT094225). Peptides were dissolved in 0.1 % TFA, and quality control was performed using an Ultimate 3000 Nano Ultra High-Pressure Chromatography (UPLC) system with a PepSwift Monolithic® Trap 200 µm * 5 mm (Thermo Fisher Scientific).

Sample were analyzed by high-resolution LC-MS/MS using an Ultimate 3000 Nano Ultra High-Pressure Chromatography (UPLC) system (Thermo Fisher Scientific) coupled with an Orbitrap Eclipse™ Tribrid™ Mass Spectrometer via an EASY-spray (Thermo Fisher Scientific). Peptide separation was carried out with an Acclaim™ PepMap™ 100 C18 column (Thermo Fisher Scientific) using a 180 min gradient: 0 min, 3% B; 115 min, 28% B; 125 min, 35% B (solvent B corresponds to 84% acetonitrile, 0.1% formic acid) at a flow rate of 250 nL/min. The Orbitrap Eclipse™ was operated in a DDA mode and MS1 survey scans were acquired from m/z 300 to 1,500 at a resolution of 120,000 using the Orbitrap mode. The most intense ions were isolated for 3 s with a 1.2 m/z window and then fragmented by high-energy collision-induced dissociation (HCD) with a normalized

collision energy of 32%, considering a dynamic exclusion of 30 s. MS/MS spectra were recorded using normal speed IonTrap mode.

For full proteome analysis used to normalize persulfidome data, 150 µg of original NBF-Cl samples were diluted with PBS and precipitated to remove traces of SDS. Protein pellets were resuspended in 6 M guanidine hydrochloride (GuHCl) and 40 µg of protein was taken from each sample for further steps. Samples were diluted with digestion buffer to reach final concentration of 0.3 M GuHCl. All other steps were performed in the same way as abovementioned. Samples were analyzed using a 180 min gradient: 0 min, 3% B; 120 min, 30% B; 125 min, 35% B at a flow rate of 250 nL/min. All other parameters were the same as for persulfidome data except dynamic exclusion which was set at 40 s.

Data were evaluated in PEAKS ONLINE software using 15 ppm precursor mass error tolerance, 0.5 Da fragment mass error tolerance, specific trypsin digestion and maximum 3 missed cleavages. For persulfidation detection, NBF (+163.00961594 Da) on C, K, R, DCP (+168.0786442 Da) on C, N-term acetylation (+42.010565 Da), and methionine oxidation (+15.994915 Da) were added as variable modifications. PSM and proteins were filtered at FDR 1 %. Data was normalized in R studio using EigenMS (76). Total proteome data were normalized based on the total ion count (TIC).

C. elegans proteomics

D4 and D10 animals were collected (~ 200 worms/condition) as previously described. Worm pellets were defrosted by adding 40 µL of 7.5 M GuHCl in 50 mM ABC. Samples were boiled for 5 min at 95 °C, left to cool down and then sonicated in Biorputor Pico at +4 ºC in the presence of glass extraction beads. Debris was removed by centrifugation at 20,000 x *g* for 10 min at 4 °C. Protein content was determined and 40 µg of protein was taken for further processing. Samples were reduced with 5 mM DTT for 1

h at 37 °C, shaking at 300 rpm and then alkylated for 30 min in the presence of 20 mM idoacetamide. Digestion and desalting steps were performed as previously described. After quality control, peptides were analyzed by high-resolution LC-MS/MS using an Ultimate 3000 Nano Ultra High-Pressure Chromatography (UPLC) system (Thermo Fisher Scientific) coupled to a timsTOF Pro (Bruker) equipped with a CaptiveSpray source. Peptide separation was carried out with an Acclaim™ PepMap™ 100 C18 column (Thermo Fisher Scientific) using a 95 min linear gradient from 3 to 38 % of B (84% Acetonitrile, 0.1% Formic Acid) at a flow rate of 400 nL/min. The timsTOF Pro2 (Bruker) was operated in PASEF mode using Compass Hystar 5.0.36.0. The TIMS setting was as follows: Mass Range 100 to 1700 m/z, 1/K0 Start 1.6 Vs/cm^2 End 1.6 Vs/cm^2, Ramp time 100 ms, Lock Duty Cycle to 100%, Capillary Voltage 1500 V, Dry Gas 3 L/min, Dry Temp 180°C. PASEF settings: 10 MS/MS scans, charge range 0-5, active exclusion for 0.4 min, Scheduling Target intensity 20000, Intensity threshold 2500, CID collision energy 49 eV. Data were evaluated with PEAKS ONLINE software using 15 ppm for precursor mass tolerance, 0.5 Da for fragment mass tolerance, specific trypsin digestion, and a maximum of 2 missed cleavages. Carbamidomethylation (+57.021464 Da) on C, N-term acetylation (+42.010565 Da), and methionine oxidation (+15.994915 Da) were added as variable modifications, PSM and proteins were filtered at FDR 1 %. Data was normalized based on the total ion count (TIC).

MALDI imaging of C. elegans

Ergothioneine standard (10 mM) was mixed 1:2 (v/v) ratio with CHCA matrix (10 mg/ml in 70:30 CH_3OH/H_2O + 0.2% TFA) and spotted onto a stainless-steel plate for MALDI analysis by dried droplet method. MALDI analysis was then carried out using the parameters stated below, with confirmatory MS/MS also performed on standards at

normalised collision energy 15, with isolation mass m/z 230. D4 N2 and *cth-1* worms were collected in M9 and washed 5 times with 1 mL of H_2O to clean animals from bacteria and remove salts from buffer solution. Worms were pipetted onto glass slides in 20 µL of H_2O and immediately dried under vacuum to remove residual water from the slide before matrix spraying. CHCA matrix (5 mg/mL in 80% Methanol + 0.2% TFA) was applied to the sample using a Sunchrom SunCollect pneumatic sprayer. Matrix was applied in 10 layers using 1st layer at 10 µL/min, 2nd layer at 20 µL/min and 3rd layer plus at 30µL/min at a speed of 'Low 10' (775 mm/s) for the x-axis and 'Medium 1' (850 mm/s) for the y-axis. Gas pressure was set to 2.8 bar and z-height at 10 mm. MSI experiments were performed on an Orbitrap QExactive HF mass spectrometer (Thermo Fisher Scientific GmbH, Bremen, Germany) coupled to an elevated pressure MALDI ion source (Spectroglyph LLC, Kennewick, WA, USA). The 349-nm MALDI laser was operated at a repetition rate of 500 Hz and pulse energy of ~2 µJ. The laser was focused to a spot size of 20 µm and the pixel sizes for analyses were 25x25µm for the worms. The high-pressure funnel (HPF) and low-pressure funnel (LPF) were operated at 98 Vpp and 75 Vpp, respectively, using 720 kHz and 825 kHz respectively. The high-pressure funnel region was held at 7 Torr for analysis. The mass spectrometer was operated in positive mode with AGC mode turned off. Resolution was set at 120,000 for m/z 200 with a mass range of m/z 50 to 600 and a set inject time of 250 ms was used, resulting in 125 shots/pixel. Instrument calibration was performed with ESI and using Thermo Pierce Calmix. Complimentary microscopy images were captured using brightfield Keyence VHX-7000N. Serial stitched images were performed using the 200x magnification.

Preliminary images were viewed in ImageInsight (Spectroglyph) and MSI processing was further performed in LipostarMSI (Molecular Horizons). Thermo RAW

(.raw) and positional files (.xml) were converted to imzML files using the built-in converter for LipostarMSI, which utilises msconvert from ProteoWizard (3.0.22317) for initial conversion to mzML format. The imzML file was then loaded into LipostarMSI using the following parameters: 5 ppm m/z tolerance, peak intensity >1%, peak detection frequency >1% and minimum spatial chaos >0.7. Hotspot removal was applied using the 99% quantile and no denoising was applied.

Detection of 4-HNE protein adducts in aged C. elegans

Worm NBF-Cl lysates were used for detection of 4-hydroxinonenal protein adducts (4-HNE). Equal protein amounts were loaded onto 10% polyacrylamide gels, resolved by SDS-PAGE and transferred to a nitrocellulose membrane. After 1 h of blocking in 5% BSA in TBST (TBS + 0.1% Tween), membranes were incubated with anti-4-HNE antibody (1:1000 in 1% BSA in TBST) overnight at +4 ^{o}C. Membranes were then washed five times with TBST and incubated for 1.5 h with secondary anti-rabbit AF680 antibody (1:20 000, 1% BSA in TBST). Levels of 4-HNE (IR short filter, 680 nm) and total protein amount (Cy2 filter, 488 nm) were visualized using Amersham Typhoon imager (Cytiva), with 4-HNE intensities normalized to total protein load.

NAD^+ measurement in C. elegans

50 animals were hand-picked into a 1.5 ml tube and washed 3 times with M9. After the last wash, worms were kept in 30 µl of M9, immediately frozen in liquid nitrogen and stored at -80 ^{o}C until all samples were collected. Once defrosted, mixtures of 60 µl 0.2 M NaOH + 1 % dodecyltrimethylammonium bromide (DTAB) and 30 µl of M9 was added to each sample (final sample volume was 120 µl). 20 µl of glass beads was quickly added to the tubes and the samples were sonicated in Bioruptor at +4 ^{o}C (5 cycles, 1 cycle: 30 s

on, 30 s off). Lysates were then centrifuged at 15 000 x g for 10 min at *+4 ºC, and the supernatant was used for quantification of NAD⁺ using the NAD/NADH-Glo™ assay kit, following the manufacturer's protocol. Samples were incubated with the kits Glo-reporter for 60 min at RT, and luminescence was recorded on a* CLARIOstar Plus plate reader (BMG LABTECH; Ultra-Glo, 540-50nm).

Cell experiments

Temperature range thermal proteome profiling (TPP)

MEF cells were grown until 90% confluency and then incubated with 400 µM ET (or vehicle control) for 4 h. TPP was performed using the previously described method (27). Briefly, cells were trypsinized and centrifuged at 300 x g for 3 min. Cell pellets were washed twice with PBS at RT and resuspended in 600 µl of PBS. 100-µL aliquots were added into 0.2-mL PCR tubes and cells were then exposed to 10 different temperatures (25, 37.4, 40.4, 43, 45.7, 48.7, 52.5, 55.5, 58.2, 60.9, 63.8 °C) for 5 min. Samples were cooled down in a water bath at 25 °C for 5 min and then lysed in 100 µl of PBS with 0.1% NP40 by three freeze-thaw cycles. Lysates were ultracentrifuged for 20 min at 100 000 x g, and the supernatant was collected. Reduction and alkylation were carried out by first incubating the samples with 1 mM DTT for 1 h at 37 °C followed by 30 min incubation at 37 °C with 5 mM iodoacetamide. Samples were diluted to 0.3 M GuHCl using ABC buffer and digested with a 1:20 trypsin ratio. Desalted peptides were resuspended in 100 mM triethylammonium bicarbonate (TEAB) and labeled using TMT10plex™ Isobaric Label Reagents following the manufacturer's protocol. After quenching the reaction with 0.4% of hydroxylamine, samples were desalted and dried. Remaining traces of detergent were removed on Detergent Removal Spin columns (Thermo Scientific, Cat# 87777) and peptide quality control was carried out as previously described. Samples were fractionated

using Pierce™ High pH Reversed-Phase Peptide Fractionation Kit (Thermo Scientific, Cat# 84868) to increase protein identification and coverage.

Fractions were analyzed by high-resolution LC-MS/MS using a Dionex UltiMate 3000 RSLC Systems (RSLC) system (Thermo Fisher Scientific) coupled with an Orbitrap Eclipse™ Tribrid™ Mass Spectrometer via an EASY-spray (Thermo Fisher Scientific). Peptide separation was performed with an Acclaim™ PepMap™ 100 C18 column (Thermo Fisher Scientific) using a 120min non-linear gradient (Fraction 1: 0 min, 3% B; 120 min, 35 % B; F2, F3, F4, F5: 0 min, 3 % B; 5 min, 9 % B; 120 min, 35 % B; F6, F7: 0 min, 3 % B; 5 min, 11 % B; 120 min, 35 % B; F8: 0 min, 3 % B; 8 min, 15 % B; 120 min, 35 % B) at a flow rate of 250 nL/min. The Orbitrap Eclipse™ was operated in a DDA mode, and MS1 survey scans were acquired from m/z 300 to 1,500 at a resolution of 120,000 using the Orbitrap mode. MS2 scans were carried out for 3 seconds with high-energy collision-induced dissociation (HCD) at 32 % using the Orbitrap mode at a resolution of 50,000.

Thermo ".Raw" files were converted into mzML files using proteowizard tool (77). The search was performed using Fragpipe's (78) pre-built TMT 10 workflow. Briefly, 20 ppm was used for the precursor and the fragment mass tolerance. Enzymatic cleavage was set for trypsin and 2 missed cleavages. TMT precursor mass (+ 229.16293 Da) on K and peptide N-terminus as well as carbamidomethylation (+ 57.02146 Da) on C residue were used as fixed modifications. Oxidation (+15.9949 Da) on M residue and N-terminal acetylation (+42.0106 Da) were set as variable modifications. PSM and proteins were filtered using FDR 1 %. No normalization was applied in Fragpipe. Data analysis was then performed using the computational workflow InflectSSP (79) on Rstudio providing

normalization of protein abundancies, curve fitting function, p-value and FDR adjusted p-value for comparison between ET and vehicle-exposed cells.

Intracellular H_2S imaging

WT and $CSE^{-/-}$ MEF cells were plated in an 8-well chambered coverslip (IBIDI) at 20 000 cells per well, stained with fluorescent sensor SF7-AM as described previously (80) and treated according to the experimental set up. Following treatment, cells were incubated with 1 µM Hoechst in DMEM for 20 min and the media was then replaced with phenol red-free DMEM. All images were acquired using 20 ms exposure, 5% laser intensity and excitation/emission 488/525 nm for SF7-AM and 200 ms exposure, 20% laser intensity and excitation/emission 405/450 nm for Hoechst. Images were acquired using a Zyla 4.2 PLUS sCMOS camera attached to an Andor DragonFly 500 confocal spinning disk mounted on a Nikon Eclipse TiE microscope using a CFI Plan Apochormat lambda 100X oil immersion objective. Images were analyzed using Fiji ImageJ. The image processing workflow was automated using the following novel Fiji ImageJ macro scripts written by Dr Roy Chowdury in Dr Julien Prudent's laboratory (MRC Mitochondrial Biology Unit, University of Cambridge, Cambridge, UK). The integrated density of 10-50 cells per replicate was used to quantify fluorescence intensity.

MEF cell proliferation

MEF cells were seeded at a density of 2,500 cells/well in a 96-well plate in full medium and left overnight to attach. The next day, in order to remove traces of cysteine, wells were washed twice with non-cysteine containing media. Cells were then incubated with media supplemented with 10% FCS, standard concentration of methionine and different concentration of L-cystine (0 – 200 µM) and ET (0 – 400 µM) for 20 h. Media was

removed and MTT reagent, diluted in media, was added to the wells and incubated for 3 h. Crystals formed on the cell surfaces were dissolved in isopropanol supplemented with 4 mM HCl and 0.1% NP40. Absorbance was measured at 562 nm using Multiscan FC Microplate Photometer (Thermo Scientific).

Cell survival assays

10,000-20,000 cells were seeded per well in 96-well plate and treated according to the experimental design. Following defined treatment, cells were exposed to MTT reagent as described.

Measurement of lipid peroxidation using C11-BODIPY (581/591)

MEF WT cells were treated with different concentrations of ET for 24 h and then exposed to 1 μM RSL3 for 3 h. Further steps were performed as previously described (81). Sample acquisition was performed on a Cytek Biosciences Aurora 5L spectral flow cytometer. Median fluorescence intensity of the raw data channel B2-A (525/17 nm) was extracted and further analyzed.

HUVEC cell cycle monitoring

HEK293T cells were plated in a density of 40,000 cells/cm^2 and 24 h later were co-transfected with psPAX2, (Addgene plasmid #12260), pMD2.G (Addgene plasmid #12259) and the target plasmids (Cdt-mKO and Geminin-GFP, Riken) in the presence of polyethylamine (1 μg/μL, Sigma). Supernatant containing viral particles were collected 72 and 96 h after transfection, filtered through a 0.45 μm filter and stored in -80 ^{o}C until use. HUVECs were transduced for 24 hours with 1:1 ECGM-2: Viral volumes in the presence of 8 μg/ml polybrene (Santa Cruz). After transduction, cells were seeded in 96

well plates at a density of 4,000 cells per well and monitored under a live cell imaging system (Incucyte S3, Sartorius)

HUVEC proliferation

HUVEC were seeded onto 24 well plates (Sarstedt, Germany) at a density of 15,000 cells/well. Cells were treated with control siRNA (50 pmol) or siRNA directed against CSE (50 pmol, custome synthesis, Eurogentec) using Lipofectamine RNAiMAX (Invitrogen, Karlsruhe, Germany) for 72 h prior to experimentation. 16 images/well at magnification × 10 were taken every 4 h using an IncuCyte S3 live-cell analysis system (Essen BioScience, United Kingdom). Cell confluence was measured for up to 4 days. Image processing and analysis were performed using the following parameters: segmentation adjustment 1.8; clean up: hole fill 0 μm2; adjust size (pixels): 0; filter: minimum 350 μm2 area, no maximum, eccentricity: no minimum, no maximum.

Sprouting

The spheroid sprouting assay was performed as previously described (82). At least five spheroids per group were analyzed for each cell batch.

NAD^+ measurement in cells

MEF WT cells were grown in 96-well plates and treated with different concentrations of ET for 18 h. Treatment was removed and ice-cold 1:1 mixture of PBS and *0.2 M NaOH + 1 % DTAB (135 µl) was added to each well. Plate was shaken in orbital shaker at 300 rpm for 3 min to enable homogeneous cell lysis.*

^1H NMR detection of ET in cell extracts

MEF WT and $CSE^{-/-}$ cells were grown in 100-mm dishes and treated for 16 h with 200 µM ET. On the next day (90% confluent cells), treatment was removed, and cells were washed twice with ice-cold PBS. The dish was quickly placed into a liquid nitrogen bath and incubated for 2 min. The plate was then moved to ice, 1.5 ml of ice-cold absolute methanol was added, and cells were thoroughly scraped and collected into 15 ml Bioruptor® Pico tubes. Lysates were sonicated in Bioruptor Pico at +4 ºC (5 cycles, 1 cycle: 30 s on, 30 s off) followed by centrifugation at 18,000 x g for 10 min. The supernatant was carefully removed and evaporated dry in a SpeedVac, retaining and utilizing protein pellets for normalization of sample amounts. Shortly, the pellets were dissolved in 50 mM HEPES supplemented with 2% SDS and protein concentration was determined using DC protein assay.

Samples were prepared for NMR analysis by dissolving the samples in 600 µL D_2O. Additionally a 1 mM solution of 3-(Trimethylsilyl) propionic-2,2,3,3-d_4 acid (TMSP-d_4) was added as internal standard and transferred to a 5 mm borosilicate NMR tube. The software TopSpin 3.6.5. was used for the signal acquisition and processing of the NMR spectra. All measurements were performed at 7 °C. For signal acquisition, a double watergate pulse sequence with excitation sculpting for water suppression was used to acquire the 1H NMR spectra. A relaxation delay of 5 s was selected. The radio frequency power of 62.5 kHz was used to perform the µ and µ/2 pulses which were combined with 2 ms selective rectangular shape pulses to efficiently suppress the 1H resonance of the H_2O. The latter was chosen as the transmitter frequency (O1). Signal accumulation was achieved by 512 scans for each spectrum with an acquisition time of 1.7 s. The data were processed by using Fourier transformation, zero and first order phase correction, automatic baseline correction and by applying a 0.3 Hz line broadening using a Lorentzian window function.

For an absolute concentration determination ERETIC2 reference was used (83,84). To calibrate an ERETIC reference a 10 mmol/L sucrose solution was used as a calibration compound. Based on the sucrose refence, an electronic signal was placed in each NMR spectrum and the signal corresponding to the calibration compound was integrated and normalized according to the number of protons of this compound (85).

Metabolic analysis of metabolites from transsulfuration pathway

MEF WT cells were grown in 60-mm dishes and treated or not with 400 μM ET for 2h in full medium. Cells were washed two times with warm PBS and collected by trypsinization. Trypsin was quenched, cells were centrifuged for 5 min at 300 x g, washed two more times with PBS and cell pellets were frozen in liquid nitrogen. Metabolites were extracted by addition of 350 μL of ice-cold methanol supplemented with 0.1 % formic acid and 5 mM TCEP. The cell lysate was sonicated in Bioruptor Pico at +4 ºC and vortexed to improve metabolite extraction. Samples were then centrifuged at 15000 rpm for 30 min at 4 ºC, supernatants were collected and dried in SpeedVac. The protein concentrations were measured from the pellets using BCA assay and used for post-acquisition data normalization. Dried extracts were dissolved in 80 μL of borate buffer and 20 μL of AQC reagent was added to derivatize amino acids. Samples were incubated for 1 min at RT followed by incubation at 55 ºC for 10 min. The reaction mixtures were cooled on ice and transferred to clean autosampler inserts for LC-MS/MS analysis.

LC-MS/MS analysis of derivatized amino acids

Amino acid-AQC derivatives were identified and quantified using liquid chromatography (Vanquish Duo UHPLC; Thermo Fisher Scientific, Waltham, MA, USA) coupled with Orbitrap Fusion Lumos Tribrid Mass Spectrometer (Thermo Fisher Scientific,

Waltham, MA, USA). Briefly, 3 µL of the final reaction mixture was injected and separated using a reversed-phase AccQ·Tag Ultra C18 (1.7 µm, 2.1 × 100 mm; Waters Corporation, Milford, USA) column with a flow rate of 0.4 mL/min. The binary solvent system consists of mobile phase A (water) and mobile phase B (ACN) both buffered with 0.1% formic acid. The elution gradient conditions were as follows: 0.1 % B, 0–0.54min; 9.1 % B, 5.74 min; 21.2 % B, 7.74 min; 90 % B, 10 min; 90 % B, 12 min; 0.1% B, 12.5–18 min (86). The MS datasets were acquired in positive-ion mode within the mass range of 65–850 m/z. The optimized heated electrospray ionization (HESI) source and data-dependent acquisition parameters were used as described earlier (87). Precursor ion m/z, retention time, and fragmentation pattern of the amino acid-AQC derivatives were established and verified using authentic metabolite standards of cysteine (292.0751 m/z, 5.16 min) and homocysteine (306.0907 m/z, 6.13 min). Whereas, accurate mass (≤ 3 ppm) and diagnostic fragment ion (171.0547 m/z) were used to confirm the cystathionine-AQC derivative (563.1707 m/z, 5.94 min). In cell extracts, amino acid-AQC derivatives were identified and quantified according to the precursor ion m/z, retention time, and diagnostic fragment ions. Chromatogram and mass spectral data were processed to obtain peak area values using the Quan Browser application in Xcalibur software (Thermo Fisher Scientific). The final quantitative results were normalized to the protein concentrations and relative changes across the samples were expressed as arbitrary units.

Persulfidation detection in cell lysates

MEF WT cells were grown in T75 flask and lyzed under native conditions at 90% confluency. After two washes with cold PBS, 1 ml of RIPA buffer (50 mM Tris, 150 mM $NaCl_2$, 2 mM EDTA, 1 % IGEPAL, 0.5 % sodium deoxycholate, 0.1 % SDS, pH 7.4) was

added. Cells were gently scraped, lysate was collected and additionally homogenized with syringe and needle. Insoluble parts were removed by centrifugation at 20,000 x g for 10 min at +4 ^{o}C and protein concentration was measured. Lysates were then split into 3 tubes: CON (without ET and SDS), ET (with ET without SDS) and ET+SDS (with both ET and SDS). 20% SDS solution was added to the ET+SDS tube to reach 2%, and the same volume of H_2O was added to the other two tubes. ET (final concentration 400 µM) or H_2O were then added to corresponding tubes. After 30 min incubation at RT, SDS was quickly added to non-SDS-containing tubes to denature the proteins and lysates were blocked with 5 mM NBF-Cl for 1 h at 37 ^{o}C. Samples were precipitated by methanol/chloroform precipitation and the pellets were washed as described. Proteins were suspended in HEPES + 2 % SDS, adjusted and switched to selectively label persulfides using Dimedone Switch method (26). The same protein amounts were mixed with Laemmli 4X buffer supplemented with 10% β-mercaptoethanol. Samples were boiled for 5 min at 95 ^{o}C and resolved by SDS-PAGE. Gels were recorded on Amersham Typhoon at 635 nm for Cy5, and 488 nm for NBF-Cl signal which was used as a loading control.

Bioenergetic Analysis by XF24e Analyzer

Oxygen consumption rate (OCR), as an indicator of cellular respiration, and extracellular acidification rate (ECAR), as an indicator of lactate and bicarbonate production, were determined simultaneously using an XF2e Analyzer (88). WT or $CSE^{-/-}$ MEFs were plated at a density of 7.5×10^4 cells per well in a 24-well XF V7 plate (BD Bioscience), incubated overnight in the presence or absence of ET, washed, resuspended in appropriate assay medium and analyzed. OCR and ECAR were reported as an average of three differential absolute rates (pmoles/min for OCR and mpH/min for ECAR). All experiments were repeated at least three times. Modulators used for Seahorse

measurements were provided by Sigma-Aldrich, MO, USA. Parameters of the mitochondrial respiration were evaluated in the assay medium consisting of bicarbonate-free DMEM (SeaHorse Bioscience) supplemented with 25 mM glucose, 1 mM pyruvate, and 2 mM glutamine. Mitochondrial respiration was monitored in the basal state and after sequential injections of the mitochondrial modulators oligomycin (1 μM), 2,4-dinitrophenylhydrazine (DNP, 100 μM), and antimycin (ANT)/rotenone (ROT); 1 μM both). Glycolytic activity is estimated in the assay medium and the base medium without any exogenous fuel substrate supplementation. ECAR values were estimated in the basal state and after sequential injections of 10 mM glucose, oligomycin (1 mM), 2-deoxyglucose (2-DG; 100 mM).

Intracellular CoQ redox state

The CoQ redox state was determined by mass-spectrometry as described previously (89). WT and $CSE^{-/-}$ MEF cells (1 x 10^6 cells / plate) were washed rapidly with cold PBS twice and then scraped into 200 μL PBS, added to a mixture of 300 μL acidified methanol (0.1% (w/v) HCl) and 250 μL hexane and vortexed to extract CoQ. The hexane phase was separated by centrifugation at 17,000 × g for 5 min. The hexane (top) layer was transferred into MS vials and dried under the stream of nitrogen. The crude residue from samples was resuspended in 200 μL methanol containing 2 mM ammonium formate, overlaid with Argon and analysed by LC-MS/MS using an I-Class Acquity LC system attached to a Xevo TQ-S triple quadrupole mass spectrometer (Waters). Samples were stored in a refrigerated autosampler (8 °C) and 2 μL sample was injected into a 15 μL flowthrough needle and separated by RP-HPLC at 45 °C using an Acquity C18 column (2.1 × 50 mm, 1.7 μM; Waters). The isocratic mobile phase was 2 mM ammonium formate in methanol used at 0.8 mL/min over 5 min. The mass spectrometer was operated in

positive ion mode with multiple reaction monitoring. The following settings were used for electrospray ionisation in positive ion mode: capillary voltage – 1.7 kV; cone voltage – 30 V; ion source temperature –100 °C; collision energy – 22 V. Nitrogen and argon were used as curtain and collision gases, respectively. Transitions used for quantification were: UQ9, 812.9 > 197.2; UQ9H2, 814.9 > 197.2. Samples were quantified using MassLynx 4.1 software to determine the peak area for UQ9 and UQ9H2

Biochemical experiments

Measurement of CSE-catalyzed H_2S production from ET

The experiment was performed following previously described procedures with small modifications (30). Briefly, 100 mM HEPES (pH 7.4), 0.4 mM lead acetate, 9 µg of CSE and different combinations of substrates were mixed in a final volume of 1 mL. Reactions were recorded on an Agilent Cary 8454 UV-VIS Spectrophotometer (Agilent Technologies) for 5 min at 37 ^{o}C, where an increase of absorbance at 390 nm directly corresponded to H_2S production and lead sulfide formation. H_2S concentration was calculated using molar extinction coefficient for lead sulfide determined for this experimental design (8178 M^{-1} cm^{-1}).

Michaelis-Menten kinetics of human recombinant CSE with ET

The kinetics of H_2S release was continuously monitored by formation of lead sulfide as described above. Since we observed that the solution of 0.4 mM lead acetate in 100 mM HEPES (pH 7.4) is not stable unless cysteine is present (milky white opalescence is formed within minute), which prevented us from directly measuring the reaction of ET and CSE, we opted for establishing those kinetic parameters indirectly using competitive two-substrate equation and the equimolar mixture of ET and cysteine. Knowing the actual

concentration of ET and cysteine and by separately establishing the K_m and V_{max} for cysteine as a substrate, we could estimate the Michaelis-Menten kinetic parameters for the reaction of ET with CSE.

Measurement of ET desulfuration in presence of CSE

Purified CSE (10 µg/mL) in 100 mM HEPES (pH 7.4) was mixed with 1 mM ET and the reaction mixture was incubated at 37 ºC. Every minute, an aliquot was taken and immediately combined with 1 mM NBF-Cl solution and 2% SDS in the same buffer. After 30 min at 37 ºC, the solution was transferred to a 1-cm cuvette and recorded on UV-Vis spectrophotometer. ET concentration for each time point was calculated based on the standard curve including different ET concentrations.

LC-MS detection of CSE-catalyzed hercynine formation

100 µM ET was mixed with 1.5 µg of CSE and incubated in 50 mM HEPES for 10 min at RT. Every minute, aliquot was taken and mixed with ACN (1:1, v/v). LC/MS analysis was performed on I-Class ACQUITY UPLC system (Waters) coupled with Waters Xevo TQ-S Mass Spectrometer. The binary solvent system consisted of solvent A (5% ACN, 0.1% formic acid) and solvent B (90% ACN, 0.1% formic acid). Samples were separated on I-Class ACQUITY UPLC BEH C18 column (1 x 50 mm, 130 Å, 1.7 µm, Waters) using the following gradient: 0-1 min, 5% B; 3-4 min, 50% B; 6-8 min, 100% B; 8-15 min, 5% B. The MS datasets were required in positive ion mode.

NMR Spectroscopy of PLP and ET reaction

1H NMR measurements were performed on a Bruker Avance III HD spectrometer operating at 400 MHz. The 1H NMR spectra of pure PLP and ET in D2O were used to identify the product in the studied sample. It is worth mentioning, that -NH aromatic

protons of ET were not observable under those conditions. In order to monitor reaction over time, 1H NMR spectrum of equimolar PLP-ET mixture was recorded every 1 h at 298 K.

UV-Vis spectra of PLP and ET reaction

100 mM HEPES (pH 7.4), 1.5 mM ET and 150 µM PLP were mixed in a final volume of 1 mL and the reaction was conducted at RT. UV-Vis spectra were recorded every minute for total of 3 h and the product formation was monitored at 333 nm.

ESI-TOF MS monitoring of PLP or CSE reaction with ET

Mass spectrometry was performed on maXis 5G, Bruker Daltonic (Bremen, Germany), an ESI-TOF MS capable of resolution of at least 40,000 FWHM.

Measurement of GPDH activity

Glycerol-3-phosphate dehydrogenase (GPDH) from rabbit muscle was diluted in 50 mM HEPES (pH 7.4) to reach a final concentration of 13.3 nM (0.5 ng / µL) and added into black 96-well plate. Sodium disulfide (Na_2S_2) was dissolved in ultrapure H_2O just before use and quickly added in 1:0, 1:0.1, 1:1 and 1:5 enzyme to Na_2S_2 ratio. Dihydroxyacetone phosphate (DHP) was then added to a final concentration of 0.4 mM and a reaction volume of 100 µL. Detection was performed in a CLARIOstar Plus plate reader (BMG LABTECH) and recorded for 5 min at 37 ^oC before NADH (0.2 mM final) was injected by the machine to initiate the reaction. A decrease in fluorescence corresponding to consumption of NADH was monitored using a monochromator with excitation/emission wavelengths of 355 ± 20/455 ± 30 nm, respectively.

Detection of GPDH persulfidation by MS

GPDH from rabbit muscle was cleaned on Bio-Spin® P-6 Gel columns to remove traces of original storage solution. Concentrated protein was further diluted with 50 mM TRIS pH 7.4 to reach a concentration of 1.15 mg/mL. 15 µg of protein was used for each condition (final concentration in reaction was 26.6 µM). The same volume of different

Na_2S_2 stock solutions (freshly dissolved in ultrapure H_2O) was added to reach different protein to Na_2S_2 ratios (1:0, 1:1, 1:2, 1:5, 1:10). The mixture was incubated for 15 min at 37 ^oC and immediately quenched with iodoacetamide (100 times excess compared to the highest concentration of Na_2S_2). Proteins were then desaturated by the addition of 7 M GuHCl in 50 mM ABC to reach a final concentration of 3 M. Samples were incubated for 30 min in the dark and then diluted 6 times with 50 mM ABC supplemented with 1 mM $CaCl_2$. Trypsin was added at a 1:20 ratio (0.75 µg) and incubated for 16 h at 37 ^oC. Samples were further processed for LC/MS measurement as described. Sample were analyzed by high-resolution LC-MS/MS using an Ultimate 3000 Nano Ultra High-Pressure Chromatography (UPLC) system (Thermo Fisher Scientific) coupled with an Orbitrap Q Exactive HF Mass Spectrometer via an EASY-spray (Thermo Fisher Scientific). Peptide separation was carried out with an Acclaim™ PepMap™ 100 C18 column (Thermo Fisher Scientific) using a 150 min gradient: 0 min, 3% B; 95 min, 35% (solvent B corresponds to 84 % acetonitrile, 0.1% formic acid) at a flow rate of 250 nL/min. The Orbitrap Q Exactive was operated in a DDA mode and MS1 survey scans were acquired from m/z 300 to 1,500 at a resolution of 60,000 using the Orbitrap mode. The top 15 most intense ions were isolated with a 1.6 m/z window and then fragmented by HCD with a normalized collision energy of 32%, considering a dynamic exclusion of 12 s. Search against the sequence of rabbit cGPDH was performed in PEAKS ONLINE using described parameters and following variable modifications: carbamidomethylation (+ 57.02146 Da) on C residue, S-carbamidomethylation on C (89.086464), oxidation (+15.9949 Da) on M residue and N-terminal acetylation (+42.0106 Da).

Experiments with rats

Endurance test using treadmill apparatus

Treadmill apparatus for small experimental animals (NeuroSciLaBG-Treadmill, Elunit, Belgrade, Serbia) used in this study comprised of a single moving belt and four plexiglass-separated running compartments. To encourage rats to engage in running, each running compartment featured an electrified metal grid with a low-intensity electric shock (0.2 mA) positioned at the starting edge as negative stimulation, alongside a dark area at the ending edge serving as positive stimulation. Rats were positioned on the moving belt and directed to run in the opposite direction to the belt movement, toward the positive stimulation, while avoiding the negative stimulation. Moreover, using accompanying software, a predetermined protocol for belt movement (duration and speed), as well as belt inclination, was established beforehand. Throughout the entirety of the treadmill protocol, the belt remained at a 0° incline. Prior to endurance tests, rats underwent a period of adaptation and familiarization with the treadmill apparatus over three consecutive days (20 minutes per day, belt speed: 10 m/min). For endurance testing, the initial belt speed was set at 5 m/min for 5 minutes. Subsequently, the speed was incrementally increased by 1 m/min every minute until reaching 21 m/min, where it remained constant. The rats underwent treadmill running until they exhibited signs of exhaustion. Exhaustion was characterized by the rat remaining seated on the metal grid shocker plate for more than 10 seconds without showing any signs of attempting to resume running. The recorded test parameters for each rat were the time to exhaustion in minutes, as well as the total distance covered during the run in meters.

Blood and tissue collection

Animals were euthanized by decapitation. Blood and quadriceps muscle samples were collected and routinely processed for biochemical, microscopic and immunoassays. The relative mass of gastrocnemius muscles was calculated as ratio of muscle/total body weight (mg/mg body weight).

Biochemical serum analysis

After blood isolation, serum was prepared and stored at −80°C until further analysis. Lactate in serum was determined fluorometrically (Shimadzu UV-160 spectrophotometer, Kyoto, Japan) using L-Lactate Assay kit.

Metabolite detection in rat muscle

Detection of different metabolites in rat muscle tissue was performed using commercially available kits. Sample homogenization and metabolite detection was done following the manufacturer's protocol for each metabolite of interest. Oxaloacetate, pyruvate, Gro3P and lactate levels were determined using corresponding kits from Sigma Aldrich. $NADP^+$, NADPH, and NAD^+, NADH abundances were measured using NADP/NADPH-Glo™ and NAD^+/NADH-Glo™ kits from Promega.

Immunoblotting

Homogenates of skeletal rat muscle were prepared in sucrose buffer containing protease and phosphatase inhibitors. Protein content in the samples was estimated by the method of Lowry et al. (90). 10 or 20 µg of total protein extracts were separated by SDS-PAGE and transferred onto polyvinylidene fluoride (PVDF) membranes (10600023, GE Healthcare Life Sciences). After 1 h of blocking in 5% BSA, membranes were incubated overnight with primary antibody followed by incubation with an appropriate

secondary antibody. Antigen detection was performed by an enhanced chemiluminescence detection system using an iBright CL1500 Imaging System (Thermo Fisher Scientific). The following primary antibodies were used in this study: anti-vinculin, anti-CSE (1:500), anti-GAPDH, anti-phospho S6, anti-S6, anti-TOM20 (1:1000), anti-VEGFR (1:1000), anti-SIRT1 (1:1000), anti-PGC-1α (1:1000) and β-tubulin (1:2000). HRP-conjugated secondary antibodies were used at following ratios: anti-rabbit (1:20000) and anti-mouse (1:2000). Lysine acetylation levels in rat NBF-Cl samples were detected using anti-Ac-Lysine antibody (1:500) and corresponding secondary antibody. NBF-Cl signal was used as a measure of total protein content.

Microscopy of muscle tissue sections

Immediately after isolation, quadricep muscle tissue was fixed overnight in 10% formaldehyde at 4°C. After 24 h, the tissue was routinely processed for embedding in paraffin blocks. The tissue was cut into 5-µm-thin sections that were deparaffinized with xylene and rehydrated in graded ethanol prior to staining. Antigen retrieval (pH 6.6, microwave boiling, 5 min) and blocking of nonspecific binding with normal goat serum (1:10) were performed before incubation with primary antibodies. Samples were then incubated overnight at 4 °C with mouse anti-wheat germ agglutinin (WGA) (1:100) for assessment of skeletal muscle capillarization. Fluorescently labelled WGA-AF488 is widely used for quantitative assessment of capillarisation by measuring the number of capillary profiles relative to the number of myocyte profiles, capillary density, capillary length and surface area (91). For the assessment of the MuSCs, the section were stained with anti-Pax-7 antibody (1:200). In the case of Pax-7 detection, the sections were further incubated with secondary goat anti-mouse IgG Alexa Fluor 488 (1:200) antibody, for one hour at room temperature. The nuclei were counterstained with Hoechst 33342 dye (1

µg/mL) and embedded in Mowiol (Sigma-Aldrich). The slides from four animals per group were examined by fluorescent microscopy (Zeiss Imager Z1, AXIO, Carl 4 Oxidative Medicine and Cellular Longevity Zeiss Meditec AG, Germany). Quantification of PAX7-positive stem cells per 100 nuclei is presented. 2-3 images per animal were analyzed.

Electron microscopy

Muscles samples were removed from two animals per group after decapitation and immediately cut into slices. Tissue slices were immersed in 4% glutaraldehyde solution in 0.1 M phosphate buffer (PB) (pH 7.4) for 24 h, and postfixed with 1% OsO4 in the same buffer for 1 h. Samples were dehydrated in a graded ethanol series and embedded in Araldite and Harderner resin. Precise ultrathin sectioning was performed using Leica UC7 Ultramicrotome with a Diatome ultra 45° diamond knife (Diatome, Switzerland). Grids with ultrathin sections were stained with uranyl acetate and lead citrate, and examined under a JEM-1400 transmission electron microscope (TEM, Japan Electron Optics Laboratory Co., Ltd).

Persulfidation levels of cytosolic GPDH in rat muscle tissue

NBF-Cl muscle extracts from vehicle and ET-treated rats were adjusted to equal protein amounts and incubated with 250 µM DCP-Bio1 for 1.5 h at 37 ^{o}C. Samples were precipitated and protein pellets were dissolved in PBS supplemented with 1% SDS and adjusted. 30 µg of each sample was taken for estimation of total protein levels, and the rest was diluted up to 0.1% SDS and incubated with 40 µl (slurry volume) of precleaned Pierce™ High-Capacity Streptavidin Agarose for 4 h at RT on ferris wheel. Samples were then centrifuged for 1 min at 500 x g and left to settle for 5 min on ice. Sample supernatants were removed, and beads were washed 2 times with 1 ml of PBS supplemented with

0.01% Tween and 3 times with PBS. Bound proteins were eluted by boiling the beads in 1x Laemmli buffer for 10 min at 95 ^{o}C while shaking at 650 rpm. The supernatant was carefully transferred to a new tube and ran on SDS-PAGE. Samples for total GPDH were reduced, boiled and further processed in the same way as persulfidated fractions. After protein transfer and BSA blocking, membranes were incubated with an anti-GPDH antibody (1:1000, 1 % BSA in TBST) and corresponding secondary antibody. Signals were visualized using Amersham Typhoon and ratios of GPDH-SSH to total GPDH was used for comparison.

Activity of cytosolic GPDH in rat muscle tissue

Frozen muscle tissues from vehicle and ET-treated rats were lysed and cGPDH activity estimated following previously described protocol (53).

3.6.3. Quantification and statistical analysis

Plotting of the data was performed using GraphPad Prism version 10.2.0. Western blot, microscopy and gel images were analyzed in Image J. Semantic space, PC analysis and KEGG enrichment bar plots were generated in R studio. Lifespan curves were assessed by Log-rank (Mantel-Cox) in GraphPad. Statistical tests and significances are mentioned in the figure legends. *p<0.05, **p<0.01, ***p<0.001, ****p<0.0001. Illustrations were created by Biorender.com.

Data availability. The mass spectrometry proteomics data have been deposited to the ProteomeXchange Consortium via the PRIDE partner repository with the dataset identifier PXD051587 and PXD051609.

Acknowledgement. We thank Prof Beatriz Alvarez (University of Uruguay) for helpful discussions about PLP/ET mechanism, Ingo Feldman and Susanne Krois (ISAS e.V.) for technical assistance with MS and help with metabolomic analysis of amino acids.

Funding. This study was funded by European Research Council (ERC) under the European Union's Horizon 2020 research and innovation programme (Grant Agreement No. 864921). VO, AS, NS, JZ and MM acknowledge support from The Ministry of Science, Technological Development and Innovation of the Republic of Serbia (contract no. 451-03-47/2023-01/200007). MPM acknowledges the support by the Medical Research Council UK (MC_UU_00028/4) and by a Wellcome Trust Investigator award (220257/Z/20/Z). SIB was supported by the Deutsche Forschungsgemeinschaft (Emmy Noether Program BI 2163/1-1). MKD was supported with a scholarship from Onassis Foundation.

Declaration of interests: Authors declare no competing interests.

3.7. References

1. D'Amico D, Andreux PA, Valdés P, Singh A, Rinsch C, Auwerx J. Impact of the Natural Compound Urolithin A on Health, Disease, and Aging. Trends Mol Med. 2021;27(7):687–99.
2. Madeo F, Eisenberg T, Pietrocola F, Kroemer G. Spermidine in health and disease. Science (80-). 2018;359(6374).
3. Membrez M, Migliavacca E, Christen S, Yaku K, Trieu J, Lee AK, et al. Trigonelline is an NAD+ precursor that improves muscle function during ageing and is reduced in human sarcopenia. Nat Metab 2024. 2024;1–15.
4. Singh P, Gollapalli K, Mangiola S, Schranner D, Yusuf MA, Chamoli M, et al. Taurine deficiency as a driver of aging. Science (80-). 2023;380(6649).
5. Tian X, Thorne JL, Moore JB. Ergothioneine: An underrecognised dietary micronutrient required for healthy ageing? Br J Nutr. 2023;129(1):104–14.
6. Cheah IK, Halliwell B. Ergothioneine; antioxidant potential, physiological function and role in disease. Biochim Biophys Acta - Mol Basis Dis. 2012;1822(5):784–93.

7. Cheah IK, Halliwell B. Ergothioneine, recent developments. Redox Biol. 2021;42:101868.

8. Paul BD. Ergothioneine: A Stress Vitamin with Antiaging, Vascular, and Neuroprotective Roles? Antioxidants Redox Signal. 2022;36(16–18):1306–17.

9. Halliwell B, Cheah I. Are age-related neurodegenerative diseases caused by a lack of the diet-derived compound ergothioneine? Free Radic Biol Med. 2024;217(March):60–7.

10. Tucker RAJ, Cheah IK, Halliwell B. Specificity of the ergothioneine transporter natively expressed in HeLa cells. Biochem Biophys Res Commun. 2019;513(1):22–7.

11. Cheah IK, Ong RLS, Gruber J, Yew TSK, Ng LF, Chen CB, et al. Knockout of a putative ergothioneine transporter in Caenorhabditis elegans decreases lifespan and increases susceptibility to oxidative damage. Free Radic Res. 2013 Dec;47(12):1036–45.

12. Akanmu D, Cecchini R, Aruoma OI, Halliwell B. The antioxidant action of ergothioneine. Arch Biochem Biophys. 1991;288(1):10–6.

13. Van Laer K, Hamilton CJ, Messens J. Low-molecular-weight thiols in thiol-disulfide exchange. Antioxidants Redox Signal. 2013;18(13):1642–53.

14. Katsube M, Ishimoto T, Fukushima Y, Kagami A, Shuto T, Kato Y. Ergothioneine promotes longevity and healthy aging in male mice. GeroScience. 2024 Mar;46(4):3889–909.

15. Wu LY, Kan CN, Cheah IK, Chong JR, Xu X, Vrooman H, et al. Low Plasma Ergothioneine Predicts Cognitive and Functional Decline in an Elderly Cohort Attending Memory Clinics. Antioxidants. 2022;11(9).

16. Tyshkovskiy A, Bozaykut P, Borodinova AA, Gerashchenko M V., Ables GP, Garratt M, et al. Identification and Application of Gene Expression Signatures Associated with Lifespan Extension. Cell Metab. 2019 Sep;30(3):573-593.e8.

17. Bansal A, Zhu LJ, Yen K, Tissenbaum HA. Uncoupling lifespan and healthspan in caenorhabditis elegans longevity mutants. Proc Natl Acad Sci U S A. 2015 Jan;112(3):E277–86.

18. Pincus Z, Mazer TC, Slack FJ. Autofluorescence as a measure of senescence in C. elegans: Look to red, not blue or green. Aging (Albany NY). 2016;8(5):889–98.

19. Mouchiroud L, Houtkooper RH, Moullan N, Katsyuba E, Ryu D, Cantó C, et al. XThe NAD+/sirtuin pathway modulates longevity through activation of mitochondrial UPR and FOXO signaling. Cell. 2013;154(2):430.

20. Narayan V, Ly T, Pourkarimi E, Murillo AB, Gartner A, Lamond AI, et al. Deep Proteome Analysis Identifies Age-Related Processes in C. elegans. Cell Syst [Internet]. 2016 Aug 24 [cited 2019 Nov 14];3(2):144–59. Available from: https://pubmed.ncbi.nlm.nih.gov/27453442/

21. Walther DM, Kasturi P, Zheng M, Pinkert S, Vecchi G, Ciryam P, et al. Widespread Proteome Remodeling and Aggregation in Aging C. elegans. Cell [Internet]. 2015 May 7 [cited 2019 Nov 14];161(4):919–32. Available from: https://linkinghub.elsevier.com/retrieve/pii/S0092867415003207

22. Zaorska E, Hutsch T, Gawryś-Kopczyńska M, Ostaszewski R, Ufnal M, Koszelewski D. Evaluation of thioamides, thiolactams and thioureas as hydrogen sulfide (H 2 S)donors for lowering blood pressure. Bioorg Chem. 2019;88:102941.

23. Wang ZD, Yoshida M, George B. Theoretical study on the thermal decomposition of

thiourea. Comput Theor Chem. 2013;1017:91–8.

24. Filipovic MRR, Zivanovic J, Alvarez B, Banerjee R. Chemical Biology of H2S Signaling through Persulfidation. Vol. 118, Chemical Reviews. 2018. p. 1253–337.

25. Vignane T, Filipovic MR. Emerging chemical biology of protein persulfidation. Antioxid Redox Signal. 2023;39(1–3):19–39.

26. Zivanovic J, Kouroussis E, Kohl JB, Adhikari B, Bursac B, Schott-Roux S, et al. Selective Persulfide Detection Reveals Evolutionarily Conserved Antiaging Effects of S-Sulfhydration. Cell Metab [Internet]. 2019 Dec [cited 2019 Nov 16];30(6):1152-1170.e13. Available from: https://linkinghub.elsevier.com/retrieve/pii/S1550413119305625

27. Savitski MM, Reinhard FBM, Franken H, Werner T, Savitski MF, Eberhard D, et al. Tracking cancer drugs in living cells by thermal profiling of the proteome. Science (80-). 2014 Oct 3;346(6205).

28. Perrin J, Werner T, Kurzawa N, Rutkowska A, Childs DD, Kalxdorf M, et al. Identifying drug targets in tissues and whole blood with thermal-shift profiling. Nat Biotechnol. 2020;38(3):303–8.

29. Murail S, de Vries SJ, Rey J, Moroy G, Tufféry P. SeamDock: An Interactive and Collaborative Online Docking Resource to Assist Small Compound Molecular Docking. Front Mol Biosci. 2021;8(September):1–8.

30. Chiku T, Padovani D, Zhu W, Singh S, Vitvitsky V, Banerjee R. H2S Biogenesis by Human Cystathionine gamma-Lyase Leads to the Novel Sulfur Metabolites Lanthionine and Homolanthionine and Is Responsive to the Grade of Hyperhomocysteinemia. J Biol Chem. 2009 Apr;284(17):11601–12.

31. Carlsson J, Kierstan MPJ, Brocklehurst K. Reactions of L ergothioneine and some other aminothiones with 2,2’ and 4,4’ dipyridyl disulphides and of L ergothioneine with iodoacetamide. 2 Mercaptoimidazoles, 2 and 4 thiopyridones, thiourea and thioacetamide as highly reactive neutral sulphur nucleop. Biochem J. 1974;139(1):221–35.

32. Mulay P, Chen C, Krishna V. Enzyme-independent catabolism of cysteine with pyridoxal-5′-phosphate. Sci Rep. 2023;13(1):1–9.

33. Hameed S, Ikegami K, Sugiyama E, Matsushita S, Kimura Y, Hayasaka T, et al. Direct profiling of the phospholipid composition of adult Caenorhabditis elegans using whole-body imaging mass spectrometry. Anal Bioanal Chem. 2015;407(25):7589–602.

34. Gründemann D, Hartmann L, Flögel S. The ergothioneine transporter (ETT): substrates and locations, an inventory. FEBS Lett. 2022 May;596(10):1252–69.

35. Paul BD, Snyder SH. The unusual amino acid L-ergothioneine is a physiologic cytoprotectant. Cell Death Differ. 2010;17(7):1134–40.

36. Barayeu U, Schilling D, Eid M, Xavier da Silva TN, Schlicker L, Mitreska N, et al. Hydropersulfides inhibit lipid peroxidation and ferroptosis by scavenging radicals. Nat Chem Biol. 2023;19(1):28–37.

37. Wu Z, Khodade VS, Chauvin JPR, Rodriguez D, Toscano JP, Pratt DA. Hydropersulfides Inhibit Lipid Peroxidation and Protect Cells from Ferroptosis. J Am Chem Soc. 2022;144(34):15825–37.

38. Hanna D, Kumar R, Banerjee R. A Metabolic Paradigm for Hydrogen Sulfide Signaling via Electron Transport Chain Plasticity. Antioxid Redox Signal. 2023 Jan;38(1–3).

39. Pfleger J, He M, Abdellatif M. Mitochondrial complex II is a source of the reserve respiratory capacity that is regulated by metabolic sensors and promotes cell survival. Cell Death Dis. 2015;6(7):1–14.

40. Das A, Huang GX, Bonkowski MS, Longchamp A, Li C, Schultz MB, et al. Impairment of an Endothelial NAD+-H2S Signaling Network Is a Reversible Cause of Vascular Aging. Cell. 2018;173(1):74-89.e20.

41. Verdin E. NAD+ in aging, metabolism, and neurodegeneration. Science (80-). 2015;350(6265):1208–13.

42. Zhang H, Ryu D, Wu Y, Gariani K, Wang X, Luan P, et al. NAD + repletion improves mitochondrial and stem cell function and enhances life span in mice. Science (80-). 2016 Jun;352(6292):1436–43.

43. Yaku K, Okabe K, Nakagawa T. NAD metabolism: Implications in aging and longevity. Ageing Res Rev. 2018;47:1–17.

44. Ryu D, Zhang H, Ropelle ER, Sorrentino V, Mázala DAG, Mouchiroud L, et al. NAD+ repletion improves muscle function in muscular dystrophy and counters global parylation. Sci Transl Med. 2016;8(361):1–15.

45. Gomes AP, Price NL, Ling AJY, Moslehi JJ, Montgomery MK, Rajman L, et al. Declining NAD+ induces a pseudohypoxic state disrupting nuclear-mitochondrial communication during aging. Cell. 2013;155(7):1624–38.

46. Mills KF, Yoshida S, Stein LR, Grozio A, Kubota S, Sasaki Y, et al. Long-Term Administration of Nicotinamide Mononucleotide Mitigates Age-Associated Physiological Decline in Mice. Cell Metab. 2016;24(6):795–806.

47. Yoshino J, Baur JA, Imai S ichiro. NAD + Intermediates: The Biology and Therapeutic Potential of NMN and NR. Cell Metab. 2018;27(3):513–28.

48. Jiang Y fan, Lin S syuan, Chen J min, Tsai H zen, Hsieh T shih, Fu C yu. Electron tomographic analysis reveals ultrastructural features of mitochondrial cristae architecture which reflect energetic state and aging. Sci Rep. 2017 Mar;7(1):45474.

49. Picard M, White K, Turnbull DM. Mitochondrial morphology, topology, and membrane interactions in skeletal muscle: a quantitative three-dimensional electron microscopy study. J Appl Physiol. 2013 Jan;114(2):161–71.

50. Mithal DS, Chandel NS. The Gro3p factor: Restoring NAD+/NADH homeostasis to ameliorate mitochondrial disease. Cell Metab. 2021;33(10):1905–7.

51. Liu S, Fu S, Wang G, Cao Y, Li L, Li X, et al. Glycerol-3-phosphate biosynthesis regenerates cytosolic NAD+ to alleviate mitochondrial disease. Cell Metab. 2021;33(10):1974-1987.e9.

52. Mhashal AR, Romero-Rivera A, Mydy LS, Cristobal JR, Gulick AM, Richard JP, et al. Modeling the Role of a Flexible Loop and Active Site Side Chains in Hydride Transfer Catalyzed by Glycerol-3-phosphate Dehydrogenase. ACS Catal. 2020;10(19):11253–67.

53. HOUŠTĚK J, CANNON B, LINDBERG O. Glycerol-3-Phosphate Shuttle and Its Function in Intermediary Metabolism of Hamster Brown-Adipose Tissue. Eur J Biochem. 1975 May;54(1):11–8.

54. Tyshkovskiy A, Ma S, Shindyapina A V., Tikhonov S, Lee SG, Bozaykut P, et al. Distinct longevity mechanisms across and within species and their association with aging. Cell. 2023;186(13):2929-2949.e20.

55. Szabo C, Ransy C, Módis K, Andriamihaja M, Murghes B, Coletta C, et al. Regulation of mitochondrial bioenergetic function by hydrogen sulfide. Part I. Biochemical and physiological mechanisms. Vol. 171, British Journal of Pharmacology. 2014. p. 2099–122.

56. Hanna DA, Diessl J, Guha A, Kumar R, Andren A, Lyssiotis C, et al. H 2 S preconditioning induces long-lived perturbations in O 2 metabolism. Proc Natl Acad Sci. 2024 Mar;121(12).

57. Miller DL, Roth MB. Hydrogen sulfide increases thermotolerance and lifespan in Caenorhabditis elegans. [cited 2019 Nov 13];104(51):20618–22. Available from: http://www.pnas.org/cgi/doi/10.1073/pnas.0710191104

58. Qabazard B, Li L, Gruber J, Peh MT, Ng LF, Kumar SD, et al. Hydrogen Sulfide Is an Endogenous Regulator of Aging in Caenorhabditis elegans. Antioxid Redox Signal. 2014 Jun;20(16):2621–30.

59. Ng LT, Ng LF, Tang RMY, Barardo D, Halliwell B, Moore PK, et al. Lifespan and healthspan benefits of exogenous H2S in C. elegans are independent from effects downstream of eat-2 mutation. npj Aging Mech Dis. 2020 Jun;6(1):6.

60. Dóka, Ida T, Dagnell M, Abiko Y, Luong NC, Balog N, et al. Control of protein function through oxidation and reduction of persulfidated states. Sci Adv. 2020;6(1).

61. Halliwell B, Tang RMY, Cheah IK. Diet-Derived Antioxidants: The Special Case of Ergothioneine. Annu Rev Food Sci Technol. 2023 Mar;14(1):323–45.

62. Ruberto AA, Logan SM, Storey KB. Temperature and serine phosphorylation regulate glycerol-3-phosphate dehydrogenase in skeletal muscle of hibernating Richardson's ground squirrels. Biochem Cell Biol. 2019 Apr;97(2):148–57.

63. Membrez M, Migliavacca E, Christen S, Yaku K, Trieu J, Lee AK, et al. Trigonelline is an NAD+ precursor that improves muscle function during ageing and is reduced in human sarcopenia. Nat Metab 2024. 2024;6(March):1–15.

64. Fovet T, Guilhot C, Delobel P, Chopard A, Py G, Brioche T. Ergothioneine Improves Aerobic Performance Without Any Negative Effect on Early Muscle Recovery Signaling in Response to Acute Exercise. Front Physiol. 2022 Feb;13.

65. Maini Rekdal V, van der Luijt CRB, Chen Y, Kakumanu R, Baidoo EEK, Petzold CJ, et al. Edible mycelium bioengineered for enhanced nutritional value and sensory appeal using a modular synthetic biology toolkit. Nat Commun. 2024;15(1).

66. Kraus JP, Hašek J, Kožich V, Collard R, Venezia S, Janošíková B, et al. Cystathionine γ-lyase: Clinical, metabolic, genetic, and structural studies. Mol Genet Metab. 2009 Aug;97(4):250–9.

67. Sbodio JI, Snyder SH, Paul BD. Transcriptional control of amino acid homeostasis is disrupted in Huntington's disease. Proc Natl Acad Sci. 2016 Aug;113(31):8843–8.

68. Stiernagle T. Maintenance of C. elegans. WormBook. 2006;(1999):1–11.

69. Bibli SI, Hu J, Looso M, Weigert A, Ratiu C, Wittig J, et al. Mapping the Endothelial Cell S -Sulfhydrome Highlights the Crucial Role of Integrin Sulfhydration in Vascular Function. Circulation. 2021;143(9):935–48.

70. Okkenhaug H, Chauve L, Masoudzadeh F, Okkenhaug L, Casanueva O. Worm-align and Worm_CP, Two Open-Source Pipelines for Straightening and Quantification of Fluorescence Image Data Obtained from Caenorhabditis elegans. J Vis Exp. 2020 May;(159).

71. Byrne JJ, Soh MS, Chandhok G, Vijayaraghavan T, Teoh JS, Crawford S, et al. Disruption of mitochondrial dynamics affects behaviour and lifespan in Caenorhabditis elegans. Cell Mol Life Sci. 2019 May;76(10):1967–85.

72. Escorcia W, Ruter DL, Nhan J, Curran SP. Quantification of Lipid Abundance and Evaluation of Lipid Distribution in Caenorhabditis elegans by Nile Red and Oil Red O Staining. J Vis Exp. 2018 Mar;(133).

73. Kim D, Paggi JM, Park C, Bennett C, Salzberg SL. Graph-based genome alignment and genotyping with HISAT2 and HISAT-genotype. Nat Biotechnol. 2019 Aug;37(8):907–15.

74. Liao Y, Smyth GK, Shi W. featureCounts: an efficient general purpose program for assigning sequence reads to genomic features. Bioinformatics. 2014 Apr;30(7):923–30.

75. Love MI, Huber W, Anders S. Moderated estimation of fold change and dispersion for RNA-seq data with DESeq2. Genome Biol. 2014 Dec;15(12):550.

76. Karpievitch Y V., Taverner T, Adkins JN, Callister SJ, Anderson GA, Smith RD, et al. Normalization of peak intensities in bottom-up MS-based proteomics using singular value decomposition. Bioinformatics. 2009;25(19):2573–80.

77. Chambers MC, Maclean B, Burke R, Amodei D, Ruderman DL, Neumann S, et al. A cross-platform toolkit for mass spectrometry and proteomics. Nat Biotechnol. 2012 Oct;30(10):918–20.

78. Kong AT, Leprevost F V., Avtonomov DM, Mellacheruvu D, Nesvizhskii AI. MSFragger: Ultrafast and comprehensive peptide identification in mass spectrometry-based proteomics. Nat Methods. 2017 Apr;14(5):513–20.

79. McCracken NA, Peck Justice SA, Wijeratne AB, Mosley AL. Inflect: Optimizing Computational Workflows for Thermal Proteome Profiling Data Analysis. J Proteome Res. 2021 Apr 2;20(4):1874–88.

80. Miljkovic JL, Burger N, Gawel JM, Mulvey JF, Norman AAI, Nishimura T, et al. Rapid and selective generation of H2S within mitochondria protects against cardiac ischemia-reperfusion injury. Redox Biol. 2022 Sep 1;55:102429.

81. Doll S, Freitas FP, Shah R, Aldrovandi M, da Silva MC, Ingold I, et al. FSP1 is a glutathione-independent ferroptosis suppressor. Nature. 2019 Nov;575(7784):693–8.

82. Drekolia MK, Talyan S, Cordellini Emídio R, Boon RA, Guenther S, Looso M, et al. Unravelling the impact of aging on the human endothelial lncRNA transcriptome. Front Genet. 2022 Oct;13.

83. Wider G, Dreier L. Measuring Protein Concentrations by NMR Spectroscopy. J Am Chem Soc. 2006 Mar;128(8):2571–6.

84. Cullen CH, Ray GJ, Szabo CM. A comparison of quantitative nuclear magnetic resonance methods: internal, external, and electronic referencing. Magn Reson Chem. 2013 Nov;51(11):705–13.

85. Jeanclos E, Schlötzer J, Hadamek K, Yuan-Chen N, Alwahsh M, Hollmann R, et al. Glycolytic flux control by drugging phosphoglycolate phosphatase. Nat Commun. 2022 Nov;13(1):6845.

86. Ng DHJ, Chan LY, Fitzner L, Keppler JK, Ismail SM, Hird S, et al. A novel screening method for free non-standard amino acids in human plasma samples using AccQ·Tag reagents and LC-MS/MS. Anal Methods. 2023;15(4):445–54.

87. Kasarla SS, Flocke V, Saw NMT, Fecke A, Sickmann A, Gunzer M, et al. In-vivo tracking of deuterium metabolism in mouse organs using LC-MS/MS. J Chromatogr A. 2024 Feb;1717:464691.

88. Vlaski-Lafarge M, Loncaric D, Perez L, Labat V, Debeissat C, Brunet de la Grange P, et al. Bioenergetic Changes Underline Plasticity of Murine Embryonic Stem Cells. Stem Cells. 2019 Apr;37(4):463–75.

89. Burger N, Logan A, Prime TA, Mottahedin A, Caldwell ST, Krieg T, et al. A sensitive mass spectrometric assay for mitochondrial CoQ pool redox state in vivo. Free Radic Biol Med. 2020;147(November 2019):37–47.

90. Lowry O, Rosebrough N, Farr AL, Randall R. PROTEIN MEASUREMENT WITH THE FOLIN PHENOL REAGENT. J Biol Chem. 1951 Nov;193(1):265–75.

91. Black MJ, Bertram JF, Johnston CI. Effect of angiotensin-converting enzyme inhibition on myocardial vascularization in the adolescent and adult spontaneously hypertensive rat. J Hypertens. 2001 Apr;19(4):785–94.

4. Age-induced persulfidation changes in *C. elegans*

[1]Dunja Petrovic, [1]Luke Slade, [1]Milos R. Filipovic

[1]Leibniz Institute for Analytical Sciences, ISAS e.V., Dortmund, Germany

Corresponding author: Milos R. Filipovic

In preparation

Author contributions:

Dunja Petrovic prepared the samples and performed gene expression data analysis. Dunja Petrovic was responsible for the collection and processing of *C. elegans* persulfidome and total proteome datasets, including sample preparation for mass spectrometry (MS) analysis and the subsequent data analysis and visualization. Luke Slade contributed to the collection of biological replicates for the *C. elegans* persulfidome analysis. Milos R. Filipovic conceived and supervised the whole study, designed the experiments and analyzed and interpreted data.

4.1. Introduction

C. elegans has been an invaluable model system for aging research due to its simplicity, short lifespan and ease of genetic manipulation (1). These advantages are complemented by its highly conserved signaling pathways and significant genetic homology with humans (2). The age-dependent deterioration observed at molecular, cellular and tissue level overlaps between humans and worms. A recent study revealed that over 70% of essential *C. elegans* genes have human homologues, 90% of which are implicated in human diseases (3). Protein aggregation is an inherent part of aging in both *C. elegans* and humans even in the absence of disease. Many proteins prone to aggregation are highly conserved between these two species and detected in human disease aggregates (4). Moreover, *C. elegans* models of neurodegenerative and age-related human proteinopathies have provided significant insights into the molecular mechanisms underlaying these pathological conditions in humans (5,6). As *C. elegans* age, it exhibits anatomical, functional, and behavioral changes including cessation of reproduction, reduced and uncoordinated movement, and higher sensitivity to stress (2,7). Impaired proteome integrity is one of the primary hallmarks of aging, characterized by defects in translational fidelity, post-translational protein processing, and the removal of damaged proteins (6). Protein stability, function and degradation are highly dependent on post-translational modifications (PTM) and dysregulation of their dynamics play a significant role in proteome remodeling. Certain PTMs, such as acetylation, phosphorylation, SUMOylation and ubiquitination, have been already associated with aging and longevity in *C. elegans* (6).

Endogenously produced hydrogen sulfide (H_2S) is an important mediator of lifespan-extending genetic, pharmacological and behavioral interventions although the mechanisms underlying its effects remain poorly understood (8–11). Additionally, exogenous H_2S supplementation has been shown to promote both lifespan and healthspan in *C. elegans,* though via different mechanisms than those stimulating endogenous H_2S production (12). Increasing evidence suggest that H_2S modulates cellular signaling pathways and biological processes through a post-translational modification of cysteine resides known as persulfidation (PSSH) (13,14). PSSH is an evolutionary conserved PTM across different species and its decline with age renders protein more susceptible to excessive oxidation, contributing to overall disruption of proteostasis and aging process (11).

In this study we used *C. elegans* as a model to investigate whether and how persulfidation is remodeled during aging and to elucidate its impact on key physiological processes. By understanding the role of this PTM in aging, we aim to uncover new mechanisms that contribute to the regulation of lifespan and healthspan in *C. elegans,* but also in other species.

4.2. Results

Several independent proteomic studies found that CSE levels decrease with age in *C. elegans* (15,16). Given that its genome contains more than one orthologue of each mammalian gene coding for H_2S producing enzymes, we first examined how mRNA levels of these genes change in wild type *C. elegans* (N2 Bristol strain) with age. Specifically, *C. elegans* possesses two genes coding for CSE (*cth-1* and *cth-2*), two for CBS (*cbs-1* and

cbs-2) and seven genes encoding orthologues of MST (*mpst1-7*). For this purpose, we harvested worms at three distinct ages: Day1 (D1), Day7 (D7) and Day14 (D14) of adulthood, representing the early, mid and late phases of adulthood. To avoid interference from progeny and prevent starvation or overcrowding, worms were grown in the presence of 5-Fluoro-2′-deoxyuridine (FuDR), a commonly used chemical that inhibits DNA replication and reproduction in *C. elegans* (17).

Our results confirmed previous findings showing decrease in expression of both *cth-1* and *cth-2*. Additionally, we observed a general, age-dependent decline in expression of nearly all examined genes, with the most pronounced effects in *cth-2*. Interestingly, *cbs-2* was the only gene that showed consistent upregulation with age. Previous studies have suggested that CBS-2 is not involved in H_2S production, but instead plays a role in cellular division, making our findings a valuable contribution to the limited knowledge of CBS-2 expression patterns and function (Figure 4.1).

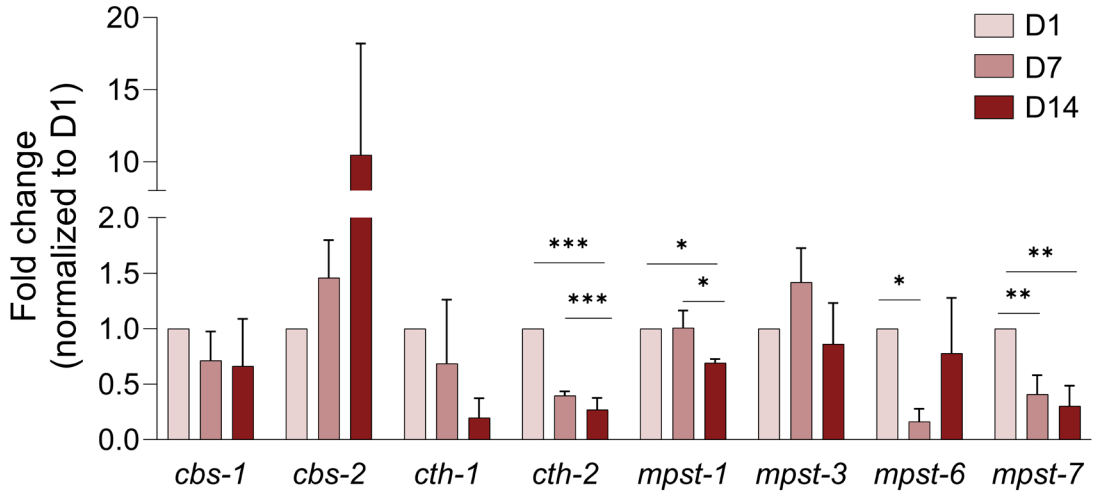


Figure 4.1 Expression profiles of genes encoding for putative H_2S producing enzymes in *C. elegans* genome.

Each bar represents the average value of three biological replicates. For the representation samples were normalized to Day1 within each replicate. Difference in expression levels among different ages was performed for each gene separately using one-way ANOVA (***p<0.001, **p<0.01, *p<0.05).

The overall decline in the expression of genes encoding enzymes involved in endogenous H_2S production, suggest that protein persulfidation, a PTM directly dependent on H_2S production, may also be affected in aging animals. Zivanovic et al. previously examined persulfidation dynamics in aging *C. elegans*, using the dimedone switch method and in-gel detection of modified proteins. The results indicate a steady decrease in PSSH levels from D1 to D7, accompanied by an increase of sulfonylation, a highly irreversible oxidative modification of cysteines (11). However, in-gel detection provided limited information on specific protein targets contributing to these changes. To

address this gap, we performed an in-depth proteomic analysis to map *C. elegans* persulfidome for the first time. Based on previous results, we chose to monitor persulfidation in Day 0 (D0), Day 4 (D4) and Day 10 (D10). D0 represent the young adult stage before fertility is reached, minimizing the contribution from egg persulfidome. D4 represent mid-life, post reproductive animals, while D10 corresponds to late adulthood, when some worms already exhibit signs of aging, including mortality. In order to exclude any confounding effects on physiological aging process, we also omitted FuDR for this set of experiments, therefore including reproduction as an important contributor to the aging. Proteins were extracted and labeled following dimedone-switch protocol, which enables selective enrichment of persulfidated proteins, followed by proteomic analysis. We identified 2031 proteins in at least 2 out of 3 analyzed biological replicates of each age, with 1774 proteins detected in all analyzed samples. Principal Component analysis (PCA) confirmed reproducibility in protein quantification, showing distinct clustering of replicates from different ages (Figure 4.2.A)

We further assessed changes in persulfidation with age. Using a 30% change as a threshold for significantly changing proteins along p value cutoff of 0.05, we detected 1530 proteins with significant alternations across all three ages. A heatmap of the data revealed significant remodeling of the persulfidome with age, with a more complex pattern than initially anticipated. Persulfidation levels were highest at D0, followed by a drastic decrease at D4 and then partial recovery at D10, though not to D0 levels. This suggest that persulfidation changes are not strictly unidirectional but fluctuate during *C. elegans* lifespan. The drop at D4 may be related to the cessation of reproduction and general change in animal's physiology at that stage (Figure 4.2.B, Supplementary table S4.1).

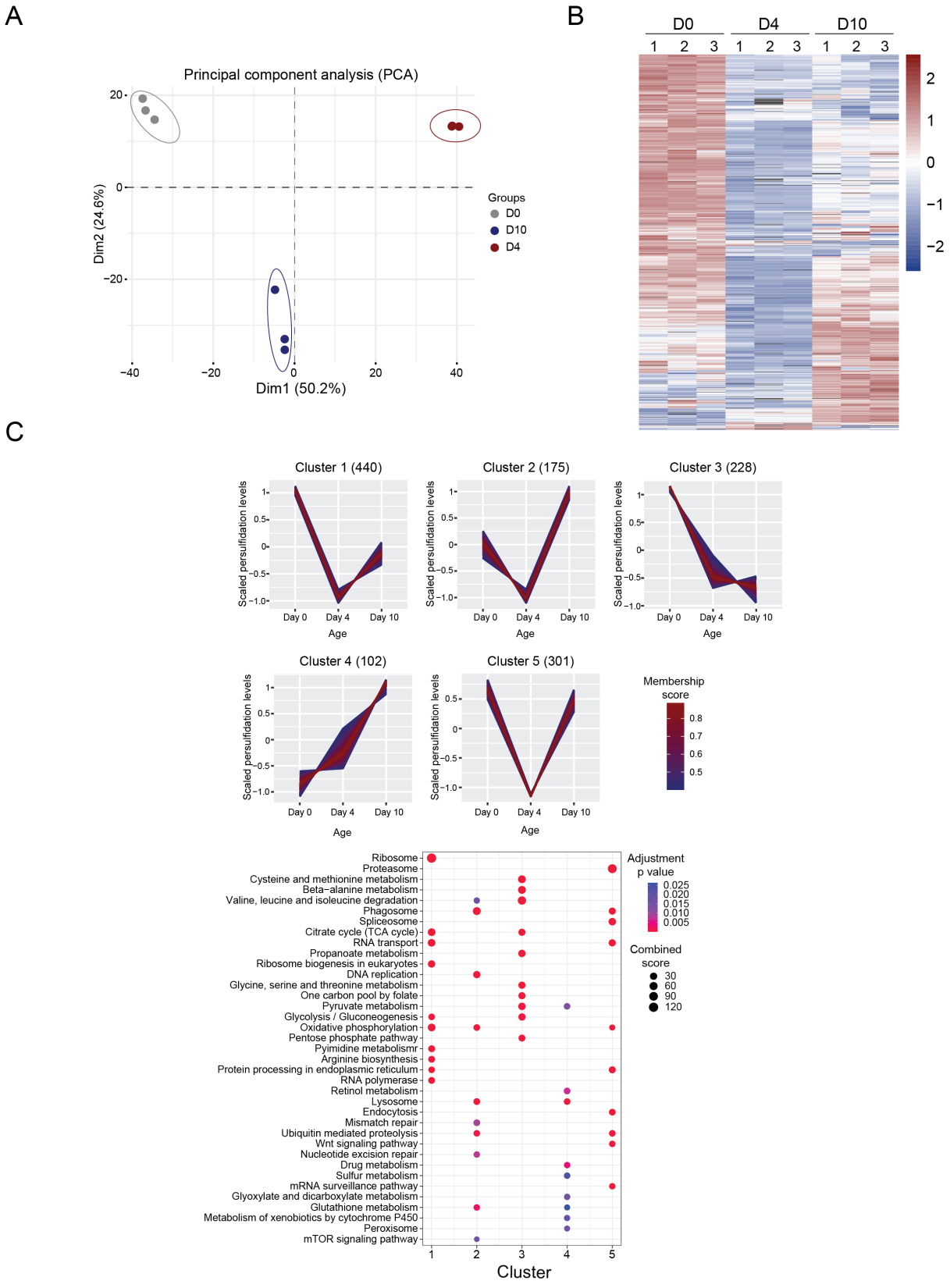


Figure 4.2 Persulfidome remodeling in aging *C. elegans*.

(**A**) Principal Component Analysis (PCA) showing the reproducibility of quantification across replicates. (**B**) Heatmap of 1530 proteins with significantly changing persulfidation in at least one out of three presented ages (n=3, Welch's test, p value threshold 0.05, log2 fold change threshold 0.38). (**C**) Hierarchical cluster analysis of the same set of proteins as in (B). KEGG pathway enrichment of individual clusters was performed using WormEnrichr and presented terms were filtered using Benjamini adjusted p value threshold of 0.05.

To better understand the observed changes, we grouped the significantly changing proteins into six clusters based on the trend of change across different ages. KEGG pathway enrichment analysis for each cluster, performed using WormEnrichr, provided insights into potential biological relevance of the observed changes. For example, cluster 3 which is characterized by a gradual decrease from D0 to D10, was enriched in amino acid and glucose metabolism pathways. In contrast, cluster 4, which showed gradual upregulation towards D10 was enriched in sulfur and glutathione metabolism as well as peroxisome-related pathways which are involved in hydrogen peroxide metabolism and fatty acids oxidation, suggesting the important role of oxidative reactions in aging (Figure 4.2.C, Supplementary table S4.1).

Volcano plots comparing individual time points, revealed more than 1000 proteins with significantly reduced persulfidation at D4 compared to D0, and over 800 proteins with increased persulfidation between D4 to D10 (Figure 4.3A, Supplementary table S4.1). A Venn diagram analysis of significantly changing proteins across all time points, identified nearly 300 proteins that changed in all comparisons being mostly involved in ribosome biogenesis, RNA processing and degradation and cysteine and methionine metabolism. KEGG enrichment of unique changes between two ages furthermore suggests that persulfidation might be involved in regulation of distinct processes at defined time points but not throughout the whole C. *elegans* lifespan (Figure 4.3B).

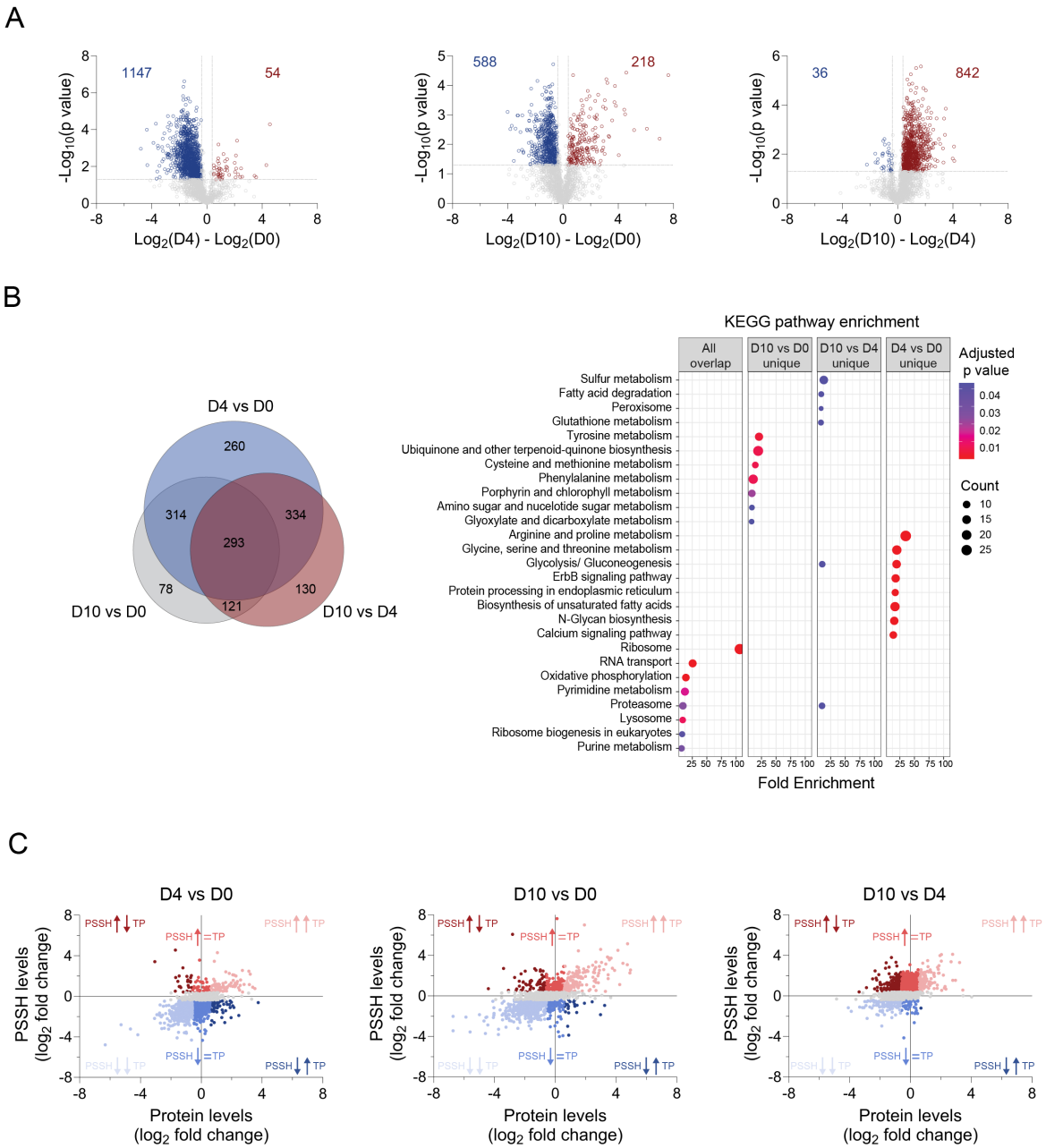


Figure 4.3 Persulfidome remodeling in aging *C. elegans* and its correlation to the changes in total proteome.

(**A**) Volcano plot analysis of persulfidome changes between different ages. Dots in red represent proteins with significantly increased PSSH levels while blue dots correspond to the proteins with significantly lower PSSH levels (Welch's test, n=3; applied thresholds: p value<0.05, log2 fold change threshold 0.38) (**B**) Venn diagram showing overlap of significantly changing proteins among different comparisons. Almost 300 proteins significantly change across all three

comparisons. KEGG pathway enrichment of the intersection as well as unique parts of three different comparisons in Venn diagram. Presented KEGG terms passed Benjamini adjusted p value threshold of 0.05. (**C**) Double scatter plots analysis of persulfidome and protein expression relationship. Log2 fold changes within the persulfidome (y-axis) were plotted against total protein changes for the same comparison(x-axis). PSSH – persulfidome changes, TP – total proteome changes.

Persulfidation changes may also result from proteome remodeling during aging. Although this does not negate the overall changes in persulfidation levels, it can influence data interpretation. We therefore decided to compare how *C. elegans* persulfidome changes in context of total proteome remodeling.

Two independent studies performed in-depth quantitative proteomic analysis in aging *C. elegans* yielding different conclusions. Narayan et al. quantified more than 9000 proteins (out of > 11 000 detected) across three ages (Day 1, Day 5 and Day 10), reporting only 8% of proteome strikingly changing with aging, with relatively same number of proteins changing in both directions (15). In contrast, Walther et al. detected more than 5000 proteins with one-third showing at least 2-fold changes across wider range of ages (Day 1, Day 6, Day 12, Day 17 and Day 22) along with significant fraction of proteome increasing with age (16). Given these discrepancies, we performed our own total proteome analysis using the same conditions as for persufidome measurement. We then overlapped the list of all quantified proteins in both datasets and filtered for the proteins present in persulfidome dataset which resulted in 1871 proteins (> 90% of quantified proteins) present in both datasets (Figure 4.3C).

Since we observed significant age-induced remodeling of total proteome, we performed in-depth analysis of this dataset along with persulfidome characterization. In total proteome dataset, we quantified 4356 proteins in at least two replicates with 4056 proteins present in all three replicates. The clear separation of datasets belonging to

different ages in PCA plot confirmed the significant differences among these datasets, as well as the reproducibility of the quantification method (Figure 4.4.A). Our analysis detected 2730 proteins changing in at least one out of all three ages, using 1.5 fold-change (50% change) and p value cutoff at 0.05 (Supplementary table S4.2).

While the general trend indicated a decrease in the protein levels with age, substantial number of proteins were upregulated at both D4 and D10 compared to D0 (Figure 4.4.B). KEGG pathway enrichment analysis of six identified clusters showed that proteins involved in ribosomal biogenesis, RNA transport and degradation and proteasome formation were significantly downregulated, while those involved in lysosome formation and DNA repair pathways were massively upregulated at D10, suggesting increased requirements for autophagy and repair of DNA damage accumulated in time (Figure 4.4.C, Supplementary table S4.2).

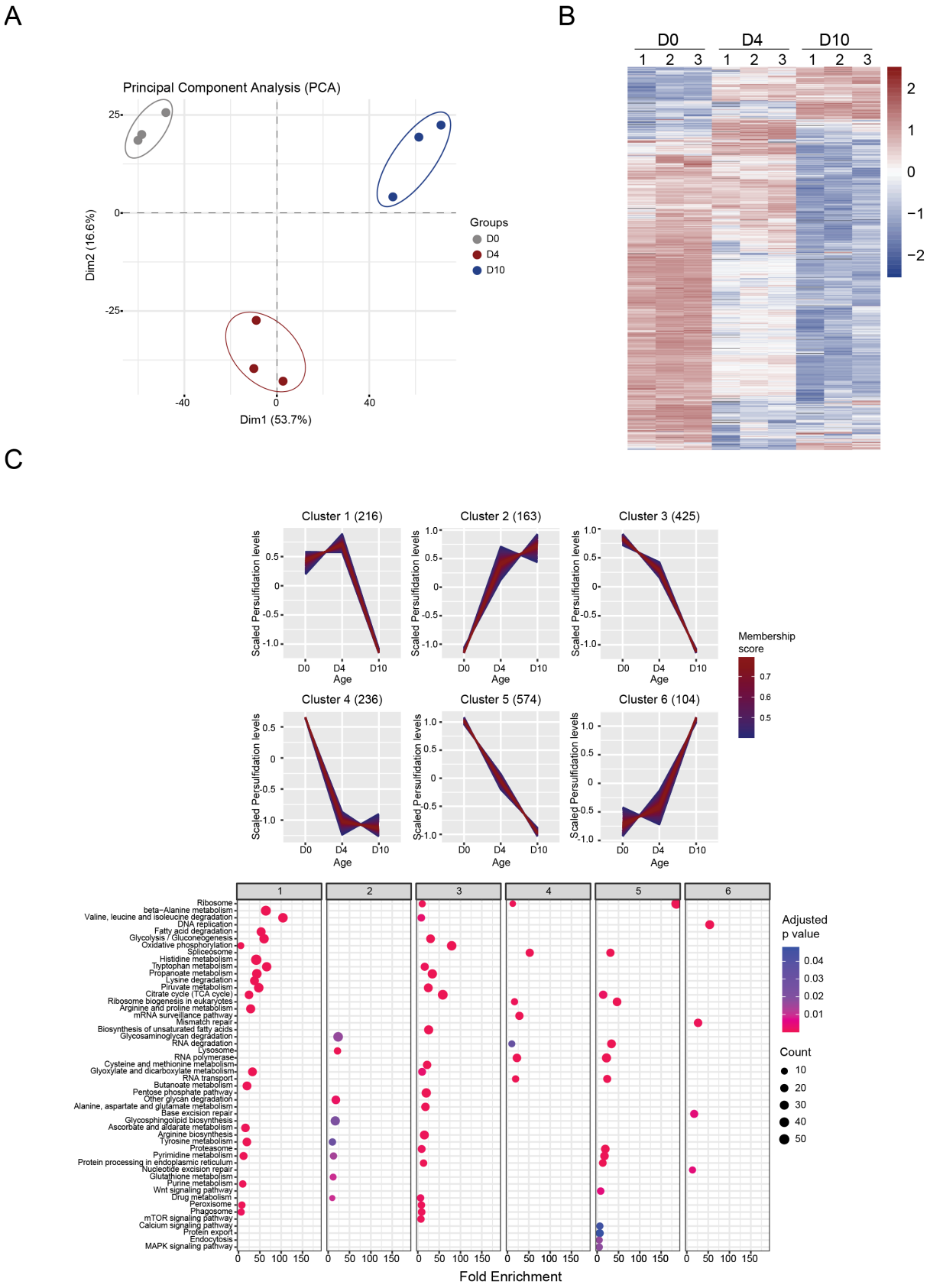


Figure 4.4 Aging induces profound remodeling of *C. elegans* proteome.

(**A**) Principal Component Analysis (PCA) showing the reproducibility of quantification across replicates. (**B**) Heatmap of 2730 proteins significantly changing in at least one out of three presented ages (n=3, Welch's test, p value threshold 0.05, log2 fold change threshold 0.58). (**C**) Hierarchical cluster analysis of the same set of proteins as in (B). KEGG pathway enrichment of individual clusters was performed using WormEnrichr and presented terms were filtered using Benjamini adjusted p value threshold of 0.05.

Comparison of individual ages revealed that the most prominent differences are observed between D0 and D10 with more than 1800 proteins being downregulated later in life (Figure 4.5A, Supplementary table S4.2). When we took a closer look at significantly changing proteins, we observed more than 400 protein targets changing in all three comparisons, while significant portion of proteins was only significantly changing between two ages (more than 500 proteins changing only between D10 and D0). When we performed KEGG enrichment for the proteins present in the intersection of all three comparisons, as well as the ones limited to only one comparison, we could see the difference among enriched pathways. Proteins which constantly change in age are mostly involved in RNA metabolism and degradation, ribosome biogenesis but also cysteine and methionine metabolism. On the other hand, proteins unique for D10 vs D0 comparison are components of proteasome degradation pathways but also protein metabolism and processing (Figure 4.5.B). We also had a closer look at the changes of H_2S producing enzymes to compare to our gene expression results. While both CTH-2 and MPST-1 showed gradual decrease in protein levels with age (although the changes for both proteins were significant only between D0 and D10), MPST-3 did not show the same pattern, but more an upregulation at D4 which matches the pattern we observed at gene expression level (Figure 4.5.C). Although CTH-1 did also show a trend of decrease

towards D10, it did not pass the significance threshold due to the variability among the replicates.

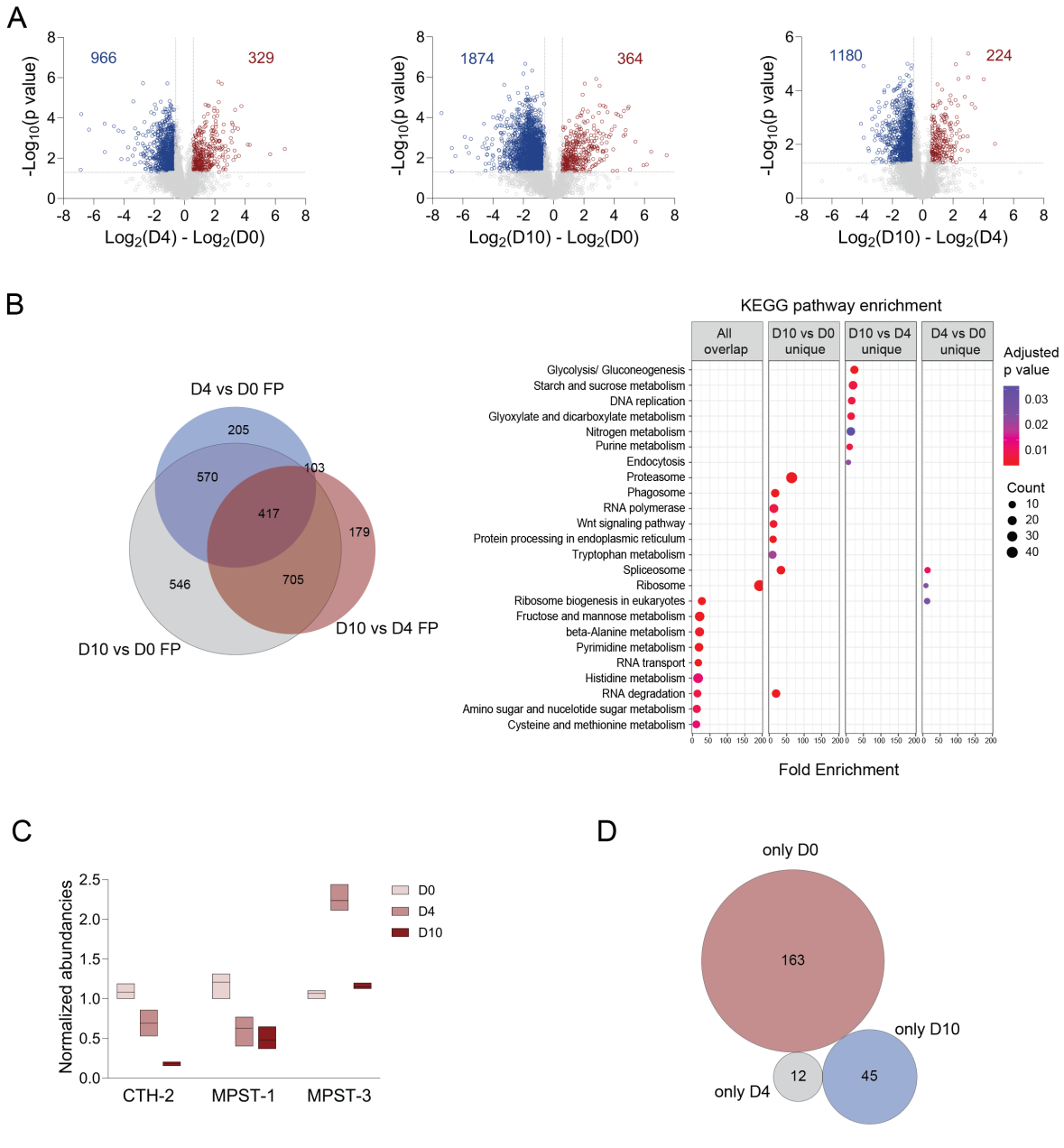


Figure 4.5 Age-specific changes in *C. elegans* proteome.

(**A**) Volcano plot analysis of changes in protein abundance between different ages. Dots in red represent proteins with significantly increased PSSH levels while blue dots correspond to the proteins with significantly lower PSSH levels (Welch's test, n=3; applied thresholds: p value<0.05, log2 fold change threshold 0.58) (**B**) Venn diagram showing overlap of significantly changing

proteins among different comparisons. More than 400 proteins significantly change across all three comparisons. KEGG pathway enrichment of the intersection as well as unique parts of three different comparisons in Venn diagram. Presented KEGG terms passed Benjamini adjusted p value threshold of 0.05. (**C**) Protein levels of H_2S producing enzymes detected in total proteome dataset. (**D**) Venn diagram showing the number of proteins identified in all three replicates of one age but not in other ages.

Proteome remodeling is commonly examined by focusing on proteins that show significant changes in abundance across different ages. However, we also aimed to explore whether and which proteins are exclusively expressed at specific life stages. For this purpose, we extracted all identified proteins across ages and filtered for proteins consistently detected in all replicates of one age group while being absent in the others. This approach led to identification of more than 160 proteins uniquely present at D0 but not identified at D4 or D10. Similarly, over 40 proteins were exclusively detected at D10, while more than 60 proteins were present at both D4 and D10 but not D0. A deeper characterization of identified proteins, through both experimental validation and functional analysis, is required to determine whether they really play time-limited biological roles throughout *C. elegans* lifespan or their absence is due to the technical variability and efficiency of protein extraction.

4.3. Discussion

In this study we conducted a comprehensive analysis of *C. elegans* persulfidome, examining its dynamics throughout aging and its connection to the remodeling of proteostasis. The analysis of age-related changes in the expression of genes encoding H_2S-producing enzymes revealed an overall decline in their expression most notably at

D14 compared to D0. This observation aligns with the lower protein levels of enzymes such as CTH-2 and MPST-1, which we detected in our proteomic analysis, in agreement with previous studies. However, further research is needed to precisely determine the contribution of all relevant genes and their products to endogenous H_2S production. Interestingly, both *mpst-3* gene expression and MPST-3 protein levels increase at specific points during the *C. elegans* lifespan, suggesting a potentially more prominent role in the post-reproductive phase. We also observed significant upregulation of *cbs-2 gene*, however due to the high variation at D14 (ranging from a 2-fold to a 17-fold increase), statistical significance was not reached. A recent study demonstrated that CBS-2 is involved in the repair of double-strand breaks induced during meiosis, indicating that its increased expression may be necessary to counteract accumulating DNA damage with age.

Based on gene expression results and the known perturbation in H_2S metabolism during aging, we employed a chemoselective proteomic approach to map the persulfidome across three distinct stages of the *C. elegans*. In this study, we quantified over 2000 persulfidation targets, of which 75% showed significant changes in at least one age comparison. The number of detected proteins and modulation of their PSSH levels during *C. elegans* lifespan suggests that persulfidation is a relevant and highly dynamic post-translational modification involved in regulation of numerous biological processes in this organism. Zivanovic et al. previously showed that persulfidation levels decrease with age across species due to the reduced endogenous H_2S production (11). While in-gel detection revealed the gradual drop in PSSH levels during aging, our persulfidome analysis using proteomic approach identified more complex non-linear changes with age. Persulfidation levels were significantly lower at D4 compared to D0 and D10, but the

difference between D0 and D10 was less pronounced, suggesting that a certain percentage of persulfidation might be restored during mid-life. This observation indicates that persulfidation might have an important role in signaling, as D4 marks the onset of reproduction cessation along with significant decline in somatic function. Translated to humans, it is tempting to compare this with recent data showing that aging indeed affects organismal proteome and metabolome in two main peaks, one at ~44 and one at ~60 years of age (18). The former would correspond well to the D4 old worms. Furthermore, our group has observed similar U-shaped change in persulfidome in aging mice, with strongest decline in 10-month-old mice and then gradual partial recovery at later ages (19).

What are the implications of such change? In the context of evolutionarily-conserved protective hypothesis of persulfidation's role, the decline that occurs until mid-life could be seen in two ways: (i) as an individual biomarker of severity of aging and/or (ii) as a consequence of "first aging wave" that would then pre-define the health span and lifespan of an individual. Although cells try to recover and restore the persulfidation levels later in life, it is plausible that the extent of PSSH decline that occurs at this midlife point is what predisposes the cells for age-related diseases by affecting the primary and antagonistic hallmarks of aging (20).

To better understand the global changes in persulfidation, we performed clustering and enrichment analysis of significantly altered persulfidated proteins. Proteins involved in amino acid metabolism (including cysteine metabolism), the TCA cycle and the pentose phosphate pathway exhibited gradual decline in persulfidation over time. In contrast, proteins involved in ubiquitin-proteasome degradation pathway and autophagy showed increased persulfidation with time. This suggests that persulfidation might have a role in

regulating protein turnover, an important quality control mechanism which declines with age.

We also compared persulfidation changes to total protein levels at each time point to assess the influence of proteome remodeling on the observed PSSH alternations. While normalization is required to account for significant changes in protein abundance, direct comparisons can be challenging due to the technical limitations, sample composition and the interpretation of observed results. For instance, if both PSSH and total protein levels increase to the same extent, one might conclude that PSSH levels remain unchanged. However, from a cellular perspective, there would be still more persulfidated molecules of a specific protein compared to control condition. Although normalization did affect the protein PSSH levels to certain extent, the profound downregulation of PSSH at D4 remained significant even after adjusting for total protein.

In addition to persulfidome analysis, we also examined the age-related changes in total proteome of *C. elegans*. While two prior high-throughput studies have extensively addressed this topic, they reached different conclusions which encouraged us to perform our own analysis using the same experimental setup as for the persulfidome analysis. Our label-free proteomic analysis quantified over 4300 proteins with 60% changing in at least one time point. Although, we detected fewer proteins compared to the previous studies (Narayan et. al quantified more than 9000 while Walther et al profiled more than 5000 proteins), likely due to differences in protein extraction and sample preparation (we did not perform fractional lysis or peptide fractionation to enhance detection), our data revealed extensive proteome remodeling throughout aging. Another key difference between our datasets and the one previously published is that we grow synchronized cultures without the use of FuDR which is known to affect protein expression (21).

Interestingly, Walther et al. reported a more prominent increase in protein abundance with aging, while we observed a global decrease in protein levels in D10 animals compared to both D0 and D4. Cluster analysis revealed that downregulated targets were peroxisomal proteins, proteasomal subunits and proteins involved in ribosome and spliceosome complex formation. While our observations contrast with age-dependent upregulation of proteasomal proteins noted by Walther et al., they align with Narayan et al.'s findings of a general downregulation of peroxisomal proteins.

In conclusion, this chapter highlights the relevance of persulfidation as a PTM in *C. elegans* with persulfidated targets involved in numerous processes ranging from DNA repair to amino acid metabolism and protein turnover. These findings raise numerous questions for future studies. Using mutants for H_2S-producing enzymes as well as known *C. elegans* longevity models could clarify persulfidation's contribution to lifespan extension. Given the role of H_2S in lifespan-extending interventions such as dietary restriction, exposure to low temperatures and germline ablation, studying persulfidation in these contexts would clarify whether a common mechanism underlies these interventions or if distinct pathways converge on similar outcomes.

4.4. Experimental Methods

C. elegans maintenance

Wild type *C. elegans* (N2 Bristol) strain was grown at 20 ºC on standard nematode growth medium (NGM) seeded with E. coli OP50-1 grown for 16 hours (37 ºC with shaking at 180 rpm) as a food source. Worm maintenance was performed following standard techniques(22).

Gene expression analysis using qPCR

For gene expression analysis, gravid, well-fed wild type (N2) adults were bleached and obtained eggs were placed in M9 buffer overnight to hatch. The next day, worms were placed onto 100-mm plates and grown until L4 stage when they were transferred to plates containing 25 µM FuDR. Worms were transferred every few days to prevent starvation. Animals were collected at day 1 (D1), day 7 (D7), day 14 (D14), washed three times with M9 to remove dead embryos and bacteria, and 1mL of Trizol was added to worm pellet. Samples were immediately frozen in liquid nitrogen and stored at -80 ºC for downstream analysis. Worm extracts were subjected to five freeze-thaw cycles (fast defrosting in water bath at 37 ºC followed by vortexing for 30 s and freezing in liquid nitrogen) to improve sample lysis. After the last cycle, 200 µL of chloroform:isoamyl alcohol mix (24:1, v/v) was added, samples were vigorously shaken for 15 s, incubated for 2 min at RT and centrifuged at 12 000 x g for 15 min. The upper aqueous phase was carefully transferred to a new tube, one volume of absolute isopropanol was added, and samples were placed at -20 ºC for one hour. After centrifugation at 12 000 x g for 10 min at 4 ºC, supernatant was removed and RNA pellet was washed twice with ice-cold 75% ethanol. After the second wash, samples were left to dry to remove any traces of ethanol. Dried RNA pellets

were dissolved in RNAse free water and RNA concentration was measured on Nanodrop. Samples were diluted to 200 ng/ µL and 44 µL was used for DNA removal using DNA-free™ Kit (Invitrogen) and following manufacturer's protocol. 500 ng of DNA-free samples were used for reverse transcription step following the protocol supplied with High-Capacity cDNA Reverse Transcription Kit (Invitrogen). Briefly, 10 µl of isolated RNA was mixed with 2X reverse transcription (RT) master mix prepared using the following calculation:

Reagent	Volume (in µL)
10X RT Buffer	2
25X dNTP Mix (100 mM)	0.8
10X Random Primers	2
MultiScribe Reverse Transcriptase	1
RNAse Inhibitor (20U/µL)	1
Nuclease-free H_20	3.2

The reverse transcription was performed using the following conditions:

Settings	Step1	Step2	Step3	Step4
Temperature	25 °C	37 °C	85 °C	4 °C
Time	10 min	120 min	5 min	Hold

Obtained cDNA (diluted 50 times) was used to perform qPCR using HOT FIREPol® EvaGreen® qPCR Mix Plus. The reaction was prepared using the following protocol (per well):

Reagent	Volume in µL (per reaction)
5X HOT FIREPol® EvaGreen® qPCR Mix Plus	3
Primer mix (FW+RV, 10 µM each)	0.4
RNAse free water	3.6
cDNA	8

The measurement was performed in technical triplicates using the following conditions:

	Step	Temperature	Time
qPCR amplification	activation of HOT FIREPol® DNA Polymerase	95 ºC	15 min
	denaturation	95 ºC	15 sec
	hybridization	60-65 ºC	20 sec
	elongation	72 ºC	20 sec
Melting curve step	denaturation	95 ºC	30 sec
	thermal gradient	55-95 ºC (0.5 ºC steps)	

Data analysis was performed in CFX Manager (BioRad). Mean Cq value for each analyzed sample and gene was calculated as an average of three technical replicates. Relative normalized expression was calculated using D1 as a control sample. Based on previous validation, *cdc-42* and *pmp-3* genes were used as reference genes to normalize gene expression levels.

The following primers were used in this study:

Gene name	Forward primer (Fw)	Reverse primer (Rv)
cbs-1	CGTCCAACTCCACTTGTCCC	GCTTTGTCAGCGGTACGGTC
cbs-2	GAATCCACTGGCACACTATGAG	GCCAAGGACCACTAGATCAATC
cth-1	ACTTTCTCTCGGCGCAGAC	CACCTCCGATTGCACGTTG
cth-2	AATCAGGTGGTCCCGCCAATC	ACGAGTTGGGTTTCCAGCAC
mpst-1	CAGAGCTTCTTGTGAAAGGC	CAGGATGTGATTGTCGGTTG
mpst-3	ACGTATGCACCAACAGCCAC	GGCAGAGTCAAGGCCAAAGTG
mpst-6	GGTGGTATGGCTGCTGCTTC	CGGATTGAACGACACCTTGGG
mpst-7	GCGTCTCAGCTACAGTAACC	ATTGATGGGCGAGGCAAAC

C. elegans persulfidome analysis

For persulfidome analysis, worms were synchronized by bleaching. Isolated eggs were placed in M9 buffer and incubated for 14 h at 20 °C with gentle shaking (130 rpm) to hatch. Worms were grown on 100-mm NGM plates (~ 1000 worms/plate) and transferred every day using M9 buffer. On the day of collection worms were collected into 15-mL falcons and washed at least three times to remove bacteria and progeny. After the last wash, M9 was removed and pellet corresponding to 150 µL was flash frozen in liquid N2 and used for downstream analysis. Worm pellets were kept on ice and quickly defrosted by addition of 1 mL HEN lysis buffer (50 mM HEPES, 1 mM EDTA, 0.1 mM Neocuproine, 1% IGEPAL, 2% SDS, pH 7.4) supplemented with 10 mM NBF-Cl and 1% protease inhibitor prior to use. Suspension was mixed well and transferred to 15 mL Bioruptor® Pico Tubes (Diagenode, C30010017) containing 200 µL of glass beads. Samples were lysed by sonication in Biorputor Pico at +4 °C. Lysates were incubated for 2 h at 37 °C followed by centrifugation at 18,000 x g for 15 min at 4 °C to remove debris. Proteins were precipitated twice by methanol/chloroform precipitation (water/methanol/chloroform, 4:4:1, v/v/v) and washed twice with ice-cold methanol. Pellets were dissolved in PBS supplemented with 0.2% SDS and equal amounts of protein were incubated with Pierce™ NeutrAvidin™ Agarose beads to remove endogenously biotinylated proteins. After 2 h of mixing at room temperature, supernatant was removed and precipitated once. Proteins were suspended in PBS supplemented with 2 % SDS and incubated for 1.5 h at 37 °C with 250 µM DCP-Bio1 to specifically label persulfides. Excess probe was removed by precipitation and obtained pellets were dissolved in PBS supplemented with 0.1% SDS and adjusted to equal protein amount. Samples were then incubated for 4 h at RT with Pierce™ High-Capacity Streptavidin Agarose to enrich persulfidated proteins. Unbound

proteins and detergent were removed by washing the beads with 28 mL of PBS and 8 mL of H_2O on Pierce™ disposable columns. Enriched proteins were eluted by incubating the beads with 2.25 M ammonium hydroxide solution for 16 h at RT. Eluates were then collected from the columns, lyophilized and subsequently dissolved in digestion buffer (50 mM ammonium bicarbonate (ABC), 1 mM CaCl2). Trypsin was added at enzyme/protein ratio 1/20 and digestion was performed at 37 ºC for 16 h. Samples were desalted using Oasis HLB cartridges (Waters, WAT094225). Peptides were dissolved in 0.1 % TFA, and quality control was performed using an Ultimate 3000 Nano Ultra High-Pressure Chromatography (UPLC) system with a PepSwift Monolithic® Trap 200 µm * 5 mm (Thermo Fisher Scientific).

Sample were analyzed by high-resolution LC-MS/MS using an Ultimate 3000 Nano Ultra High-Pressure Chromatography (UPLC) system (Thermo Fisher Scientific) coupled with an Orbitrap Eclipse™ Tribrid™ Mass Spectrometer via an EASY-spray (Thermo Fisher Scientific). Peptide separation was carried out with an Acclaim™ PepMap™ 100 C18 column (Thermo Fisher Scientific) using a 95 min gradient: 0 min, 3% B; 95 min, 35% B (solvent B corresponds to 84% acetonitrile, 0.1% formic acid) at a flow rate of 250 nL/min. The Orbitrap Eclipse™ was operated in a DDA mode and MS1 survey scans were acquired from m/z 300 to 1,500 at a resolution of 120,000 using the Orbitrap mode. The most intense ions were isolated for 3 s with a 1.2 m/z window and then fragmented by high-energy collision-induced dissociation (HCD) with a normalized collision energy of 32%, considering a dynamic exclusion of 30 s. MS/MS spectra were recorded using normal speed IonTrap mode. Data were evaluated in PEAKS ONLINE software using 15 ppm precursor mass error tolerance, 0.5 Da fragment mass error tolerance, specific trypsin digestion and maximum 2 missed cleavages. For persulfidation detection, NBF

(+163.00961594 Da) on C, K, R, DCP (+168.0786442 Da) on C, N-term acetylation (+42.010565 Da), and methionine oxidation (+15.994915 Da) were added as variable modifications. PSM and proteins were filtered at FDR 1 %.

C. elegans total proteome analysis

D0, D4 and D10 animals were grown and collected as described in previous section. Worm pellets were defrosted by adding 6 M GuHCl in 50 mM ABC. Samples were boiled for 5 min at 95 °C, left to cool down and then sonicated in Biorputor Pico at +4 °C in the presence of glass extraction beads. Debris was removed by centrifugation at 20,000 x g for 10 min at 4 °C. Protein content was determined and 40 µg of protein was taken for further processing. Samples were reduced with 5 mM DTT for 1 h at 37 °C, shaking at 300 rpm and then alkylated for 30 min in the presence of 20 mM iodoacetamide. Digestion and desalting steps were performed as previously described. After quality control, samples were analyzed by high-resolution LC-MS/MS using an Ultimate 3000 Nano Ultra High-Pressure Chromatography (UPLC) system (Thermo Fisher Scientific) coupled with an Orbitrap Eclipse™ Tribrid™ Mass Spectrometer via an EASY-spray (Thermo Fisher Scientific). Peptide separation was carried out with an Acclaim™ PepMap™ 100 C18 column (Thermo Fisher Scientific) using a 155 min gradient: 0 min, 3% B; 155 min, 35% B (solvent B corresponds to 84% acetonitrile, 0.1% formic acid) at a flow rate of 250 nL/min. The Orbitrap Eclipse™ was operated in a DDA mode and MS1 survey scans were acquired from m/z 300 to 1,500 at a resolution of 120,000 using the Orbitrap mode. The most intense ions were isolated for 3 s with a 1.2 m/z window and then fragmented by high-energy collision-induced dissociation (HCD) with a normalized collision energy of 32%, considering a dynamic exclusion of 40 s. MS/MS spectra were recorded using

normal speed IonTrap mode. Data were evaluated with PEAKS ONLINE software using 15 ppm for precursor mass tolerance, 0.5 Da for fragment mass tolerance, specific trypsin digestion, and a maximum of 2 missed cleavages. Carbamidomethylation (+57.021464 Da) on C, N-term acetylation (+42.010565 Da), and methionine oxidation (+15.994915 Da) were added as variable modifications, PSM and proteins were filtered at FDR 1 %. Data was normalized based on the total ion count (TIC).

Data analysis and visualization

Persulfidome datasets were normalized in R using EigenMS script (23). Data filtering and Welch's test for both proteomic datasets were performed in Perseus (24). Volcano and box plots were generated in GraphPad. Venn diagrams were created using BioVenn web application (25). KEGG and GO term enrichments were performed using WormEnrichr enrichment analysis tool and the data were visualized in R (26,27).

4.5. References

1. Brenner S. THE GENETICS OF *CAENORHABDITIS ELEGANS*. Genetics. 1974 May 1;77(1):71–94.
2. Zhang S, Li F, Zhou T, Wang G, Li Z. Caenorhabditis elegans as a Useful Model for Studying Aging Mutations. Front Endocrinol (Lausanne). 2020 Oct 5;11.
3. Qin Z, Johnsen R, Yu S, Chu JSC, Baillie DL, Chen N. Genomic Identification and Functional Characterization of Essential Genes in *Caenorhabditis elegans*. G3 Genes|Genomes|Genetics. 2018 Mar 1;8(3):981–97.
4. David DC, Ollikainen N, Trinidad JC, Cary MP, Burlingame AL, Kenyon C. Widespread Protein Aggregation as an Inherent Part of Aging in C. elegans. PLoS Biol. 2010 Aug 10;8(8):e1000450.
5. Alexander AG, Marfil V, Li C. Use of Caenorhabditis elegans as a model to study Alzheimerâ€™s disease and other neurodegenerative diseases. Front Genet. 2014 Sep 5;5.
6. Zhang WH, Koyuncu S, Vilchez D. Insights Into the Links Between Proteostasis and Aging From C. elegans. Frontiers in Aging. 2022 Mar 18;3.

7. Bansal A, Zhu LJ, Yen K, Tissenbaum HA. Uncoupling lifespan and healthspan in *Caenorhabditis elegans* longevity mutants. Proceedings of the National Academy of Sciences. 2015 Jan 20;112(3).

8. Lee HJ, Noormohammadi A, Koyuncu S, Calculli G, Simic MS, Herholz M, et al. Prostaglandin signals from adult germline stem cells delay somatic ageing of Caenorhabditis elegans. Nat Metab. 2019 Aug 19;1(8):790–810.

9. Wei Y, Kenyon C. Roles for ROS and hydrogen sulfide in the longevity response to germline loss in *Caenorhabditis elegans*. Proceedings of the National Academy of Sciences. 2016 May 17;113(20).

10. Hine C, Harputlugil E, Zhang Y, Ruckenstuhl C, Lee BC, Brace L, et al. Endogenous Hydrogen Sulfide Production Is Essential for Dietary Restriction Benefits. Cell. 2015 Jan;160(1–2):132–44.

11. Zivanovic J, Kouroussis E, Kohl JB, Adhikari B, Bursac B, Schott-Roux S, et al. Selective Persulfide Detection Reveals Evolutionarily Conserved Antiaging Effects of S-Sulfhydration. Cell Metab. 2019 Dec;30(6):1152-1170.e13.

12. Ng LT, Ng LF, Tang RMY, Barardo D, Halliwell B, Moore PK, et al. Lifespan and healthspan benefits of exogenous H2S in C. elegans are independent from effects downstream of eat-2 mutation. NPJ Aging Mech Dis. 2020 Jun 10;6(1):6.

13. Vignane T, Filipovic MR. Emerging Chemical Biology of Protein Persulfidation. Antioxid Redox Signal. 2023 Jul 1;39(1–3):19–39.

14. Filipovic MR, Zivanovic J, Alvarez B, Banerjee R. Chemical Biology of H 2 S Signaling through Persulfidation. 2017; Available from: https://pubs.acs.org/sharingguidelines

15. Narayan V, Ly T, Pourkarimi E, Murillo AB, Gartner A, Lamond AI, et al. Deep Proteome Analysis Identifies Age-Related Processes in C. elegans. Cell Syst. 2016 Aug;3(2):144–59.

16. Walther DM, Kasturi P, Zheng M, Pinkert S, Vecchi G, Ciryam P, et al. Widespread Proteome Remodeling and Aggregation in Aging C. elegans. Cell. 2015 May;161(4):919–32.

17. Mitchell DH, Stiles JW, Santelli J, Sanadi DR. Synchronous Growth and Aging of Caenorhabditis elegans in the Presence of Fluorodeoxyuridine. J Gerontol. 1979 Jan 1;34(1):28–36.

18. Shen X, Wang C, Zhou X, Zhou W, Hornburg D, Wu S, et al. Nonlinear dynamics of multi-omics profiles during human aging. Nat Aging. 2024 Aug 14;

19. Vignane T, Hugo M, Hoffmann C, Katsouda A, Petric J, Wang H, et al. Protein thiol alterations drive aberrant phase separation in aging. bioRxiv [Internet]. 2023 Jan 1;2023.11.07.566021. Available from: http://biorxiv.org/content/early/2023/11/08/2023.11.07.566021.abstract

20. López-Otín C, Blasco MA, Partridge L, Serrano M, Kroemer G. Hallmarks of aging: An expanding universe. Cell. 2023 Jan;186(2):243–78.

21. Feldman N, Kosolapov L, Ben-Zvi A. Fluorodeoxyuridine Improves Caenorhabditis elegans Proteostasis Independent of Reproduction Onset. PLoS One. 2014 Jan 21;9(1):e85964.

22. Stiernagle T. Maintenance of C. elegans. WormBook. 2006;

23. Karpievitch Y V, Taverner T, Adkins JN, Callister SJ, Anderson GA, Smith RD, et al.

Normalization of peak intensities in bottom-up MS-based proteomics using singular value decomposition. 2009;25(19):2573–80. Available from: http://sourceforge.net.

24. Tyanova S, Temu T, Sinitcyn P, Carlson A, Hein MY, Geiger T, et al. The Perseus computational platform for comprehensive analysis of (prote)omics data. Nat Methods. 2016 Sep 27;13(9):731–40.

25. Hulsen T, de Vlieg J, Alkema W. BioVenn – a web application for the comparison and visualization of biological lists using area-proportional Venn diagrams. BMC Genomics. 2008;9(1):488.

26. Kuleshov M V., Jones MR, Rouillard AD, Fernandez NF, Duan Q, Wang Z, et al. Enrichr: a comprehensive gene set enrichment analysis web server 2016 update. Nucleic Acids Res. 2016 Jul 8;44(W1):W90–7.

27. Chen EY, Tan CM, Kou Y, Duan Q, Wang Z, Meirelles GV, et al. Enrichr: interactive and collaborative HTML5 gene list enrichment analysis tool. BMC Bioinformatics. 2013 Dec 15;14(1):128.

5. Role of H_2S and protein persulfidation in cellular stress response

[1]Dunja Petrovic, [2]Jan Lj. Miljkovic, [2]Jordan L. Morris, [1]Milos R. Filipovic

[1]Leibniz Institute for Analytical Sciences, ISAS e.V., Dortmund, Germany

[2]MRC Mitochondrial Biology Unit, University of Cambridge, Keith Peters Building, CB2 0XY, UK

Corresponding author: Milos R. Filipovic

In preparation

Author contributions:

Dunja Petrovic conducted all the experiments with the exception of mitochondrial imaging. She also performed the analysis and visualization of all the presented results, apart from those related to mitochondrial imaging. Jan Miljkovic and Jordan L. Morris were responsible for mitochondrial imaging, including the subsequent analysis and data representation. Milos R. Filipovic conceived and supervised the entire study, designed the experiments and analyzed and interpreted data.

5.1. Introduction

Cellular processes are compartmentalized within distinct structures and organelles, each contributing to cellular homeostasis through specific functions. Mitochondria, often referred to as the energetic hubs of the cells, are not only central for energy and cofactor production, but also serve as a primary source of ROS production (1,2). On the other hand, ER and Golgi are primarily responsible for folding, maturation, and secretion of proteins - processes highly dependent on redox reactions (3,4). Due to their high metabolic activity and abundance of reactions that can result in cellular damage, cells have developed organelle-specific protective mechanisms accompanied with more general stress response to maintain cellular homeostasis. Although initiated in a single organelle, the stress response is usually not limited to the place of its generation, therefore influencing the metabolism of the whole cell. Integrated stress response (ISR) is a conserved pathway in eukaryotic cells which is activated upon wide spectrum of stimuli including the stress induced in mitochondria, Golgi apparatus and endoplasmic reticulum (ER) (5–7). This pathway converges on the phosphorylation of the alpha subunit of eIF2 (eIF2α), which results in remodeling of global translation and activation of transcriptional and metabolic processes required for cell survival (8). ISR can be both protective and maladaptive depending on the physiological context. Persistent activation of ISR leads to cell death and it is one of the hallmarks of neurodegenerative diseases including Alzheimer's disease, Parkinson's disease and Huntington's disease (9). Conversely, loss-of-function mutations of PERK and GCN2 lead to development of metabolic disorders in humans and animal models (10–12). Thus, both the activation and proper resolution of ISR are crucial for maintaining cellular homeostasis.

While mitochondrial and ER stress responses have been extensively studied, much less is known about Golgi-induced stress response. A common feature of ISR activation across all three organelles is ATF-4-dependent upregulation of CSE expression which leads to increased levels of its downstream metabolites such as cysteine, GSH and H_2S (5,7,13–15). This suggests that CSE might act as both an organelle-specific and general protective factor potentially playing a role in the mediation and termination of ISR. Induction of Golgi stress and ISR-dependent upregulation of CSE levels in cellular model of Huntington's disease improves survival in cysteine-deprived media (5).

The aim of this study is to explore CSE-driven changes in the persulfidome under Golgi- and mitochondria-induced stress and to identify potential targets whose activity may be altered by changes in their persulfidation status. Furthermore, we are interested in seeing how absence of CSE impacts activation, mediation and resolution of ISR.

5.2. Results

Golgi stress in WT Mouse Embryonic Fibroblast (MEF) was induced by treating the cells with 5 μM monensin for 18 h (5). Under these conditions cellular proliferation and growth were inhibited, although without induction of cellular death (data not shown). We applied dimedone switch method to selectively label and enrich persulfidated proteins and quantified 3018 proteins present in at least three out of four biological replicates in each condition. Principal component analysis (PCA) showed clear separation of two datasets (Figure 5.1A). Further analysis using 30% change and p value cutoff of 0.05 revealed 530 proteins significantly changing between two conditions, out of which 246 had increased while 284 proteins had decreased PSSH levels (Figure 5.1B, Supplementary table S5.1).

Gene ontology (GO) analysis revealed distinct biological terms enriched for two groups. Proteins with lower persulfidation were involved in biological processes such as cytoplasmic and mitochondrial translation, ribosome assembly, succinate metabolism and respiration (Figure 5.1C,D, Supplementary table S5.1). In agreement with this, mitochondria, ribosomal complexes as well as components involved in cellular division were among the most enriched cellular components (Figure 5.1E). On the other hand, proteins with increased persulfidation were mostly involved in biosynthetic processes such as steroid, cholesterol and amino acid synthesis but also vesicular transport and organization of extracellular matrix (Figure 5.1C,D, Supplementary table S5.1). All the components of endomembrane system including Golgi apparatus, ER and lysosome were also significantly enriched (Figure 5.1E). These results suggest that monensin induces global remodeling of cellular metabolic pathways which is not exclusively maintained within the limits of endomembrane system but also involves mitochondrial and cytoplasmic processes.

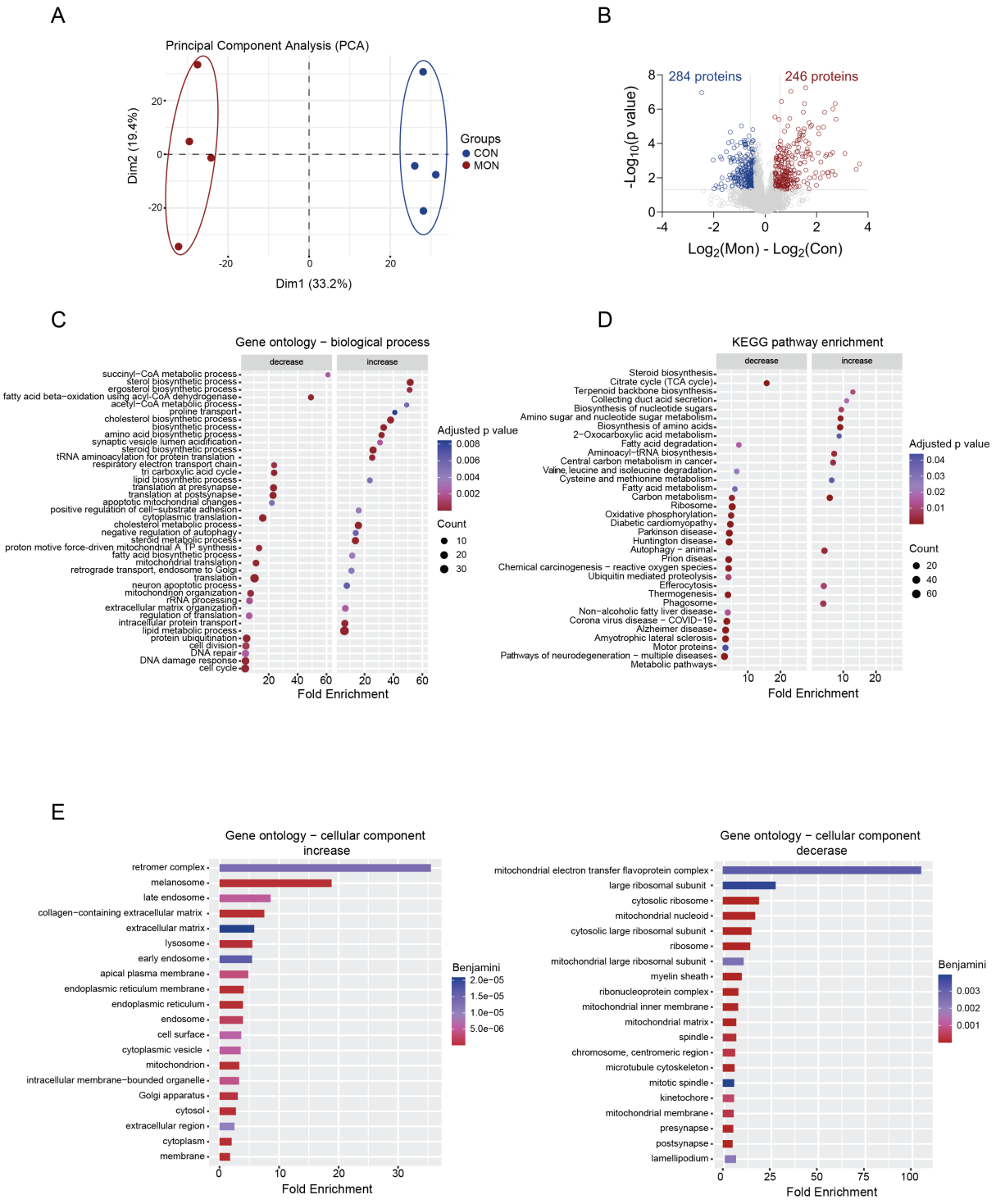


Figure 5.1 Chemoproteomic analysis of protein persulfidation reveals substantial alternations in persulfidome upon monensin-induced Golgi stress.

(**A**) Principal component analysis (PCA) showing the reproducibility of quantification across all analyzed replicates. (**B**) Volcano plot analysis of persulfidome changes induced by monensin. Dots in red represent proteins with significantly increased PSSH levels while blue dots correspond

to the proteins with significantly lower PSSH levels (Welch's test, n = 4; applied thresholds: p value<0.05, log2 fold change 0.38). (**C**) Gene Ontology (GO) term enrichment (biological process) of 530 proteins with significantly changing persulfidation levels. Significant GO terms passed the Benjamini adjusted p value threshold of 0.01. (**D**) KEGG pathway enrichment analysis of the same set of proteins like in (C). Significant KEGG terms passed the Benjamini adjusted p value threshold of 0.05. (**E**) Gene Ontology (GO) term enrichment (cellular component) of the same set of proteins like in (C) and (D). Significant GO terms passed the Benjamini adjusted p value threshold of 0.01. Enriched terms for proteins with significantly increasing and decreasing PSSH levels were plotted separately.

To examine whether the corresponding changes in persulfidation levels are dependent on the overall proteome remodeling, we also performed label free full proteome analysis of the same samples before the switch step with DCPBio. We quantified 3445 proteins present in minimum three out of four biological replicates in each condition. We then overlapped list of all quantified proteins in both datasets and filtered for proteins only present in persulfidome. We detected 2586 common proteins in both datasets (~ 75%) with 472 proteins (out of initial 530 proteins) having significantly changing PSSH levels (Figure 5.2A). In the next step we selected all significantly changing proteins in persulfidome data using only p value threshold of 0.05 (fold change cutoff of 30% was not used for this purpose) and normalized the change in persulfidome to the change of total protein levels. When we applied the same fold change cutoff as for the non-normalized data (30 %, log2 change ± 0.38) we detected 149 proteins with decreased and 83 proteins with increased PSSH levels which in total corresponds to approximately 9% of detected proteins compared to 18% in non-normalized dataset (Figure 5.2B). Therefore, normalization halved the number of significantly changing persulfidated proteins. When we overlapped significantly changing proteins before and after normalization, we got 195 proteins commonly changing while more than 270 proteins lost the significance after

normalization (Figure 5.2C, Supplementary table S5.2). Although the obtained numbers are useful to get general information on the influence of normalization on the number of changing proteins it still does not answer whether the change of protein targets that stay significant before and after normalization follows the same trend. To visualize the potential changes of individual protein targets, we used double scatter plot representation. Data before normalization to protein amount was plotted on X axis, while the data after normalization was plotted on Y axis. We then used Log2 cutoff ± 0.38 to filter both data sets simultaneously and obtained 9 different clusters depending on the pattern of change in each dataset (Figure 5.2D). For example, dark red dots represent proteins whose PSSH levels were lower in the treatment compared to control in non-normalized set but then significantly increased upon normalization. This observation suggests that decrease in total protein amount upon treatment is much bigger compared to the decrease in PSSH levels of the same protein, leading to overall higher persulfidation upon treatment with monensin. On the other hand, dark blue dots correspond to the proteins which had increased persulfidation before normalization, but they significantly decreased upon normalization (Figure 5.2D). Substantial number of proteins preserved the same direction of change after normalization (desaturated blue and red dots), while light grey dots present proteins that lost significance upon normalization (Figure 5.2D). When we performed enrichment analysis for the proteins significantly changing after the normalization step, the numbers of identified terms decreased with few differences compared to the analysis of non-normalized samples (Figure 5.2E-G). Although the pattern did not drastically change, interestingly, proteins involved in translation and ribosome assembly now had increased PSSH levels, suggesting that the drop in protein abundance was much more profound (Figure 5.2E). KEGG pathway enrichment revealed that proteins with lower post-

normalization PSSH levels are involved in pathways of neurodegeneration, including Alzheimer disease (Figure 5.2F).

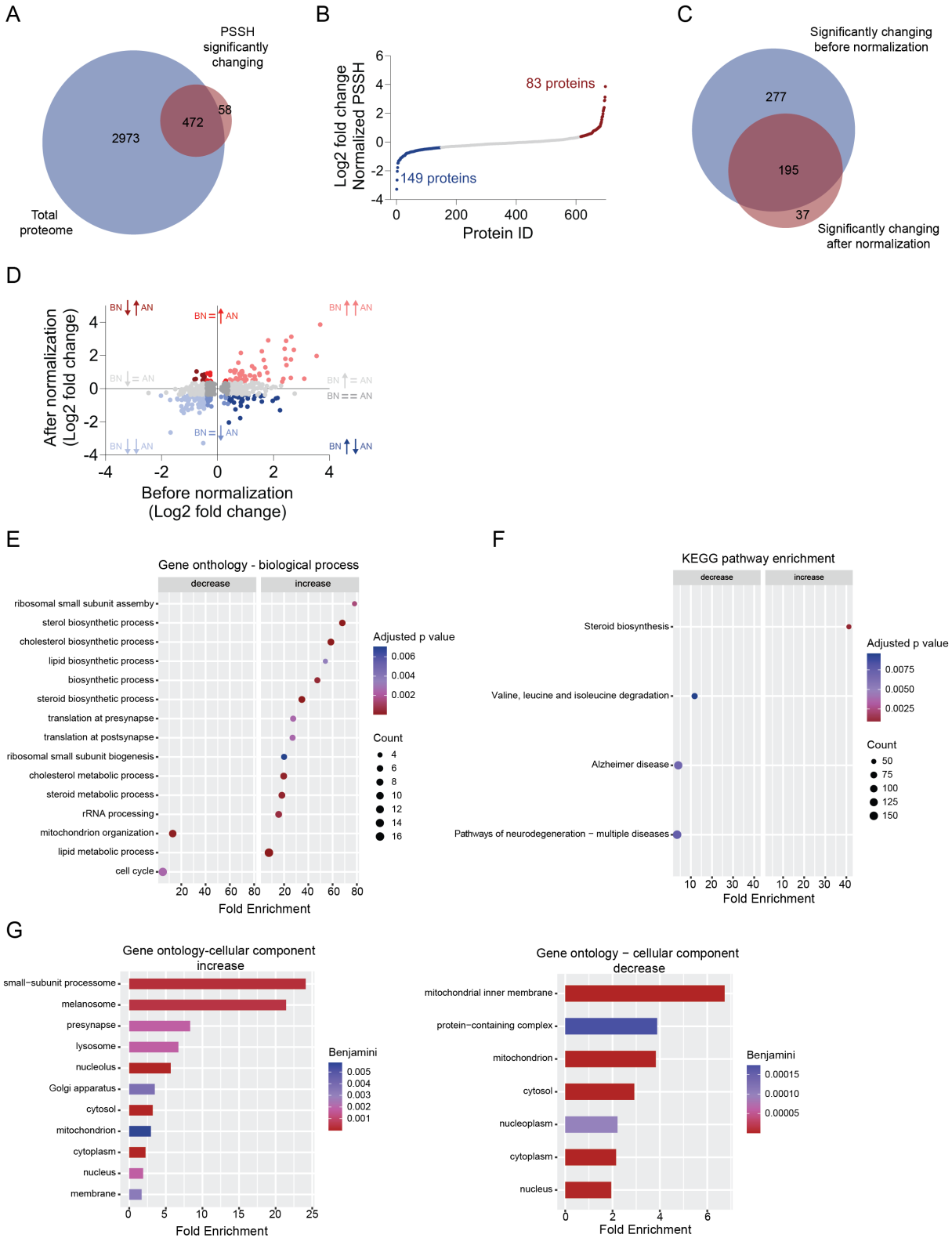


Figure 5.2 Effects of persulfidome normalization to total protein levels.

(**A**) Venn diagram representing the overlap between all proteins quantified in total proteome and proteins with significantly changing PSSH levels. 58 proteins from persulfidome data set could not be found in total proteome dataset. (**B**) Waterfall plot showing the effect of normalization of proteins in persulfidome dataset (filtered for the ones which pass p value threshold of 0.05 based on Welch's test) to total protein. Dots in red correspond to proteins whose PSSH levels are significantly higher (monensin vs control) after normalization, while blue dots present proteins with significantly lower PSSH after normalization. The log2 fold change of 0.38 was used as a threshold for normalized proteins. (**C**) Venn diagram showing the overlap of significantly changing proteins before and after normalization to total protein. (**D**) Double scatter plot showing the changes of individual proteins before and after normalization. Log2 fold change values correspond to the difference between monensin and control datasets calculated in Welch's test. Each color corresponds to the proteins with the same pattern of change (the labels of the same colors indicate the direction of protein's change before and after normalization; BN – before normalization, AN – after normalization). (**E**) GO term enrichment (biological process) of 232 proteins with significantly changing persulfidation levels after normalization. Significant GO terms passed the Benjamini adjusted p value threshold of 0.01. (**F**) KEGG pathway enrichment analysis of the same set of proteins like in (E). Significant KEGG terms passed the Benjamini adjusted p value threshold of 0.05. (**G**) Gene Ontology (GO) term enrichment (cellular component) of the same set of proteins like in (E) and (F). Significant GO terms passed the Benjamini adjusted p value threshold of 0.01. Enriched terms for proteins with significantly increasing and decreasing PSSH levels were plotted separately.

We also had a closer look at full proteome dataset independently of persulfidome (Figure 5.3A, Supplementary table S5.3). Monensin induced significant protein remodeling with 352 proteins significantly changing (50% change, p value < 0,05) out of which 105 had higher abundance and 247 had lower abundance compared to the control (Figure 5.3B). One of the most prominently upregulated proteins was CSE (log2 fold difference 1.76), confirming its importance in mediation of Golgi-induced stress response (Figure 5.3C). Enrichment analysis of significantly changing proteins revealed the similar

pattern as observed for persulfidome analysis. The most downregulated processes were mitochondrial and cytoplasmic translation as well as mitochondrial respiration, while all cellular resources were directed towards amino acid and lipid synthesis (Figure 5.3E-F, Supplementary table S5.3).

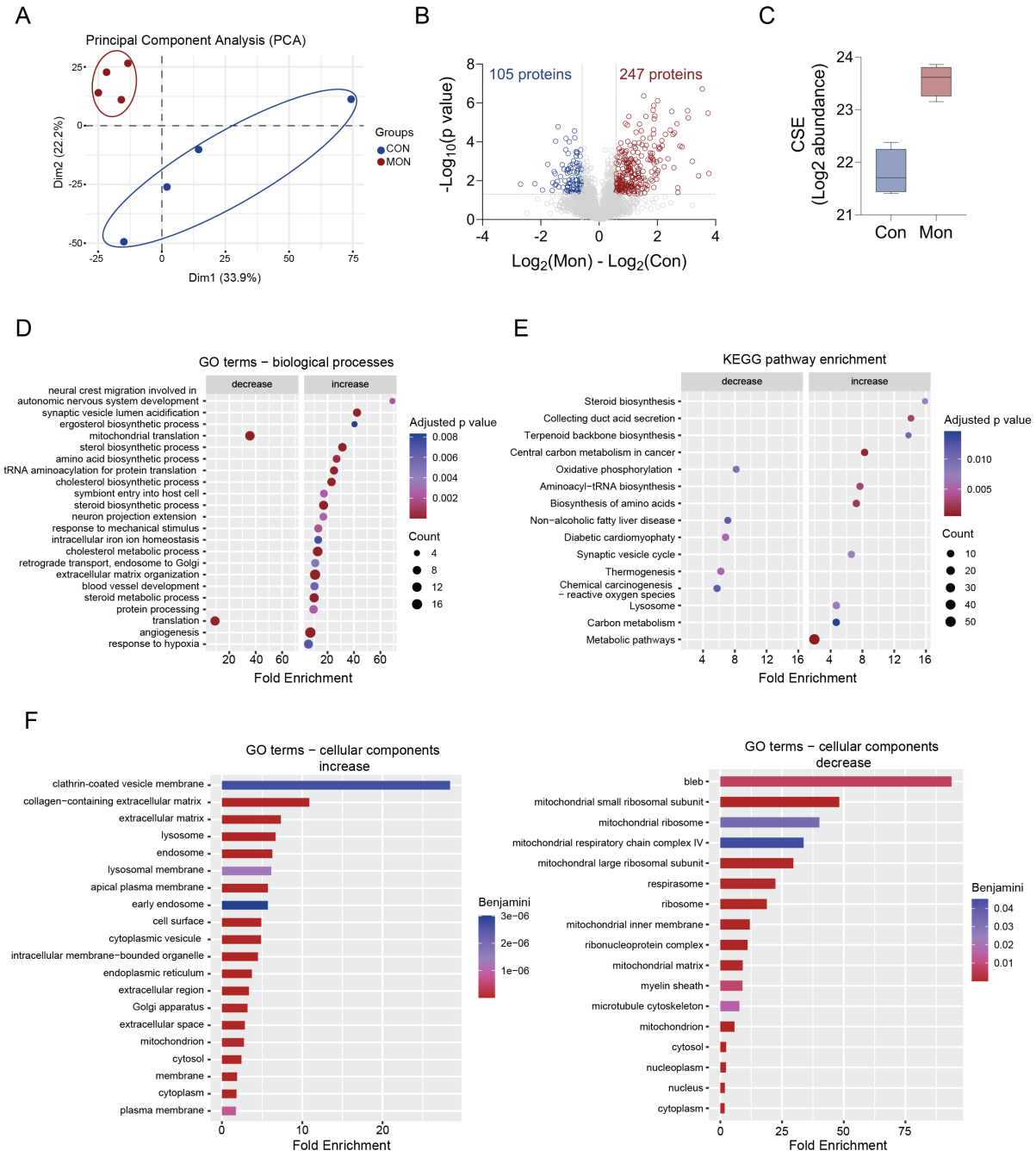


Figure 5.3 Proteome remodeling in monensin-induced Golgi stress.

(**A**) Principal component analysis (PCA) showing the reproducibility of quantification across all analyzed replicates. (**B**) Volcano plot analysis of proteome changes induced by monensin. Dots in red represent proteins significantly increased in abundance while blue dots correspond to the proteins with decreased abundance (Welch's test, n = 4; applied thresholds: p value<0.05, log2 fold change 0.58). (**C**) Statistically significant increase in CSE levels upon monensin treatment. The values were extracted from total proteome data (p value <0.05, log2 fold change 1.76). (**D**) Gene Ontology (GO) term enrichment (biological process) of 352 significantly changing proteins. Significant GO terms passed the Benjamini adjusted p value threshold of 0.01. (**E**) KEGG pathway enrichment analysis of the same set of proteins like in (D). Significant KEGG terms passed the Benjamini adjusted p value threshold of 0.01. (**F**) Gene Ontology (GO) term enrichment (cellular component) of the same set of proteins like in (D) and (E). Significant GO terms passed the Benjamini adjusted p value threshold of 0.01. Enriched terms for proteins with significantly increasing and decreasing PSSH levels were plotted separately.

We further wanted to examine how CSE and H_2S-driven persulfidation modulates mitochondrial stress response using WT and CSE knockout cells ($CSE^{-/-}$). Mitochondrial activation of ISR can be induced by different stressor, but we opted for rotenone, an inhibitor of mitochondrial complex I. We exposed cells to 0.5 µM rotenone during different times and monitored the changes in cellular physiology and stress response. We confirmed rotenone-dependent induction of ISR through increased phosphorylation of eIF2α and upregulation of ATF4 (Figure 5.4A). The activation of ISR was present in both cell lines, suggesting that $CSE^{-/-}$ could also initiate the response. Rotenone treatment also upregulated CSE in WT cells in a time-dependent manner (Figure 5.4B,C). If the CSE-dependent H_2S production drives protein persulfidation we expect to see a global increase in persulfidation levels of WT but not in $CSE^{-/-}$. Cells were exposed to stressor up to 8 h and persulfidation was measured using dimedone-switch method adapted for in-gel detection. Analysis of the three biological replicates revealed consistent and time-dependent increase of PSSH levels in WT but not in $CSE^{-/-}$ cells (Figure 5.4B). The

obtained results suggest that the persulfidation changes are in agreement with changes in CSE expression (Figure 5.4B).

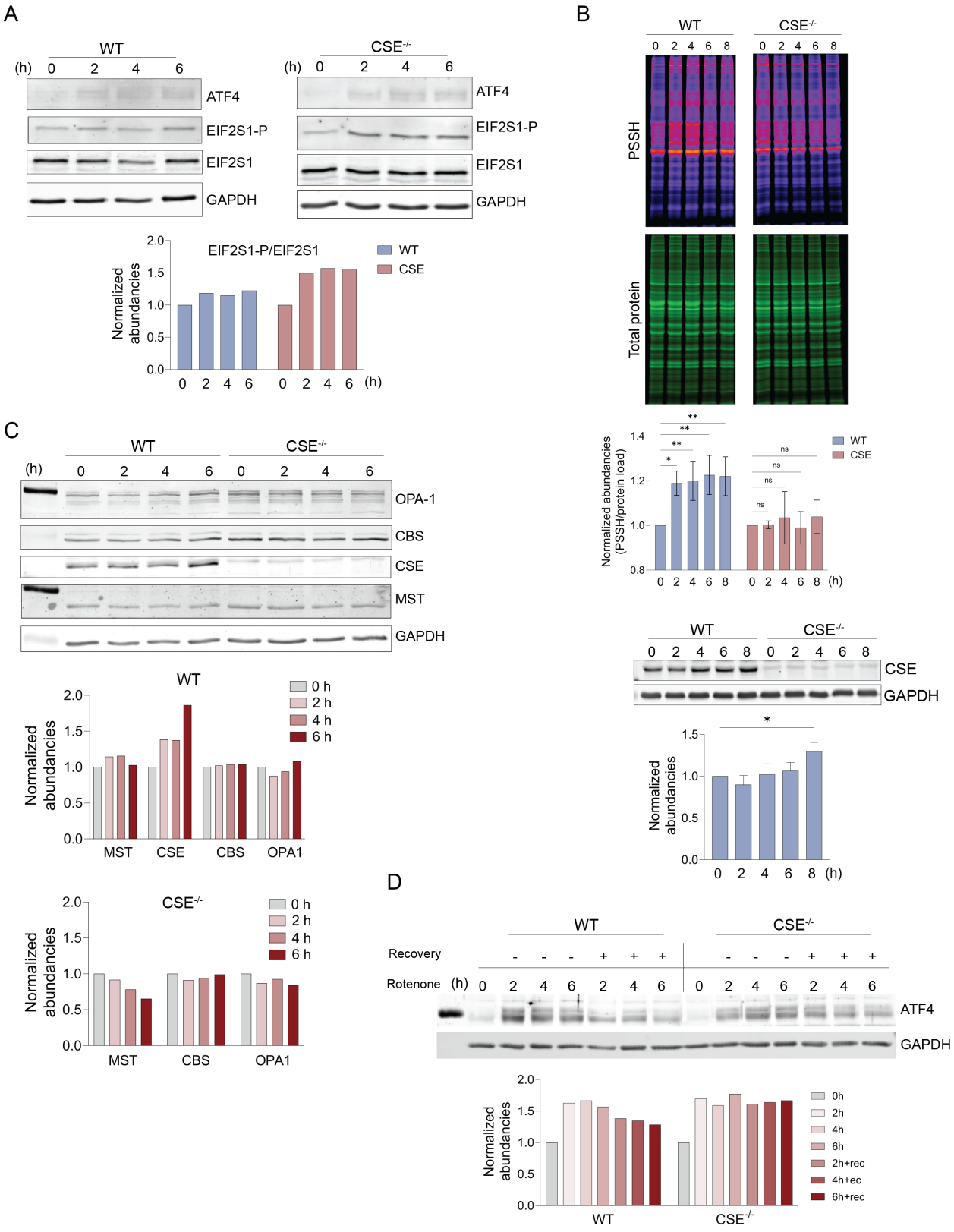


Figure 5.4 Mitochondrial stress increases persulfidation in CSE-dependent manner.

(**A**) ISR is activated in both WT and $CSE^{-/-}$ upon exposure to 0.5 μM rotenone. (**B**) Rotenone increases persulfidation in WT but not $CSE^{-/-}$ cells. This matches the time-dependent upregulation of CSE. (**C**) Rotenone does not upregulate other H_2S producing enzymes, neither induces OPA-1 proteolytic cleavage. (**D**) ISR induced in WT and $CSE^{-/-}$ differs in both amplitude and duration under same the conditions.

We then examined whether other H_2S enzymes could contribute to the observed effects. However, we did not observe the changes in expression of CBS and MST, suggesting that the increase in persulfidation is CSE dependent (Figure 5.4C). ISR initiated in mitochondria is initially sensed by mitochondrial protease OMA1 which cleaves DELE1 resulting in a formation of its short from required for activation of HRI kinase in the cytoplasm (16). Under stress, OMA1 can also cleave OPA1, a protein involved in cellular fusion. OPA-1 exists in several different isoforms and the change in their ratios is induced by different mitochondrial stressors (17). However, rotenone did not induce the cleavage of OPA-1 suggesting that it mainly acts through DELE1 and HRI (Figure 5.4C). We next questioned whether lack of CSE results in different amplitude and duration of stress response in $CSE^{-/-}$. Although examination of the acute stress can give us some insights, monitoring the cell recovery upon removal of stressor indicates the cell's capacity to restore basal cellular functions and overcome stress-induced damage.

We therefore treated cells for several hours, removed the stressor and left cells to recover for 17 h in regular media. While both cell lines showed strong upregulation of ATF4 in the acute phase, the response was much stronger in WT compared to $CSE^{-/-}$ (Figure 5.4D). Interestingly, removal of the stressor and termination of the response had different dynamics. While in WT, initial activation was profound, the ATF4 expression

significantly reduced upon recovery. However, the response in $CSE^{-/-}$ stayed continuously high even after stressor removal. This observation might suggest that $CSE^{-/-}$ cannot activate ISR to its full capacity and the mechanisms coping with the cells damage need to be maintain at higher levels for longer time periods or that H_2S produced by CSE is playing a role in resolving the ISR. On the other hand, persistent ISR activation results in apoptosis, so it would be useful to monitor whether $CSE^{-/-}$ enter apoptosis under sublethal concentrations for WT or they require much longer time to recover.

Mitochondrial dynamics and morphology disruption are the first hallmarks of mitochondrial stress. Acute treatment with rotenone induces fragmentation of mitochondrial network, therefore we chose this parameter to visualize the potential difference in WT and $CSE^{-/-}$ response. We opted for 1 h treatment and 1 μM rotenone concentration as it was sufficient to induce the difference. While different parameters of mitochondrial morphology did not significantly differ between WT and $CSE^{-/-}$, rotenone treatment induced substantial remodeling of mitochondrial network in $CSE^{-/-}$ resulting in decrease in mitochondrial length and area which is even more profound in the recovery phase (Figure 5.5A). This suggest that lack of CSE decreases the capacity of ISR to cope with the stress. We decided to try another mitochondrial stressor and see if we could observe the same effects. 3-nitropropionic acid is (3-NP) is a known suicide inhibitor on mitochondrial complex II which also affects mitochondrial morphology (18). 3-NP induced certain level of fragmentation in $CSE^{-/-}$, and although significant, this effect was not as severe as in presence of rotenone. We then wanted to check whether activation 3-NP induces ISR but surprisingly ATF4 and CSE levels stayed unchanged. Furthermore, none of the other H_2S producing enzymes were upregulated and the changes in mitochondrial dynamics were not dependent on OPA-1 processing (Figure 5.5C). Lack of ISR activation

might explain the difference in the observed effects of two different stressor (Figure 5.5C). Increased sensitivity of $CSE^{-/-}$ might be still the consequence of insufficient H_2S production required to cope with increasing ROS levels.

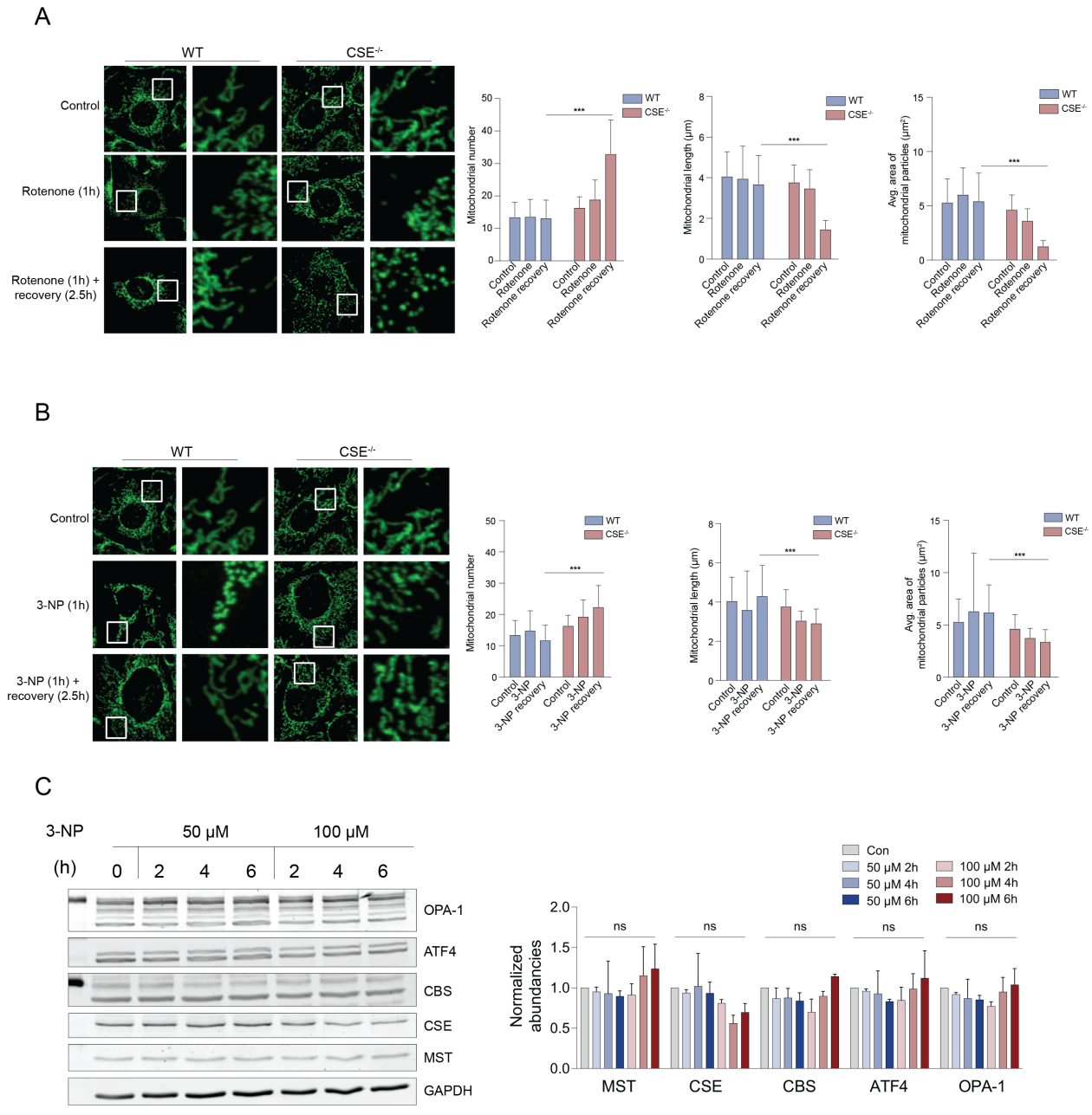


Figure 5.5. Treatment with rotenone significantly affects mitochondrial morphology.

(**A**) Representative images and quantification of mitochondrial morphology upon rotenone treatment using TOM20 immunofluorescence. $CSE^{-/-}$ cells are more sensitive to rotenone, even

after removal of the stressor. (**B**) Representative images and quantification of mitochondrial morphology upon 3-nitropropionic acid (3-NP) treatment using TOM20 immunofluorescence. 3-NP induces fragmentation of mitochondria in $CSE^{-/-}$. (**C**) 3-NP does not activate ISR, nor it affects the levels of H_2S producing enzymes in WT cells. The analysis was performed using one-way ANOVA (n=2).

5.3. Discussion

This chapter provides an insight into the potential role of H_2S and protein persulfidation in regulation of cellular stress response induced by disruptions in Golgi apparatus function and mitochondrial respiration. CSE is a known mediator of ISR and the primary source of protective molecules such as GSH and H_2S. While GSH is mostly involved in cellular redox reactions, the role of H_2S extends beyond this mechanism. Studies on ER-induced ISR revealed that H_2S becomes the dominant product of CSE during the later phases of stress response where its elevated levels modulate stress response and cellular metabolism through persulfidation of specific protein targets (15,19).

Although the initial response to stressors is similar across different organelles, previous studies have demonstrated that inhibiting distinct functions even within the same organelle leads to expression of different genes and activates unique downstream signaling pathways (7). Having this is mind, we wanted to compare the potential overlap and unique aspects of stress responses initiated in different organelles and investigate the importance of CSE and its activity in these cellular conditions.

We focused on studying Golgi stress since the mechanisms underlaying its stress response are still vague. Monensin, a known inducer of ATF4-dependent CSE expression, was used to better characterize its effect on the persulfidome and proteome remodeling

(5). We observed several ISR-related features such as decrease in global translation in both mitochondria and cytoplasm alongside reduced mitochondrial respiration. These responses likely help prevent further damage caused by faulty maturation and transport of newly synthetized proteins due to Golgi dysfunction. Proteomic analysis revealed upregulation of CSE with its abundance increasing more than three-fold, but also general upregulation of biosynthetic processes involved in synthesis of lipids and amino acids. Since the Golgi is a membrane-rich organelle crucial for vesicular trafficking and membrane maintenance, the upregulation of cholesterol and lipid biosynthesis may serve as a compensatory mechanism to restore damaged membranous structures. Our results also suggest that Golgi stress results in the remodeling of extracellular matrix and cellular contacts. This is not surprising having in mind that Golgi is the central hub for post-translational modification and proteolytic processing of matrix components (20). Some of the most upregulated proteins in the total proteome dataset included Amyloid-beta A4 protein (APP) and Integral membrane protein 2B (ITM2B/BRI2). APP is a type I membrane protein that undergoes extensive proteolytic cleavage during its transport through exocytic and endocytic pathways. Its accumulation under Golgi stress has been previously documented (21). Dysregulated synthesis of its proteolytic amyloid beta (Aβ) peptides results in their extracellular accumulation and amyloid plaque formation, a hallmark of Alzheimer's disease (AD) (22). On the other hand, BRI2 is a known suppressor of Aβ proteolytic formation, therefore preventing its aggregation (23). Our results suggest that induction of Golgi stress promotes accumulation of APP through increased expression of BRI2. This might suggest that induction of mild Golgi stress can reduce Aβ plaque formation. Prior studies have already shown that Golgi fragmentation and disrupted

communication between Golgi and ER largely contribute to development of neurodegenerative diseases (24,25).

In addition to stress-induced changes in total proteome, persulfidome also undergoes extensive remodeling which does not always align with the observed proteome pattern. Previous studies have shown that monensin increases total H_2S levels as well as global persulfidation (13,14,26). Our proteomic analysis revealed both upregulation and downregulation of persulfidation, with more than 500 significantly changing targets. The discrepancy between these findings can be attributed to methodological differences. In-gel detection of protein persulfidation enables simultaneous detection of both PSSH and protein levels from the same sample, allowing for direct comparison. In contrast, proteomic analysis requires separate preparation and examination of persulfidome and total proteome samples, making direct comparison more complex and prone to inaccuracies. Furthermore, analysis of enriched persulfidome might results in the detection of generally low abundant proteins which are hardly detected in a complex sample without including additional steps to increase sample coverage. Comparison of persulfidome and total proteome datasets in our study led to loss of almost 60 proteins which were significantly changing in persufidome dataset but could not be detected in total proteome. Therefore, the normalization step performed in this study is more of a qualitative character and should be interpreted with caution. Interestingly, some of the most enriched persulfidated targets which stay significant after normalization are associated with pathways involved in neurodegenerative diseases. Proteins belonging to this group are regulatory subunits of 26S proteasome and regulatory subunits of NADH dehydrogenase which forms Complex I in mitochondria. Proteins with significantly higher persulfidation levels were mostly involved in steroid and cholesterol biosynthesis

pathways but also lysosomal protein degradation. Interestingly, cathepsins belonging to cysteine cathepsin family were among the proteins with the highest persulfidation levels. This suggest that persulfidation of cysteine residues can play important role in the regulation of their function and proteolysis of damaged and misfolded proteins. In vitro experiments on single proteins could provide valuable insights into the potential persulfidation-mediated regulation of their activity. Both cathepsin B and Z contain multiple cysteines residues, which may result in differential outcomes depending on the number of modified residues.

CSE-mediated protein persulfidation is also required for proper mediation of ISR during mitochondrial stress. Cells lacking CSE exhibit lower persulfidation and prolonged activation of ATF4 even upon removal of the stressor. Several factor could explain this: protective mechanism involved in restoration of the basal cellular function may be insufficient to counteract the extent of induced damage, resulting in apoptosis. Alternatively, CSE might also have an important role in the termination of ISR which could also explain the sustained activation of ATF-4. Profound mitochondrial fragmentation in $CSE^{-/-}$ cells suggests that they are more sensitive compared to WT when exposed to the same concentration of rotenone. Moreover, the toxicity of this mitochondrial inhibitor increases during recovery, indicating that the effects of acute stress become chronic even in the absence of the stressor. Use of another mitochondrial inhibitor, 3-NP, on the other hand showed that CSE might be also required for the ISR-independent cellular response, although to a lesser extent compared to the ISR-related mechanisms.

The dysfunction of organelles observed following treatment with various compounds closely mirrors the conditions observed in different pathological states. Golgi fragmentation is a hallmark of AD, while rotenone-induced mitochondrial dysfunction

correlates well with Parkinson's disease (25,27). These conditions are also associated with the perturbation in H_2S metabolism. Therefore, our findings shed the light on potentially much more complex role of H_2S in both physiological and pathological conditions. This also does not exclude the possibility that upon chronic activation of ISR due to the disruption of certain signaling components, H_2S might transition from protective to detrimental role.

5.4. Experimental Methods

Cell culture

WT and $CSE^{-/-}$ mouse embryonic fibroblasts (MEF) are kind gift from Professor Bindu Paul (Johns Hopkins University). Cell lines were generated from CSE+/+ and $CSE^{-/-}$ mice and immortalized using SV40T antigen (28). MEFs were grown in DMEM (4.5 g/L glucose) supplemented with 2 mM glutamine, 1% penicillin-streptomycin and 10% calf serum at 37 ^oC and 5%CO_2.

Persulfidome analysis

For persulfidome analysis, WT MEF grown in T-75 flask were exposed to 5 μM monensin (original stock in absolute ethanol, diluted 1000 times in cell medium) for 18 h and immediately lysed to selectively label persulfides. Briefly, cells were washed twice with cold PBS and 3 ml of lysis buffer was added (50 mM HEPES, 1 mM EDTA, 0.1 mM Neocuproine, 1% IGEPAL, 2% SDS, pH 7.4, supplemented with 5 mM NBD-Cl and 1% protease inhibitor). Cells were scraped, collected into an epi tube and incubated at 37 ^oC for 2 h. Proteins were precipitated twice by methanol/chloroform precipitation

(water/methanol/chloroform, 4:4:1, v/v/v) and centrifuged at 15 000 x g for 15 min at 4 °C after each cycle. Obtained protein pellets were washed twice with ice-cold methanol and left to dry at room temperature (RT). Samples were then resuspended in PBS supplemented with 0.2 % SDS, protein concentration was determined using DC Protein Assay (Biorad) and equal amounts of proteins (800 µg) were incubated with Pierce™ NeutrAvidin™ Agarose beads to remove endogenously biotinylated proteins. After 2 h of mixing at RT, supernatant was removed and precipitated once. Proteins were suspended in PBS supplemented with 2 % SDS and incubated for 1.5 h at 37 °C with 250 µM DCP-Bio1 to specifically label persulfides. Excess probe was removed by precipitation and obtained pellets were dissolved in PBS supplemented with 0.1% SDS and adjusted to equal protein amount. Samples were then incubated for 4 h at RT with Pierce™ High-Capacity Streptavidin Agarose to enrich persulfidated proteins. Unbound proteins and detergent were removed by washing the beads with 28 mL of PBS and 8 mL of H_2O on Pierce™ disposable columns. Enriched proteins were eluted by incubating the beads with 2.25 M ammonium hydroxide solution for 16 h at RT. Eluates were then collected from the columns, lyophilized and subsequently dissolved in digestion buffer (50 mM ammonium bicarbonate (ABC), 1 mM CaCl2). Trypsin was added at enzyme:protein ratio 1:20 and digestion was performed at 37 °C for 16 h. Samples were desalted using Oasis HLB cartridges (Waters, WAT094225). Peptides were dissolved in 0.1 % TFA, and quality control was performed using an Ultimate 3000 Nano Ultra High-Pressure Chromatography (UPLC) system with a PepSwift Monolithic® Trap 200 µm * 5 mm (Thermo Fisher Scientific).

Sample were analyzed by high-resolution LC-MS/MS using an Ultimate 3000 Nano Ultra High-Pressure Chromatography (UPLC) system (Thermo Fisher Scientific) coupled

with an Orbitrap Eclipse™ Tribrid™ Mass Spectrometer via an EASY-spray (Thermo Fisher Scientific). Peptide separation was carried out with an Acclaim™ PepMap™ 100 C18 column (Thermo Fisher Scientific) using a 95 min gradient: 0 min, 3% B; 85 min, 25% B; 95 min, 35% B (solvent B corresponds to 84% acetonitrile, 0.1% formic acid) at a flow rate of 250 nL/min. The Orbitrap Eclipse™ was operated in a DDA mode and MS1 survey scans were acquired from m/z 300 to 1,500 at a resolution of 120,000 using the Orbitrap mode. The most intense ions were isolated for 3 s with a 1.2 m/z window and then fragmented by high-energy collision-induced dissociation (HCD) with a normalized collision energy of 32%, considering a dynamic exclusion of 30 s. MS/MS spectra were recorded using normal speed IonTrap mode.

Data were evaluated in PEAKS ONLINE software using 15 ppm precursor mass error tolerance, 0.5 Da fragment mass error tolerance, specific trypsin digestion and maximum 2 missed cleavages. For persulfidation detection, NBF (+163.00961594 Da) on C, K, R, DCP (+168.0786442 Da) on C, N-term acetylation (+42.010565 Da), and methionine oxidation (+15.994915 Da) were added as variable modifications. PSM and proteins were filtered at FDR 1 %.

Total proteome analysis

For total proteome analysis used to normalize persulfidome data, 100 µg of original NBD-Cl samples (before DCPBio step) were diluted with PBS and precipitated to remove traces of SDS. Protein pellets were resuspended in 6 M guanidine hydrochloride (GuHCl) in 50 mM ABC and 40 µg of protein was taken from each sample for further steps. Samples were diluted with digestion buffer to reach final concentration of 0.3 M GuHCl. Obtained peptides were further processed in the same way as explained for persulfidome

analysis. Samples were analyzed using a 125 min gradient: 0 min, 3% B; 117 min, 28% B; 125 min, 35% B at a flow rate of 250 nL/min. All other parameters were the same as for persulfidome data except dynamic exclusion which was set at 40 s.

Data were evaluated in PEAKS ONLINE software using 15 ppm precursor mass error tolerance, 0.5 Da fragment mass error tolerance, specific trypsin digestion and maximum 2 missed cleavages. For total proteome detection, NBF (+163.00961594 Da) on C, K, R, N-term acetylation (+42.010565 Da), and methionine oxidation (+15.994915 Da) were added as variable modifications. PSM and proteins were filtered at FDR 1 %. Total proteome data were normalized based on the total ion count (TIC).

In-gel detection of protein persulfidation

WT MEFs were exposed to 0.5 µM rotenone for different time periods. At the end of the treatment, cells were washed twice with cold PBS and lysed in 1 ml of lysis buffer (50 mM HEPES, 1 mM EDTA, 0.1 mM Neocuproine, 1% IGEPAL, 2% SDS, pH 7.4, supplemented with 5 mM NBD-Cl and 1% protease inhibitor). Cells were scraped, collected into an epi tube and incubated at 37 ^{o}C for 2 h. Proteins were precipitated twice by methanol/chloroform precipitation (water/methanol/chloroform, 4:4:1, v/v/v) and centrifuged at 15 000 x g for 15 min at 4 ^{o}C after each cycle. Obtained protein pellets were washed twice with ice-cold methanol and left to dry at room temperature (RT). Proteins were suspended in 50 mM HEPES supplemented with 2% SDS, adjusted to same concentrations (3 mg/ml) and switch step using Daz2:Cy5 click mix was performed for 1h at 37 ^{o}C. Samples were then precipitated twice, and dried pellets were dissolved in 50 mM HEPES supplemented with 2 % SDS and adjusted to the same protein concentrations. 4X Laemlli sample buffer (Biorad) supplemented with 10% β-

mercapthoethanol was added at sample:Laemlli buffer ratio 3:1 and samples were then boiled for 5 min at 95 ^oC to fully reduce disulfide bonds and denaturate proteins. Following SDS page, gels were recorded on Amersham Typhoon at 635 nm for Cy5, and 488 nm for NBD-Cl signal which was used as a loading control.

Daz-2:Cy5 click mix was prepared by sequentially adding final concentrations of 1 mM Daz-2, 1 mM Cyanine5 alkyne, 2 mM copper(II)-TBTA complex and 4 mM ascorbic acid in 15 mM PBS buffer containing 30% acetonitrile. The solution was incubated at RT overnight and then quenched with 20 mM EDTA for 2h at RT while mixing.

Immunoblotting

WT or $CSE^{-/-}$ MEF cells were exposed to 0.5 μM rotenone in the complete medium for the time indicated in the figures (precisely: 0, 2, 4, 6 or 8 h). 3-nitroproiponic acid (3-NP) was used at concentrations of 50 and 100 μM. Stock solutions of both compounds were dissolved in DMSO and used immediately. The required dilutions were made in media while keeping DMSO percentage below 0.001%. If the experimental design included the recovery period, media containing rotenone was removed, cells were washed twice with warm, complete media and fresh media without stressor was added to cells for the next 17 hours. Proteins were extracted by lysing cell on ice in the presence of RIPA (50 mM Tris, 150 mM NaCl, 2 mM EDTA, 1% IGEPAL, 0.5% sodium deoxycholate, 2% SDS) buffer supplemented with 1% protease inhibitor. Protein content was estimated using DC Protein Assay (Biorad), samples were adjusted to equal concentrations and 4X Laemlli sample buffer was added at sample:Laemlli buffer ratio 3:1. Samples were then boiled for 5 min at 95 ^oC to fully reduce disulfide bonds and denaturate proteins. 30 μg of protein was loaded per lane onto 10% polyacrylamide gel and SDS-PAGE was first run at

100 V (for proteins to pack in the stacking gel) and then at 150 V until the end of protein separation. Proteins were transferred onto nitrocellulose membrane using Trans-Blot SD-Semi-Dry system using the following parameters: 19V, 0.2A during 1 h. The quality of transfer was checked by shortly incubating the membrane in Ponceau-S solution. Membrane was then blocked in 5% BSA in TBS supplemented with 0.1% Tween (TBST) for 1 h at RT followed by overnight incubation with primary antibodies. The following antibodies were used in this study: GAPDH (MAB374-AF488, Sigma; 1:20 000), CSE (kind gift from prof. Paul; 1:4000), ATF4 (11815, Cell Signaling; 1:1000), CBS (ab135626, abcam; 1:1000), MST (HPA001240, Sigma; 1:1000), OPA1 (612606, BD Technologies; 1:1000), EIF2S1 (AHO0802, Invitrogen; 1:1000), EIF2S1-P (GTX24837, GeneTex; 1:1000). All antibodies were prepared in 1% BSA in TBST. Upon incubation, antibody was removed, and membrane was washed five times for 5 min with TBST. Membranes were then incubated with corresponding fluorescent secondary antibodies (1:20 000 in 1% BSA – TBST) for 2h at room temperature. After 5 washes, membranes were visualized using Amersham Typhoon. Quantification was performed in Fiji (29).

Microscopic analysis of mitochondrial morphology

For microscopic analysis of mitochondria, MEF WT and $CSE^{-/-}$ cells were seeded on 170 µm cover slips using 24 well plate at 25 x 10^4 cells/well in complete DMEM medium. The day after medium was replaced with the fresh one, cells were treated with 1 µM of rotenone or 100 µM 3-nitropropionic acid (3-NP) for 1 h in complete DMEM medium. Another set of same samples was treated as described, but following treatment, cells were washed three times with complete DMEM medium and left for 2.5 h to recover. After treatments, cell medium was rapidly aspirated and cells were immediately overlayed with 4 % paraformaldehyde solution in PBS (pH 7.4) and cells were fixed for 20 min at 37 °C.

After fixation, cells were washed with PBS and remaining paraformaldehyde was quenched by incubating cells in 20 mM ammonium chloride solution for 15 min at RT. After quenching, cells were washed three times with PBS, permeabilized with 0.1 % Triton X-100 in PBS for 20 min and proteins were blocked with 10 % FBS solution in PBS for 30 min at 37 ^{o}C. After blocking, cells were exposed to rabbit anti mouse TOM20 antibody (abcam, 1:1000) in 5 % FBS solution in PBS overnight at 4 ^{o}C. Next day, cells were washed 3 times with PBS and exposed to fluorescently labeled goat anti rabbit IgG (AlexaFluoro488, 1:1000, Invitrogen) antibody in PBS for 2 h in dark at RT. After immunoprobing, cells were washed three times with PBS and mounted on microscopy slides using ProLong Gold mounting medium.

Images were acquired using a CFI Plan Apochormat lambda 100x objective of the Nikon Eclipse Ti-E microscope, coupled to an Andor Dragonfly spinning disk confocal system equipped with an Andor Ixon camera, and 405 nm excitation lasers was used for TOM20 visualization, respectively. Ten z-stacks of 0.2 µm each were acquired for a total scanning size of 1.8 µm. Images were acquired using the Fusion user interface (Andor) and analyzed using Fiji ImageJ. The image processing workflow was automated using the following novel Fiji ImageJ macro scripts written by Dr Roy Chowdury in Dr Julien Prudent's laboratory (MRC Mitochondrial Biology Unit, University of Cambridge, Cambridge, UK):

1. batch_FlatR: Uses onboard tools in Fiji to batch process Z-stack multichannel image data and returns maximum intensity projection multichannel images as tiff files.

2. batchsplitR: Uses maximum intensity projection multi-channel images in tiff format as input and returns single channel images as separate tiff files for further processing.

3. modifyR: Uses onboard tools in Fiji to enhance contrast by histogram equalisation with the same values across a batch of images. The macro further uses the Smooth function to reduce noise across the same batch of images. This macro is used specifically to limit any cosmetic alterations to individual images which might skew the final intensity measurement.

4. measureR_Indexed: This macro limits the measurement parameters in Fiji to calculate the intensity values using pixel values across a batch of preselected ROIs. The macro returns an excel sheet tabulating the mean, min, max, integrated density and raw integrated density for all the pixel values within the batch of ROIs. The integrated density of total cell number per biological replicate was used to quantify fluorescence intensity.

Data analysis and visualization

Persulfidome datasets were normalized in R using EigenMS script (30). Data filtering and Welch's test for both proteomic datasets were performed in Perseus (31). Volcano and box plots were generated in GraphPad. Venn diagrams were created using BioVenn web application (32). KEGG and GO term enrichments were performed using The Database for Annotation, Visualization and Integrated Discovery (DAVID) (33,34) and the data was visualized in R.

5.5. References

1. Wong HS, Dighe PA, Mezera V, Monternier PA, Brand MD. Production of superoxide and hydrogen peroxide from specific mitochondrial sites under different bioenergetic conditions. Journal of Biological Chemistry. 2017 Oct;292(41):16804–9.
2. Stehling O, Lill R. The Role of Mitochondria in Cellular Iron-Sulfur Protein Biogenesis: Mechanisms, Connected Processes, and Diseases. Cold Spring Harb Perspect Biol. 2013 Aug 1;5(8):a011312–a011312.
3. Farquhar MG, Palade GE. The Golgi apparatus: 100 years of progress and controversy. Trends Cell Biol. 1998 Jan;8(1):2–10.
4. Jiang Z, Hu Z, Zeng L, Lu W, Zhang H, Li T, et al. The role of the Golgi apparatus in oxidative stress: is this organelle less significant than mitochondria? Free Radic Biol Med. 2011 Apr;50(8):907–17.
5. Sbodio JI, Snyder SH, Paul BD. Golgi stress response reprograms cysteine metabolism to confer cytoprotection in Huntington's disease. Proceedings of the National Academy of Sciences. 2018 Jan 23;115(4):780–5.
6. Teske BF, Wek SA, Bunpo P, Cundiff JK, McClintick JN, Anthony TG, et al. The eIF2 kinase PERK and the integrated stress response facilitate activation of ATF6 during endoplasmic reticulum stress. Mol Biol Cell. 2011 Nov 15;22(22):4390–405.
7. Quirós PM, Prado MA, Zamboni N, D'Amico D, Williams RW, Finley D, et al. Multi-omics analysis identifies ATF4 as a key regulator of the mitochondrial stress response in mammals. Journal of Cell Biology. 2017 Jul 3;216(7):2027–45.
8. Pakos-Zebrucka K, Koryga I, Mnich K, Ljujic M, Samali A, Gorman AM. The integrated stress response. EMBO Rep. 2016 Oct 14;17(10):1374–95.
9. Costa-Mattioli M, Walter P. The integrated stress response: From mechanism to disease. Science (1979). 2020 Apr 24;368(6489).
10. Zhang P, McGrath B, Li S, Frank A, Zambito F, Reinert J, et al. The PERK Eukaryotic Initiation Factor 2α Kinase Is Required for the Development of the Skeletal System, Postnatal Growth, and the Function and Viability of the Pancreas. Mol Cell Biol. 2002 Jun 1;22(11):3864–74.
11. Harding HP, Zeng H, Zhang Y, Jungries R, Chung P, Plesken H, et al. Diabetes Mellitus and Exocrine Pancreatic Dysfunction in Perk−/− Mice Reveals a Role for Translational Control in Secretory Cell Survival. Mol Cell. 2001 Jun;7(6):1153–63.
12. Delépine M, Nicolino M, Barrett T, Golamaully M, Mark Lathrop G, Julier C. EIF2AK3, encoding translation initiation factor 2-α kinase 3, is mutated in patients with Wolcott-Rallison syndrome. Nat Genet. 2000 Aug;25(4):406–9.
13. Zhu H, Liang C, Cai X, Zhang H, Liu C, Jia P, et al. Rational Design of a Targetable Fluorescent Probe for Visualizing H $_2$ S Production under Golgi Stress Response Elicited by Monensin. Anal Chem. 2020 Jan 21;92(2):1883–9.
14. Zhang Y, Wang Y, Read E, Fu M, Pei Y, Wu L, et al. Golgi Stress Response, Hydrogen Sulfide Metabolism, and Intracellular Calcium Homeostasis. Antioxid Redox Signal. 2020 Mar 20;32(9):583–601.

15. Kabil O, Yadav V, Banerjee R. Heme-dependent Metabolite Switching Regulates H2S Synthesis in Response to Endoplasmic Reticulum (ER) Stress. Journal of Biological Chemistry. 2016 Aug;291(32):16418–23.

16. Guo X, Aviles G, Liu Y, Tian R, Unger BA, Lin YHT, et al. Mitochondrial stress is relayed to the cytosol by an OMA1–DELE1–HRI pathway. Nature. 2020 Mar 19;579(7799):427–32.

17. Baker MJ, Lampe PA, Stojanovski D, Korwitz A, Anand R, Tatsuta T, et al. Stress-induced OMA1 activation and autocatalytic turnover regulate OPA1-dependent mitochondrial dynamics. EMBO J. 2014 Mar 18;33(6):578–93.

18. Liot G, Bossy B, Lubitz S, Kushnareva Y, Sejbuk N, Bossy-Wetzel E. Complex II inhibition by 3-NP causes mitochondrial fragmentation and neuronal cell death via an NMDA- and ROS-dependent pathway. Cell Death Differ. 2009 Jun 20;16(6):899–909.

19. Gao XH, Krokowski D, Guan BJ, Bederman I, Majumder M, Parisien M, et al. Quantitative H2S-mediated protein sulfhydration reveals metabolic reprogramming during the integrated stress response. Elife. 2015 Nov 23;4.

20. Hellicar J, Stevenson NL, Stephens DJ, Lowe M. Supply chain logistics – the role of the Golgi complex in extracellular matrix production and maintenance. J Cell Sci. 2022 Jan 1;135(1).

21. Suga K, Yamamoto-Hijikata S, Terao Y, Akagawa K, Ushimaru M. Golgi stress induces upregulation of the ER-Golgi SNARE Syntaxin-5, altered βAPP processing, and Caspase-3-dependent apoptosis in NG108-15 cells. Molecular and Cellular Neuroscience. 2022 Jul;121:103754.

22. Murphy MP, LeVine H. Alzheimer's Disease and the Amyloid-β Peptide. Journal of Alzheimer's Disease. 2010 Jan 6;19(1):311–23.

23. Matsuda S, Giliberto L, Matsuda Y, McGowan EM, D'Adamio L. BRI2 Inhibits Amyloid β-Peptide Precursor Protein Processing by Interfering with the Docking of Secretases to the Substrate. The Journal of Neuroscience. 2008 Aug 27;28(35):8668–76.

24. Joshi G, Chi Y, Huang Z, Wang Y. Aβ-induced Golgi fragmentation in Alzheimer's disease enhances Aβ production. Proceedings of the National Academy of Sciences. 2014 Apr 17;111(13).

25. Joshi G, Bekier ME, Wang Y. Golgi fragmentation in Alzheimer's disease. Front Neurosci. 2015 Sep 24;9.

26. Zivanovic J, Kouroussis E, Kohl JB, Adhikari B, Bursac B, Schott-Roux S, et al. Selective Persulfide Detection Reveals Evolutionarily Conserved Antiaging Effects of S-Sulfhydration. Cell Metab. 2019 Dec;30(6):1152-1170.e13.

27. Sherer TB, Betarbet R, Testa CM, Seo BB, Richardson JR, Kim JH, et al. Mechanism of toxicity in rotenone models of Parkinson's disease. J Neurosci. 2003 Nov 26;23(34):10756–64.

28. Sbodio JI, Snyder SH, Paul BD. Transcriptional control of amino acid homeostasis is disrupted in Huntington's disease. Proceedings of the National Academy of Sciences. 2016 Aug 2;113(31):8843–8.

29. Schindelin J, Arganda-Carreras I, Frise E, Kaynig V, Longair M, Pietzsch T, et al. Fiji: an open-source platform for biological-image analysis. Nat Methods. 2012 Jul 28;9(7):676–82.

30. Karpievitch Y V, Taverner T, Adkins JN, Callister SJ, Anderson GA, Smith RD, et al.

Normalization of peak intensities in bottom-up MS-based proteomics using singular value decomposition. 2009;25(19):2573–80. Available from: http://sourceforge.net.

31. Tyanova S, Temu T, Sinitcyn P, Carlson A, Hein MY, Geiger T, et al. The Perseus computational platform for comprehensive analysis of (prote)omics data. Nat Methods. 2016 Sep 27;13(9):731–40.

32. Hulsen T, de Vlieg J, Alkema W. BioVenn – a web application for the comparison and visualization of biological lists using area-proportional Venn diagrams. BMC Genomics. 2008;9(1):488.

33. Huang DW, Sherman BT, Lempicki RA. Systematic and integrative analysis of large gene lists using DAVID bioinformatics resources. Nat Protoc. 2009 Jan 18;4(1):44–57.

34. Sherman BT, Hao M, Qiu J, Jiao X, Baseler MW, Lane HC, et al. DAVID: a web server for functional enrichment analysis and functional annotation of gene lists (2021 update). Nucleic Acids Res. 2022 Jul 5;50(W1):W216–21.

6. Conclusions and future perspectives

This thesis explores various aspects of the protective and signaling properties of H_2S, mediated through protein persulfidation (PSSH). Continuous advancements in techniques for measuring both H_2S and persulfidation have gradually uncovered the significance of this mechanism in regulating fundamental biological processes (31,49,55). Growing evidence, including findings from this work suggest that PSSH is a widespread post-translational modification (PTM) that affects proteins involved in numerous processes, extending beyond a specific subset of proteins (120,127,129,236). The preservation of PSSH across species further supports the idea that it is a pivotal and ancient PTM (49). The regulated endogenous production of H_2S coupled with the enzymatic removal of PSSH, indicates that this modification is not byproduct of stochastic processes or enzymatic reactions (31,86). Instead, its formation appears to be a targeted response to certain stimuli such as global increase of protein sulfenylation driven by signaling events or excessive ROS production (49).

Protein PTMs offer a rapid and cost-efficient way for cells to adapt to changing environments and regulate cellular functions. However, proteins, along with other biomolecules, are the first targets of cellular damage. PTMs involved in signal transduction are typically transient and reversible modifications whose formation and removal are tightly regulated. As cells age, their ability to maintain this dynamic regulation diminishes, leading to the accumulation of irreversible PTMs and the collapse of proteostasis.

In this work, we used different model systems, such as *C. elegans* and mammalian cell lines, to gain deeper insights into the role of PSSH in physiological aging process but also in response to stress, as an aspect of organismal physiology largely affected by age.

Each model system presents its own strengths and limitations, making them complementary when used together. We chose *C. elegans* as a relatively simple organism but with all the features required to follow the entire aging process on an organismal level. In contrast, in vitro cell cultures provide a simplified model of cell´s environment, which is useful for understanding molecular aspect of the changes observed at the higher organizational levels.

Our finding showed that the *C. elegans* persulfidome is not static, but it fluctuates with age in a more complex pattern than anticipated. While we identified pathways predominantly affected by PSSH remodeling, our results are only a foundation for deeper functional studies. Understanding global changes in the persulfidome is valuable but focusing on specific tissues or structures in *C. elegans* may help explain the contributions of individual entities to the observed changes. Several studies suggest that different tissues exhibit asynchronous aging dynamics, indicating that certain tissues may drive organismal aging (231,284,285). In *C. elegans*, germline has a significant impact on somatic function and plays a crucial role in the animal's aging (286,287). On the other hand, germline is essential for lifespan extension at cold temperatures, a process dependent on endogenous H_2S (220). Thus, it would be intriguing to explore whether signals from the germline drive persulfidation changes in somatic tissues. This hypothesis aligns with our observation of a significant decrease in the persulfidome coinciding with the onset of reproductive cessation in worms.

Unfortunately, in-depth studying of PSSH in individual tissues are challenging due to the instability and reactivity of persulfides which might interfere with the time-demanding process of tissue isolation. However, adaptations of the dimedone switch method could be explored to address this challenge. Moreover, this labeling method has been adapted

for microscopic analysis of PSSH, providing an opportunity to compare its dynamics across different worm structures and at various time points.

We further explored the importance of H_2S and PSSH in stress response, as an important parameter of cellular fitness. Cells are constantly exposed to both intrinsic and extrinsic stressors and their ability to counteract these stresses and restore basal physiological functions diminishes with age. Our findings indicate that CSE-dependent H_2S production, triggered by different stressors, alters the persulfidation status of proteins involved in stress response pathways and is required for proper stress resolution. A more detailed analysis could reveal whether these persulfidation changes serve primarily as a protective mechanism against protein overoxidation or as a signaling modification that modulates protein activity and function. It is likely that both mechanisms are relevant, with their relative contributions varying depending on the type, intensity, and the duration of stress.

The multitude of PTMs present within the cell, highlights the complexity of potential interactions between these modifications and their combined impact on cellular processes. PSSH is not the only PTM whose dynamics is associated with aging (288,289). Therefore, integrating high-throughput data on various PTMs and examining how they correlate could provide insights into the coordinated regulation of protein fate. Identifying common proteins modified by different PTMs may further clarify how these modifications regulate protein function in stress and aging. PTMs also affect protein structure, and modifying one residue may facilitate or hinder further modification on the nearby residues. Development of dimedone switch method for site-centric proteomic analysis of modified cysteines would be an invaluable tool for these purposes.

Both endogenous H_2S and PSSH levels decline with age and maintaining those levels high might be beneficial for healthy aging. While supplementation with synthetic H_2S donors has shown some benefits, they come with significant limitations such as solubility in water, differing decomposition rates and H_2S release kinetics, uncertain intracellular localization, and often poorly understood release mechanisms, including "turn-on" processes that require a series of chemical or enzymatic transformations. None of these factors can mimic the natural spatio-temporal kinetics of H_2S production within cells.

Our work provides evidence that ET, an organosulfur compound found in natural food sources, may serve as an alternative substrate for CSE (with Km similar to its natural substrates, cysteine and homocysteine) boosting H_2S formation and protein persulfidation. This leads to a global protection of proteins but also results in specific activation of cytosolic GPD resulting in an increase of NAD^+/NADH levels, in a way that is similar, if not more efficient, than the use of NAD precursors such as NR or NMN. Indeed, we could observe preservation of mitochondrial function and morphology in cells, *C. elegans* and rats, increased muscle mass, stemness and vascularization and enhanced performance of even old animal. Future studies, trying to combine ISR as a boost for CSE and ET as its alternative substrate could provide even better therapeutic approaches for health and lifespan extension.

References

1. Patel BH, Percivalle C, Ritson DJ, Duffy CD, Sutherland JD. Common origins of RNA, protein and lipid precursors in a cyanosulfidic protometabolism. Nat Chem. 2015 Apr 16;7(4):301–7.
2. Filipovic MR, Zivanovic J, Alvarez B, Banerjee R. Chemical Biology of H 2 S Signaling through Persulfidation. 2017; Available from: https://pubs.acs.org/sharingguidelines
3. Abe K, Kimura H. The possible role of hydrogen sulfide as an endogenous neuromodulator. The Journal of Neuroscience. 1996 Feb 1;16(3):1066–71.
4. Hosoki R, Matsuki N, Kimura H. The Possible Role of Hydrogen Sulfide as an Endogenous Smooth Muscle Relaxant in Synergy with Nitric Oxide. Biochem Biophys Res Commun. 1997 Aug;237(3):527–31.
5. Elrod JW, Calvert JW, Morrison J, Doeller JE, Kraus DW, Tao L, et al. Hydrogen sulfide attenuates myocardial ischemia-reperfusion injury by preservation of mitochondrial function. Proceedings of the National Academy of Sciences. 2007 Sep 25;104(39):15560–5.
6. Bhatia M. H2S and Inflammation: An Overview. In 2015. p. 165–80.
7. Blackstone E, Morrison M, Roth MB. H $_2$ S Induces a Suspended Animation-Like State in Mice. Science (1979). 2005 Apr 22;308(5721):518–518.
8. Rickard D, Iii GWL. Chemistry of Iron Sulfides. 2007; Available from: https://pubs.acs.org/sharingguidelines
9. Schoonen MAA, Barnes HL. An approximation of the second dissociation constant for H2S. Geochim Cosmochim Acta. 1988 Mar;52(3):649–54.
10. Hughes MN, Centelles MN, Moore KP. Making and working with hydrogen sulfide. Free Radic Biol Med. 2009 Nov;47(10):1346–53.
11. Olson KR. A Practical Look at the Chemistry and Biology of Hydrogen Sulfide. Antioxid Redox Signal. 2012 Jul;17(1):32–44.
12. Cuevasanta E, Denicola A, Alvarez B. Mö ller MN (2012) Solubility and Permeation of Hydrogen Sulfide in Lipid Membranes. PLoS One [Internet]. 2012;7(4):34562. Available from: www.plosone.org
13. Riahi S, Rowley CN. Why Can Hydrogen Sulfide Permeate Cell Membranes? J Am Chem Soc [Internet]. 2014;136:28. Available from: http://pubs.acs.org.
14. Zhao W. The vasorelaxant effect of H2S as a novel endogenous gaseous KATP channel opener. EMBO J. 2001 Nov 1;20(21):6008–16.
15. Whiteman M, Cheung NS, Zhu YZ, Chu SH, Siau JL, Wong BS, et al. Hydrogen sulphide: a novel inhibitor of hypochlorous acid-mediated oxidative damage in the brain? Biochem Biophys Res Commun. 2005 Jan;326(4):794–8.
16. Jha S, Calvert JW, Duranski MR, Ramachandran A, Lefer DJ. Hydrogen sulfide attenuates hepatic ischemia-reperfusion injury: role of antioxidant and antiapoptotic signaling. American Journal of Physiology-Heart and Circulatory Physiology. 2008 Aug;295(2):H801–

6.

17. Powell CR, Dillon KM, Matson JB. A review of hydrogen sulfide (H2S) donors: Chemistry and potential therapeutic applications. Biochem Pharmacol. 2018 Mar;149:110–23.

18. Yagdi E, Cerella C, Dicato M, Diederich M. Garlic-derived natural polysulfanes as hydrogen sulfide donors: Friend or foe? Food and Chemical Toxicology. 2016 Sep;95:219–33.

19. Miljkovic JLj, Burger N, Gawel JM, Mulvey JF, Norman AAI, Nishimura T, et al. Rapid and selective generation of H2S within mitochondria protects against cardiac ischemia-reperfusion injury. Redox Biol. 2022 Sep;55:102429.

20. Li L, Whiteman M, Guan YY, Neo KL, Cheng Y, Lee SW, et al. Characterization of a Novel, Water-Soluble Hydrogen Sulfide–Releasing Molecule (GYY4137). Circulation. 2008 May 6;117(18):2351–60.

21. Li L, Salto-Tellez M, Tan CH, Whiteman M, Moore PK. GYY4137, a novel hydrogen sulfide-releasing molecule, protects against endotoxic shock in the rat. Free Radic Biol Med. 2009 Jul;47(1):103–13.

22. Liu Z, Han Y, Li L, Lu H, Meng G, Li X, et al. The hydrogen sulfide donor, <scp>GYY</scp> 4137, exhibits anti-atherosclerotic activity in high fat fed apolipoprotein <scp>E</scp> $^{-/-}$ mice. Br J Pharmacol. 2013 Aug 26;169(8):1795–809.

23. Qabazard B, Li L, Gruber J, Peh MT, Ng LF, Kumar SD, et al. Hydrogen Sulfide Is an Endogenous Regulator of Aging in *Caenorhabditis elegans*. Antioxid Redox Signal. 2014 Jun;20(16):2621–30.

24. Kang J, Li Z, Organ CL, Park CM, Yang C tao, Pacheco A, et al. pH-Controlled Hydrogen Sulfide Release for Myocardial Ischemia-Reperfusion Injury. J Am Chem Soc. 2016 May 25;138(20):6336–9.

25. Park CM, Zhao Y, Zhu Z, Pacheco A, Peng B, Devarie-Baez NO, et al. Synthesis and evaluation of phosphorodithioate-based hydrogen sulfide donors. Mol Biosyst. 2013;9(10):2430.

26. Le Trionnaire S, Perry A, Szczesny B, Szabo C, Winyard PG, Whatmore JL, et al. The synthesis and functional evaluation of a mitochondria-targeted hydrogen sulfide donor, (10-oxo-10-(4-(3-thioxo-3H-1,2-dithiol-5-yl)phenoxy)decyl)triphenylphosphonium bromide (AP39). Med Chem Commun. 2014;5(6):728–36.

27. Fox BC, Slade L, Torregrossa R, Pacitti D, Szabo C, Etheridge T, et al. The mitochondria-targeted hydrogen sulfide donor AP39 improves health and mitochondrial function in a <scp> *C. elegans* </scp> primary mitochondrial disease model. J Inherit Metab Dis. 2021 Mar 20;44(2):367–75.

28. Ellwood RA, Hewitt JE, Torregrossa R, Philp AM, Hardee JP, Hughes S, et al. Mitochondrial hydrogen sulfide supplementation improves health in the *C. elegans* Duchenne muscular dystrophy model. Proceedings of the National Academy of Sciences. 2021 Mar 2;118(9).

29. Zhao F li, Fang F, Qiao P feng, Yan N, Gao D, Yan Y. AP39, a Mitochondria-Targeted Hydrogen Sulfide Donor, Supports Cellular Bioenergetics and Protects against Alzheimer's Disease by Preserving Mitochondrial Function in APP/PS1 Mice and Neurons. Oxid Med Cell Longev. 2016 Jan 31;2016(1).

30. Ahmad A, Olah G, Szczesny B, Wood ME, Whiteman M, Szabo C. AP39, A Mitochondrially Targeted Hydrogen Sulfide Donor, Exerts Protective Effects in Renal Epithelial Cells

Subjected to Oxidative Stress in Vitro and in Acute Renal Injury in Vivo. Shock. 2016 Jan;45(1):88–97.

31. Wedmann R, Onderka C, Wei S, Szijártó IA, Miljkovic JLj, Mitrovic A, et al. Improved tag-switch method reveals that thioredoxin acts as depersulfidase and controls the intracellular levels of protein persulfidation. Chem Sci. 2016;7(5):3414–26.

32. Steiger AK, Zhao Y, Pluth MD. Emerging Roles of Carbonyl Sulfide in Chemical Biology: Sulfide Transporter or Gasotransmitter? Antioxid Redox Signal. 2018 Jun;28(16):1516–32.

33. Zheng Y, Yu B, Ji K, Pan Z, Chittavong V, Wang B. Esterase-Sensitive Prodrugs with Tunable Release Rates and Direct Generation of Hydrogen Sulfide. Angewandte Chemie International Edition. 2016 Mar 24;55(14):4514–8.

34. Zhao Z, Malinowski ER. Window factor analysis of methylene blue in water. J Chemom. 1999 Mar;13(2):83–94.

35. Chen X, Jhee KH, Kruger WD. Production of the Neuromodulator H2S by Cystathionine β-Synthase via the Condensation of Cysteine and Homocysteine. Journal of Biological Chemistry. 2004 Dec;279(50):52082–6.

36. Chiku T, Padovani D, Zhu W, Singh S, Vitvitsky V, Banerjee R. H2S Biogenesis by Human Cystathionine γ-Lyase Leads to the Novel Sulfur Metabolites Lanthionine and Homolanthionine and Is Responsive to the Grade of Hyperhomocysteinemia. Journal of Biological Chemistry. 2009 Apr;284(17):11601–12.

37. Wintner EA, Deckwerth TL, Langston W, Bengtsson A, Leviten D, Hill P, et al. A monobromobimane-based assay to measure the pharmacokinetic profile of reactive sulphide species in blood. Br J Pharmacol. 2010 Jun 24;160(4):941–57.

38. Li H, Fang Y, Yan J, Ren X, Zheng C, Wu B, et al. Small-molecule fluorescent probes for H2S detection: Advances and perspectives. TrAC Trends in Analytical Chemistry. 2021 Jan;134:116117.

39. Hartle MD, Pluth MD. A practical guide to working with H_2S at the interface of chemistry and biology. Chem Soc Rev. 2016;45(22):6108–17.

40. Lin VS, Chen W, Xian M, Chang CJ. Chemical probes for molecular imaging and detection of hydrogen sulfide and reactive sulfur species in biological systems. Chem Soc Rev. 2015;44(14):4596–618.

41. Olson KR, DeLeon ER, Liu F. Controversies and conundrums in hydrogen sulfide biology. Nitric Oxide. 2014 Sep;41:11–26.

42. Vitvitsky V, Banerjee R. H2S Analysis in Biological Samples Using Gas Chromatography with Sulfur Chemiluminescence Detection. In 2015. p. 111–23.

43. Furne J, Saeed A, Levitt MD. Whole tissue hydrogen sulfide concentrations are orders of magnitude lower than presently accepted values. American Journal of Physiology-Regulatory, Integrative and Comparative Physiology. 2008 Nov;295(5):R1479–85.

44. Koga R, Miyoshi Y, Sakaue H, Hamase K, Konno R. Mouse d-Amino-Acid Oxidase: Distribution and Physiological Substrates. Front Mol Biosci. 2017 Dec 4;4.

45. Cao X, Ding L, Xie Z zhong, Yang Y, Whiteman M, Moore PK, et al. A Review of Hydrogen Sulfide Synthesis, Metabolism, and Measurement: Is Modulation of Hydrogen Sulfide a Novel Therapeutic for Cancer? Antioxid Redox Signal. 2019 Jul;31(1):1–38.

46. Nagahara N, Ito T, Kitamura H, Nishino T. Tissue and subcellular distribution of mercaptopyruvate sulfurtransferase in the rat: confocal laser fluorescence and immunoelectron microscopic studies combined with biochemical analysis. Histochem Cell Biol. 1998 Aug 5;110(3):243–50.

47. Enokido Y, Suzuki E, Iwasawa K, Namekata K, Okazawa H, Kimura H. Cystathionine β-synthase, a key enzyme for homocysteine metabolism, is preferentially expressed in the radial glia/astrocyte lineage of developing mouse CNS. The FASEB Journal. 2005 Nov 13;19(13):1854–6.

48. Paul BD, Sbodio JI, Xu R, Vandiver MS, Cha JY, Snowman AM, et al. Cystathionine γ-lyase deficiency mediates neurodegeneration in Huntington's disease. Nature. 2014 May 26;509(7498):96–100.

49. Zivanovic J, Kouroussis E, Kohl JB, Adhikari B, Bursac B, Schott-Roux S, et al. Selective Persulfide Detection Reveals Evolutionarily Conserved Antiaging Effects of S-Sulfhydration. Cell Metab. 2019 Dec;30(6):1152-1170.e13.

50. Zhao W, Ndisang JF, Wang R. Modulation of endogenous production of H_2S in rat tissues. Can J Physiol Pharmacol. 2003 Sep 1;81(9):848–53.

51. Nicholls P, Kim JK. Sulphide as an inhibitor and electron donor for the cytochrome *c* oxidase system. Can J Biochem. 1982 Jun 1;60(6):613–23.

52. Khan AA, Schuler MM, Prior MG, Yong S, Coppock RW, Florence LZ, et al. Effects of hydrogen sulfide exposure on lung mitochondrial respiratory chain enzymes in rats. Toxicol Appl Pharmacol. 1990 May;103(3):482–90.

53. Hildebrandt TM, Grieshaber MK. Three enzymatic activities catalyze the oxidation of sulfide to thiosulfate in mammalian and invertebrate mitochondria. FEBS J. 2008 Jul 28;275(13):3352–61.

54. Libiad M, Yadav PK, Vitvitsky V, Martinov M, Banerjee R. Organization of the Human Mitochondrial Hydrogen Sulfide Oxidation Pathway. Journal of Biological Chemistry. 2014 Nov;289(45):30901–10.

55. Vignane T, Filipovic MR. Emerging Chemical Biology of Protein Persulfidation. Antioxid Redox Signal. 2023 Jul 1;39(1–3):19–39.

56. Zhu W, Lin A, Banerjee R. Kinetic Properties of Polymorphic Variants and Pathogenic Mutants in Human Cystathionine γ-Lyase. Biochemistry. 2008 Jun 1;47(23):6226–32.

57. Schaffer S, Kim HW. Effects and Mechanisms of Taurine as a Therapeutic Agent. Biomol Ther (Seoul). 2018 May 1;26(3):225–41.

58. Singh S, Padovani D, Leslie RA, Chiku T, Banerjee R. Relative Contributions of Cystathionine β-Synthase and γ-Cystathionase to H2S Biogenesis via Alternative Trans-sulfuration Reactions. Journal of Biological Chemistry. 2009 Aug;284(33):22457–66.

59. Yadav PK, Martinov M, Vitvitsky V, Seravalli J, Wedmann R, Filipovic MR, et al. Biosynthesis and Reactivity of Cysteine Persulfides in Signaling. J Am Chem Soc. 2016 Jan 13;138(1):289–99.

60. Kabil O, Yadav V, Banerjee R. Heme-dependent Metabolite Switching Regulates H2S Synthesis in Response to Endoplasmic Reticulum (ER) Stress. Journal of Biological Chemistry. 2016 Aug;291(32):16418–23.

61. Sun Q, Collins R, Huang S, Holmberg-Schiavone L, Anand GS, Tan CH, et al. Structural

Basis for the Inhibition Mechanism of Human Cystathionine γ-Lyase, an Enzyme Responsible for the Production of H2S. Journal of Biological Chemistry. 2009 Jan;284(5):3076–85.

62. Huang S, Chua JH, Yew WS, Sivaraman J, Moore PK, Tan CH, et al. Site-Directed Mutagenesis on Human Cystathionine-γ-Lyase Reveals Insights into the Modulation of H2S Production. J Mol Biol. 2010 Feb;396(3):708–18.

63. Echizen H, Hanaoka K, Shimamoto K, Hibi R, Toma-Fukai S, Ohno H, et al. Discovery of a cystathionine γ-lyase (CSE) selective inhibitor targeting active-site pyridoxal 5′-phosphate (PLP) via Schiff base formation. Scientific Reports | [Internet]. 123AD;13:16456. Available from: https://doi.org/10.1038/s41598-023-43536-6

64. Yuan G, Vasavda C, Peng YJ, Makarenko V V., Raghuraman G, Nanduri J, et al. Protein kinase G–regulated production of H $_2$ S governs oxygen sensing. Sci Signal. 2015 Apr 21;8(373).

65. Renga B, Cipriani S, Carino A, Simonetti M, Zampella A, Fiorucci S. Reversal of Endothelial Dysfunction by GPBAR1 Agonism in Portal Hypertension Involves a AKT/FOXOA1 Dependent Regulation of H2S Generation and Endothelin-1. PLoS One. 2015 Nov 5;10(11):e0141082.

66. Agrawal N, Banerjee R. Human Polycomb 2 Protein Is a SUMO E3 Ligase and Alleviates Substrate-Induced Inhibition of Cystathionine β-Synthase Sumoylation. PLoS One. 2008 Dec 24;3(12):e4032.

67. Liu Y, Liao R, Qiang Z, Zhang C. Pro-inflammatory cytokine-driven PI3K/Akt/Sp1 signalling and H2S production facilitates the pathogenesis of severe acute pancreatitis. Biosci Rep. 2017 Apr 30;37(2).

68. Yang G, Pei Y, Teng H, Cao Q, Wang R. Specificity Protein-1 as a Critical Regulator of Human Cystathionine γ-Lyase in Smooth Muscle Cells. Journal of Biological Chemistry. 2011 Jul;286(30):26450–60.

69. Sen N, Paul BD, Gadalla MM, Mustafa AK, Sen T, Xu R, et al. Hydrogen Sulfide-Linked Sulfhydration of NF-κB Mediates Its Antiapoptotic Actions. Mol Cell. 2012 Jan;45(1):13–24.

70. Sbodio JI, Snyder SH, Paul BD. Regulators of the transsulfuration pathway. Br J Pharmacol. 2019 Feb 23;176(4):583–93.

71. Hourihan JM, Kenna JG, Hayes JD. The Gasotransmitter Hydrogen Sulfide Induces Nrf2-Target Genes by Inactivating the Keap1 Ubiquitin Ligase Substrate Adaptor Through Formation of a Disulfide Bond Between Cys-226 and Cys-613. Antioxid Redox Signal. 2013 Aug 10;19(5):465–81.

72. Hassan MI, Boosen M, Schaefer L, Kozlowska J, Eisel F, von Knethen A, et al. Platelet-derived growth factor-BB induces cystathionine γ-lyase expression in rat mesangial cells via a redox-dependent mechanism. Br J Pharmacol. 2012 Aug 24;166(8):2231–42.

73. Nicholls P, Kim JK. Oxidation of sulphide by cytochrome aa3. Biochimica et Biophysica Acta (BBA) - Bioenergetics. 1981 Sep;637(2):312–20.

74. Vitvitsky V, Yadav PK, An S, Seravalli J, Cho US, Banerjee R. Structural and Mechanistic Insights into Hemoglobin-catalyzed Hydrogen Sulfide Oxidation and the Fate of Polysulfide Products. Journal of Biological Chemistry. 2017 Mar;292(13):5584–92.

75. Zhao K, Li S, Wu L, Lai C, Yang G. Hydrogen Sulfide Represses Androgen Receptor

Transactivation by Targeting at the Second Zinc Finger Module. Journal of Biological Chemistry. 2014 Jul;289(30):20824–35.

76. Das TN, Huie RE, Neta P, Padmaja S. Reduction Potential of the Sulfhydryl Radical: Pulse Radiolysis and Laser Flash Photolysis Studies of the Formation and Reactions of ·SH and HSSH· ⁻ in Aqueous Solutions. J Phys Chem A. 1999 Jul 1;103(27):5221–6.

77. Carballal S, Trujillo M, Cuevasanta E, Bartesaghi S, Möller MN, Folkes LK, et al. Reactivity of hydrogen sulfide with peroxynitrite and other oxidants of biological interest. Free Radic Biol Med. 2011 Jan;50(1):196–205.

78. Paulsen CE, Carroll KS. Cysteine-Mediated Redox Signaling: Chemistry, Biology, and Tools for Discovery. Chem Rev. 2013 Jul 10;113(7):4633–79.

79. Miseta A, Csutora P. Relationship Between the Occurrence of Cysteine in Proteins and the Complexity of Organisms. Mol Biol Evol. 2000 Aug 1;17(8):1232–9.

80. Filipovic MR. Persulfidation (S-sulfhydration) and H2S. In 2015. p. 29–59.

81. Toohey JI. Sulphane sulphur in biological systems: a possible regulatory role. Biochemical Journal. 1989 Dec 15;264(3):625–32.

82. Benchoam D, Cuevasanta E, Roman J V., Banerjee R, Alvarez B. Acidity of persulfides and its modulation by the protein environments in sulfide quinone oxidoreductase and thiosulfate sulfurtransferase. Journal of Biological Chemistry. 2024 May;300(5):107149.

83. Benchoam D, Semelak JA, Cuevasanta E, Mastrogiovanni M, Grassano JS, Ferrer-Sueta G, et al. Acidity and nucleophilic reactivity of glutathione persulfide. Journal of Biological Chemistry. 2020 Nov;295(46):15466–81.

84. Chauvin JR, Pratt DA. On the Reactions of Thiols, Sulfenic Acids, and Sulfinic Acids with Hydrogen Peroxide. Angewandte Chemie International Edition. 2017 May 22;56(22):6255–9.

85. Gao XH, Krokowski D, Guan BJ, Bederman I, Majumder M, Parisien M, et al. Quantitative H2S-mediated protein sulfhydration reveals metabolic reprogramming during the integrated stress response. Elife. 2015 Nov 23;4.

86. Dóka É, Pader I, Bíró A, Johansson K, Cheng Q, Ballagó K, et al. A novel persulfide detection method reveals protein persulfide- and polysulfide-reducing functions of thioredoxin and glutathione systems. Sci Adv. 2016 Jan;2(1).

87. Longen S, Richter F, Köhler Y, Wittig I, Beck KF, Pfeilschifter J. Quantitative Persulfide Site Identification (qPerS-SID) Reveals Protein Targets of H2S Releasing Donors in Mammalian Cells. Sci Rep. 2016 Jul 14;6(1):29808.

88. Fan K, Chen Z, Liu H. Evidence that the ProPerDP method is inadequate for protein persulfidation detection due to lack of specificity. Sci Adv. 2020 Aug 14;6(33).

89. Fu L, Liu K, He J, Tian C, Yu X, Yang J. Direct Proteomic Mapping of Cysteine Persulfidation. Antioxid Redox Signal. 2020 Nov 20;33(15):1061–76.

90. Zhang D, Macinkovic I, Devarie-Baez NO, Pan J, Park C, Carroll KS, et al. Detection of Protein S-Sulfhydration by a Tag-Switch Technique. Angewandte Chemie International Edition. 2014 Jan 7;53(2):575–81.

91. Park CM, Macinkovic I, Filipovic MR, Xian M. Use of the “Tag-Switch” Method for the Detection of Protein S-Sulfhydration. In 2015. p. 39–56.

92. Cuevasanta E, Lange M, Bonanata J, Coitiño EL, Ferrer-Sueta G, Filipovic MR, et al. Reaction of Hydrogen Sulfide with Disulfide and Sulfenic Acid to Form the Strongly Nucleophilic Persulfide. Journal of Biological Chemistry. 2015 Nov;290(45):26866–80.

93. Yang J, Gupta V, Carroll KS, Liebler DC. Site-specific mapping and quantification of protein S-sulphenylation in cells. Nat Commun. 2014 Sep 1;5(1):4776.

94. Greiner R, Pálinkás Z, Bäsell K, Becher D, Antelmann H, Nagy P, et al. Polysulfides Link H_2S to Protein Thiol Oxidation. Antioxid Redox Signal. 2013 Nov 20;19(15):1749–65.

95. Arndt S, Baeza-Garza CD, Logan A, Rosa T, Wedmann R, Prime TA, et al. Assessment of H2S in vivo using the newly developed mitochondria-targeted mass spectrometry probe MitoA. Journal of Biological Chemistry. 2017 May;292(19):7761–73.

96. Yadav PK, Yamada K, Chiku T, Koutmos M, Banerjee R. Structure and Kinetic Analysis of H2S Production by Human Mercaptopyruvate Sulfurtransferase. Journal of Biological Chemistry. 2013 Jul;288(27):20002–13.

97. Mikami Y, Shibuya N, Kimura Y, Nagahara N, Ogasawara Y, Kimura H. Thioredoxin and dihydrolipoic acid are required for 3-mercaptopyruvate sulfurtransferase to produce hydrogen sulfide. Biochemical Journal. 2011 Nov 1;439(3):479–85.

98. Jackson MR, Melideo SL, Jorns MS. Human Sulfide:Quinone Oxidoreductase Catalyzes the First Step in Hydrogen Sulfide Metabolism and Produces a Sulfane Sulfur Metabolite. Biochemistry. 2012 Aug 28;51(34):6804–15.

99. Kessler D. Enzymatic activation of sulfur for incorporation into biomolecules in prokaryotes. FEMS Microbiol Rev. 2006 Nov;30(6):825–40.

100. Mueller EG. Trafficking in persulfides: delivering sulfur in biosynthetic pathways. Nat Chem Biol. 2006 Apr 17;2(4):185–94.

101. Krishnan N, Fu C, Pappin DJ, Tonks NK. H_2S-Induced Sulfhydration of the Phosphatase PTP1B and Its Role in the Endoplasmic Reticulum Stress Response. Sci Signal. 2011 Dec 13;4(203).

102. Lu J, Holmgren A. The thioredoxin antioxidant system. Free Radic Biol Med. 2014 Jan;66:75–87.

103. Cheng Z, Zhang J, Ballou DP, Williams CH. Reactivity of Thioredoxin as a Protein Thiol-Disulfide Oxidoreductase. Chem Rev. 2011 Sep 14;111(9):5768–83.

104. Geng B, Yang J, Qi Y, Zhao J, Pang Y, Du J, et al. H2S generated by heart in rat and its effects on cardiac function. Biochem Biophys Res Commun. 2004 Jan;313(2):362–8.

105. Distrutti E, Sediari L, Mencarelli A, Renga B, Orlandi S, Antonelli E, et al. Evidence That Hydrogen Sulfide Exerts Antinociceptive Effects in the Gastrointestinal Tract by Activating K_{ATP} Channels. Journal of Pharmacology and Experimental Therapeutics. 2006 Jan;316(1):325–35.

106. Li H, Feng SJ, Zhang GZ, Wang SX. Correlation of Lower Concentrations of Hydrogen Sulfide with Atherosclerosis in Chronic Hemodialysis Patients with Diabetic Nephropathy. Blood Purif. 2014;38(3–4):188–94.

107. Srilatha B, Adaikan PG, Li L, Moore PK. Hydrogen Sulphide: A Novel Endogenous Gasotransmitter Facilitates Erectile Function. J Sex Med. 2007 Sep;4(5):1304–11.

108. Kimura H. Hydrogen Sulfide Induces Cyclic AMP and Modulates the NMDA Receptor.

Biochem Biophys Res Commun. 2000 Jan;267(1):129–33.

109. Yong QC, Choo CH, Tan BH, Low CM, Bian JS. Effect of hydrogen sulfide on intracellular calcium homeostasis in neuronal cells. Neurochem Int. 2010 Feb;56(3):508–15.

110. Lee SW, Hu Y, Hu L, Lu Q, Dawe GS, Moore PK, et al. Hydrogen sulphide regulates calcium homeostasis in microglial cells. Glia. 2006 Aug 22;54(2):116–24.

111. Nagai Y, Tsugane M, Oka J, Kimura H. Hydrogen sulfide induces calcium waves in astrocytes. The FASEB Journal. 2004 Mar 20;18(3):557–9.

112. Whiteman M, Armstrong JS, Chu SH, Jia-Ling S, Wong B, Cheung NS, et al. The novel neuromodulator hydrogen sulfide: an endogenous peroxynitrite 'scavenger'? J Neurochem. 2004 Aug 2;90(3):765–8.

113. Lu M, Hu LF, Hu G, Bian JS. Hydrogen sulfide protects astrocytes against H2O2-induced neural injury via enhancing glutamate uptake. Free Radic Biol Med. 2008 Dec;45(12):1705–13.

114. Elsey DJ, Fowkes RC, Baxter GF. Regulation of cardiovascular cell function by hydrogen sulfide (H_2S). Cell Biochem Funct. 2010 Mar 26;28(2):95–106.

115. Shen Y, Shen Z, Luo S, Guo W, Zhu YZ. The Cardioprotective Effects of Hydrogen Sulfide in Heart Diseases: From Molecular Mechanisms to Therapeutic Potential. Oxid Med Cell Longev. 2015;2015:1–13.

116. Papapetropoulos A, Pyriochou A, Altaany Z, Yang G, Marazioti A, Zhou Z, et al. Hydrogen sulfide is an endogenous stimulator of angiogenesis. Proceedings of the National Academy of Sciences. 2009 Dec 22;106(51):21972–7.

117. Fang LP, Lin Q, Tang CS, Liu XM. Hydrogen sulfide attenuates epithelial–mesenchymal transition of human alveolar epithelial cells. Pharmacol Res. 2010 Apr;61(4):298–305.

118. Fang L, Li H, Tang C, Geng B, Qi Y, Liu X. Hydrogen sulfide attenuates the pathogenesis of pulmonary fibrosis induced by bleomycin in rats. Can J Physiol Pharmacol. 2009 Jul;87(7):531–8.

119. Bhatia M, Wong FL, Fu D, Lau HY, Moochhala SM, Moore PK. Role of hydrogen sulfide in acute pancreatitis and associated lung injury. The FASEB Journal. 2005 Apr 25;19(6):1–17.

120. Sen N, Paul BD, Gadalla MM, Mustafa AK, Sen T, Xu R, et al. Hydrogen Sulfide-Linked Sulfhydration of NF-κB Mediates Its Antiapoptotic Actions. Mol Cell. 2012 Jan;45(1):13–24.

121. Whiteman M, Winyard PG. Hydrogen sulfide and inflammation: the good, the bad, the ugly and the promising. Expert Rev Clin Pharmacol. 2011 Jan 10;4(1):13–32.

122. Mustafa AK, Gadalla MM, Sen N, Kim S, Mu W, Gazi SK, et al. H_2S Signals Through Protein S-Sulfhydration. Sci Signal. 2009 Nov 10;2(96).

123. Jarosz AP, Wei W, Gauld JW, Auld J, Özcan F, Aslan M, et al. Glyceraldehyde 3-phosphate dehydrogenase (GAPDH) is inactivated by S-sulfuration in vitro. Free Radic Biol Med. 2015 Dec;89:512–21.

124. Vandiver MS, Paul BD, Xu R, Karuppagounder S, Rao F, Snowman AM, et al. Sulfhydration mediates neuroprotective actions of parkin. Nat Commun. 2013 Mar 27;4(1):1626.

125. Yang G, Zhao K, Ju Y, Mani S, Cao Q, Puukila S, et al. Hydrogen Sulfide Protects Against

Cellular Senescence *via S* -Sulfhydration of Keap1 and Activation of Nrf2. Antioxid Redox Signal. 2013 May 20;18(15):1906–19.

126. Calvert JW, Jha S, Gundewar S, Elrod JW, Ramachandran A, Pattillo CB, et al. Hydrogen Sulfide Mediates Cardioprotection Through Nrf2 Signaling. Circ Res. 2009 Aug 14;105(4):365–74.

127. Xie ZZ, Shi MM, Xie L, Wu ZY, Li G, Hua F, et al. Sulfhydration of p66Shc at Cysteine59 Mediates the Antioxidant Effect of Hydrogen Sulfide. Antioxid Redox Signal. 2014 Dec 20;21(18):2531–42.

128. Zhao K, Ju Y, Li S, Altaany Z, Wang R, Yang G. S-sulfhydration of <scp>MEK</scp> 1 leads to <scp>PARP</scp> -1 activation and <scp>DNA</scp> damage repair. EMBO Rep. 2014 Jul 5;15(7):792–800.

129. Mustafa AK, Sikka G, Gazi SK, Steppan J, Jung SM, Bhunia AK, et al. Hydrogen Sulfide as Endothelium-Derived Hyperpolarizing Factor Sulfhydrates Potassium Channels. Circ Res. 2011 Nov 11;109(11):1259–68.

130. Trio PZ, You S, He X, He J, Sakao K, Hou DX. Chemopreventive functions and molecular mechanisms of garlic organosulfur compounds. Food Funct. 2014;5(5):833.

131. Lucarini E, Micheli L, Trallori E, Citi V, Martelli A, Testai L, et al. Effect of glucoraphanin and sulforaphane against chemotherapy-induced neuropathic pain: Kv7 potassium channels modulation by H_2S release *in vivo*. Phytotherapy Research. 2018 Nov 2;32(11):2226–34.

132. Martelli A, Piragine E, Citi V, Testai L, Pagnotta E, Ugolini L, et al. Erucin exhibits vasorelaxing effects and antihypertensive activity by H_2S-releasing properties. Br J Pharmacol. 2020 Feb 15;177(4):824–35.

133. Citi V, Martelli A, Testai L, Marino A, Breschi M, Calderone V. Hydrogen Sulfide Releasing Capacity of Natural Isothiocyanates: Is It a Reliable Explanation for the Multiple Biological Effects of Brassicaceae? Planta Med. 2014 Jun 25;80(08/09):610–3.

134. Tanret C. A new base taken from rye ergot, ergothioneine. Ann Chim Phys . 1909;18:114–24.

135. Cumming BM, Chinta KC, Reddy VP, Steyn AJC. Role of Ergothioneine in Microbial Physiology and Pathogenesis. Antioxid Redox Signal. 2018 Feb 20;28(6):431–44.

136. Wei L, Liu L, Gong W. Structure of mycobacterial ergothioneine-biosynthesis C-S lyase EgtE. Journal of Biological Chemistry. 2024 Jan;300(1):105539.

137. Barger G, Ewins AJ. CCLVII.—The constitution of ergothioneine: a betaine related to histidine. J Chem Soc, Trans. 1911;99(0):2336–41.

138. Carlsson J, Kierstan MPJ, Brocklehurst K. Reactions of <scp>l</scp> -ergothioneine and some other aminothiones with 2,2′- and 4,4′-dipyridyl disulphides and of <scp>l</scp> -ergothioneine with iodoacetamide. 2-Mercaptoimidazoles, 2- and 4-thiopyridones, thiourea and thioacetamide as highly reactive neutral sulphur nucleophiles. Biochemical Journal. 1974 Apr 1;139(1):221–35.

139. Melville DB, Eich S, Ludwig ML. THE BIOSYNTHESIS OF ERGOTHIONEINE. Journal of Biological Chemistry. 1957 Feb;224(2):871–7.

140. Seebeck FP. In Vitro Reconstitution of Mycobacterial Ergothioneine Biosynthesis. J Am Chem Soc. 2010 May 19;132(19):6632–3.

141. Bello MH, Barrera-Perez V, Morin D, Epstein L. The Neurospora crassa mutant NcΔEgt-1 identifies an ergothioneine biosynthetic gene and demonstrates that ergothioneine enhances conidial survival and protects against peroxide toxicity during conidial germination. Fungal Genetics and Biology. 2012 Feb;49(2):160–72.

142. Ishikawa Y, Israel SE, Melville DB. Participation of an Intermediate Sulfoxide in the Enzymatic Thiolation of the Imidazole Ring of Hercynine to Form Ergothioneine. Journal of Biological Chemistry. 1974 Jul;249(14):4420–7.

143. Hu W, Song H, Sae Her A, Bak DW, Naowarojna N, Elliott SJ, et al. Bioinformatic and Biochemical Characterizations of C–S Bond Formation and Cleavage Enzymes in the Fungus *Neurospora crassa* Ergothioneine Biosynthetic Pathway. Org Lett. 2014 Oct 17;16(20):5382–5.

144. Burn R, Misson L, Meury M, Seebeck FP. Anaerobic Origin of Ergothioneine. Angewandte Chemie International Edition. 2017 Oct 2;56(41):12508–11.

145. Akanmu D, Cecchini R, Aruoma OI, Halliwell B. The antioxidant action of ergothioneine. Arch Biochem Biophys. 1991 Jul;288(1):10–6.

146. Aruoma OI, Whiteman M, England TG, Halliwell B. Antioxidant Action of Ergothioneine: Assessment of Its Ability to Scavenge Peroxynitrite. Biochem Biophys Res Commun. 1997 Feb;231(2):389–91.

147. Franzoni F, Colognato R, Galetta F, Laurenza I, Barsotti M, Di Stefano R, et al. An in vitro study on the free radical scavenging capacity of ergothioneine: comparison with reduced glutathione, uric acid and trolox. Biomedicine & Pharmacotherapy. 2006 Sep;60(8):453–7.

148. Stoffels C, Oumari M, Perrou A, Termath A, Schlundt W, Schmalz HG, et al. Ergothioneine stands out from hercynine in the reaction with singlet oxygen: Resistance to glutathione and TRIS in the generation of specific products indicates high reactivity. Free Radic Biol Med. 2017 Dec;113:385–94.

149. Zhu BZ, Mao L, Fan RM, Zhu JG, Zhang YN, Wang J, et al. Ergothioneine Prevents Copper-Induced Oxidative Damage to DNA and Protein by Forming a Redox-Inactive Ergothioneine−Copper Complex. Chem Res Toxicol. 2011 Jan 14;24(1):30–4.

150. Servillo L, Castaldo D, Casale R, D'Onofrio N, Giovane A, Cautela D, et al. An uncommon redox behavior sheds light on the cellular antioxidant properties of ergothioneine. Free Radic Biol Med. 2015 Feb;79:228–36.

151. Jenny KA, Mose G, Haupt DJ, Hondal RJ. Oxidized Forms of Ergothioneine Are Substrates for Mammalian Thioredoxin Reductase. Antioxidants. 2022 Jan 19;11(2):185.

152. Wolff JB. Ergothionase from Escherichia coli. Journal of Biological Chemistry. 1962 Mar;237(3):874–81.

153. Maurer A, Leisinger F, Lim D, Seebeck FP. Structure and Mechanism of Ergothionase from *Treponema denticola*. Chemistry – A European Journal. 2019 Aug 6;25(44):10298–303.

154. Muramatsu H, Maguchi H, Harada T, Kashiwagi T, Kim CS, Kato S ichiro, et al. Identification of the gene encoding 3-(5-oxo-2-thioxoimidazolidin-4-yl) propionic acid desulfhydrase in *Burkholderia* sp. HME13. Biosci Biotechnol Biochem. 2021 Feb 24;85(3):626–9.

155. Beliaeva MA, Leisinger F, Seebeck FP. *In Vitro* Reconstitution of a Five-Step Pathway for Bacterial Ergothioneine Catabolism. ACS Chem Biol. 2021 Feb 19;16(2):397–403.

156. Nalivaiko EY, Vasseur CM, Seebeck FP. Enzyme-Catalyzed Oxidative Degradation of

Ergothioneine. Angewandte Chemie International Edition. 2024 Feb 19;63(8).

157. Gründemann D, Harlfinger S, Golz S, Geerts A, Lazar A, Berkels R, et al. Discovery of the ergothioneine transporter. Proceedings of the National Academy of Sciences. 2005 Apr 5;102(14):5256–61.

158. Yee SW, Buitrago D, Stecula A, Ngo HX, Chien H, Zou L, et al. Deorphaning a solute carrier 22 family member, SLC22A15, through functional genomic studies. The FASEB Journal. 2020 Dec 30;34(12):15734–52.

159. Zhang Y, Gonzalez-Gutierrez G, Legg KA, Walsh BJC, Pis Diez CM, Edmonds KA, et al. Discovery and structure of a widespread bacterial ABC transporter specific for ergothioneine. Nat Commun. 2022 Dec 8;13(1):7586.

160. Tamai I, Yabuuchi H, Nezu J ichi, Sai Y, Oku A, Shimane M, et al. Cloning and characterization of a novel human pH-dependent organic cation transporter, OCTN1. FEBS Lett. 1997 Dec 8;419(1):107–11.

161. Shimizu T, Masuo Y, Takahashi S, Nakamichi N, Kato Y. Organic cation transporter Octn1-mediated uptake of food-derived antioxidant ergothioneine into infiltrating macrophages during intestinal inflammation in mice. Drug Metab Pharmacokinet. 2015 Jun;30(3):231–9.

162. Paul BD, Snyder SH. The unusual amino acid L-ergothioneine is a physiologic cytoprotectant. Cell Death Differ. 2010 Jul 13;17(7):1134–40.

163. Nakamura T, Sugiura S, Kobayashi D, Yoshida K, Yabuuchi H, Aizawa S, et al. Decreased Proliferation and Erythroid Differentiation of K562 Cells by siRNA-induced Depression of OCTN1 (SLC22A4) Transporter Gene. Pharm Res. 2007 Aug 1;24(9):1628–35.

164. Kato Y, Kubo Y, Iwata D, Kato S, Sudo T, Sugiura T, et al. Gene Knockout and Metabolome Analysis of Carnitine/Organic Cation Transporter OCTN1. Pharm Res. 2010 May 12;27(5):832–40.

165. Pfeiffer C, Bach M, Bauer T, Campos da Ponte J, Schömig E, Gründemann D. Knockout of the ergothioneine transporter ETT in zebrafish results in increased 8-oxoguanine levels. Free Radic Biol Med. 2015 Jun;83:178–85.

166. Tian X, Thorne JL, Moore JB. Ergothioneine: an underrecognised dietary micronutrient required for healthy ageing? British Journal of Nutrition. 2023 Jan 14;129(1):104–14.

167. Tang RMY, Cheah IKM, Yew TSK, Halliwell B. Distribution and accumulation of dietary ergothioneine and its metabolites in mouse tissues. Sci Rep. 2018 Jan 25;8(1):1601.

168. Cheah IK, Tang RMY, Yew TSZ, Lim KHC, Halliwell B. Administration of Pure Ergothioneine to Healthy Human Subjects: Uptake, Metabolism, and Effects on Biomarkers of Oxidative Damage and Inflammation. Antioxid Redox Signal. 2017 Feb 10;26(5):193–206.

169. Dumitrescu DG, Gordon EM, Kovalyova Y, Seminara AB, Duncan-Lowey B, Forster ER, et al. A microbial transporter of the dietary antioxidant ergothioneine. Cell. 2022 Nov;185(24):4526-4540.e18.

170. Li RWS, Yang C, Sit ASM, Kwan YW, Lee SMY, Hoi MPM, et al. Uptake and Protective Effects of Ergothioneine in Human Endothelial Cells. Journal of Pharmacology and Experimental Therapeutics. 2014 Sep;350(3):691–700.

171. D'Onofrio N, Servillo L, Giovane A, Casale R, Vitiello M, Marfella R, et al. Ergothioneine oxidation in the protection against high-glucose induced endothelial senescence: Involvement of SIRT1 and SIRT6. Free Radic Biol Med. 2016 Jul;96:211–22.

172. Hseu YC, Lo HW, Korivi M, Tsai YC, Tang MJ, Yang HL. Dermato-protective properties of ergothioneine through induction of Nrf2/ARE-mediated antioxidant genes in UVA-irradiated Human keratinocytes. Free Radic Biol Med. 2015 Sep;86:102–17.

173. Ko HJ, Kim J, Ahn M, Kim JH, Lee GS, Shin T. Ergothioneine alleviates senescence of fibroblasts induced by UVB damage of keratinocytes via activation of the Nrf2/HO-1 pathway and HSP70 in keratinocytes. Exp Cell Res. 2021 Mar;400(1):112516.

174. Obayashi K, Kurihara K, Okano Y, Masaki H, Yarosh DB. L-Ergothioneine scavenges superoxide and singlet oxygen and suppresses TNF-alpha and MMP-1 expression in UV-irradiated human dermal fibroblasts. J Cosmet Sci. 2005;56(1):17–27.

175. Hseu YC, Vudhya Gowrisankar Y, Chen XZ, Yang YC, Yang HL. The Antiaging Activity of Ergothioneine in UVA-Irradiated Human Dermal Fibroblasts via the Inhibition of the AP-1 Pathway and the Activation of Nrf2-Mediated Antioxidant Genes. Oxid Med Cell Longev. 2020 Feb 12;2020:1–13.

176. Markova NG, Karaman-Jurukovska N, Dong KK, Damaghi N, Smiles KA, Yarosh DB. Skin cells and tissue are capable of using l-ergothioneine as an integral component of their antioxidant defense system. Free Radic Biol Med. 2009 Apr;46(8):1168–76.

177. Katsube M, Ishimoto T, Fukushima Y, Kagami A, Shuto T, Kato Y. Ergothioneine promotes longevity and healthy aging in male mice. Geroscience. 2024 Mar 6;46(4):3889–909.

178. Salama SA, Abd-Allah GM, Mohamadin AM, Elshafey MM, Gad HS. Ergothioneine mitigates cisplatin-evoked nephrotoxicity via targeting Nrf2, NF-κB, and apoptotic signaling and inhibiting γ-glutamyl transpeptidase. Life Sci. 2021 Aug;278:119572.

179. Dare A, Channa ML, Nadar A. L-ergothioneine and its combination with metformin attenuates renal dysfunction in type-2 diabetic rat model by activating Nrf2 antioxidant pathway. Biomedicine & Pharmacotherapy. 2021 Sep;141:111921.

180. Fovet T, Guilhot C, Delobel P, Chopard A, Py G, Brioche T. Ergothioneine Improves Aerobic Performance Without Any Negative Effect on Early Muscle Recovery Signaling in Response to Acute Exercise. Front Physiol. 2022 Feb 9;13.

181. Rahman I, Gilmour PS, Jimenez LA, Biswas SK, Antonicelli F, Aruoma OI. Ergothioneine inhibits oxidative stress- and TNF-α-induced NF-κB activation and interleukin-8 release in alveolar epithelial cells. Biochem Biophys Res Commun. 2003 Mar;302(4):860–4.

182. Maeda T, Hirayama M, Kobayashi D, Miyazawa K, Tamai I. Mechanism of the Regulation of Organic Cation/Carnitine Transporter 1 (*SLC22A4*) by Rheumatoid Arthritis-Associated Transcriptional Factor RUNX1 and Inflammatory Cytokines. Drug Metabolism and Disposition. 2007 Mar;35(3):394–401.

183. Pan HY, Ye ZW, Zheng QW, Yun F, Tu MZ, Hong WG, et al. Ergothioneine exhibits longevity-extension effect in *Drosophila melanogaster via* regulation of cholinergic neurotransmission, tyrosine metabolism, and fatty acid oxidation. Food Funct. 2022;13(1):227–41.

184. Teruya T, Chen YJ, Kondoh H, Fukuji Y, Yanagida M. Whole-blood metabolomics of dementia patients reveal classes of disease-linked metabolites. Proceedings of the National Academy of Sciences. 2021 Sep 14;118(37).

185. Hatano T, Saiki S, Okuzumi A, Mohney RP, Hattori N. Identification of novel biomarkers for Parkinson's disease by metabolomic technologies. J Neurol Neurosurg Psychiatry. 2016 Mar;87(3):295–301.

186. Kameda M, Teruya T, Yanagida M, Kondoh H. Frailty markers comprise blood metabolites involved in antioxidation, cognition, and mobility. Proceedings of the National Academy of Sciences. 2020 Apr 28;117(17):9483–9.

187. Cheah IK, Feng L, Tang RMY, Lim KHC, Halliwell B. Ergothioneine levels in an elderly population decrease with age and incidence of cognitive decline; a risk factor for neurodegeneration? Biochem Biophys Res Commun. 2016 Sep;478(1):162–7.

188. Smith E, Ottosson F, Hellstrand S, Ericson U, Orho-Melander M, Fernandez C, et al. Ergothioneine is associated with reduced mortality and decreased risk of cardiovascular disease. Heart. 2020 May;106(9):691–7.

189. Song TY, Chen CL, Liao JW, Ou HC, Tsai MS. Ergothioneine protects against neuronal injury induced by cisplatin both in vitro and in vivo. Food and Chemical Toxicology. 2010 Dec;48(12):3492–9.

190. Yang NC, Lin HC, Wu JH, Ou HC, Chai YC, Tseng CY, et al. Ergothioneine protects against neuronal injury induced by β-amyloid in mice. Food and Chemical Toxicology. 2012 Nov;50(11):3902–11.

191. Song TY, Lin HC, Chen CL, Wu JH, Liao JW, Hu ML. Ergothioneine and melatonin attenuate oxidative stress and protect against learning and memory deficits in C57BL/6J mice treated with D-galactose. Free Radic Res. 2014 Sep 21;48(9):1049–60.

192. Wijesinghe P, Whitmore CA, Campbell M, Li C, Tsuyuki M, To E, et al. Ergothioneine, a dietary antioxidant improves amyloid beta clearance in the neuroretina of a mouse model of Alzheimer's disease. Front Neurosci. 2023 Mar 14;17.

193. Cheah IK, Ng L, Ng L, Lam VY, Gruber J, Huang CYW, et al. Inhibition of amyloid-induced toxicity by ergothioneine in a transgenic *Caenorhabditis elegans* model. FEBS Lett. 2019 Aug 30;593(16):2139–50.

194. Jang JH, Aruoma OI, Jen LS, Chung HY, Surh YJ. Ergothioneine rescues PC12 cells from β-amyloid-induced apoptotic death. Free Radic Biol Med. 2004 Feb;36(3):288–99.

195. Brenner S. THE GENETICS OF *CAENORHABDITIS ELEGANS*. Genetics. 1974 May 1;77(1):71–94.

196. Chalfie M. Mutations that lead to reiterations in the cell lineages of C. elegans. Cell. 1981 Apr;24(1):59–69.

197. Sulston John E., Horvitz H.Robert. Abnormal cell lineages in mutants of the nematode Caenorhabditis elegans. Dev Biol. 1981 Feb;82(1):41–55.

198. Chalfie M, Tu Y, Euskirchen G, Ward WW, Prasher DC. Green Fluorescent Protein as a Marker for Gene Expression. Science (1979). 1994 Feb 11;263(5148):802–5.

199. Fire A, Xu S, Montgomery MK, Kostas SA, Driver SE, Mello CC. Potent and specific genetic interference by double-stranded RNA in Caenorhabditis elegans. Nature. 1998 Feb;391(6669):806–11.

200. Boeck ME, Huynh C, Gevirtzman L, Thompson OA, Wang G, Kasper DM, et al. The time-resolved transcriptome of *C. elegans*. Genome Res. 2016 Oct;26(10):1441–50.

201. Walther DM, Kasturi P, Zheng M, Pinkert S, Vecchi G, Ciryam P, et al. Widespread Proteome Remodeling and Aggregation in Aging C. elegans. Cell. 2015 May;161(4):919–32.

202. Rodriguez M, Snoek LB, De Bono M, Kammenga JE. Worms under stress: C. elegans stress response and its relevance to complex human disease and aging. Trends in Genetics. 2013 Jun;29(6):367–74.

203. Qin Z, Johnsen R, Yu S, Chu JSC, Baillie DL, Chen N. Genomic Identification and Functional Characterization of Essential Genes in *Caenorhabditis elegans*. G3 Genes|Genomes|Genetics. 2018 Mar 1;8(3):981–97.

204. Ng LF, Ng LT, van Breugel M, Halliwell B, Gruber J. Mitochondrial DNA Damage Does Not Determine C. elegans Lifespan. Front Genet. 2019 Apr 12;10.

205. Santonicola P, Germoglio M, d'Abbusco DS, Adamo A. Functional characterization of Caenorhabditis elegans cbs-2 gene during meiosis. Sci Rep. 2020 Dec 1;10(1):20913.

206. Budde MW, Roth MB. The Response of *Caenorhabditis elegans* to Hydrogen Sulfide and Hydrogen Cyanide. Genetics. 2011 Oct 1;189(2):521–32.

207. Wang B, Pandey T, Long Y, Delgado-Rodriguez SE, Daugherty MD, Ma DK. Co-opted genes of algal origin protect C. elegans against cyanogenic toxins. Current Biology. 2022 Nov;32(22):4941-4948.e3.

208. Burton NO, Riccio C, Dallaire A, Price J, Jenkins B, Koulman A, et al. Cysteine synthases CYSL-1 and CYSL-2 mediate C. elegans heritable adaptation to P. vranovensis infection. Nat Commun. 2020 Apr 8;11(1):1741.

209. Miller DL, Roth MB. Hydrogen sulfide increases thermotolerance and lifespan in *Caenorhabditis elegans*. Proceedings of the National Academy of Sciences. 2007 Dec 18;104(51):20618–22.

210. Miller DL, Budde MW, Roth MB. HIF-1 and SKN-1 Coordinate the Transcriptional Response to Hydrogen Sulfide in Caenorhabditis elegans. PLoS One. 2011 Sep 29;6(9):e25476.

211. Jiang H, Guo R, Powell-Coffman JA. The *Caenorhabditis elegans hif-1* gene encodes a bHLH-PAS protein that is required for adaptation to hypoxia. Proceedings of the National Academy of Sciences. 2001 Jul 3;98(14):7916–21.

212. An JH, Blackwell TK. SKN-1 links *C. elegans* mesendodermal specification to a conserved oxidative stress response. Genes Dev. 2003 Aug 1;17(15):1882–93.

213. Ma DK, Vozdek R, Bhatla N, Horvitz HR. CYSL-1 Interacts with the O2-Sensing Hydroxylase EGL-9 to Promote H2S-Modulated Hypoxia-Induced Behavioral Plasticity in C. elegans. Neuron. 2012 Mar;73(5):925–40.

214. Horsman JW, Heinis FI, Miller DL. A Novel Mechanism To Prevent H2S Toxicity in *Caenorhabditis elegans*. Genetics. 2019 Oct 1;213(2):481–90.

215. Fawcett EM, Hoyt JM, Johnson JK, Miller DL. Hypoxia disrupts proteostasis in *Caenorhabditis elegans*. Aging Cell. 2015 Feb 16;14(1):92–101.

216. Qabazard B, Ahmed S, Li L, Arlt VM, Moore PK, Stürzenbaum SR. C. elegans Aging Is Modulated by Hydrogen Sulfide and the sulfhydrylase/cysteine Synthase cysl-2. PLoS One. 2013 Nov 8;8(11):e80135.

217. Ng LT, Ng LF, Tang RMY, Barardo D, Halliwell B, Moore PK, et al. Lifespan and healthspan benefits of exogenous H2S in C. elegans are independent from effects downstream of eat-2 mutation. NPJ Aging Mech Dis. 2020 Jun 10;6(1):6.

218. Oh KH, Kim H. Reduced IGF signaling prevents muscle cell death in a *Caenorhabditis*

elegans model of muscular dystrophy. Proceedings of the National Academy of Sciences. 2013 Nov 19;110(47):19024–9.

219. Wei Y, Kenyon C. Roles for ROS and hydrogen sulfide in the longevity response to germline loss in *Caenorhabditis elegans*. Proceedings of the National Academy of Sciences. 2016 May 17;113(20).

220. Lee HJ, Noormohammadi A, Koyuncu S, Calculli G, Simic MS, Herholz M, et al. Prostaglandin signals from adult germline stem cells delay somatic ageing of Caenorhabditis elegans. Nat Metab. 2019 Aug 19;1(8):790–810.

221. Hine C, Harputlugil E, Zhang Y, Ruckenstuhl C, Lee BC, Brace L, et al. Endogenous Hydrogen Sulfide Production Is Essential for Dietary Restriction Benefits. Cell. 2015 Jan;160(1–2):132–44.

222. López-Otín C, Blasco MA, Partridge L, Serrano M, Kroemer G. The Hallmarks of Aging. Cell. 2013 Jun;153(6):1194–217.

223. López-Otín C, Blasco MA, Partridge L, Serrano M, Kroemer G. Hallmarks of aging: An expanding universe. Cell. 2023 Jan;186(2):243–78.

224. Narayan V, Ly T, Pourkarimi E, Murillo AB, Gartner A, Lamond AI, et al. Deep Proteome Analysis Identifies Age-Related Processes in C. elegans. Cell Syst. 2016 Aug;3(2):144–59.

225. Li H, Zhang C, Sun W, Li L, Wu B, Bai S, et al. Exogenous hydrogen sulfide restores cardioprotection of ischemic post-conditioning via inhibition of mPTP opening in the aging cardiomyocytes. Cell Biosci. 2015 Dec 30;5(1):43.

226. Perridon BW, Leuvenink HGD, Hillebrands JL, van Goor H, Bos EM. The role of hydrogen sulfide in aging and age-related pathologies. Aging. 2016 Sep 27;8(10):2264–89.

227. Longchamp A, Mirabella T, Arduini A, MacArthur MR, Das A, Treviño-Villarreal JH, et al. Amino Acid Restriction Triggers Angiogenesis via GCN2/ATF4 Regulation of VEGF and H2S Production. Cell. 2018 Mar;173(1):117-129.e14.

228. Das A, Huang GX, Bonkowski MS, Longchamp A, Li C, Schultz MB, et al. Impairment of an Endothelial NAD+-H2S Signaling Network Is a Reversible Cause of Vascular Aging. Cell. 2018 Mar;173(1):74-89.e20.

229. Yang L, Cao Y, Zhao J, Fang Y, Liu N, Zhang Y. Multidimensional Proteomics Identifies Declines in Protein Homeostasis and Mitochondria as Early Signals for Normal Aging and Age-associated Disease in Drosophila*[S]. Molecular & Cellular Proteomics. 2019 Oct;18(10):2078–88.

230. David DC, Ollikainen N, Trinidad JC, Cary MP, Burlingame AL, Kenyon C. Widespread Protein Aggregation as an Inherent Part of Aging in C. elegans. PLoS Biol. 2010 Aug 10;8(8):e1000450.

231. Chen YR, Harel I, Singh PP, Ziv I, Moses E, Goshtchevsky U, et al. Tissue-specific landscape of protein aggregation and quality control in an aging vertebrate. Dev Cell. 2024 Jul;59(14):1892-1911.e13.

232. Akter S, Fu L, Jung Y, Conte M Lo, Lawson JR, Lowther WT, et al. Chemical proteomics reveals new targets of cysteine sulfinic acid reductase. Nat Chem Biol. 2018 Nov 3;14(11):995–1004.

233. Sbodio JI, Snyder SH, Paul BD. Golgi stress response reprograms cysteine metabolism to confer cytoprotection in Huntington's disease. Proceedings of the National Academy of

Sciences. 2018 Jan 23;115(4):780–5.

234. Yang G, Wu L, Jiang B, Yang W, Qi J, Cao K, et al. H $_2$ S as a Physiologic Vasorelaxant: Hypertension in Mice with Deletion of Cystathionine γ-Lyase. Science (1979). 2008 Oct 24;322(5901):587–90.

235. Snijder PM, Baratashvili M, Grzeschik NA, Leuvenink HGD, Kuijpers L, Huitema S, et al. Overexpression of Cystathionine γ-Lyase Suppresses Detrimental Effects of Spinocerebellar Ataxia Type 3. Molecular Medicine. 2015 Jan 13;21(1):758–68.

236. Giovinazzo D, Bursac B, Sbodio JI, Nalluru S, Vignane T, Snowman AM, et al. Hydrogen sulfide is neuroprotective in Alzheimer's disease by sulfhydrating GSK3β and inhibiting Tau hyperphosphorylation. Proceedings of the National Academy of Sciences. 2021 Jan 26;118(4).

237. Vabulas RM, Raychaudhuri S, Hayer-Hartl M, Hartl FU. Protein Folding in the Cytoplasm and the Heat Shock Response. Cold Spring Harb Perspect Biol. 2010 Dec 1;2(12):a004390–a004390.

238. Hetz C. The unfolded protein response: controlling cell fate decisions under ER stress and beyond. Nat Rev Mol Cell Biol. 2012 Feb 18;13(2):89–102.

239. Costa-Mattioli M, Walter P. The integrated stress response: From mechanism to disease. Science (1979). 2020 Apr 24;368(6489).

240. Pakos-Zebrucka K, Koryga I, Mnich K, Ljujic M, Samali A, Gorman AM. The integrated stress response. EMBO Rep. 2016 Oct 14;17(10):1374–95.

241. García MA, Meurs EF, Esteban M. The dsRNA protein kinase PKR: Virus and cell control. Biochimie. 2007 Jun;89(6–7):799–811.

242. Dey M, Cao C, Dar AC, Tamura T, Ozato K, Sicheri F, et al. Mechanistic Link between PKR Dimerization, Autophosphorylation, and eIF2α Substrate Recognition. Cell. 2005 Sep;122(6):901–13.

243. Guo X, Aviles G, Liu Y, Tian R, Unger BA, Lin YHT, et al. Mitochondrial stress is relayed to the cytosol by an OMA1–DELE1–HRI pathway. Nature. 2020 Mar 19;579(7799):427–32.

244. Hinnebusch AG. TRANSLATIONAL REGULATION OF *GCN4* AND THE GENERAL AMINO ACID CONTROL OF YEAST. Annu Rev Microbiol. 2005 Oct 1;59(1):407–50.

245. Zhang P, McGrath BC, Reinert J, Olsen DS, Lei L, Gill S, et al. The GCN2 eIF2α Kinase Is Required for Adaptation to Amino Acid Deprivation in Mice. Mol Cell Biol. 2002 Oct 1;22(19):6681–8.

246. Chen JJ. Translational control by heme-regulated eIF2α kinase during erythropoiesis. Curr Opin Hematol. 2014 May;21(3):172–8.

247. Teske BF, Wek SA, Bunpo P, Cundiff JK, McClintick JN, Anthony TG, et al. The eIF2 kinase PERK and the integrated stress response facilitate activation of ATF6 during endoplasmic reticulum stress. Mol Biol Cell. 2011 Nov 15;22(22):4390–405.

248. Palam LR, Baird TD, Wek RC. Phosphorylation of eIF2 Facilitates Ribosomal Bypass of an Inhibitory Upstream ORF to Enhance CHOP Translation. Journal of Biological Chemistry. 2011 Apr;286(13):10939–49.

249. Zhou D, Palam LR, Jiang L, Narasimhan J, Staschke KA, Wek RC. Phosphorylation of eIF2 directs ATF5 translational control in response to diverse stress conditions. J Biol Chem.

2008 Mar 14;283(11):7064–73.

250. Lee YY, Cevallos RC, Jan E. An Upstream Open Reading Frame Regulates Translation of GADD34 during Cellular Stresses That Induce eIF2α Phosphorylation. Journal of Biological Chemistry. 2009 Mar;284(11):6661–73.

251. Lassot I, Ségéral E, Berlioz-Torrent C, Durand H, Groussin L, Hai T, et al. ATF4 Degradation Relies on a Phosphorylation-Dependent Interaction with the SCF $^{\beta TrCP}$ Ubiquitin Ligase. Mol Cell Biol. 2001 Mar 1;21(6):2192–202.

252. Igarashi T, Izumi H, Uchiumi T, Nishio K, Arao T, Tanabe M, et al. Clock and ATF4 transcription system regulates drug resistance in human cancer cell lines. Oncogene. 2007 Jul 19;26(33):4749–60.

253. Afonyushkin T, Oskolkova O V., Philippova M, Resink TJ, Erne P, Binder BR, et al. Oxidized Phospholipids Regulate Expression of ATF4 and VEGF in Endothelial Cells via NRF2-Dependent Mechanism: Novel Point of Convergence Between Electrophilic and Unfolded Protein Stress Pathways. Arterioscler Thromb Vasc Biol. 2010 May;30(5):1007–13.

254. Yang X, Matsuda K, Bialek P, Jacquot S, Masuoka HC, Schinke T, et al. ATF4 Is a Substrate of RSK2 and an Essential Regulator of Osteoblast Biology. Cell. 2004 Apr;117(3):387–98.

255. Brand MD, Orr AL, Perevoshchikova IV, Quinlan CL. The role of mitochondrial function and cellular bioenergetics in ageing and disease. British Journal of Dermatology. 2013 Jul;169:1–8.

256. Osellame LD, Blacker TS, Duchen MR. Cellular and molecular mechanisms of mitochondrial function. Best Pract Res Clin Endocrinol Metab. 2012 Dec;26(6):711–23.

257. Stehling O, Lill R. The Role of Mitochondria in Cellular Iron-Sulfur Protein Biogenesis: Mechanisms, Connected Processes, and Diseases. Cold Spring Harb Perspect Biol. 2013 Aug 1;5(8):a011312–a011312.

258. Baker MJ, Lampe PA, Stojanovski D, Korwitz A, Anand R, Tatsuta T, et al. Stress-induced OMA1 activation and autocatalytic turnover regulate OPA1-dependent mitochondrial dynamics. EMBO J. 2014 Mar 18;33(6):578–93.

259. Malka F, Guillery O, Cifuentes-Diaz C, Guillou E, Belenguer P, Lombès A, et al. Separate fusion of outer and inner mitochondrial membranes. EMBO Rep. 2005 Sep;6(9):853–9.

260. Song Z, Ghochani M, McCaffery JM, Frey TG, Chan DC. Mitofusins and OPA1 Mediate Sequential Steps in Mitochondrial Membrane Fusion. Mol Biol Cell. 2009 Aug;20(15):3525–32.

261. Breckenridge DG, Kang BH, Kokel D, Mitani S, Staehelin LA, Xue D. Caenorhabditis elegans drp-1 and fis-2 Regulate Distinct Cell-Death Execution Pathways Downstream of ced-3 and Independent of ced-9. Mol Cell. 2008 Aug;31(4):586–97.

262. Kanazawa T, Zappaterra MD, Hasegawa A, Wright AP, Newman-Smith ED, Buttle KF, et al. The C. elegans Opa1 Homologue EAT-3 Is Essential for Resistance to Free Radicals. PLoS Genet. 2008 Feb 29;4(2):e1000022.

263. Rolland SG, Lu Y, David CN, Conradt B. The BCL-2–like protein CED-9 of *C. elegans* promotes FZO-1/Mfn1,2– and EAT-3/Opa1–dependent mitochondrial fusion. Journal of Cell Biology. 2009 Aug 24;186(4):525–40.

264. Losón OC, Song Z, Chen H, Chan DC. Fis1, Mff, MiD49, and MiD51 mediate Drp1

recruitment in mitochondrial fission. Mol Biol Cell. 2013 Mar;24(5):659–67.

265. Westermann B. Mitochondrial dynamics in model organisms: What yeasts, worms and flies have taught us about fusion and fission of mitochondria. Semin Cell Dev Biol. 2010 Aug;21(6):542–9.

266. Bao XR, Ong SE, Goldberger O, Peng J, Sharma R, Thompson DA, et al. Mitochondrial dysfunction remodels one-carbon metabolism in human cells. Elife. 2016 Jun 16;5.

267. Quirós PM, Prado MA, Zamboni N, D'Amico D, Williams RW, Finley D, et al. Multi-omics analysis identifies ATF4 as a key regulator of the mitochondrial stress response in mammals. Journal of Cell Biology. 2017 Jul 3;216(7):2027–45.

268. Kaspar S, Oertlin C, Szczepanowska K, Kukat A, Senft K, Lucas C, et al. Adaptation to mitochondrial stress requires CHOP-directed tuning of ISR. Sci Adv. 2021 May 28;7(22).

269. Melber A, Haynes CM. UPRmt regulation and output: a stress response mediated by mitochondrial-nuclear communication. Cell Res. 2018 Mar 9;28(3):281–95.

270. Houtkooper RH, Mouchiroud L, Ryu D, Moullan N, Katsyuba E, Knott G, et al. Mitonuclear protein imbalance as a conserved longevity mechanism. Nature. 2013 May 23;497(7450):451–7.

271. Nargund AM, Pellegrino MW, Fiorese CJ, Baker BM, Haynes CM. Mitochondrial Import Efficiency of ATFS-1 Regulates Mitochondrial UPR Activation. Science (1979). 2012 Aug 3;337(6094):587–90.

272. Owusu-Ansah E, Song W, Perrimon N. Muscle Mitohormesis Promotes Longevity via Systemic Repression of Insulin Signaling. Cell. 2013 Oct;155(3):699–712.

273. Jiang Z, Hu Z, Zeng L, Lu W, Zhang H, Li T, et al. The role of the Golgi apparatus in oxidative stress: is this organelle less significant than mitochondria? Free Radic Biol Med. 2011 Apr;50(8):907–17.

274. Farquhar MG, Palade GE. The Golgi apparatus: 100 years of progress and controversy. Trends Cell Biol. 1998 Jan;8(1):2–10.

275. Chen X, Shi C, He M, Xiong S, Xia X. Endoplasmic reticulum stress: molecular mechanism and therapeutic targets. Signal Transduct Target Ther. 2023 Sep 15;8(1):352.

276. Wang M, Kaufman RJ. Protein misfolding in the endoplasmic reticulum as a conduit to human disease. Nature. 2016 Jan 20;529(7586):326–35.

277. Walter P, Ron D. The Unfolded Protein Response: From Stress Pathway to Homeostatic Regulation. Science (1979). 2011 Nov 25;334(6059):1081–6.

278. Dickhout JG, Carlisle RE, Jerome DE, Mohammed-Ali Z, Jiang H, Yang G, et al. Integrated Stress Response Modulates Cellular Redox State via Induction of Cystathionine γ-Lyase. Journal of Biological Chemistry. 2012 Mar;287(10):7603–14.

279. Harding HP, Zhang Y, Zeng H, Novoa I, Lu PD, Calfon M, et al. An Integrated Stress Response Regulates Amino Acid Metabolism and Resistance to Oxidative Stress. Mol Cell. 2003 Mar;11(3):619–33.

280. Yadav V, Gao XH, Willard B, Hatzoglou M, Banerjee R, Kabil O. Hydrogen sulfide modulates eukaryotic translation initiation factor 2α (eIF2α) phosphorylation status in the integrated stress-response pathway. Journal of Biological Chemistry. 2017 Aug;292(32):13143–53.

281. Zhang Y, Wang Y, Read E, Fu M, Pei Y, Wu L, et al. Golgi Stress Response, Hydrogen Sulfide Metabolism, and Intracellular Calcium Homeostasis. Antioxid Redox Signal. 2020 Mar 20;32(9):583–601.

282. Zhu H, Liang C, Cai X, Zhang H, Liu C, Jia P, et al. Rational Design of a Targetable Fluorescent Probe for Visualizing H_2S Production under Golgi Stress Response Elicited by Monensin. Anal Chem. 2020 Jan 21;92(2):1883–9.

283. Łowicki D, Huczyński A. Structure and Antimicrobial Properties of Monensin A and Its Derivatives: Summary of the Achievements. Biomed Res Int. 2013;2013:1–14.

284. Wang X, Jiang Q, Song Y, He Z, Zhang H, Song M, et al. Ageing induces tissue-specific transcriptomic changes in *Caenorhabditis elegans*. EMBO J. 2022 Apr 19;41(8).

285. Roux AE, Yuan H, Podshivalova K, Hendrickson D, Kerr R, Kenyon C, et al. Individual cell types in C. elegans age differently and activate distinct cell-protective responses. Cell Rep. 2023 Aug;42(8):112902.

286. Calculli G, Lee HJ, Shen K, Pham U, Herholz M, Trifunovic A, et al. Systemic regulation of mitochondria by germline proteostasis prevents protein aggregation in the soma of *C. elegans*. Sci Adv. 2021 Jun 25;7(26).

287. Eder M, Martin OMF, Oswal N, Sedlackova L, Moutinho C, Del Carmen-Fabregat A, et al. Systematic mapping of organism-scale gene-regulatory networks in aging using population asynchrony. Cell. 2024 Jul;187(15):3919-3935.e19.

288. Zhang WH, Koyuncu S, Vilchez D. Insights Into the Links Between Proteostasis and Aging From C. elegans. Frontiers in Aging. 2022 Mar 18;3.

289. Koyuncu S, Loureiro R, Lee HJ, Wagle P, Krueger M, Vilchez D. Rewiring of the ubiquitinated proteome determines ageing in C. elegans. Nature. 2021 Aug 12;596(7871):285–90.